GENERALIZED FINITE ELEMENT METHOD FOR MULTISCALE ANALYSIS

A Dissertation

by

LIN ZHANG

Submitted to the Office of Graduate Studies of
Texas A&M University
in partial fulfillment of the requirements for the degree of

DOCTOR OF PHILOSOPHY

August 2003

Major Subject: Aerospace Engineering

GENERALIZED FINITE ELEMENT METHOD FOR MULTISCALE ANALYSIS

A Dissertation

by

LIN ZHANG

Submitted to Texas A&M University
in partial fulfillment of the requirements
for the degree of

DOCTOR OF PHILOSOPHY

Approved as to style and content by:

T. Strouboulis
(Chair of Committee)

J. Whitcomb
(Member)

J. N. Reddy
(Member)

J. Pasciak
(Member)

W. Haisler
(Head of Department)

August 2003

Major Subject: Aerospace Engineering

ABSTRACT

Generalized Finite Element Method for Multiscale Analysis. (August 2003)
Lin Zhang, B.S., Computational Mathematics, Fudan University;
M.S., Computational Mathematics, Fudan University
Chair of Advisory Committee: Dr. T. Strouboulis

This dissertation describes a new version of the Generalized Finite Element Method (GFEM), which is well suited for problems set in domains with a large number of internal features (e.g. voids, inclusions, etc.), which are practically impossible to solve using the standard FEM. The main idea is to employ the *mesh-based* handbook functions which are solutions of boundary value problems in domains extracted from vertex patches of the employed mesh and are pasted into the global approximation by the Partition of Unity Method (PUM). It is shown that the p-version of the Generalized FEM using mesh-based handbook functions is capable of achieving very high accuracy.

It is also analyzed that the effect of the main factors affecting the accuracy of the method namely: (a) The data and the buffer included in the handbook domains, and (b) The accuracy of the numerical construction of the handbook functions. The robustness of the method is illustrated by several model problems defined in domains with a large number of closely spaced voids and/or inclusions with various shapes, including the heat conduction problem defined on domains with porous media and/or a real composite material.

To my family: my wife, *Lan*, and my daughters, *Sherry* and *Sarah*

ACKNOWLEDGMENTS

I would like to express my sincere appreciation to the chairman of my advisory committee, Dr. Theofanis Strouboulis, for his invaluable guidance, assistance and encouragement throughout this effort. I am indebted to him for his continuous support and patience.

I would like to thank Dr. J. Whitcomb, Dr. J.N. Reddy, Dr. J. Pasciak, and Dr. T. Kiffe for serving on my advisory committee. Thanks also to Dr. Vadali for his presence at my defense to substitute for Dr. Whitcomb. I especially thank Dr. Alfriend for his support and help during my graduate studies at the Department of Aerospace Engineering, Texas A&M University.

I would like to express my gratitude to Professor Ivo Babuška for his advice and encouragement during the course of this work. I am grateful to him for the invaluable discussions in the past years. I would also like to thank Dr. Oden for his help and support.

I would like to thank Dr. Kevin Copps for allowing me to use his Fortran code on which I based and developed my current GFEM code. Thanks also to my colleagues Dr. Dibyendu Datta, Mr. Delin Wang, and Mr. Realino Hidajat for their help and support.

This work was partially supported by the Office of Naval Research under Grant N00014-99-1-0726.

TABLE OF CONTENTS

CHAPTER Page

CHAPTER Page

LIST OF TABLES

TABLE Page

LIST OF FIGURES

FIGURE Page

FIGURE Page

FIGURE Page

CHAPTER I

INTRODUCTION

1.1 Motivation and background

Many problems of practical importance are described in domains with complex geometries. The typical examples include porous media, composite materials, etc. Figure 1.1 shows an example of composite materials with 16275 fibers (see [1]). A numerical solution by standard Finite Element Methods (FEM) for this kind of problems is practically impossible even with modern supercomputers. The major difficulty of standard FEM is either the scale of the computation, or the meshing of the domain, or both. Figure 1.2(b) shows a mesh with 11432 quadrilateral elements (with 12753 nodes) generated by ANSYS for a small square area (including 84 voids) cut from the domain shown in Figure 1.2(a). It would have about 2.5 million degrees of freedom if the linear standard FEM is employed for the whole problem. Especially, when the voids or inclusions are very close, it is impossible to mesh the area between voids or inclusions. Therefore, a robust method for this type of problems is of great importance for engineering analysis.

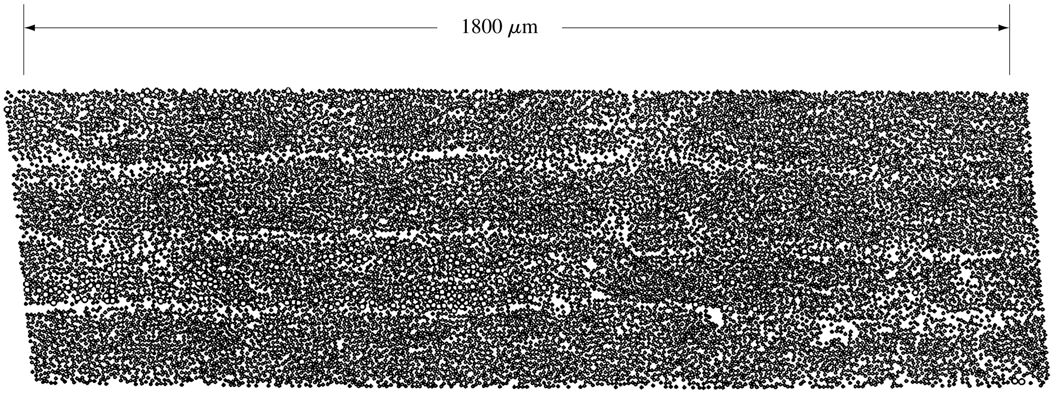

Figure 1.1. Cross section of a fiber reinforced composite with 16275 fibers

The above-mentioned problems have dominated research on the mechanics of materials for many years, and led to the study of methods to overcome/avoid the above-mentioned difficulties. A natural idea to develop robust methods could be to extract effective properties of materials for the macro-performance of material bodies without taking into account all the features in the domain of interest, that is *homogenization*. Early works in this area,

---

This dissertation follows the style of Computer Methods in Applied Mechanics and Engineering.

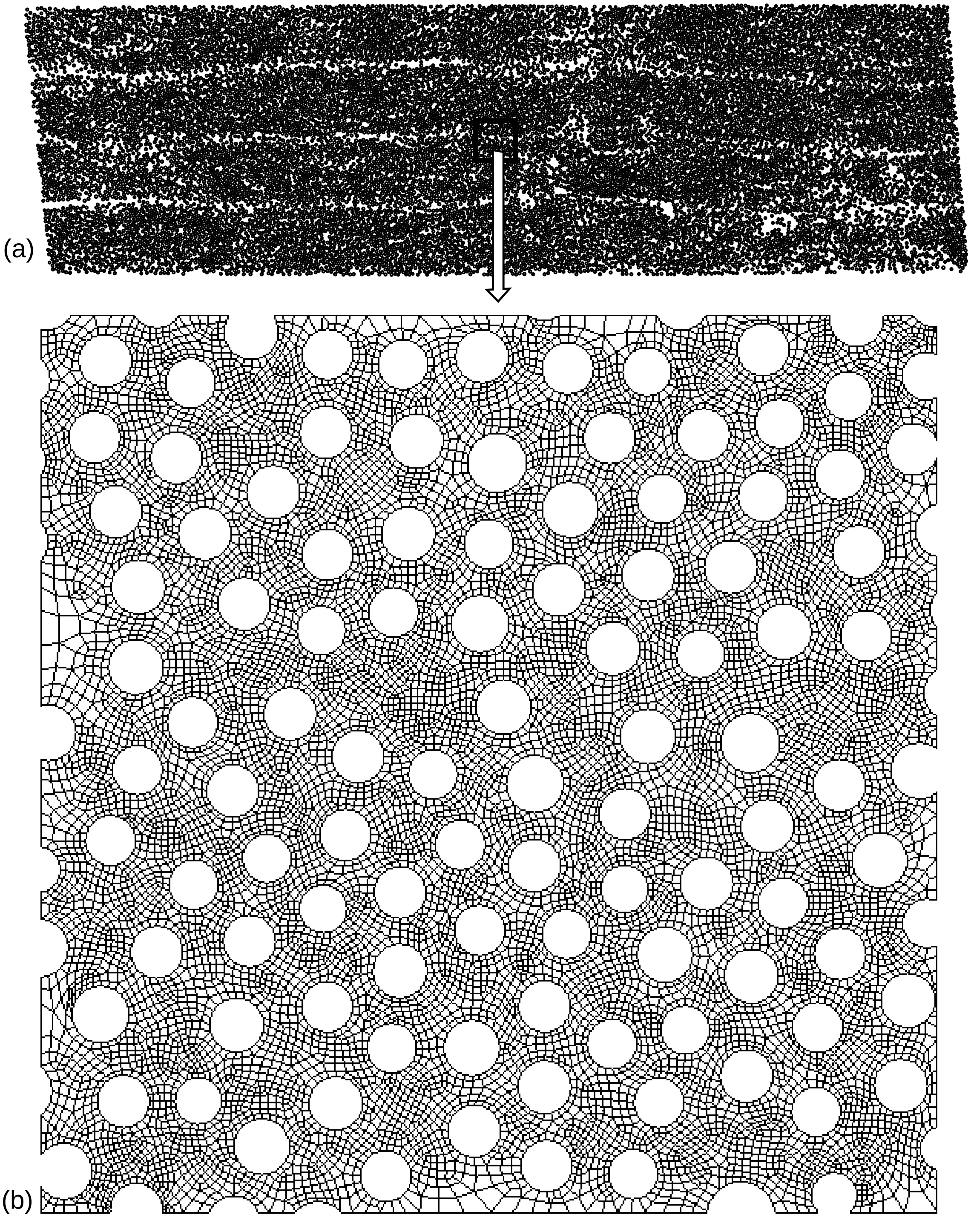

Figure 1.2. (a). A domain with 16275 voids; (b). A quadrilateral FEM mesh (with 11432 elements and 12753 nodes) generated by ANSYS for a small square area, which only includes 84 voids, cutting from the domain shown in (a).

including those by Hill [2] and Hashin and Shtrikman [3], are based on the assumption of existence of a *Representative Volume Element* (RVE). The mathematical aspects of asymptotic homogenization, wherein the microstructure is assumed to be periodic, have been studied in details and can be found in the works of Babuška et al. [4–11], Bensoussan et al. [12], Jikov et al. [13], Sanchez-Palencia [14], Cioranescu et al. [15, 16], and Bakhvalov and Panasenko [17].

The *Multiscale Analysis* is another straightforward idea for the above-mentioned problems. Since the macro-behavior of material bodies depends upon micromechanical properties, the macro-analysis for the problems must be more reliable if the information about the local micromechanical properties can be utilized. For this purpose, various methods have been proposed, such as Adaptive Hierarchical Modeling (developed by Oden et al. [18–25]), X-FEM (extended FEM, developed by Belytschko et al. [26–35]), Multiscale Finite Element Method (developed by Hou et al. [36–39]), VCFEM (Voronoi Cell Finite Element Method, developed by Ghosh et al. [40–43]), and Generalized FEM (GFEM, developed by Babuška and Strouboulis, et al. [44–54]).

Based on the work of a posteriori error estimation (see Babuška and Strouboulis [55], and Oden el al. [56–62], and the references therein), the concept of Adaptive Hierarchical Modeling was introduced by Oden el al. [18–25] as a methodology that provides a multilevel description of the physical phenomenon of interest. The hierarchical description of the problem is set up ranging from the coarsest possible description to the most detailed description. Instead of choosing one level of description from the hierarchy, they use a posteriori error estimate of the modeling error associated with a particular description to adaptively select a suitable characterization of the problem. The model at the coarsest level in the hierarchy is characterized by homogenized material properties and this is referred to as the homogenized problem. The adequacy of the solution to this homogenized problem, compared to the fine-scale solution, is then estimated using a posteriori error estimate. In regions where the modeling error exceeds a preset tolerance, a finer-scale model is used and a correction to the homogenized solution is computed. The Adaptive Hierarchical Modeling method enables us to know how accurate our solution is. However, they use the standard FEM to solve for the solution at each level of the hierarchy. This restricts the method only for the problems with not very complex geometries.

Belytschko et al. proposed an extension of the standard FEM, called X-FEM [26, 27, 29–35]. Similar to the Generalized FEM, the X-FEM also employs the Partition of Unity Method (PUM) to patch the special functions, level set functions, into the FEM approximation. The key point of X-FEM is the selection of the level set functions which reflect the local geometrical characters of features. But unlike the handbook functions employed by the Generalized FEM, the level set functions is not expected to reflect the local behavior of the exact solution. For example, the level set function for a circular void is just the distance function which can not reflect the local properties of the global exact solution. Further, it seems that X-FEM can not solve the above-mentioned problems with a large number of features in the domain of interest.

The Multiscale Finite Element Method was developed by Hou et al. [36–39] for elliptic problems in composite materials and porous media. The method is expected to efficiently capture the large scale behavior of the solution by introducing special functions into the finite element space which reflect the local behavior of the solution around the features. In [37] the upscaling method is analyzed and various difficulties with the method are shown. In [36] an *oversampling* method is suggested, which also used a *cell solutions with buffers* similar to the handbook solutions employed by the Generalized FEM. However the method in [36] leads to the use of a non-conforming approximation! [38] presents the mathematical analysis of the oversampling method.

Ghosh et al. [40–43] introduced the Voronoi Cell Finite Element Method (VCFEM) in which the finite element mesh evolves by Dirichlet Tessellation of a representative microstructure. Tessellation of a microstructural representative material element discretizes the domain into a network of multi-sided convex "Voronoi" polygons or cells, and each Voronoi cell includes only one inclusion at most. They developed the formulations for directly treating multiple phase Voronoi polygons as elements in a finite element model, by employing the hybrid finite element method. Let us note that VCFEM would result in a large number of Voronoi polygons if it is employed for the above-mentioned problems or any real heterogeneous problems.

The Generalized FEM was introduced by Strouboulis, Copps and Babuška [49–52] as a combination of the Partition of Unity Method (PUM), which was first introduced in [11] and developed in [44–46, 48, 63, 64], and the classical Finite Element Method (FEM) (see [65, 66]). A main feature of the method is the capability of enriching the approximation by *handbook functions* which are solutions of local boundary value problems, called *handbook problems*, reflecting the local geometry and boundary conditions of the problem at hand. The handbook functions are pasted into the FEM approximation by the Partition of Unity Method (PUM), namely after they are multiplied by the *vertex hat functions*, namely the finite element basis functions of degree one, on the employed computational mesh. Another important feature of the Generalized FEM introduced in [49–52] is the capability of constructing approximate solutions using computational meshes which may overlap part of or the entire domain boundary. Hence Generalized FEM solutions can be computed using very simple meshes e.g. meshes of squares constructed by refining uniformly a square which includes the problem domain in its interior. This capability makes it possible to address local geometries and boundary conditions for which special functions may not be available or may be rather cumbersome to construct in analytical form, e.g. a square or a polygonal void, a bifurcated crack, a corner with curved edges, etc., or generalized harmonic functions (see [67, 68]) for problems with non-constant coefficients in the interior or at the boundary of the domain.

The Generalized FEM presented in [49–52] is well suited for the analysis of multi-site or hidden damage (see [69]) where one needs to solve a problem for many (e.g. thousands of) configurations of hidden or unknown damage, e.g. for a crack occuring at the most unfavorable location and orientation for the durability of a structure. But a new version of the Generalized FEM needs to be developed for the above-mentioned problems with large number of features in the domain of interest.

1.2 Goals and main contributions

In the version of Generalized FEM presented in [49–52], the construction of the stiffness coefficients involving the handbook functions requires the use of the inverse element transformation in the handbook mesh at each integration point of the global GFEM mesh which can be very CPU intensive. To address this difficulty, in this dissertation, a new version of the Generalized FEM was developed by introducing *mesh-based handbooks*, which employs handbook domains fitting exactly in the employed computational mesh, so that the transfer of the handbook functions from the handbook domains to the global mesh is straightforward and the CPU cost of numerical integrations is drastically reduced. We call this new version, Generalized FEM using *mesh-based* handbooks. In this dissertation we illustrate this method using example problems for the Laplacian in domains with a large number of closely spaced randomly distributed voids or inclusions, e.g. the problem shown in Figure 1.1; the method can be easily extended to the case that the voids are replaced by cracks or inclusions of various shapes. The reason for choosing this type of examples is because we want to show the robustness and high accuracy capability of the method for problems which cannot be practically solved by the classical FEM and to underline, *the high accuracy of the Generalized FEM is due to the enrichment by handbook functions*.

Let us give a preview of the example problem and the results to be presented below which underline these points. We will employ as our example problem, the Neumann problem (2.20) for the Laplacian in a square domain including 597 circular voids shown in Figure 1.3)(a) (see details in next chapters). Let us compute a bi-p Generalized FEM solution for this problem using $p = 1, 2$ on the 16×16 mesh of squares shown in Figure 1.3(b) with and without enrichment by vertex handbook functions, as described in [53] and in Chapter III below. Figures 1.4(a)-(d) compare the accuracy of the computed Generalized FEM solutions with and without enrichment by vertex handbook functions. Once more we see that *the enrichment by handbook functions is responsible for the high accuracy of the*

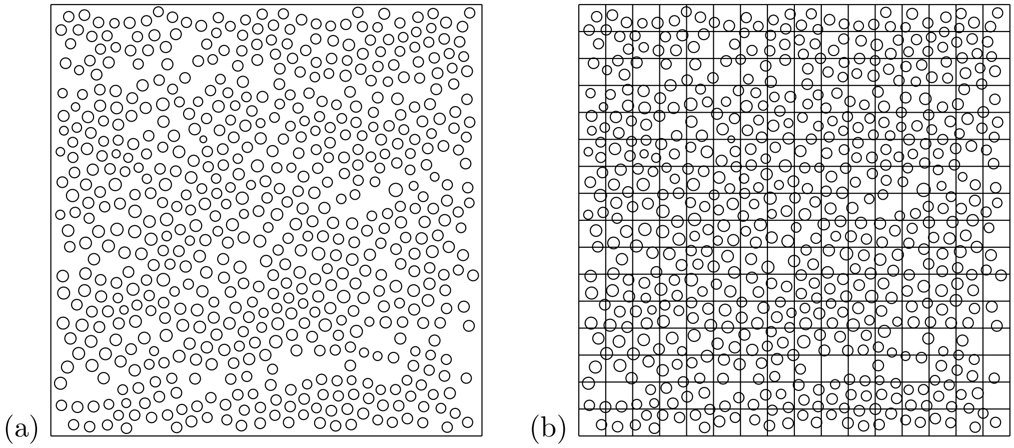

Figure 1.3. (a). The problem domain which includes 597 voids in its interior is shown here for $\gamma = 1.0$. (b). The 16×16 mesh for the problem domain shown in (a).

Generalized FEM solution.

In this dissertation, we developed and analyzed the Generalized FEM using mesh-based handbook functions. The main points of this dissertation are:

(1). Comparison of the p and p-handbook version of the Generalized FEM with the h version of the Generalized FEM, which sets into perspective the high accuracy of the Generalized FEM.

(2). Analysis of the effect of the errors in the numerical construction of the handbook functions on the accuracy of the Generalized FEM solution.

(3). Analysis of the effect of the data and of the buffer included in the definition of the handbook domains on the accuracy of the GFEM solution.

(4). Analysis of the CPU cost of the method.

(5). Analysis of the robustness of the Generalized FEM using mesh-based handbook functions for the problems with various types of features.

(6). Analysis of the robustness of the Generalized FEM using mesh-based handbook functions for the problems with large number of features.

The main conclusions are:

(1). The p-handbook version of the Generalized FEM is robust and can achieve much higher accuracy than the standard FEM or the Generalized FEM without handbook functions on comparable meshes.

(2). The p version of the Generalized FEM has similar robustness as the p-handbook version provided that it is enriched by handbook functions of degree at least one.

(3). The high accuracy of the p-handbook version of the Generalized FEM may be polluted by errors in the numerical construction of the handbook functions.

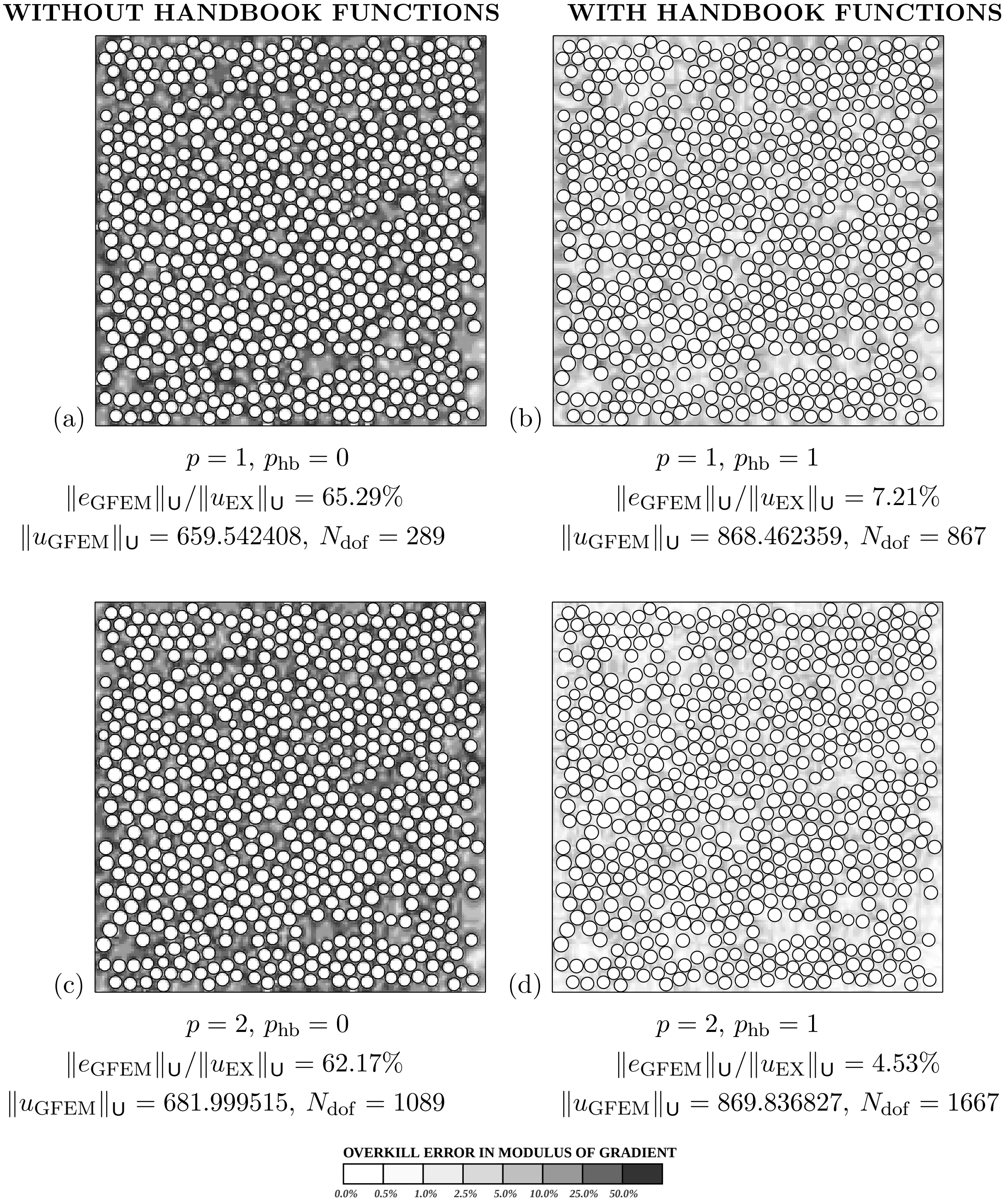

(a) $p = 1,\ p_{\mathrm{hb}} = 0$
$\|e_{\mathrm{GFEM}}\|_{\mathsf{U}}/\|u_{\mathrm{EX}}\|_{\mathsf{U}} = 65.29\%$
$\|u_{\mathrm{GFEM}}\|_{\mathsf{U}} = 659.542408,\ N_{\mathrm{dof}} = 289$

(b) $p = 1,\ p_{\mathrm{hb}} = 1$
$\|e_{\mathrm{GFEM}}\|_{\mathsf{U}}/\|u_{\mathrm{EX}}\|_{\mathsf{U}} = 7.21\%$
$\|u_{\mathrm{GFEM}}\|_{\mathsf{U}} = 868.462359,\ N_{\mathrm{dof}} = 867$

(c) $p = 2,\ p_{\mathrm{hb}} = 0$
$\|e_{\mathrm{GFEM}}\|_{\mathsf{U}}/\|u_{\mathrm{EX}}\|_{\mathsf{U}} = 62.17\%$
$\|u_{\mathrm{GFEM}}\|_{\mathsf{U}} = 681.999515,\ N_{\mathrm{dof}} = 1089$

(d) $p = 2,\ p_{\mathrm{hb}} = 1$
$\|e_{\mathrm{GFEM}}\|_{\mathsf{U}}/\|u_{\mathrm{EX}}\|_{\mathsf{U}} = 4.53\%$
$\|u_{\mathrm{GFEM}}\|_{\mathsf{U}} = 869.836827,\ N_{\mathrm{dof}} = 1667$

Figure 1.4. Generalized FEM using mesh-based handbook functions as proposed in this dissertation. Example problem of the Laplacian in a square domain including 597 closely spaced voids shown in Figure 4.1(b). Comparison of the shades of the error of the bi-p Generalized FEM solutions respectively without and with enrichment by vertex handbook functions, for (a) and (b) $p = 1$, (c) and (d) $p = 2$, computed on the 16×16 mesh obtained from uniform refinement of the square domain. Once more we see that the enrichment by handbook functions results in significant improvement in the accuracy.

(4). The accuracy of the Generalized FEM depends on the data and the buffer employed in the handbooks.

(5). The main CPU cost in the Generalized FEM is due to the precomputation of the handbook functions and the numerical integrations of the stiffness coefficients over the elements of the employed computational mesh. Both of these computations have local character, and hence may be implemented very efficiently on parallel computers.

(6). The Generalized FEM using mesh-based handbook functions is robust for the problems with various types of features.

(7). The Generalized FEM using mesh-based handbook functions has the capability of solving problems with large number of features, like the problem shown in Figure 1.1.

1.3 Outline of the dissertation

Following this Introduction, in Chapter II we briefly summarize the properties of the Generalized FEM, and give the formulations for computation. The main attributes of the Generalized FEM will also be discussed. In Chapter III, we introduce the concept of *mesh-based handbook functions*, and the creation and the computation of the mesh-based handbook functions will be described in details. Following that, in Chapter IV, the Generalized FEM using mesh-based handbook functions is fully investigated for the case of a large number of voids. The p-handbook version of the Generalized FEM is illustrated, and the cost of the Generalized FEM is also analyzed.

Furthermore, in Chapter V, the Generalized FEM using mesh-based handbook functions is extended to the cases of inclusions. The analytical special functions and the integration algorithms for this situation are also discussed. Then in Chapter VI, the Generalized FEM is extended to the cases of various features. Following that, in Chapter VII, we apply the Generalized FEM using mesh-based handbook functions to the problem shown in Figure 1.1. In Chapter VIII, we summarize the conclusions and give recommendations for the future work.

CHAPTER II

GENERALIZED FEM USING HANDBOOK FUNCTIONS

2.1 Formulation of the Generalized FEM and its properties

The Generalized FEM is obtained as a combination of the classical FEM with the PUM. The formulation and the basic properties of the PUM are summarized in the following results (for complete details see [44–46, 48]).

Definition 2.1. Let $d \in \mathsf{N}$, $\Omega \subset \mathsf{R}^d$ be an open set, $\{\Omega_i^h\}_{i=1}^{N(h)}$, $h > 0$, be a family of coverings of Ω satisfying an overlapping condition:

$$\exists M \in \mathsf{N}, \quad \forall h > 0, \quad \forall x \in \Omega, \quad \mathrm{card}\{i | x \in \Omega_i^h\} \leq M. \tag{2.1}$$

Let $\{\phi_i^h\}_{i=1}^{N(h)} \subset W^{1,\infty}(\mathsf{R}^d)$ be a family of partitions of unity subordinate to the coverings $\{\Omega_i^h\}_{i=1}^{N(h)}$ satisfying

$$\mathrm{supp}\phi_i^h \subset \mathrm{closure}(\Omega_i^h); \qquad \sum_{i=1}^{N(h)} \phi_i^h \equiv 1, \mathrm{on} \quad \Omega, \tag{2.2}$$

$$\|\phi_i^h\|_{L^\infty(\Omega)} \leq C_\infty; \qquad \|\nabla \phi_i^h\|_{L^\infty(\Omega)} \leq \frac{C_G}{\mathrm{diam}(\Omega_i^h)}, \tag{2.3}$$

for some C_∞, $C_G > 0$ independent of h.

Let $V_i^{h,p} \subset H^1(\Omega \bigcap \Omega_i^h)$ be a two parameter family of functions spaces, and define $V^{h,p}$ as

$$V^{h,p} = \left\{ v = \sum_{i=1}^{N(h)} \phi_i^h v_i^{h,p} \middle| v_i^{h,p} \in V_i^{h,p} \right\} \subset H^1(\Omega). \tag{2.4}$$

Then we have:

Theorem 2.1. (from [45]) Let Ω, $\{\Omega_i^h\}$, $\{\phi_i^h\}$, and $\{V_i^{h,p}\}$ be given as above. Let $u \in H^k(\Omega)$, $k \leq 1$, and suppose that for fixed h, p, the function u can be approximated locally by functions in $V_i^{h,p}$, i.e., for each i, there is $v_i^{h,p} \in V_i^{h,p}$ such that

$$\|u - v_i^{h,p}\|_{L^2(\Omega \bigcap \Omega_i^h)} \leq \epsilon_1(i,h,p)\|u\|_{H^k(\Omega \bigcap \Omega_i^h)}, \tag{2.5}$$

$$\|\nabla(u - v_i^{h,p})\|_{L^2(\Omega \bigcap \Omega_i^h)} \leq \epsilon_2(i,h,p)\|u\|_{H^k(\Omega \bigcap \Omega_i^h)}. \tag{2.6}$$

Then there is $v^{h,p} \in V^{h,p}$ such that

$$\|u - v^{h,p}\|_{L^2(\Omega)} \leq MC_\infty \max_{i=1,\dots,N(h)} \epsilon_1(i,h,p)\|u\|_{H^k(\Omega)}, \tag{2.7}$$

$$\|\nabla(u - v^{h,p})\|_{L^2(\Omega)} \leq \sqrt{2}M \max_i \left(C_G \frac{\epsilon_1(i,h,p)}{\operatorname{diam}(\Omega \bigcap \Omega_i^h)} + C_\infty \epsilon_2(i,h,p) \right) \|u\|_{H^k(\Omega)}. \tag{2.8}$$

where C_∞, C_G are the constants in Definition 2.1.

Let Δ_h be a finite element mesh with vertices X_i, $i = 1, ..., n_{\text{vert}}$. With each vertex X_i we associate the vertex patch

$$\Omega_i^h = \omega_{X_i}^{(0)} \overset{\text{def}}{=} \bigcup_{\substack{\tau \in \Delta_h \\ X_i \in \partial\tau}} \tau, \tag{2.9}$$

and we let ϕ_i^h be the elementwise mapped bilinear FE basis function associated with X_i. Then $\{\Omega_i^h\}_{i=1}^{n_{\text{vert}}}$ and $\Phi_{\Delta_h} = \{\phi_i^h\}_{i=1}^{n_{\text{vert}}}$ satisfy the assumptions in Definition 2.1.

We will also let $\{\psi_j^{(i)}\}_{j=1}^{n_i}$ be a set of local handbook functions associated with the patch Ω_i^h and we will let

$$\Psi_{\Delta_h} = \{\{\psi_j^{(i)}\}_{j=1}^{n_i}, i = 1, ..., n_{\text{vert}}\}. \tag{2.10}$$

The PUM solution is sought in the form

$$u_{\Delta_h;\Phi_{\Delta_h};\Psi_{\Delta_h}}^{\text{PUM}} \overset{\text{def}}{=} \sum_{i=1}^{n_{\text{vert}}} \phi_i^h \left(\sum_{j=1}^{n_i} a_j^{(i)} \ \psi_j^{(i)} \right) \tag{2.11}$$

where the coefficients $a_j^{(i)}$ are determined such that

$$\mathsf{B}(u_{\Delta_h;\Phi_{\Delta_h};\Psi_{\Delta_h}}^{\text{PUM}}, v) = \mathsf{L}(v), \quad \forall v = \phi_i^h \psi_j^{(i)}, \quad j = 1, 2, ..., n_i, \quad i = 1, 2, ..., n_{\text{vert}}, \tag{2.12}$$

in which the bilinear form $\mathsf{B}(u_{\Delta_h;\Phi_{\Delta_h};\Psi_{\Delta_h}}^{\text{PUM}}, v)$ and the linear form $\mathsf{L}(v)$ have the following definitions for the pure Neumann problem (2.20) for the Laplacian:

$$\mathsf{B}(u_{\Delta_h;\Phi_{\Delta_h};\Psi_{\Delta_h}}^{\text{PUM}}, v) = \int_\Omega \nabla u_{\Delta_h;\Phi_{\Delta_h};\Psi_{\Delta_h}}^{\text{PUM}} \cdot \nabla v d\Omega, \qquad \mathsf{L}(v) = \int_\Omega gv, \tag{2.13}$$

and the solution $u_{\Delta_h;\Phi_{\Delta_h};\Psi_{\Delta_h}}^{\text{PUM}}$ is enforced to have zero mean value:

$$\int_\Omega u_{\Delta_h;\Phi_{\Delta_h};\Psi_{\Delta_h}}^{\text{PUM}} = 0. \tag{2.14}$$

Note that a special linear equation solver may be required for solving the linear algebra problem resulting from (2.12) which can be badly conditioned; this problem was addressed in detail in [49].

From the best approximation property of the Galerkin method, we have:

$$||\nabla(u - u^{\text{PUM}}_{\Delta_h;\Phi_{\Delta_h};\Psi_{\Delta_h}})||_{L^2(\Omega)} \leq \sqrt{2}M \max_i \left(C_G \frac{\epsilon_1(i,h,p)}{\text{diam}(\Omega \bigcap \Omega_i^h)} + C_\infty \epsilon_2(i,h,p) \right) \|u\|_{H^k(\Omega)}. \tag{2.15}$$

Hence by ensuring good local approximability over the vertex patches $\Omega_i^h = \text{supp}\phi_i^h$, we get good global approximability for the PUM solution. It follows that the *accuracy of the method* can be greatly improved by judicious choice of the local spaces Ψ_{Δ_h}.

For the cases that the functions $\psi_j^{(i)}$ are harmonic polynomials, Babuška and Melenk [47, 70] have proven the following results:

Theorem 2.2. Let $\Omega \subset \mathsf{C}$ be a *bounded Lipschitz domain, star shaped with respect to a ball.* Let the exterior angle of Ω be bounded from below at each boundary point by $\lambda\pi$ with $0 < \lambda < 2$ (i.e., let Ω satisfy an exterior cone condition with cone aperture $\lambda\pi$). Assume that $f \in H^k(\Omega)$, $k \geq 1$, is halomorphic on Ω. Then there are polynomials P_p of degree $p \geq k-1$ such that

$$\|f - P_p\|_{H^j(\Omega)} \leq C(\text{diam}\Omega)^{k-j} \left(\frac{\ln p}{p} \right)^{\lambda(k-j)} \|f\|_{H^k(\Omega)}, \quad j = 0, ..., [k], \tag{2.16}$$

where the constant $C > 0$ depends only on the shape of Ω and k.

Theorem 2.3. Let Ω be a *bounded domain with a corner of exterior angle $\lambda\pi$ at the origin.* Let $f = z^\alpha \ln^\beta z$ for some $\alpha > 0$, $\beta \geq 0$. Then there are polynomials P_p of degree $p > 0$ such that

$$\|f - P_p\|_{H^j(\Omega)} \leq C(\epsilon, f)(\text{diam}\Omega)^{1+\alpha-j-\epsilon} p^{-\lambda(1+\alpha-j-\epsilon)}, \quad j = 0, 1, \tag{2.17}$$

for any $\epsilon > 0$, where $C(\epsilon, f)$ depends only on ϵ, f, and the shape of Ω.

The GFEM solution is constructed as a superposition of the PUM and the classical FEM solution using p degree FE basis on the mesh Δ_h, namely

$$u^{\text{GFEM}}_{\Delta_h;\Phi_{\Delta_h};\Psi_{\Delta_h};p} = \sum_{i=1}^{n_{\text{vert}}} \phi_i^h \left(\sum_{j=1}^{n_i} a_j^{(i)} \ \psi_j^{(i)} \right) + \sum_{k=1}^{n_{\text{FEM}}} b_k \ \tilde{\varphi}_k \tag{2.18}$$

Here $\tilde{\varphi}_k$ denotes the piecewise mapped bi-p basis function for the kth FE degree of freedom, $n_{\text{FEM}} = n_{\text{FEM}}(\Delta_h, p)$ is the number of FE degrees of freedom for the mesh Δ_h and the polynomial degree p, and

$$n = \sum_i^{n_{\text{vert}}} n_i + n_{\text{FEM}} \tag{2.19}$$

is the total number of GFEM degrees of freedom.

2.2 Main attributes of the Generalized FEM

As it was indicated in the previous section, the Generalized FEM is a combination of the Partition of Unity Method, with the classical Finite Element Method. The two main attributes of the Generalized FEM, as developed in [49–54], are the capabilities of using:

1. *Domain independent meshes.* The GFEM approximation can be constructed on meshes which are non-overlapping partitions of any domain Ω' which covers the problem domain Ω, namely $\Omega \subset \Omega'$, and when Ω' is chosen to have simple geometry, e.g. Ω' is a rectangle, they can be much simpler to construct. In contrast, the meshes used in the classical FEM are non-overlapping partitions of the problem domain Ω into simple subdomains, and if Ω has complex geometry, may be difficult to generate. The complete information about the problem domain Ω enters into the GFEM through special *integration meshes* constructed to reflect the local geometry of the problem domain in each element of the GFEM mesh by an automated adaptive numerical integration algorithm. This is much easier than constructing a standard FEM mesh in Ω, because the integration meshes need not be conforming at the element interfaces of the GFEM mesh. Let us also underline that adaptive control of the numerical integration error is essential for preserving the accuracy and optimal convergence of the GFEM (see [49]).

2. *Enrichment by handbook functions.* The GFEM approximation can be enriched by *handbook functions* which are solutions of local boundary-value problems reflecting the local geometry of the problem domain Ω and the boundary conditions of the problem of interest, e.g. corners, voids, inclusions, cracks, curved Neumann or Dirichlet boundaries, etc. The handbook functions may be obtained prior to the solution of the problem of interest, either through an analytical [49, 50] or a numerical [51, 52] construction. In [51, 52] we showed that the GFEM with judiciously selected handbook functions is capable in achieving high accuracy for problems with rather complex geometry, while employing rather coarse meshes.

Let us illustrate the above points through some sample results. For an extensive set of similar results see [51, 52].

Let Ω be the domain shown in Figure 2.1(a), let Γ denote its outer boundary, and let us consider the Neumann boundary value problem:

$$\begin{cases} -\Delta u &= 0, & \text{in} \quad \Omega, \\ \dfrac{\partial u}{\partial n} &= g \overset{\text{def}}{=} \nabla(2x-y)\cdot \mathbf{n}, & \text{on the outer boundary} \quad \Gamma, \\ \dfrac{\partial u}{\partial n} &= 0, & \text{on the boundary of the voids.} \end{cases} \tag{2.20}$$

As we have seen in [51, 52], we may compute GFEM solutions of the above problem using a mesh of square elements constructed from a nested subdivision of a square domain

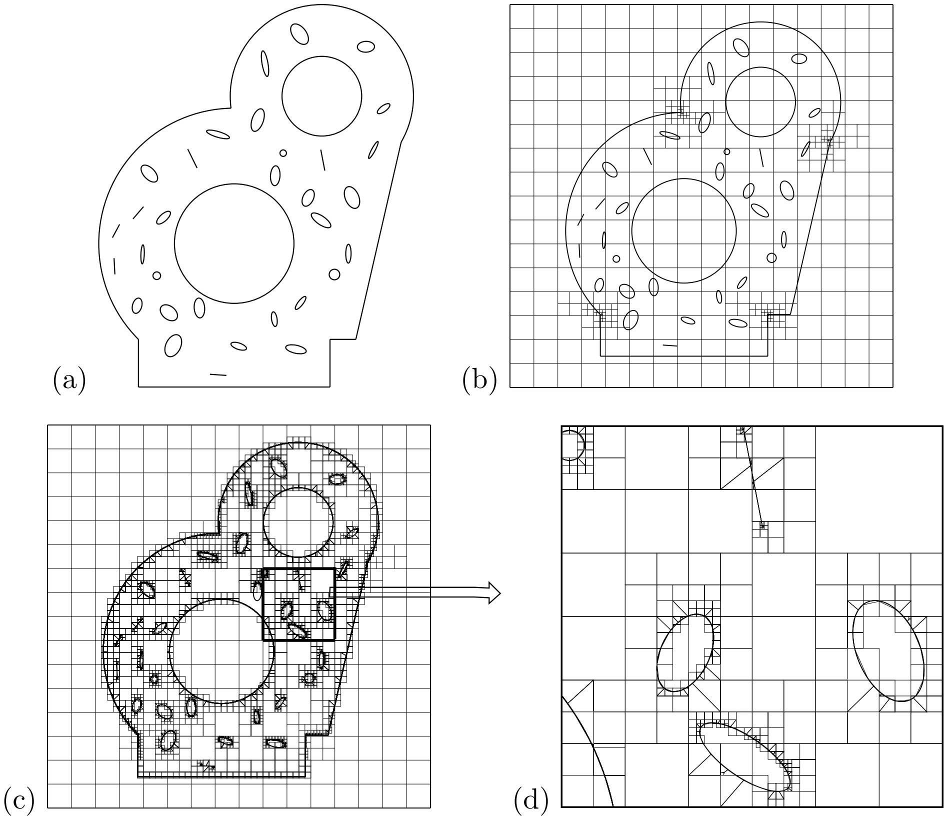

Figure 2.1. Illustration of the "meshless" character of the GFEM or more precisely its ability to construct the approximation on a mesh with geometry independent of the problem domain. (a). The problem domain Ω which has several internal voids and cracks; (b). The employed GFEM mesh obtained by subdividing uniformly a square domainΩ', which includes the problem domain Ω in its interior, $\Omega \subset \Omega'$, and by employing 4 nested refinements of the squares which overlap a reentrant corner; (c). The integration mesh employed in the computation; (d). Detail of the integration mesh.

Ω' which overlaps the domain Ω, i.e. we have $\Omega \subset \Omega'$, as shown in Figure 2.1(b). The information about the problem domain Ω and the applied boundary conditions is included into the GFEM through local integration meshes, the adaptive construction of which can be easily automated in each element. Figure 2.1(c) shows the integration mesh used in the computation given below. Let us underline that the integration mesh is constructed element by element by an automatic refinement algorithm and it does not need to be conforming at the element interfaces.

In order to show the effect of the handbook functions on the accuracy, we computed the GFEM solution of the model problem (2.20) on the mesh of Figure 2.1(b) using the: 1. biquadratic ($p = 2$) FEM basis; 2. biquadratic ($p = 2$) FEM basis with handbook functions of degree one, $p_{\text{handbook}} = 1$, (see [51, 52]) for the voids, corners and cracks added

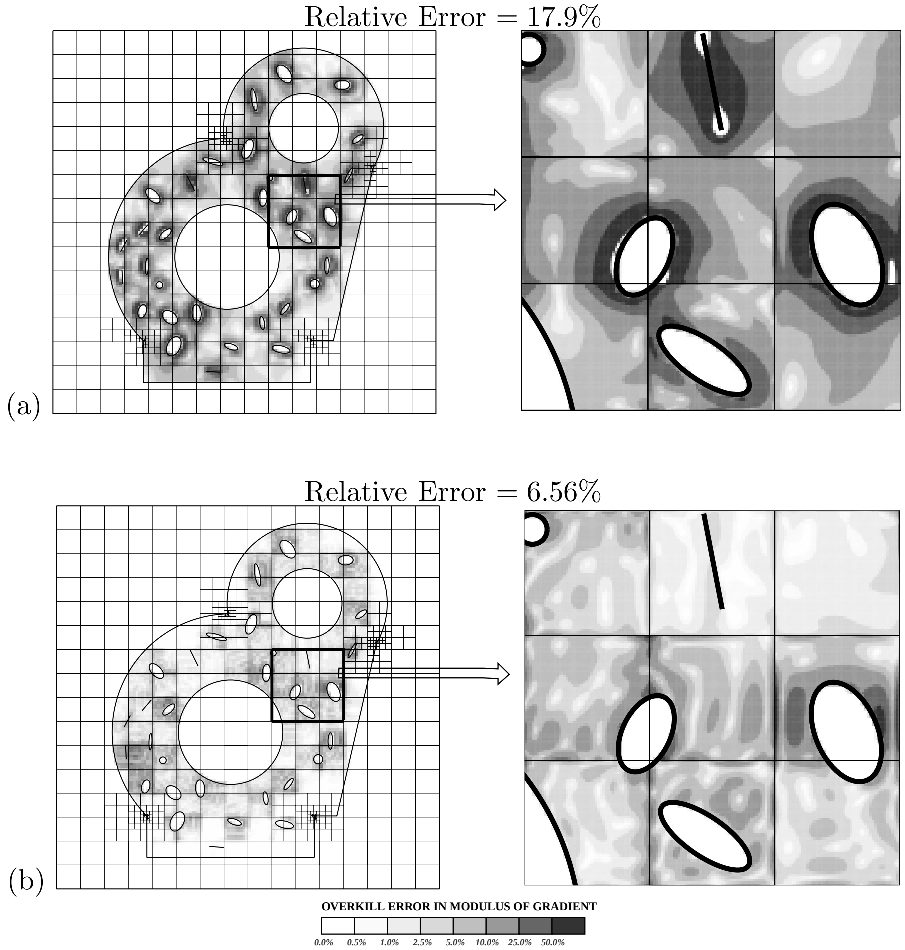

Figure 2.2. Illustration of the effect of handbook functions on the accuracy of the GFEM solution. Relative modulus of the error in the gradient for: (a) Biquadratic ($p = 2$) finite elements without any handbook functions ($||e_{\text{GFEM}}\,||_{\mathsf{U}}/||u_{\text{ov}}||_{\mathsf{U}} = 17.9\%$); and for: (b) Biquadratic ($p = 2$) finite elements with void, corner and crack handbook functions of $p_{\text{handbook}} = 1$ added at $n_{\text{layers}} = 0$ around each feature ($||e_{\text{GFEM}}||_{\mathsf{U}}/||u_{\text{ov}}||_{\mathsf{U}} = 6.56\%$).

at $n_{\text{layers}} = 0$ (see [51, 52]) around each feature. We analyzed the results by employing as exact solution an overkill GFEM solution obtained on the same mesh, using biquintic ($p = 5$) FEM basis with handbook functions of degree two, $p_{\text{handbook}} = 2$, added at $n_{\text{layers}} = 0$ around each feature.

Figure 2.2 shows the relative modulus of the error in the gradient, $|\nabla e_{\text{GFEM}}|/\ \big(\frac{1}{|\Omega|}\int_{\Omega} |\nabla u_{\text{ov}}|\big)$, for the GFEM solution without and with handbook functions included to the approximation. It can be clearly seen that the addition of void, crack and corner handbook functions into the GFEM approximation leads to very significant improvement in the overall accuracy of the GFEM solution.

In the above computations, the harmonic functions were used as handbook functions in the exterior of an elliptical void or a crack obtained by conformal mapping from the functions $\Re[z^n + z^{-n}]$, and $\Im[z^n + z^{-n}]$, $n = 1, 2, ...$, and harmonic corner functions of the form $r^\alpha(A\cos(\alpha\theta) + B\sin(\alpha\theta))$ where (r, θ) are the polar coordinates associated with the corner and A, B depend on the boundary conditions on the emanating edges from the tip of the corner. This is an example where an analytical construction of the handbook functions is available, however this is not possible in general, e.g. for a general elliptic differential operator and/or features with more complex geometry. To address the general case, the GFEM with *numerically constructed* handbook functions was introduced in [51, 52].

Let us give an illustration of the Generalized FEM using numerically constructed handbook functions as it was developed in [51, 52]. Let us consider the Neumann problem for the Laplacian in a domain including several square voids in its interior shown in Figure 2.3(a), and let us enrich FEM approximation using handbook functions for a square void, defined as solutions of the canonical boundary value problems for a single square void shown in Figure 2.3(c), and constructed numerically using the original version of GFEM (the FEM enriched by harmonic corner functions introduced in [49, 50]) on the handbook mesh shown in Figure 2.3(b). Figures 2.3(d)-(f) show the shades of the gradient of the pairs of handbook functions of degree one and two. The square void handbook functions are pasted into the GFEM approximation by the PUM after they are scaled and translated over the domain of the problem as shown in Figure 2.4(b) and then multiplied by the vertex hat functions of the employed GFEM mesh at the vertices of the elements intersecting the voids, as shown in Figure 2.4(a). As we have seen in [51, 52], the addition of handbook functions can lead to significant improvement of the accuracy of the Generalized FEM solution.

Let us compare the accuracy of the Generalized FEM with and without handbook functions for the example problem outlined above. We computed the Generalized FEM solution on a uniform mesh of squares overlapping the domain, using a bi-p FE basis enriched by the numerically constructed handbook functions for a square void as illustrated in Figures 2.3 and 2.4. Figures 2.5(a)-(f) compare the bi-p GFEM solutions enriched by the square void handbook functions with the corresponding GFEM solutions computed using only the bi-p FE basis on the same mesh, for $p = 1$, 2, and 3. It can be clearly seen that the addition of square void handbook functions significantly improves the accuracy of the GFEM solution, e.g. the relative error of the GFEM solution for $p = 3$ enriched by the square void handbook functions is 3.51%, while the one without the square void handbook functions is only 12.68%! The improvement in the accuracy can also be seen by comparing the contours of the modulus of the gradient for the computed solutions shown in Figure 2.5.

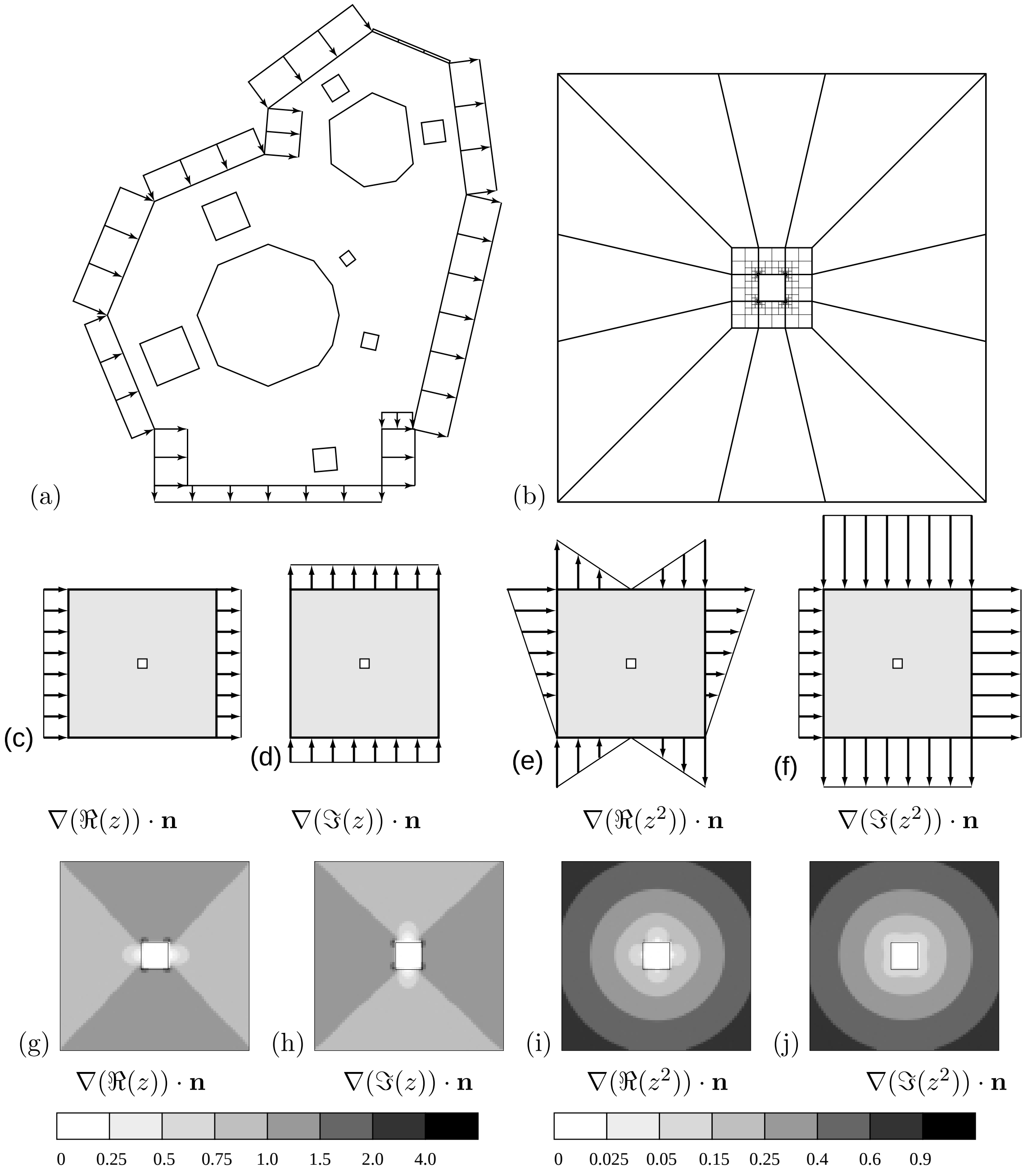

Figure 2.3. Generalized FEM using numerically constructed handbook functions. (a) The problem domain with the imposed derivative boundary conditions graphed on the boundary. (b)-(j) Numerically constructed handbook functions for a square void. (b) Detail of the handbook mesh used in the numerical construction of the handbook functions. (c)-(f) Handbook domain for a square void with the boundary conditions employed for the handbook functions of degree $p_{\mathrm{hb}} = 1$ ((c)-(d)) and $p_{\mathrm{hb}} = 2$ ((e)-(f)). (g)-(j) Shades of the relative modulus of the gradient for the handbook functions of degree one ((g)-(h)) and two ((i)-(j)).

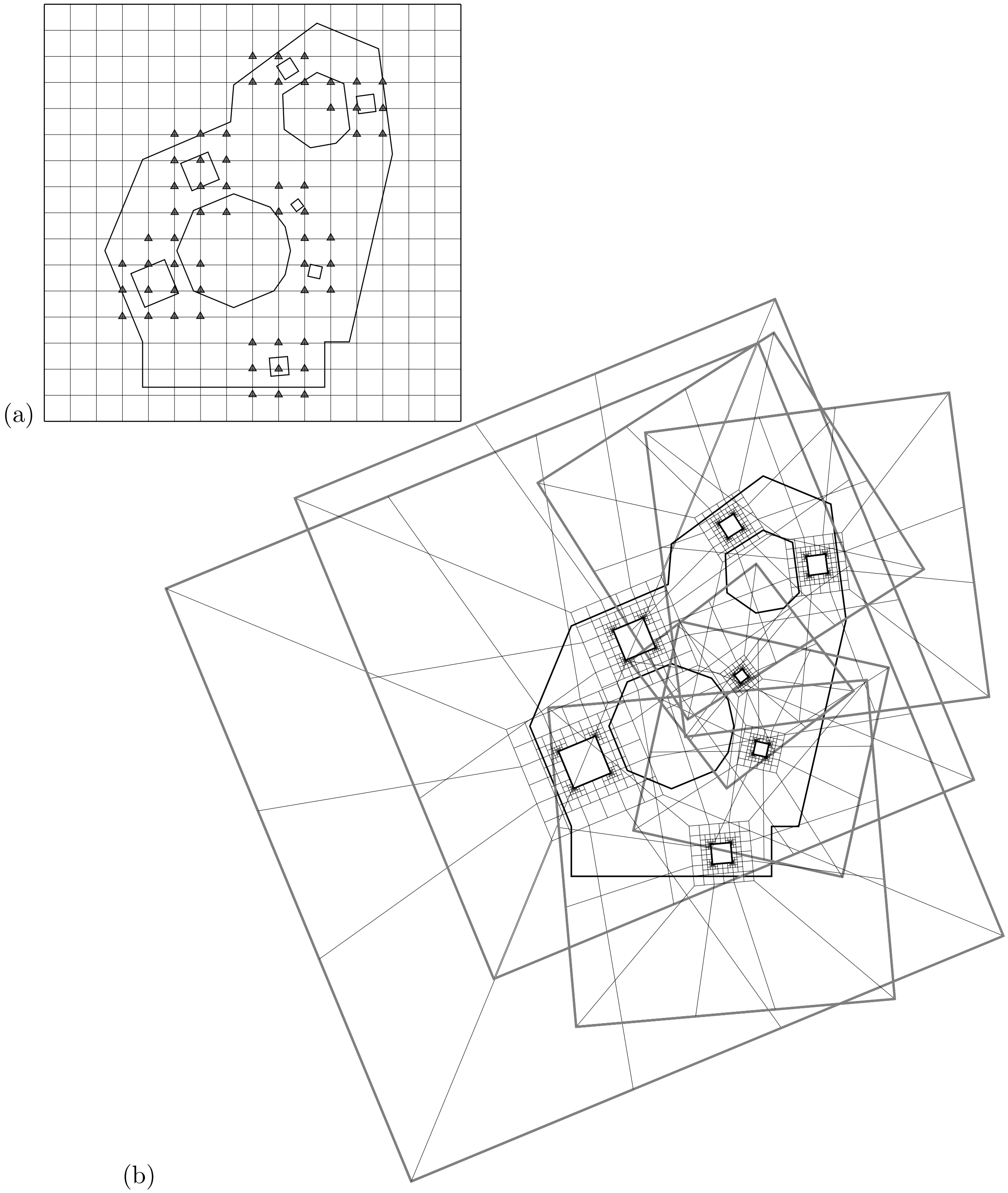

Figure 2.4. Generalized FEM using numerically constructed handbook functions. (a) A uniform mesh of squares used for the construction of Generalized FEM solutions for the model problem shown in Figure 2.3(a). The triangle symbols indicate the vertices at which the square-void handbook functions are used to enrich the GFEM solution around each square void. (b) The handbook meshes for the square voids shown on top of the problem domain, as they are used in the construction of the Generalized FEM solution.

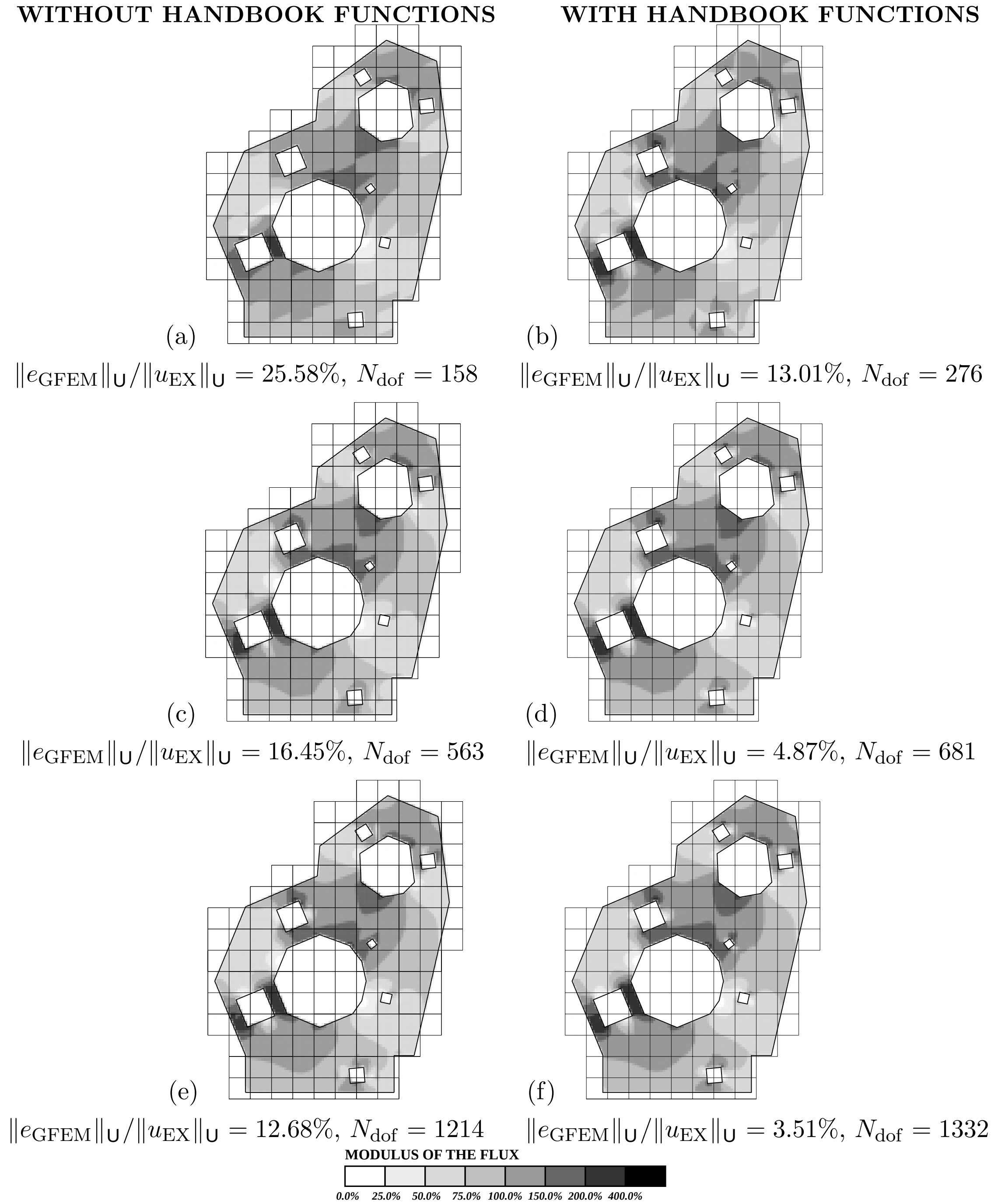

(a) $\|e_{\text{GFEM}}\|_{\mathsf{U}}/\|u_{\text{EX}}\|_{\mathsf{U}} = 25.58\%,\ N_{\text{dof}} = 158$

(b) $\|e_{\text{GFEM}}\|_{\mathsf{U}}/\|u_{\text{EX}}\|_{\mathsf{U}} = 13.01\%,\ N_{\text{dof}} = 276$

(c) $\|e_{\text{GFEM}}\|_{\mathsf{U}}/\|u_{\text{EX}}\|_{\mathsf{U}} = 16.45\%,\ N_{\text{dof}} = 563$

(d) $\|e_{\text{GFEM}}\|_{\mathsf{U}}/\|u_{\text{EX}}\|_{\mathsf{U}} = 4.87\%,\ N_{\text{dof}} = 681$

(e) $\|e_{\text{GFEM}}\|_{\mathsf{U}}/\|u_{\text{EX}}\|_{\mathsf{U}} = 12.68\%,\ N_{\text{dof}} = 1214$

(f) $\|e_{\text{GFEM}}\|_{\mathsf{U}}/\|u_{\text{EX}}\|_{\mathsf{U}} = 3.51\%,\ N_{\text{dof}} = 1332$

Figure 2.5. Generalized FEM using numerically constructed handbook functions. Shades of the relative modulus of the computed gradient for the bi-p Generalized FEM solutions computed, respectively, without and with enrichment by handbook functions for the square voids for (a), and (b) $p = 1$, (c), and (d) $p = 2$, and (e), and (f) $p = 3$ using the uniform mesh of squares shown. Note the significant effect of the handbook functions in improving the accuracy.

CHAPTER III

GENERALIZED FEM USING MESH-BASED HANDBOOK FUNCTIONS*

The main idea in the Generalized FEM with numerically constructed handbook functions illustrated above and in [51, 52] is to identify the features occuring in the domain of the problem, for which an analytical construction is not possible, e.g. a square void, a bifurcated crack etc., and to construct handbook functions for these features by solving auxiliary canonical boundary-value problems in handbook domains. The handbook functions, i.e. the solutions of these canonical problems, can then be used in the GFEM by superimposing the handbook meshes i.e. the meshes used in the numerical construction of the handbook functions over the GFEM mesh after appropriate scaling, translation and rotation. We will call this version of the method, GFEM *with handbook functions constructed in canonical domains*. This approach is suitable in the cases where the features appear in relatively few locations in the domain, like for example the bifurcated crack in the above example, and also in the cases where one or two features occur in many configurations, like for example when analyzing the effect of a hidden or battle damage (see [69]). The main difficulty with this version of GFEM is related with the transfer of the handbook functions from the handbook meshes to the global GFEM mesh. This transfer requires the use of the inverse element map in the elements of the handbook meshes and results in expensive numerical integrations of the stiffness coefficients over the global GFEM mesh. Nevertheless, when there are relatively few features in the problem domain, for which a numerical construction of handbook functions is needed, the cost of the numerical integrations is not prohibitive. Moreover, this version of GFEM is ideally suited for the analysis of multi-site or battle damage using the methods discussed in [69].

In this Chapter, we introduce a new version of the Generalized FEM which employs a different construction of handbook functions which is better suited for problems set in domains with a large number of closely spaced features, like, for example, in the domains shown in Figure 3.1.

3.1 Construction of mesh-based handbook functions

Let us consider the Neumann problem for the Laplacian (2.20) in the domain with 597 voids shown in Figure 3.1 with zero flux boundary conditions applied on the boundaries of the

---

*Reprinted with permission from ”Generalized finite element method using mesh-based handbooks: Application to problem in domains with many voids” by T. Strouboulis, L. Zhang and I. Babuška, in *Comp. Meth. Appl. Mech. Engrg.* Copyright 2003 by the Elsevier Science

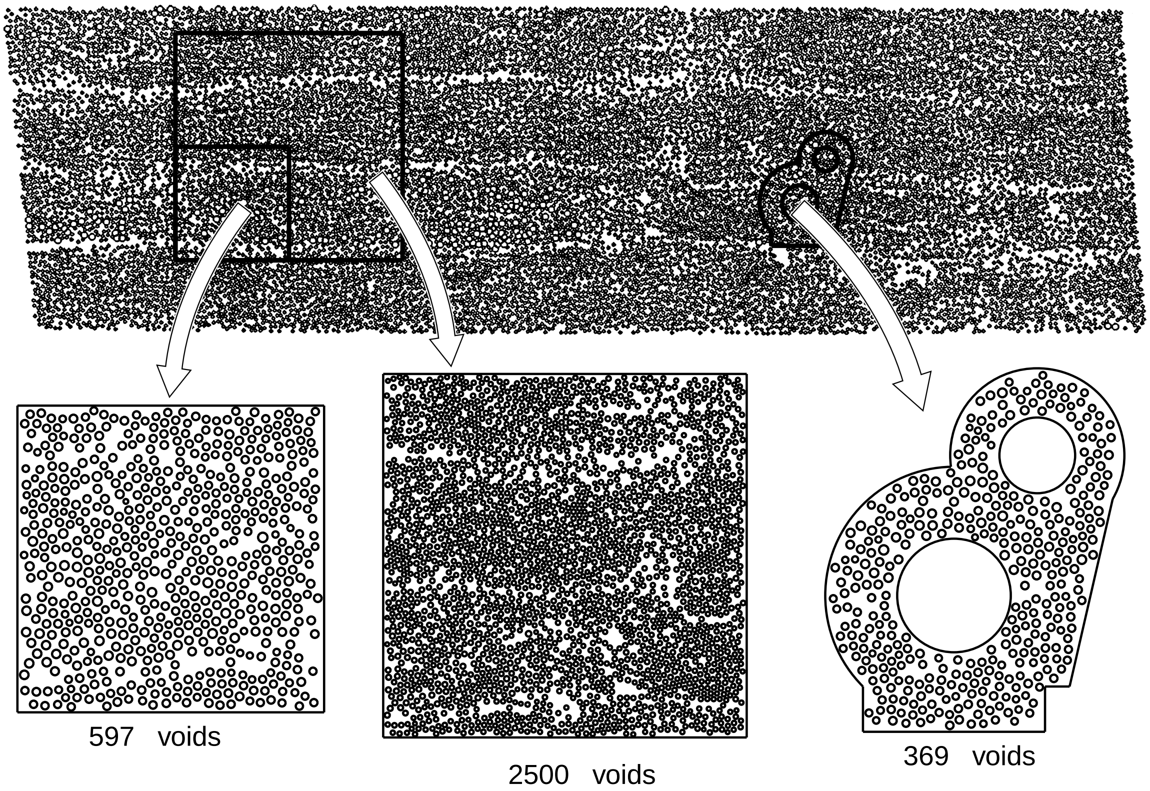

Figure 3.1. Examples of problem domains with a large number of closely spaced features.

voids.

We will construct a GFEM solution for this problem using a finite element mesh of squares Δ_h as shown in Figure 3.2(a), and the standard bi-p FEM basis on this mesh, plus vertex handbook functions constructed by solving local problems on subdomains surrounding each vertex

For a typical vertex X we will employ the subdomain $\omega_X^{(1)}$ which is the union of the elements connected to X and to the vertices of these elements, namely

$$\omega_X^{(1)} = \bigcup_{\substack{\tau\in\Delta_h \\ \partial\tau\bigcap\bar{\omega}_X^{(0)}\neq 0}} \tau. \tag{3.1}$$

We will then obtain the subdomain $\tilde{\omega}_X^{(1);d}$ by eliminating the voids which do not intersect a neighborhood of X controlled by a parameter $d \in [0,2]$, and the voids intersecting the outer boundary of $\omega_X^{(1)}$. Figure 3.2(c) (resp. Figure 3.2(d)) shows the subdomain $\tilde{\omega}_X^{(1);1/2}$ (resp. $\tilde{\omega}_X^{(1);1}$). Further, we will denote by $\psi_j^{X;d}$, the jth handbook functions associated with the vertex X, $j = 1, 2, ...$ defined as the exact solution of the following Neumann problem

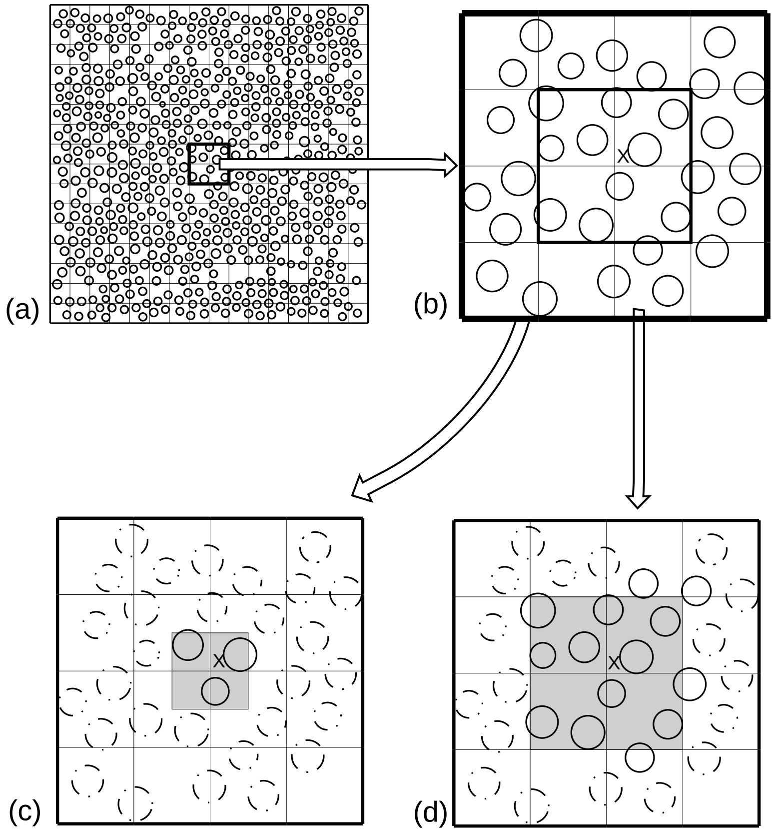

$d = \dfrac{1}{2}$ $\qquad$ $d = 1$

Figure 3.2. Creation of handbook domains $\tilde{\omega}_X^{(1);d}$ associated with a vertex X. (a) The domain Ω covered by the mesh Δ_h; (b) A typical interior vertex X with the domain $\omega_X^{(0)}$ (resp. $\omega_X^{(1)}$) with its boundary shown by thick continuous (resp. thicker) line. The domains (c) $\tilde{\omega}_X^{(1);1/2}$ and (d) $\tilde{\omega}_X^{(1);1}$, obtained from $\omega_X^{(1)}$.

$$\begin{aligned}
\Delta\psi_j^{X;d} &= 0, \qquad \text{in} \quad \tilde{\omega}_X^{(1);d}, && (3.2)\\
\frac{\partial}{\partial n}\big(\psi_j^{X;d}\big) &= \begin{cases} \nabla(\Re(z^{p_{\text{hb}}}))\cdot\mathbf{n}, & \text{if} \quad j = 2p_{\text{hb}}-1, \\ \nabla(\Im(z^{p_{\text{hb}}}))\cdot\mathbf{n}, & \text{if} \quad j = 2p_{\text{pb}}, \end{cases} \qquad \text{on} \quad \partial\omega_X^{(1)}, && (3.3)\\
\frac{\partial}{\partial n}\big(\psi_j^{X;d}\big) &= 0, \qquad \text{on} \quad \partial\tilde{\omega}_X^{(1);d} - \partial\omega_X^{(1)}, && (3.4)
\end{aligned}$$

where $p_{\text{hb}} = 1, 2, ...$, and for uniqueness we let

$$\int_{\tilde{\omega}_X^{(1);d}} \psi_j^{X;d} = 0. \tag{3.5}$$

Below we will call the GFEM with vertex handbook functions based on the subdomains $\tilde{\omega}_X^{(1);1/2}$ shown in Figure 3.2(c) (resp. $\tilde{\omega}_X^{(1);1}$ shown in Figure 3.2(d)) as GFEM with simple (resp. improved) handbook functions. Figure 3.3 shows an example of the simple versus the improved handbook functions for a typical vertex patch.

Let us also address the definition of the handbook functions $\psi_j^{X;d}$ for $X \in \Gamma$, namely when the vertex X belongs to the Neumann boundary Γ.

Let us first consider the case of a polygonal domain with straight edges, as shown in Figure 3.4(a). Similarly as in the case of interior nodes we first construct the domain $\omega_X^{(1)}$ shown in Figure 3.4(b) and then the handbook domain $\tilde{\omega}_X^{(1);d}$ as shown in Figure 3.4(c) and (d) for a corner vertex and for a vertex in the interior of a straight edge. We then construct the corresponding handbook functions $\psi_j^{X;d}$ as the exact solutions of the boundary value problems:

$$\begin{aligned} \Delta\psi_j^{X;d} &= 0, \quad \text{in} \quad \tilde{\omega}_X^{(1);d}, && (3.6)\\ \frac{\partial}{\partial n}(\psi_j^{X;d}) &= \begin{cases} \tilde{g}_X, & \text{for} \quad j = 1, \\ \tilde{g}_X + g_X^{(j)}, & \text{for} \quad j = 2, 3, ... \end{cases}, \quad \text{on} \quad \partial\omega_X^{(1)}, && (3.7)\\ \frac{\partial}{\partial n}(\psi_j^{X;d}) &= 0, \quad \text{on} \quad \partial\tilde{\omega}_X^{(1);d} - \partial\omega_X^{(1)}, && (3.8) \end{aligned}$$

where $\tilde{g}_X$ is a boundary condition on $\partial\omega_X^{(1)}$ such that

$$\tilde{g}_X\big|_{\Gamma\bigcap\partial\omega_X^{(1)}} = g\big|_{\Gamma\bigcap\partial\omega_X^{(1)}}, \tag{3.9}$$

and

$$\int_{\partial\omega_X^{(1)}} \tilde{g}_X = 0. \tag{3.10}$$

For example, for the case of the Neumann problem (2.20) we let

$$\tilde{g}_X = \nabla(x - 2y) \cdot n_{\partial\omega_X^{(1)}}$$

where $n_{\partial\omega_X^{(1)}}$ is the exterior normal of $\partial\omega_X^{(1)}$. The functions $g_X^{(j)}$ are corner functions in the wedge with vertex at X, given by

$$g_X^{(j)}(r_X, \theta_X) = \nabla(r_X^{2(j-1)}\cos(2(j-1)\theta_X)) \cdot n_{\partial\omega_X^{(1)}}, \quad j = 2, 3, ... \tag{3.11}$$

where (r_X, θ_X) are the polar coordinates associated with the vertex X.

Let us also address the case of a vertex on a curvilinear boundary, as is, for example, shown in Figure 3.5(a). Once more, we construct the vertex domain $\omega_X^{(1)}$, and the handbook domain $\omega_X^{(1);d}$, as shown, respectively, in Figure 3.5(c) and Figure 3.5(d). Then we construct the handbook functions $\psi_j^{X;d}$ as the exact solutions of the boundary value problems (3.8), with $g_X^{(j)}$ given by

$$g_X^{(j)} = \begin{cases} 0, & \text{on} \quad \partial\omega_X^{(1)}\bigcap\Gamma, \\ \dfrac{\partial u_j^*}{\partial n} + g_j^*, & \text{on} \quad \partial\omega_X^{(1)} - (\partial\omega_X^{(1)}\bigcap\Gamma). \end{cases} \tag{3.12}$$

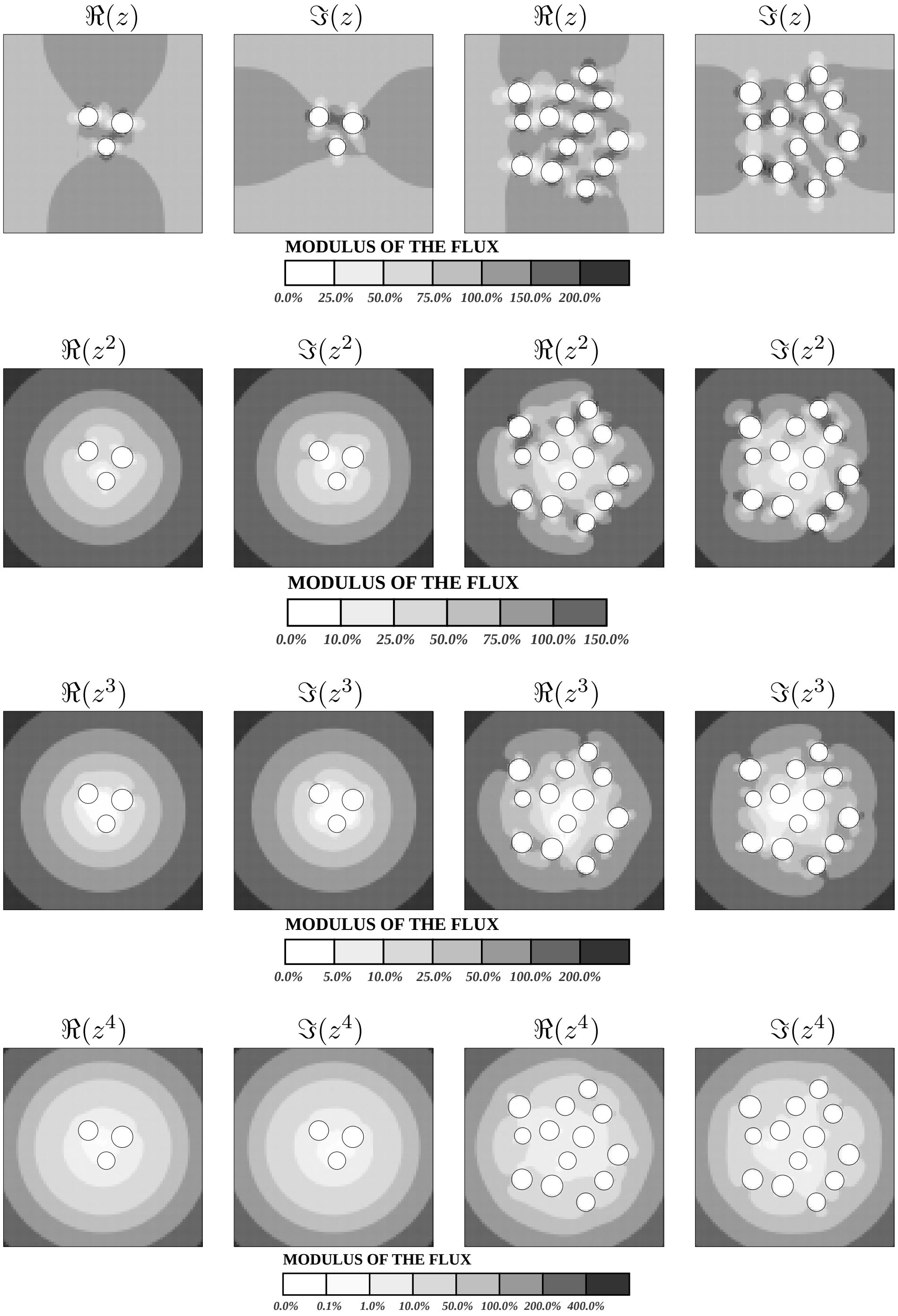

Figure 3.3. Comparison of the simple versus the improved handbook functions $\psi_j^{X;d}$ for an interior vertex X. Modulus of the gradient of handbook functions, $\psi_j^{X;d}$, for the interior vertex X shown in Figure 3.2. The left two (resp. right two) columns correspond to simple (resp. improved) handbook functions obtained for $d = 1/2$ (resp. $d = 1$).

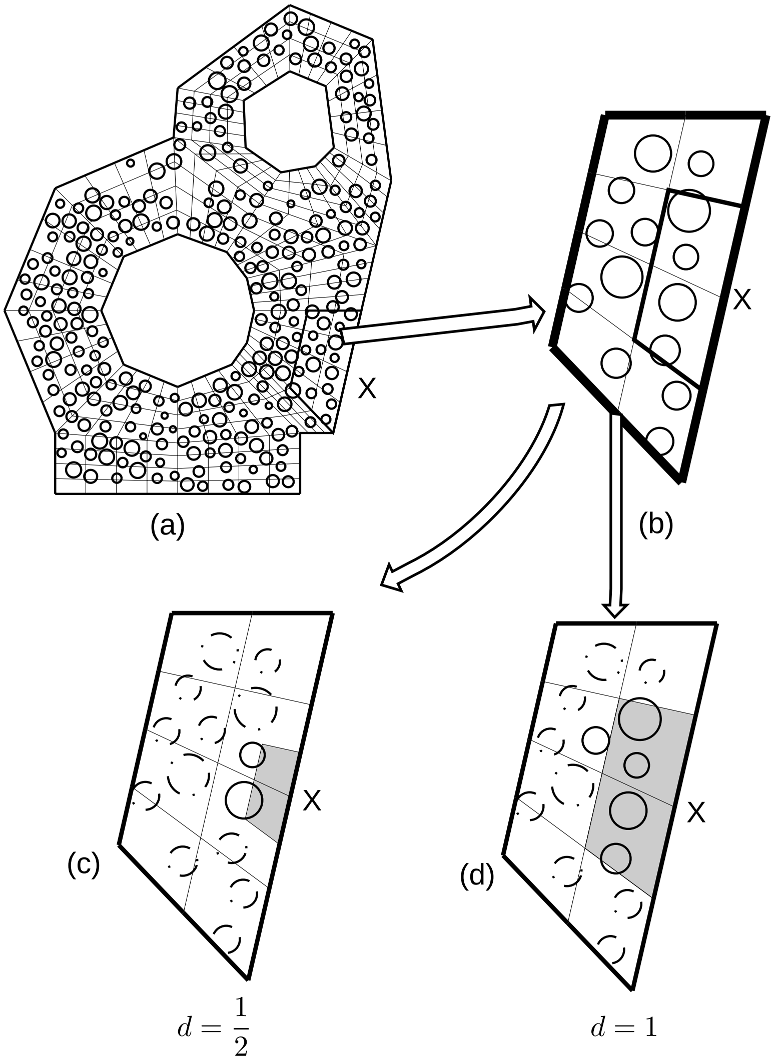

Figure 3.4. Creation of handbook domains $\tilde{\omega}_X^{(1);d}$ associated with a vertex X on boundary. (a) The domain Ω covered by the mesh Δ_h; (b) A typical boundary vertex X with the domain $\omega_X^{(0)}$ (resp. $\omega_X^{(1)}$) with its boundary shown by thick continuous (resp. thicker) line. The domains (c) $\tilde{\omega}_X^{(1);1/2}$ and (d) $\tilde{\omega}_X^{(1);1}$, obtained from $\omega_X^{(1)}$.

Here u_j^* are harmonic functions in $\omega_X^{(1)}$, and g_j^* is determined from the condition (3.10) on $\partial\omega_X^{(1)}$. For example, for the boundary handbook shown in Figure 3.5(d), we employ the corner functions

$$u_j^*(r_X, \theta_X) = r_X^{(j-1)\frac{\pi}{\beta}} \cos((j-1)\frac{\pi}{\beta}(\theta_X - \alpha)), \quad j = 2, 3, ... \tag{3.13}$$

where (r_X, θ_X) are the polar coordinates, and the meaning of the angles α and β is illustrated

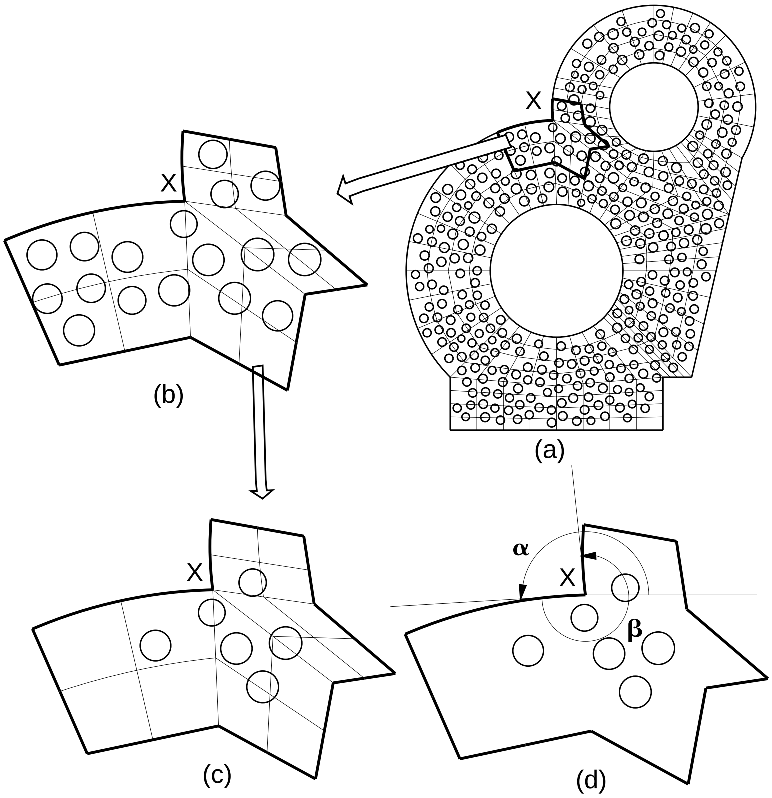

Figure 3.5. Creation of handbook domains $\tilde{\omega}_X^{(1);d}$ associated with a vertex X on curvilinear boundary. (a) The domain Ω covered by the mesh Δ_h; (b) A typical boundary vertex X with the domain $\omega_X^{(1)}$. (c) The domain $\tilde{\omega}_X^{(1);1}$. (d) Illustration of the angles α and β used in the boundary conditions for handbook problems.

by Figure 3.5(d), and

$$g_j^* = \frac{\displaystyle\int_{\partial\omega_X^{(1)} \bigcap \Gamma} \frac{\partial u_j^*}{\partial n} ds}{|\partial\omega_X^{(1)} - (\partial\omega_X^{(1)} \bigcap \Gamma)|}, \quad j = 2, 3, ... \tag{3.14}$$

3.2 Robustness of the Generalized FEM using mesh-based handbook functions

We will now illustrate the robustness of the GFEM using mesh-based handbooks for the model problem of the Laplacian in domains including many closely spaced voids. We will employ the domains shown in Figure 3.6, and in each one of these domains we will control the size of the voids using a parameter γ, $1 \leq \gamma \leq 1.375$, as shown in Figure 3.7. In each example we will study the relative error

$$e_{\mathrm{REL}}^{\mathrm{GFEM}}(\Delta_h, p, p_{\mathrm{hb}}; \gamma) = \frac{\|u_{\mathrm{EX}} - u^{\mathrm{GFEM}}(\Delta_h, p, p_{\mathrm{hb}}; \gamma)\|_{\mathsf{U}}}{\|u_{\mathrm{EX}}\|_{\mathsf{U}}} \tag{3.15}$$

as a function of γ. Here we let

$$\|v\|_{\mathsf{U}} = \sqrt{\int_{\Omega} |\nabla v|^2 d\Omega}. \tag{3.16}$$

We will see that in all the cases the relative error increases with γ, nevertheless by using improved handbooks with $p_{\mathrm{hb}} \geq 1$, we can obtain high accuracy for the entire range of γ.

We will also show that by using the p_{handbook}- (p_{hb}-) version of the GFEM, i.e. the p-version in terms of the handbook functions, we can obtain exponential convergence and very high accuracy which is robust with respect to the closeness of the voids and practically independent of the number of voids. A key point, which will become evident from our results, is that in order to achieve exponential convergence it is necessary to control the accuracy in the numerical construction of the handbook functions.

Let us outline the employed examples and their objectives.

1. *GFEM using simple handbook functions in the interior of Domain I.* In this example we employ the GFEM with simple handbook functions to solve the Neumann model problem in Domain I. The results show the robustness of the method with respect to the closeness of the voids, and also indicate a dependence of the global accuracy on the accuracy of the numerical construction of the handbook functions.

2. *GFEM using simple and improved handbooks up to the boundary of Domain II.* Here we employ the GFEM with simple and improved handbooks to solve the Neumann problem in Domain II using interior as well as boundary handbooks. This example shows that by including more information about the problem into the handbooks, i.e. by using improved instead of simple handbooks, we can get dramatic improvement in the accuracy of the GFEM solution.

3. *GFEM using hierarchical handbooks for Domain III.* In this example we employ the GFEM with a hierarchical multilevel construction of handbook functions to solve the model problem in Domain III which includes 2500 voids. Once more we see the robustness of the method with respect to the closeness of the voids, and also the influence of the accuracy in the numerical construction of the handbook functions to the global accuracy of the method.

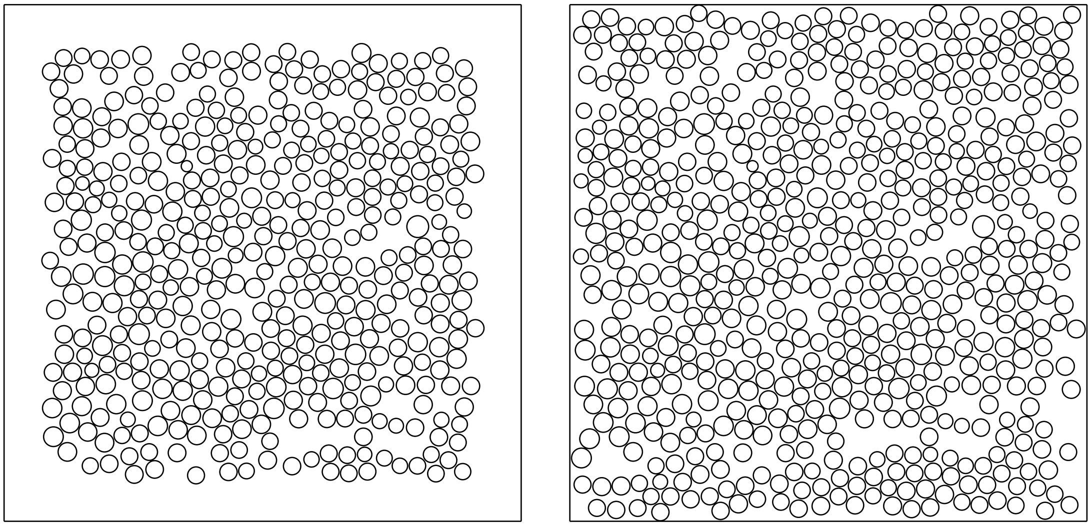

(a) Domain I (b) Domain II

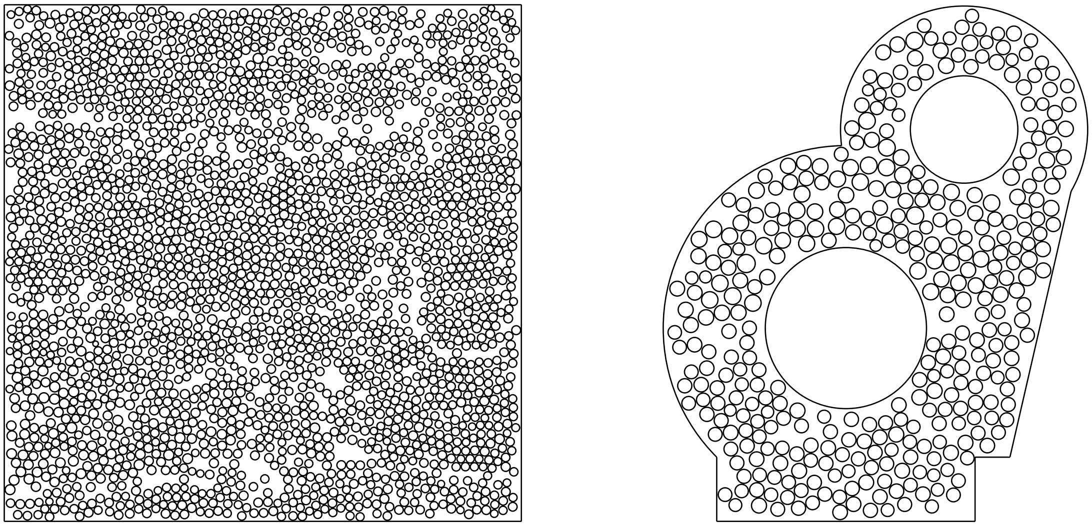

(c) Domain III (d) Domain IV

Figure 3.6. Domains I-IV used in the examples are shown for $\gamma = 1.375$.

4. *GFEM using mesh-based handbooks for problems set in the curvilinear Domains IV.* Here we illustrate the GFEM with mesh-based handbooks for the model problem in Domain IV using two types of meshes Δ_h. A classical FEM mesh $\Delta_h^{(1)}$ for the curvilinear domain Ω' overlapping the voids, and a mesh of squares $\Delta_h^{(2)}$ generated by nested subdivision of a square domain Ω' overlapping the problem domain Ω. We show that the GFEM solution can be easily computed for curvilinear domains and retains its accuracy and robustness characteristics.

5. p_{handbook}-*version of the GFEM.* In this final example we illustrate the p_{handbook}-version of the GFEM, its robustness and its potential of achieving very high accuracy through exponential convergence. Here we underline the effect of the accuracy in the numerical construction of the handbook functions in the global accuracy, and on the exponential convergence characteristics of the method.

Let us now proceed with the description of the results.

3.2.1 GFEM using simple handbook functions in the interior of Domain I

We first considered the Neumann model problem (2.20) in Domain I, shown in Figure 3.6(a) which is obtained from Domain II shown in Figure 3.6(b) by removing the voids near the boundary. Figures 3.7(b)-3.7(d) show Domain I with the radii of the voids multiplied by γ=1.125, 1.25, and 1.375, respectively.

In [51], we focused in the h-version of the GFEM. Here we employ the p-version; we fix the mesh to be the one shown in Figure 3.8, and we report the convergence of the error $e_{\text{REL}}^{\text{GFEM}}(\Delta_h, p, p_{\text{hb}}; \gamma)$ as a function of the polynomial degree p. For the construction of the GFEM solution we employed the standard bi-p FE basis enriched by simple handbook functions $\psi_j^{X;1/2}$, defined in the previous section. The handbook functions were constructed numerically using the GFEM with a bi-p FE basis of degree $p = 5$ in each handbook domain enriched by the analytical void functions for a circular void of degree $p_{\text{voids}} = 1$. We also computed the results in the case that the analytical void functions are omitted, i.e. $p_{\text{voids}} = 0$, to analyze the importance of these functions for the accurate construction of the handbook functions $\psi_j^{X;1/2}$.

As exact solution $u_{\text{EX}}(\gamma)$, we used the overkill GFEM solution computed using the overkill mesh shown in Figure 3.9(a) by employing the GFEM described in [51, 52] with bi-quartic ($p = 4$) FE basis enriched by the analytical voids functions of degree $p_{\text{voids}} = 1$ applied at the vertices of the zeroth layer $n_{\text{layers}} = 0$ around each void. Figure 3.9(b) shows the shades of the modulus of the gradient for the overkill solution for Problem I(d) ($\gamma = 1.375$).

Table 3.1 reports the values of energy norm of the approximate solutions $\|u^{\text{GFEM}}(\Delta_h, p, p_{\text{hb}}; \gamma)\|_{\mathsf{U}}$ and the overkill solution $\|u_{\text{EX}}(\gamma)\|_{\mathsf{U}}$, while Table 3.2 reports the relative errors $e_{\text{REL}}^{\text{GFEM}}(\Delta_h, p, p_{\text{hb}}; \gamma)$. From these results, it can be seen that GFEM is robust with respect to γ, and we can have

$$e_{\text{REL}}^{\text{GFEM}}(\Delta_h, 4, 1; 1.375) \leq 18\%.$$

Table 3.3 reports the relative errors $e_{\text{REL}}^{\text{GFEM}}(\Delta_h, p, p_{\text{hb}}; \gamma)$ in the case that the analytical void functions are not used in the numerical construction of the handbook functions $\psi_j^{X;1/2}$. The difference in the results between Table 3.3 and Table 3.2 reflects the difference in

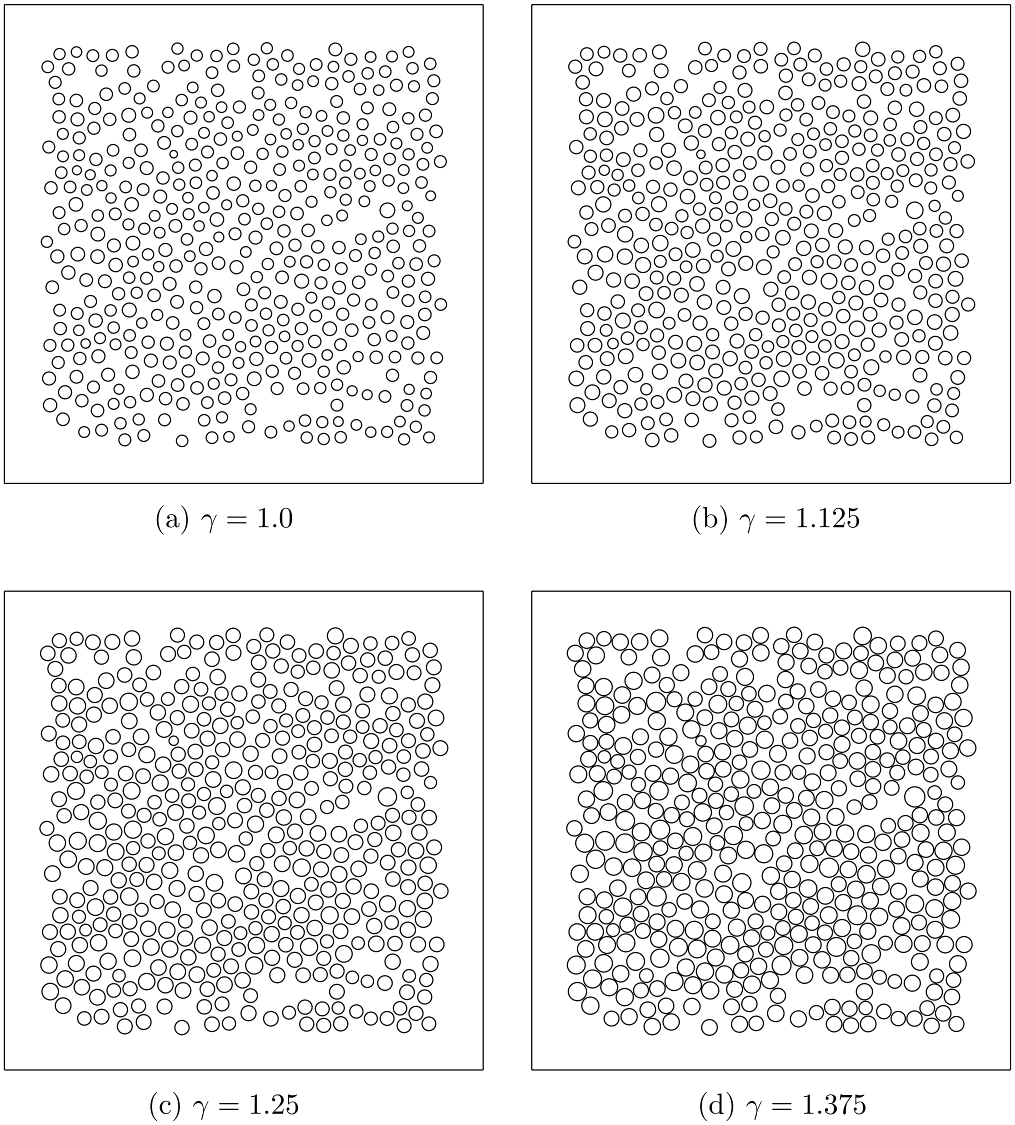
(a) $\gamma = 1.0$

(b) $\gamma = 1.125$

(c) $\gamma = 1.25$

(d) $\gamma = 1.375$

Figure 3.7. Domains for Problems I(a)-I(d) with the parameter γ increasing from 1.0 to 1.375.

the accuracy of the construction of the vertex handbook functions. Table 3.4 reports the relative errors $e_{\mathrm{REL}}^{\mathrm{GFEM}}(\Delta_h, p, 0; \gamma)$ in the case that $p_{\mathrm{hb}} = 0$, i.e. no handbook functions are constructed, and the GFEM solution is constructed by using only the bi-p basis.

Table 3.5 reports the values of the relative errors $e_{\mathrm{REL}}^{\mathrm{GFEM}}(\Delta_h, p, p_{\mathrm{hb}}; \gamma)$ for $p_{\mathrm{hb}} = 2$. Comparing Table 3.5 and Table 3.2, we see that the GFEM solutions with $p_{\mathrm{handbook}} = 2$ have better accuracy than the GFEM solutions computed using $p_{\mathrm{handbook}} = 1$, but the difference is rather small for the employed mesh Δ_h, which can also be observed from the Figure 3.10. We will explore in detail the p_{hb}-version of the GFEM, its convergence and the factors affecting in Section 3.3 below.

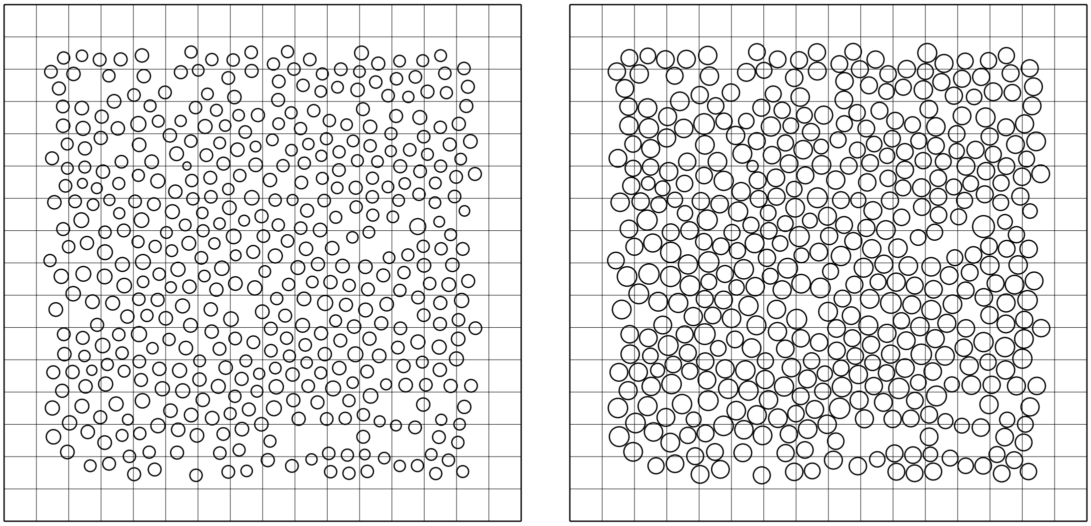

(1) $\gamma = 1.0$ (2) $\gamma = 1.375$

Figure 3.8. Meshes for Problems I(a) and I(d) with the parameter γ equals to 1.0 and 1.375, respectively.

Table 3.1. Energy norm of the approximate solutions $||u_h||_{\mathsf{U}}$ and the overkill solutions $||u_{\text{ov}}||_{\mathsf{U}}$. Analytical void functions of order $p_{\text{void}} = 1$ were employed for the simple handbook solutions $\psi_j^{X;1/2}$.

	$\gamma = 1$	$\gamma = 1.125$	$\gamma = 1.25$	$\gamma = 1.375$
$p = 1$	535.923158	566.670149	606.656390	662.571213
$p = 2$	544.115485	576.087492	617.866398	677.010972
$p = 3$	546.490465	579.909144	623.943664	687.225725
$p = 4$	547.903773	582.117702	627.509143	693.721016
$\|\|u_{\text{ov}}\|\|_{\mathsf{U}}$	550.711188	585.910927	633.136615	704.842281

Table 3.2. Relative errors $e_{\text{REL}}^{\text{GFEM}}(\Delta_h, p, p_{\text{hb}}; \gamma)$ for Problems I(a)-I(d). In these results we employed the handbook functions $\psi_j^{X;1/2}$ constructed numerically in each patch using the GFEM with a bi-quintic ($p = 5$) FE basis enriched by analytical void functions at $n_{\text{layers}} = 0$ around each void.

	$\gamma = 1$	$\gamma = 1.125$	$\gamma = 1.25$	$\gamma = 1.375$
$p = 1$	23.02%	25.42%	28.62%	34.11%
$p = 2$	15.43%	18.23%	21.83%	27.82%
$p = 3$	12.36%	14.28%	16.98%	22.22%
$p = 4$	10.08%	11.36%	13.30%	17.69%

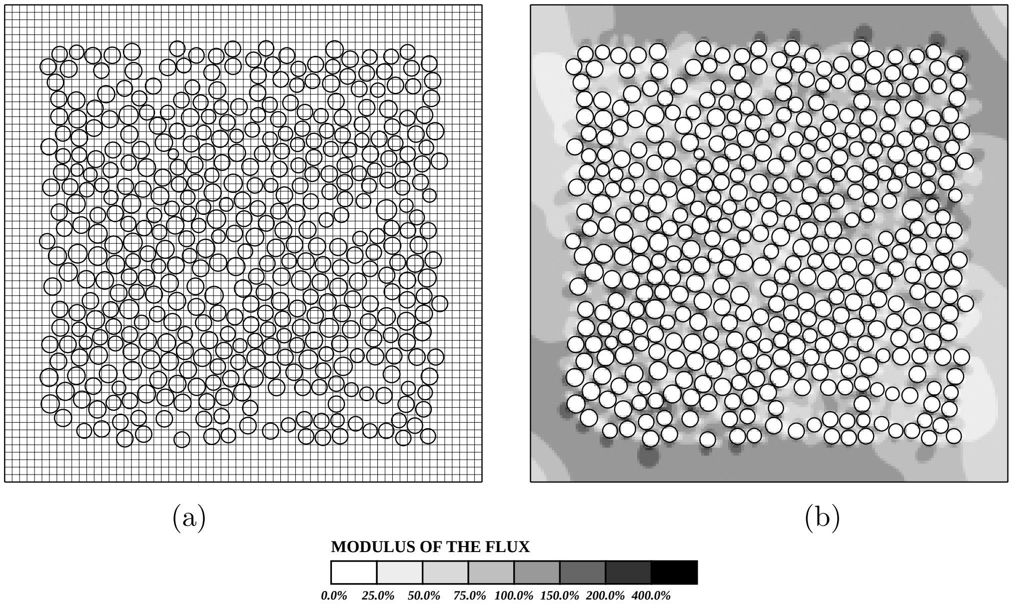
(a)

(b)

Figure 3.9. Overkill solution for Problem I(d) ($\gamma = 1.375$). (a) The employed overkill mesh Δ_h^{ov}. (b) The contours of the relative modulus of the gradient. The overkill solution was obtained by using the degree of element $p = 4$, with $p_{\text{voids}} = 1$ analytical void functions at $n_{\text{layers}} = 0$. The energy norm is $||u_{\text{ov}}||_{\mathsf{U}} = 704.842281$, the number of degree of freedom is $N_{\text{dof}} = 78010$, and the number of elements is $n_{\text{elements}} = 4096$.

Table 3.3. Relative errors $e_{\text{REL}}^{\text{GFEM}}(\Delta_h, p, p_{\text{hb}}; \gamma)$ for Problem I(a)-I(d). The approximate solutions were computed by employing the handbook functions $\psi_j^{X;1/2}$, but no analytical void functions were used in the numerical construction of these functions.

	$\gamma = 1.0$	$\gamma = 1.125$	$\gamma = 1.25$	$\gamma = 1.375$
$p = 1$	40.56%	40.90%	44.29%	48.89%
$p = 2$	36.02%	39.04%	42.20%	46.50%
$p = 3$	33.37%	35.35%	37.18%	39.91%
$p = 4$	27.64%	27.90%	27.96%	29.09%

Table 3.4. Relative errors $e_{\text{REL}}^{\text{GFEM}}(\Delta_h, p, 0; \gamma)$ for Problems I(a)-I(d). Here the GFEM solution employed only the bi-p FE basis on the mesh Δ_h.

	$\gamma = 1.0$	$\gamma = 1.125$	$\gamma = 1.25$	$\gamma = 1.375$
$p = 1$	40.56%	44.84%	50.65%	55.10%
$p = 2$	39.24%	43.01%	46.84%	51.77%
$p = 3$	35.77%	38.29%	40.63%	43.85%
$p = 4$	30.04%	30.91%	31.51%	33.00%

Table 3.5. Relative errors $e_{\mathrm{REL}}^{\mathrm{GFEM}}(\Delta_h, p, 2; \gamma)$ for Problem I(a)-I(d). The GFEM solutions were computed by employing the handbook functions $\psi_j^{X;1/2}$ of order $p_{\text{handbook}} = 2$, which were constructed numerically by employing the GFEM with bi-quintic ($p = 5$) FE basis enriched by analytical void functions with the order $p_{\text{voids}} = 1$ at the $n_{\text{layers}} = 0$ around each void.

	$\gamma = 1.0$	$\gamma = 1.125$	$\gamma = 1.25$	$\gamma = 1.375$
$p = 1$	20.43%	22.69%	25.70%	30.94%
$p = 2$	13.91%	16.36%	19.53%	25.09%
$p = 3$	10.80%	12.54%	15.03%	20.08%
$p = 4$	8.85%	10.11%	12.00%	16.31%

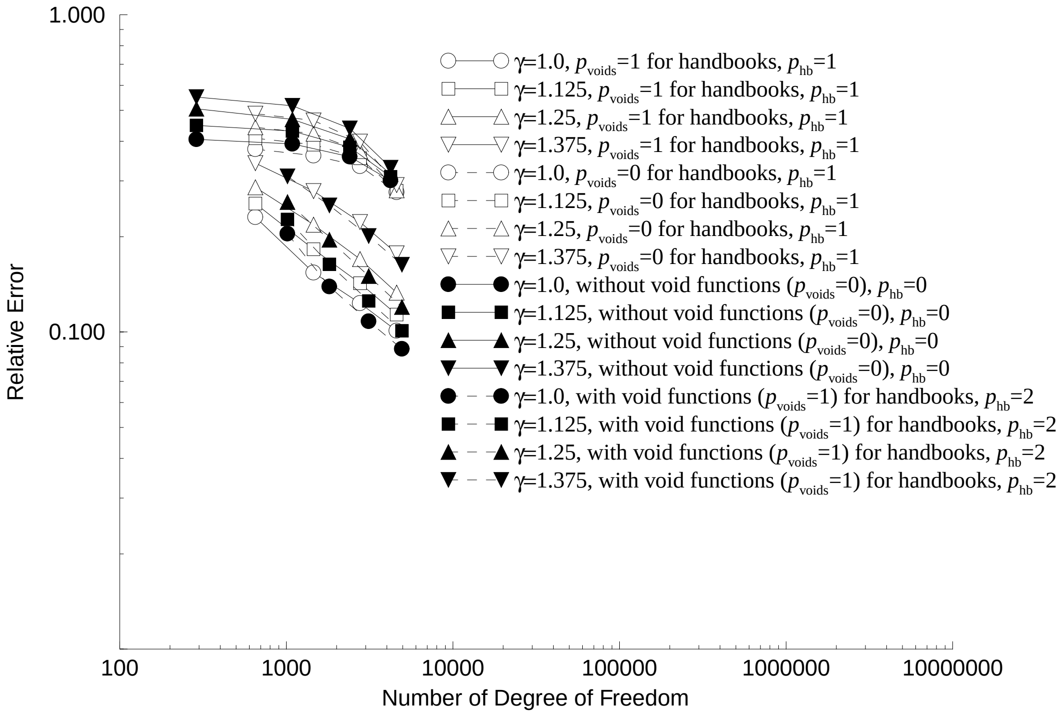

Figure 3.10. The convergence of the GFEM solutions for Problems I(a)-I(d) with four choices of handbook functions. (a) $p_{\text{hb}} = 1$, using $p_{\text{voids}} = 1$; (b) $p_{\text{hb}} = 1$, using $p_{\text{voids}} = 0$; (c) $p_{\text{hb}} = 0$; (d) $p_{\text{hb}} = 2$, using $p_{\text{voids}} = 1$.

3.2.2 GFEM using simple and improved handbooks up to the boundary of Domain II

Here, we consider the Neumann model problem (2.20) in Domain II shown in Figure 3.11. We call the problem (2.20) defined in the domain Ω_γ shown in Figure 3.11(a)-3.11(d), Problem II(a)-II(d), respectively. We computed the GFEM solution using a bi-p FE basis enriched by handbook functions up to the boundary, and compared the accuracy of the solution using simple versus improved handbook functions.

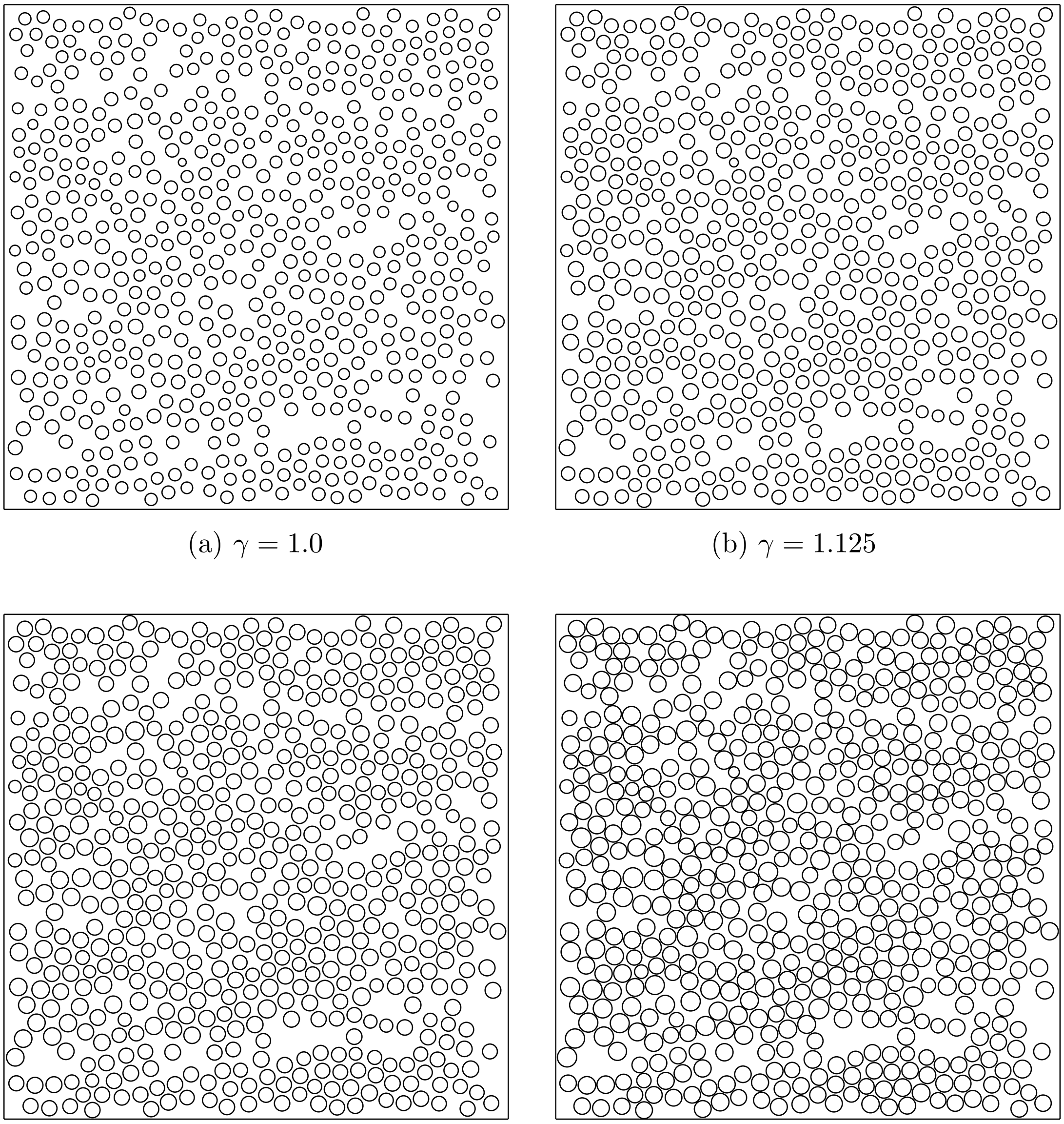

(a) $\gamma = 1.0$

(b) $\gamma = 1.125$

(c) $\gamma = 1.25$

(d) $\gamma = 1.375$

Figure 3.11. Domains for Problems II(a)-II(d) with the parameter γ from 1.0 to 1.375, respectively.

3.2.2.1 GFEM using simple handbooks

Once more, we employed as mesh Δ_h, the mesh obtained by uniformly dividing the square domain four times. Figure 3.12 shows the mesh Δ_h overlapping the problem domain for $\gamma = 1.0$ and $\gamma = 1.125$.

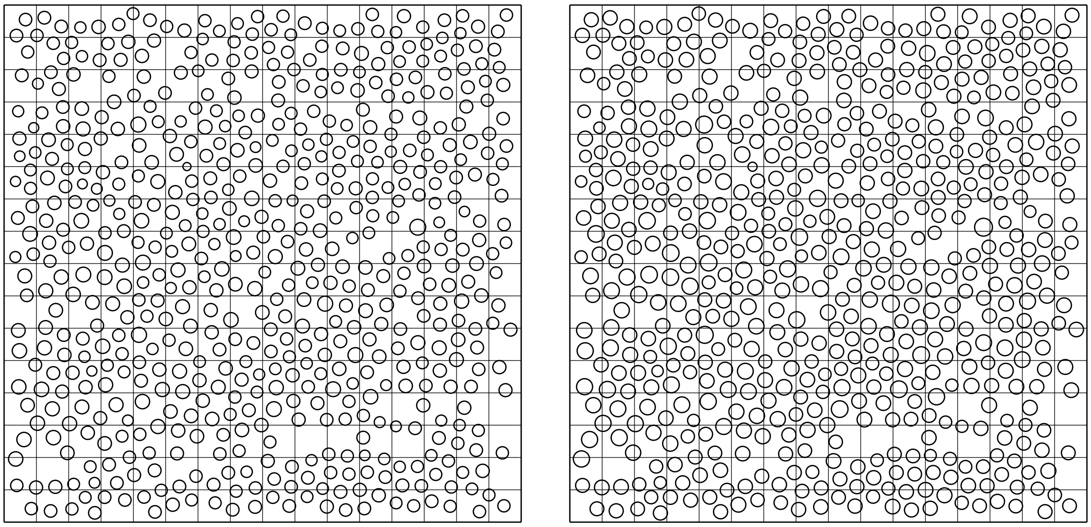
(1) $\gamma = 1.0$ (2) $\gamma = 1.125$

Figure 3.12. Meshes for Problems II(a) and II(b) with the parameter γ equals to 1.0 and 1.125, respectively.

The overkill solution u_{ov} was obtained as in previous example, i.e. by using the GFEM of [51, 52] with bi-quartic ($p = 4$) FE basis on the mesh Δ_h^{ov} enriched by analytical void functions of degree $p_{\text{voids}} = 1$ applied at $n_{\text{layers}} = 0$ around each void. Figure 3.13 shows the contour of the relative modulus of the gradient of the overkill solution and the overkill mesh for $\gamma = 1.0$.

Table 3.6 reports the values of energy norm of the GFEM solutions $\|u^{\text{GFEM}}(\Delta_h, p, p_{\text{hb}}; \gamma)\|_{\mathsf{U}}$ and the overkill solutions $\|u_{\text{EX}}(\gamma)\|_{\mathsf{U}}$ of Problem II. The GFEM solutions $u^{\text{GFEM}}(\Delta_h, p, p_{\text{hb}}; \gamma)$ were computed by using $p = 1, 2, 3$ and 4, enriched by simple handbook functions $\psi_j^{X;1/2}$ of order $p_{\text{hb}} = 1$ applied at each vertex X. For the numerical construction of the handbook functions $\psi_j^{X;1/2}$, we employed the bi-quintic ($p = 5$) FE basis enriched by the analytical void functions at $n_{\text{layers}} = 0$ around each void. Table 3.7 reports the relative errors $e_{\text{REL}}^{\text{GFEM}}(\Delta_h, p, p_{\text{hb}}; \gamma)$. From these results, it can be seen that some relative errors are not small, especially for the cases of $\gamma = 1.375$.

Next, we show that the accuracy of the GFEM solution can be greatly improved by using the improved handbook functions $\psi_j^{X;1}$ which include more information about the problem than the simple handbook functions.

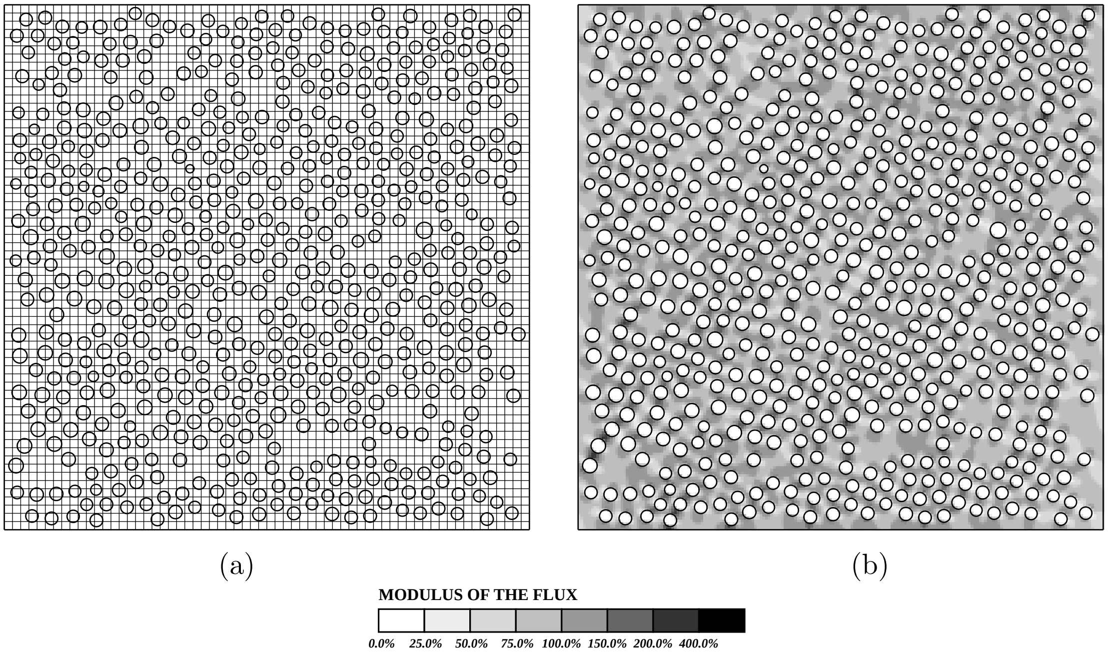

(a) (b)

Figure 3.13. Overkill solution for Problem II(a). (a) The employed mesh for overkill solution. (b) The contour of the relative modulus of the gradient. The overkill solution was obtained by using the degree of element $p = 4$, with $p_{\text{voids}} = 1$ void functions at $n_{\text{layers}} = 0$. The energy norm is $||u_{\text{ov}}||_{\mathsf{U}} = 597.4304695$, the number of degree of freedom is $N_{\text{dof}} = 80286$, and the number of elements is $n_{\text{elements}} = 4096$.

Table 3.6. Energy norms of the approximate solutions $||u^{\text{GFEM}}(\Delta_h, p, p_{\text{hb}}; \gamma)||_{\mathsf{U}}$, and the overkill solutions $||u_{\text{ov}}||_{\mathsf{U}}$ for Problems II(a)-II(d). Analytical void functions of order $p_{\text{void}} = 1$ were employed for the simple handbook solutions $\psi_j^{X;1/2}$.

	$\gamma = 1.0$	$\gamma = 1.125$	$\gamma = 1.25$	$\gamma = 1.375$
$p = 1$	576.899523	623.629644	687.604985	784.859648
$p = 2$	583.622996	632.385964	699.765120	804.114661
$p = 3$	587.720482	639.386588	711.812696	826.837669
$p = 4$	590.810268	644.376843	720.184043	843.355790
$\|\|u_{\text{ov}}\|\|_{\mathsf{U}}$	597.430470	653.098684	733.093724	870.723752

Table 3.7. Relative errors $e_{\mathrm{REL}}^{\mathrm{GFEM}}(\Delta_h, p, p_{\mathrm{hb}}; \gamma)$ for Problems II(a)-II(d). The GFEM solutions were computed by employing the handbook functions $\psi_j^{X;1/2}$ of order $p_{\mathrm{handbook}} = 1$, which were constructed numerically by employing the GFEM with bi-quintic ($p = 5$) FE basis enriched by analytical void functions with the order $p_{\mathrm{voids}} = 1$ at the $n_{\mathrm{layers}} = 0$ around each void.

	$\gamma = 1.0$	$\gamma = 1.125$	$\gamma = 1.25$	$\gamma = 1.375$
$p = 1$	25.99%	29.70%	34.68%	43.30%
$p = 2$	21.37%	24.98%	29.81%	38.36%
$p = 3$	17.96%	20.38%	23.92%	31.35%
$p = 4$	14.85%	16.29%	18.68%	24.87%

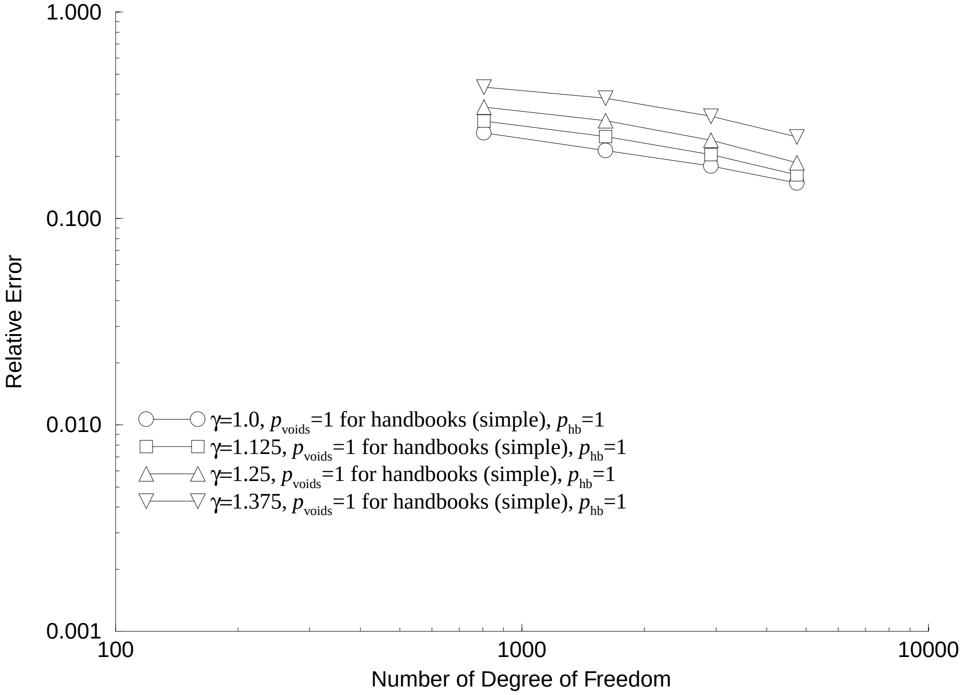

Figure 3.14. Convergence of the GFEM solutions $u^{\mathrm{GFEM}}(\Delta_h, p, p_{\mathrm{hb}}; \gamma)$ for Problems II(a)-II(d), obtained by using simple handbook functions $\psi_j^{X;1/2}$.

3.2.2.2 GFEM using improved handbooks

Let us now show that, by enriching the bi-p GFEM approximation using the improved handbook functions $\psi_j^{X;1}$, we can obtain dramatic improvement in the accuracy of the global GFEM solutions.

Let us start by analyzing the accuracy of the numerical construction of the improved handbook functions $\psi_j^{X;1}$. Figure 3.15 shows examples of typical interior, boundary and corner handbook domains. Let us first consider the interior handbooks corresponding to the domain shown in Figure 3.16(a). As in the previous example, we constructed the handbook functions $\psi_j^{X;1}$, numerically, by employing the GFEM with bi-p FE basis on the mesh shown in Figure 3.16(b), enriched by the analytical void functions of degree one, $p_{\text{voids}} = 1$, at $n_{\text{layers}} = 0$ around each void. Figure 3.17 shows the contour plots of the relative modulus of the gradient of $\psi_1^{X;1}$ and $\psi_2^{X;1}$, computed using $p = 5$. Table 3.8 reports the p convergence of the energy norm of the computed handbook solutions $\|\psi_j^{X;1}\|_{\mathsf{U}(\tilde{\omega}_X^{(1);1})}$, for $p = 1, ..., 5$. From these results, it can be seen that the energy norm of the handbook solutions, obtained using $p = 5$, has converged to at least four digits.

Let us also report the corresponding results for the typical boundary handbook shown in Figure 3.18(a), and the typical corner handbook shown in Figure 3.19(a). Once more we computed the handbook functions $\psi_j^{X;1/2}$ using the bi-p basis enriched by void functions of degree $p_{\text{voids}} = 1$ at $n_{\text{layers}} = 0$ around each void. Figure 3.18(b), and Figure 3.19(b), show the contour plots of the relative modulus of the gradient of the boundary, and corner, handbook functions, respectively, computed using $p = 5$. The p convergence of the energy norm of the computed handbook solutions $\psi_j^{X;1/2}$, for $p = 1, ..., 5$, is also reported in Table 3.8. From these results, it can be seen that the energy norm of the handbook solutions $\psi_j^{X;1/2}$, obtained using $p = 5$, has converged to at least five digits for boundary handbook functions, and six digits for corner handbook functions.

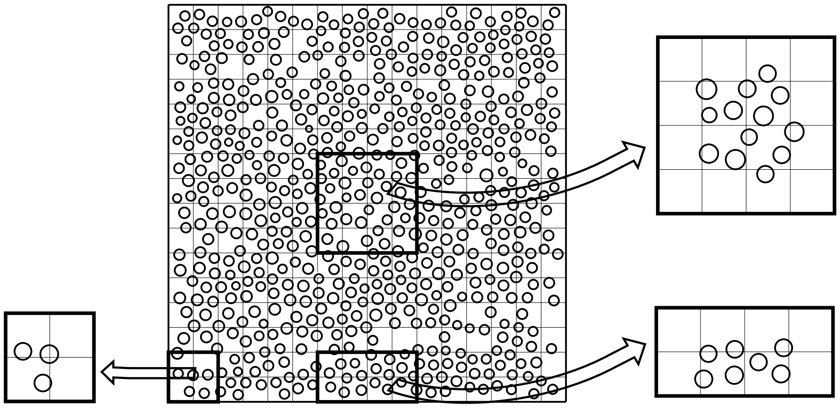

Figure 3.15. Typical examples of improved handbooks for an interior, boundary and corner vertex.

Table 3.8. p-convergence of the energy norm of the approximation of the handbook functions for the typical handbook problems, for the handbook domains shown in Figure 3.16(a), Figure 3.18(a) and Figure 3.19(a). The solutions $\psi_j^{X;1}$ were obtained by employing the variable bi-p finite element basis on the meshes shown in Figures 3.16(b), 3.18(a) and 3.19(a), enriched by analytical void functions of degree $p_{\text{voids}} = 1$ added at $n_{\text{layers}} = 0$ around each void. $E\%$ is the percentage relative difference in the energy norm of the last two solutions in the p-extension sequence for each problem.

	Interior Handbook			Boundary Handbook		Corner Handbook	
p	N	$\Re(z)$	$\Im(z)$	N	x'	N	$r^2 \cos(2\theta)$
1	267	55.323285	55.244399	151	39.151635	79	27.400615
2	475	55.467721	55.381219	259	39.201933	139	27.424249
3	811	55.469442	55.383318	431	39.202815	223	27.425277
4	1275	55.470216	55.383982	667	39.203158	343	27.425402
5	1867	55.470499	55.384369	967	39.203303	495	27.425431
	$E\%$	0.32%	0.37%	$E\%$	0.27%	$E\%$	0.15%

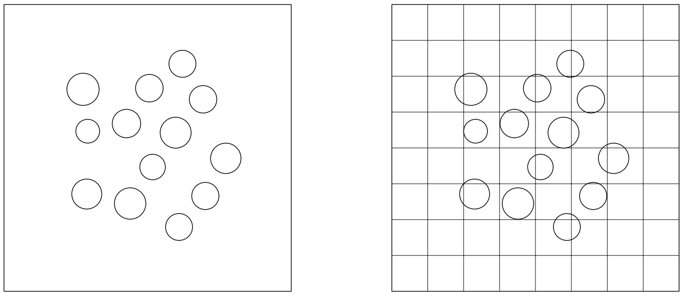

Figure 3.16. Domain and mesh for the typical example of interior handbook.

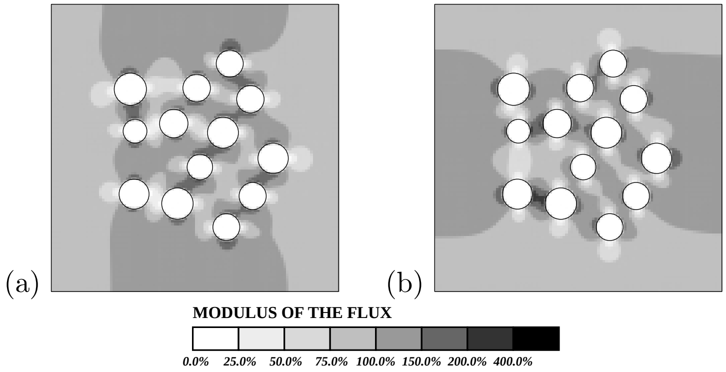

Figure 3.17. The relative modulus of the gradient for the typical interior handbook solutions $\psi_j^{X;1}$ for $p = 5$ for (a). $\Re(z)$, (b). $\Im(z)$.

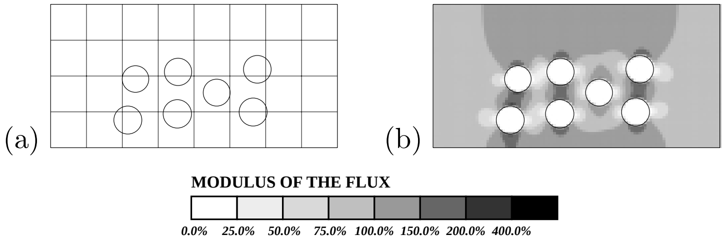

Figure 3.18. (a). The mesh for the typical boundary handbook problem. (b). The relative modulus of the gradient for the typical boundary handbook solution $\psi_1^{X;1}$ for $p = 5$.

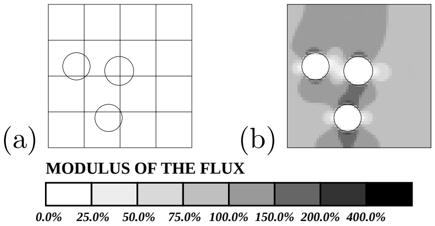

Figure 3.19. (a). The mesh for the typical corner handbook problem. (b). The relative modulus of the gradient for the typical corner handbook solution $\psi_1^{X;1}$ for $p = 5$.

Figure 3.20 shows the graph of convergence of the energy norm of the relative error $e_{\mathrm{REL}}^{\mathrm{GFEM}}(\Delta_h, p, p_{\mathrm{hb}};\gamma)$, while Table 3.9 reports the values for $\gamma = 1.0$, 1.125, 1.25 and 1.375. From these results, it can be seen that the relative error is less than 5% except for the case of $\gamma = 1.375$ and $p = 1$. Hence the use of improved handbook functions $\psi_j^{X;1}$ leads to significant improvements in the accuracy of the GFEM solution.

Table 3.9. Relative errors $e_{\mathrm{REL}}^{\mathrm{GFEM}}(\Delta_h, p, p_{\mathrm{hb}};\gamma)$ for Problems II(a)-(d). The GFEM solutions were computed by employing the improved handbook functions $\psi_j^{X;1}$ of order $p_{\mathrm{handbook}} = 1$, which were constructed numerically by employing the GFEM with bi-quintic ($p = 5$) FE basis enriched by analytical void functions with the order $p_{\mathrm{voids}} = 1$ at $n_{\mathrm{layers}} = 0$ around each void.

	$\gamma = 1.0$	$\gamma = 1.125$	$\gamma = 1.25$	$\gamma = 1.375$
$p = 1$	2.61%	3.48%	4.69%	7.25%
$p = 2$	1.85%	2.44%	3.24%	4.99%
$p = 3$	1.19%	1.63%	2.25%	3.72%
$p = 4$	0.96%	1.31%	1.85%	3.15%

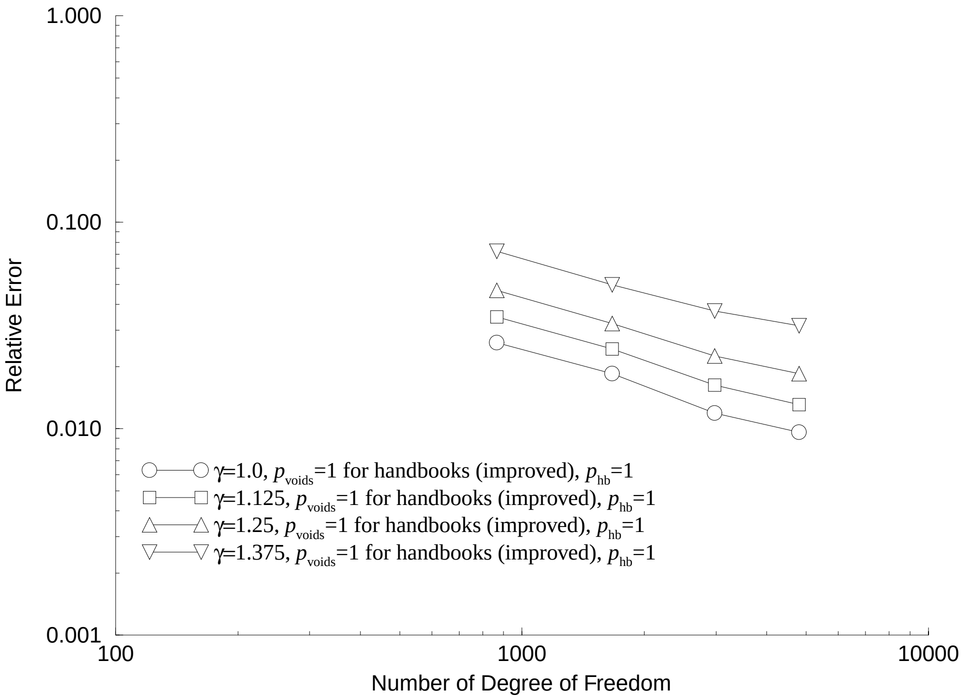

Figure 3.20. Convergence of the GFEM solutions $u^{\mathrm{GFEM}}(\Delta_h, p, p_{\mathrm{hb}}; \gamma)$ for Problems II(a)-II(d), obtained by using improved handbook functions $\psi_j^{X;1}$.

3.2.3 GFEM using hierarchical handbooks for Domain III

We will now give an example of hierarchical construction of the handbook functions which can be used for solving more complex problems.

We employed the Neumann model problem (2.20) in the Domain III shown in Figure 3.21, for $\gamma = 1.0$. Domain III has 2500 voids in its interior. As in the previous examples, we considered this problem for $\gamma = 1.0$, 1.125, 1.25 and 1.375, we call Problem III(a)-(d), respectively.

The idea of hierarchical handbooks is illustrated in Figure 3.22. First, we create the vertex handbooks corresponding to the global mesh Δ_h, then we employ the same procedure for each handbook domain, using the employed handbook meshes, recursively.

As in the previous examples, we employed the uniform mesh Δ_h obtained from four uniform refinements of the problem domain and computed the GFEM solution by using $p = 1, 2, 3$ and 4, enriched by the improved handbook functions, which were constructed numerically using a 2 level hierarchical approach.

Table 3.10 reports the values of the energy norms of the computed GFEM and overkill solutions, while Table 3.11 reports the relative values of the energy norm of the error

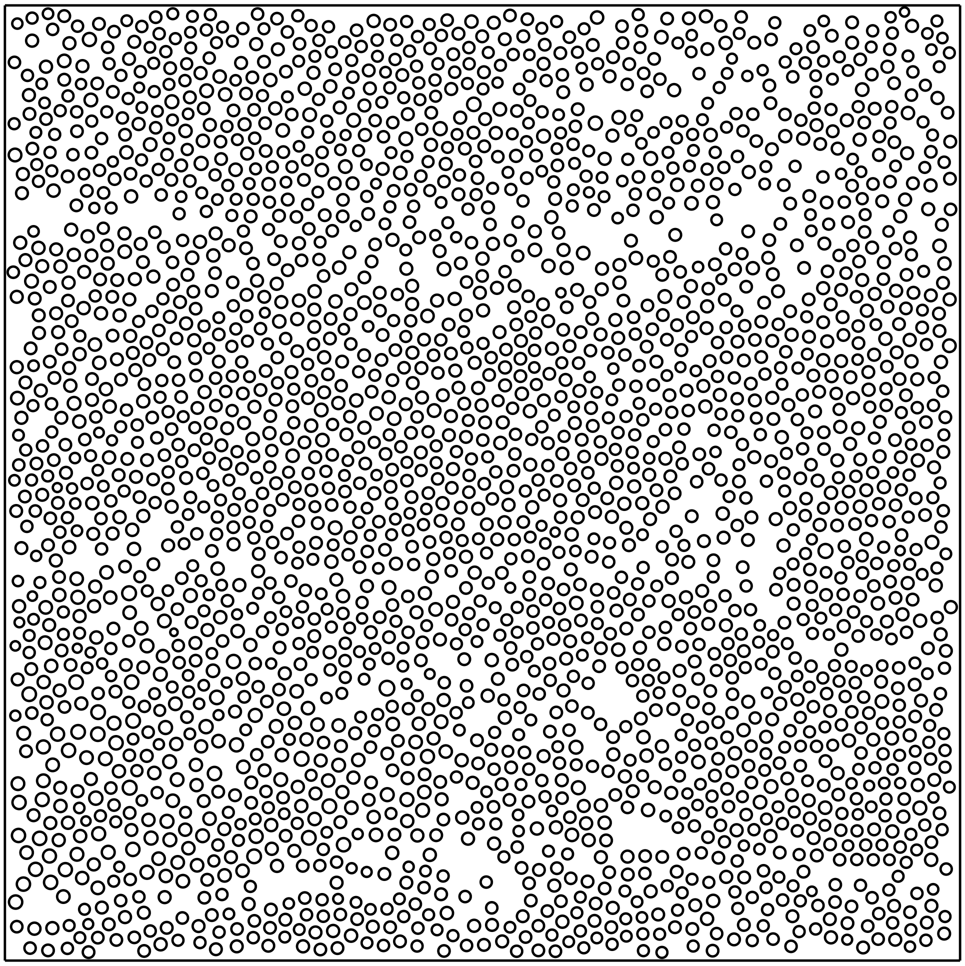

Figure 3.21. Domain III with 2500 voids for $\gamma = 1.0$.

$e_{\mathrm{REL}}^{\mathrm{GFEM}}(\Delta_h, p, p_{\mathrm{hb}}; \gamma)$ for Problems III(a)-III(d). The overkill solutions were obtained by using the bi-quintic, $p = 5$, FE basis, enriched by the handbook functions of level one which we constructed numerically as described in the previous section. Figure 3.23 shows the convergence graph of the relative error $e_{\mathrm{REL}}^{\mathrm{GFEM}}(\Delta_h, p, p_{\mathrm{hb}}; \gamma)$ of the energy norm. From these results, we see that, the GFEM with hierarchical construction of the handbook functions is almost as effective as the GFEM using the same functions constructed in the one-level construction employed in the previous sections. Nevertheless, there may be a loss of accuracy due to error accumulation from the numerical constructions at the various levels. This error accumulation can be seen in the loss of the convergence rate observed in the convergence graphs in Figure 3.23 compared with the corresponding convergence graphs in the previous examples.

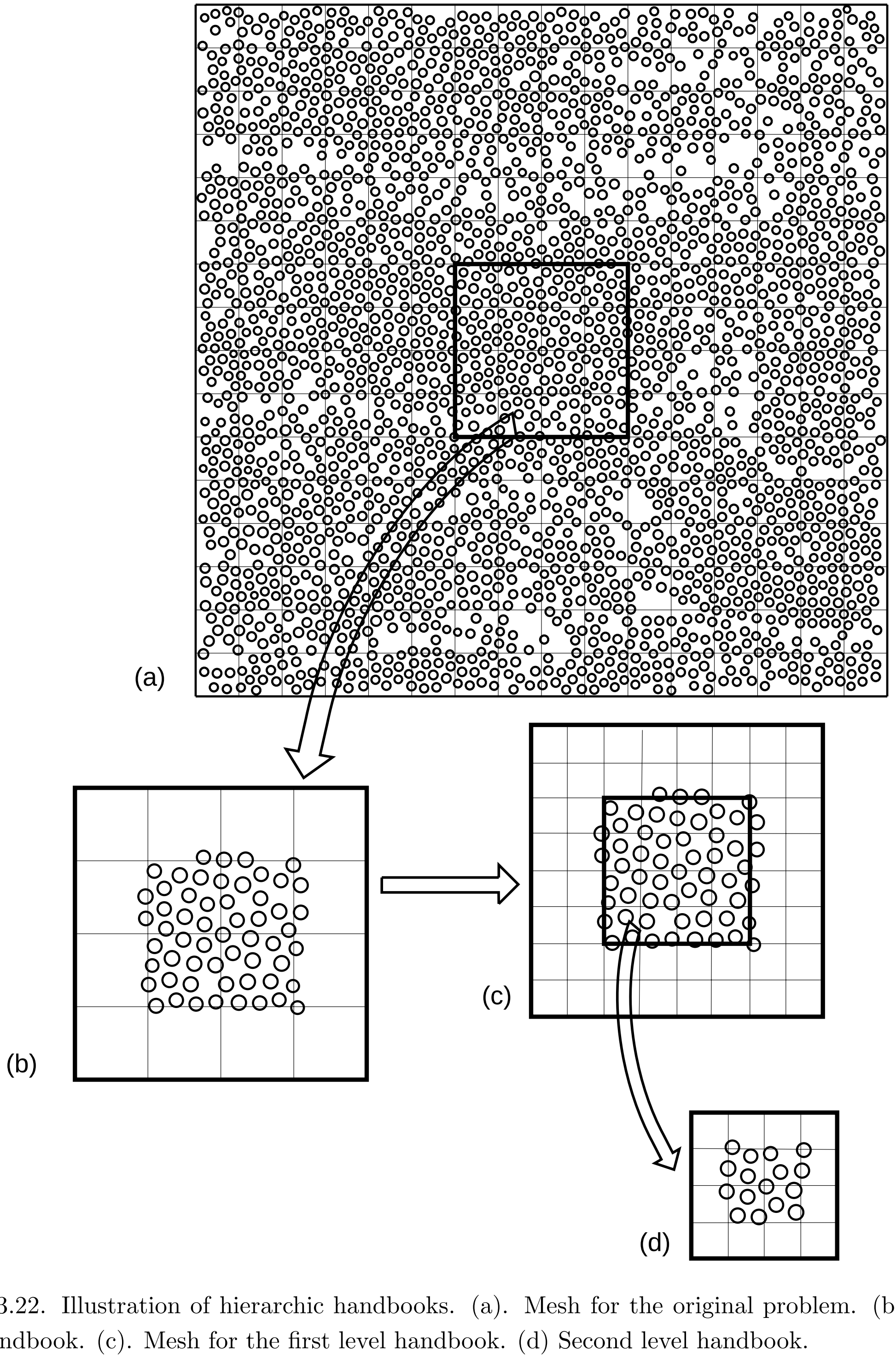

Figure 3.22. Illustration of hierarchic handbooks. (a). Mesh for the original problem. (b). First level handbook. (c). Mesh for the first level handbook. (d) Second level handbook.

Table 3.10. Energy norms of the GFEM solutions $||u^{\mathrm{GFEM}}(\Delta_h, p, p_{\mathrm{hb}}; \gamma)||_{\mathsf{U}}$, and the corresponding overkill solutions $||u_{\mathrm{ov}}||_{\mathsf{U}}$ for Problems III(a)-(d). The GFEM solutions were computed by using two levels of handbook functions.

	$\gamma = 1.0$	$\gamma = 1.125$	$\gamma = 1.25$	$\gamma = 1.375$
$p = 1$	1168.935284	1272.129223	1418.327297	1661.111930
$p = 2$	1170.506695	1274.111992	1421.313153	1666.839818
$p = 3$	1171.836636	1275.622005	1423.568787	1670.208030
$p = 4$	1172.711382	1276.849101	1425.354149	1674.199828
$\vert\vert u_{\mathrm{ov}}\vert\vert_{\mathsf{U}}$	1174.251507	1279.176820	1429.304841	1683.180698

Table 3.11. Relative errors $e_{\mathrm{REL}}^{\mathrm{GFEM}}(\Delta_h, p, p_{\mathrm{hb}}; \gamma)$ for Problems III(a)-(d). The GFEM solutions were computed by using two levels of handbook functions.

	$\gamma = 1.0$	$\gamma = 1.125$	$\gamma = 1.25$	$\gamma = 1.375$
$p = 1$	9.50%	10.48%	12.37%	16.14%
$p = 2$	7.98%	8.89%	10.56%	13.90%
$p = 3$	6.41%	7.45%	8.95%	12.39%
$p = 4$	5.12%	6.03%	7.43%	10.32%

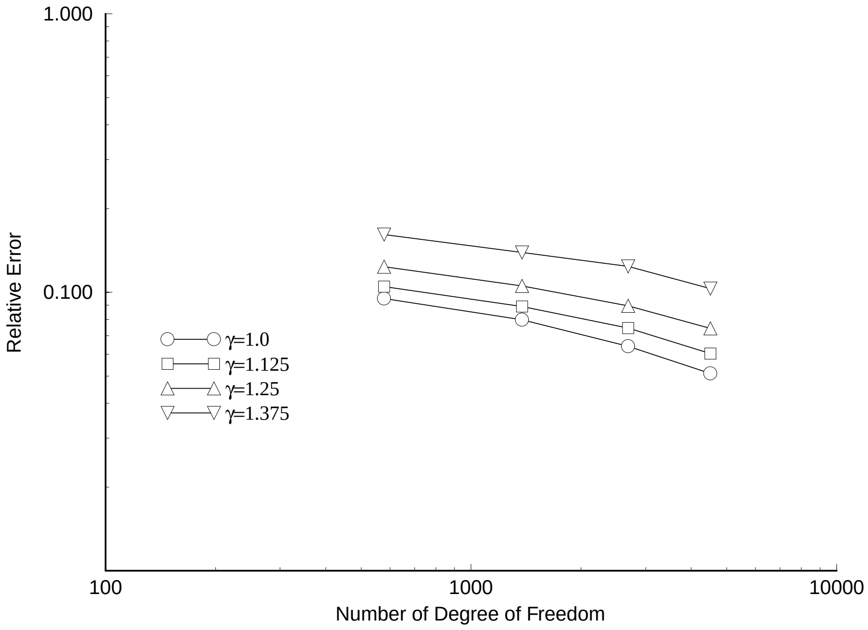

Figure 3.23. Convergence graphs of the GFEM solutions for Problems III(a)-III(d) using two levels of handbook functions.

3.2.4 GFEM using mesh-based handbooks for the model problem in curvilinear Domains IV

Here we illustrate the GFEM with mesh-based handbooks for the model Neumann problem (2.20) defined in the curvilinear Domain IV shown in Figure 3.6(d), and also in Figure 3.24 for $\gamma = 1.0$ and $\gamma = 1.375$, respectively. We employed two types of meshes Δ_h: a mesh of curvilinear quadrilaterals $\Delta_h^{(1)}$ shown in Figure 3.25(a) which is a classical FEM mesh for the curvilinear domain without the voids; and a mesh of squares $\Delta_h^{(2)}$ shown in Figure 3.25(b) which is generated by nested subdivision of a square overlapping the problem domain.

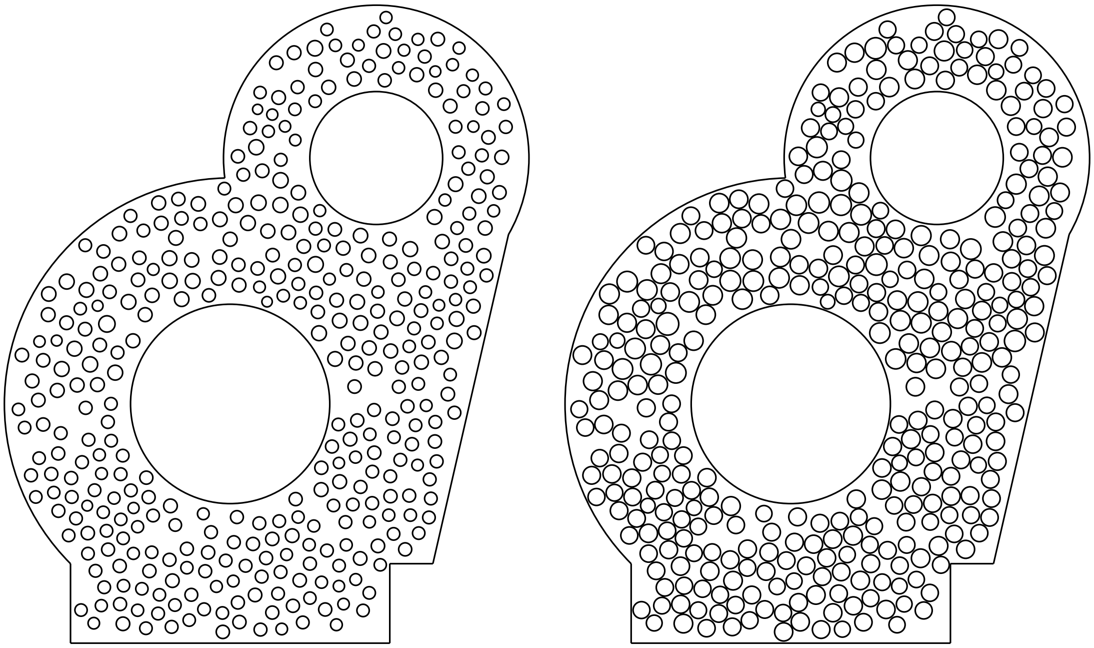
(a) $\gamma = 1.0$ (d) $\gamma = 1.375$

Figure 3.24. Domains for Problem IV(a) and IV(d) corresponding to $\gamma = 1.0$ and $\gamma = 1.375$, respectively.

As exact solution u_{EX}, we employed an overkill solution u_{ov} computed using the GFEM of [51, 52] on an overkill mesh of squares Δ_h^{ov} shown in Figure 3.26(a), which is obtained by uniformly subdividing the square 7 times, and bi-quartic ($p = 4$) FE basis enriched by the analytical void functions of order $p_{\mathrm{voids}} = 2$ applied at the vertices with zeroth layer ($n_{\mathrm{layers}} = 0$) of each void, and the analytical singular functions of order $p_{\mathrm{singular}} = 1$ at the vertices with zeroth layer ($n_{\mathrm{layers}} = 0$) of each singular point. Figure 3.26(b) shows the relative modulus of the gradient of the overkill solution for the case $\gamma = 1.0$, whose energy norm is $\|u_{\mathrm{ov}}\|_{\mathsf{U}} = 480.759460$ with 16384 elements and $N_{\mathrm{dof}} = 129159$. The energy norms of the overkill solutions for other choices of γ are reported in Table 3.12.

Table 3.12. Energy norm and number of degree of freedom of the overkill solutions of Problem IV.

	$\gamma = 1.0$	$\gamma = 1.125$	$\gamma = 1.25$	$\gamma = 1.375$
$\|\|u_{\text{ov}}\|\|_{\mathsf{U}}$	480.759460	521.600172	579.146978	674.268932
N_{dof}	129159	130221	130797	130930

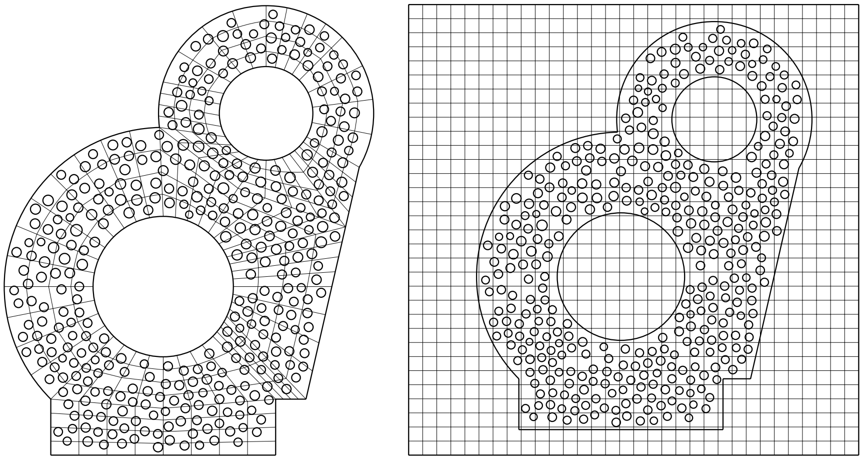

(a) (b)

Figure 3.25. The two types of meshes employed for Problem IV. (a) The mesh of curvilinear quadrilaterals $\Delta_h^{(1)}$, and (b) the mesh of squares $\Delta_h^{(2)}$, for $\gamma = 1.0$.

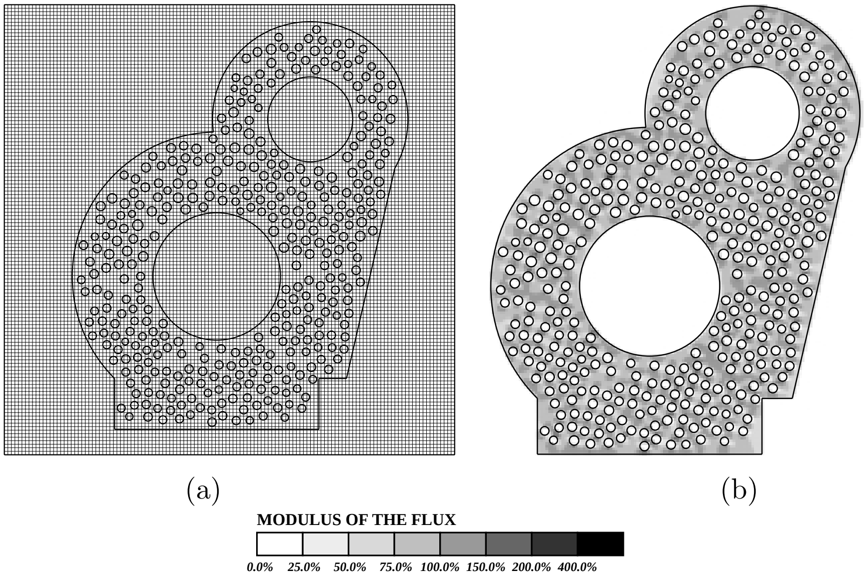

(a) (b)

Figure 3.26. Overkill solution of Problem IV. (a) Mesh used for the overkill solution, (b) relative modulus of gradient of the overkill solution, for the case $\gamma = 1.0$.

3.2.4.1 GFEM using handbooks on a mesh of curvilinear quadrilaterals $\Delta_h^{(1)}$

First, let us investigate the accuracy of the handbook functions $\psi_j^{X;1}$ when the mesh $\Delta_h^{(1)}$, shown in Figure 3.25(a), is used. Figure 3.27 shows two typical handbook domains $\tilde{\omega}_X^{(1);1}$ at singular points. We will denote the handbook problems of degree $p_{\text{hb}} = 1$ in these domains by HB12, and HB15, respectively. We constructed numerically the handbook functions $\psi_j^{X;1}$ in these domains by employing the GFEM on the meshes obtained by uniformly subdividing the initial meshes shown in Figure 3.27, using the bi-p FE basis enriched by the analytical void functions of degree $p_{\text{voids}} = 1$ added at $n_{\text{layers}} = 0$ around each void. Table 3.13 reports the p-convergence of the energy norms of the first handbook functions $\psi_1^{X;1}$ of the two typical handbooks at singular points, HB12 and HB15. Note that the relative difference between the last two solutions of each sequence of the solutions, is less than 0.3%. Figure 3.28 shows the relative modulus of the gradient of the solutions $\psi_1^{X;1/2}$ for HB12, and HB15, computed using $p = 5$.

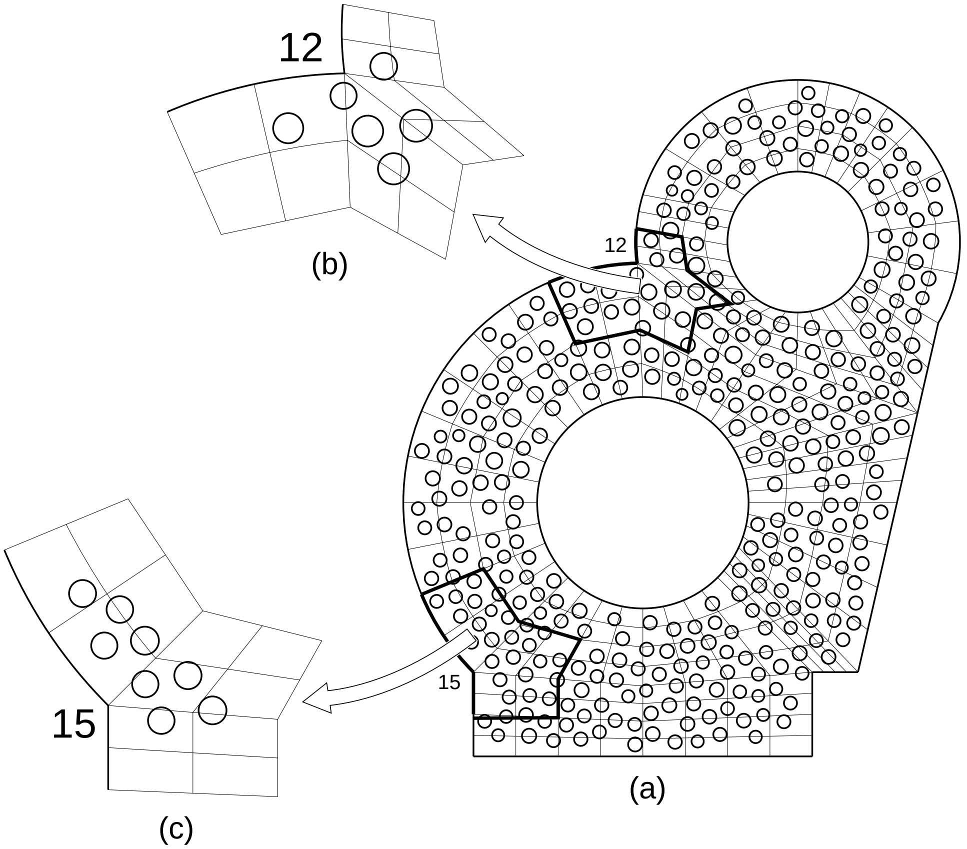

Figure 3.27. Creation of typical handbooks on the mesh $\Delta_h^{(1)}$. (a) Mesh of curvilinear quadrilaterals $\Delta_h^{(1)}$ employed for the GFEM solution. (b) and (c) Handbook domains $\tilde{\omega}_X^{(1);1}$ for the vertices X_{12} and X_{15}, respectively. The corresponding handbooks are denoted by HB12 and HB15, respectively.

Table 3.13. p-convergence of the energy norms of the handbook functions $\|\psi_1^{X;1}\|_{\mathsf{U}(\tilde{\omega}_X^{(1);1})}$ for the typical handbooks HB12 and HB15.

p	N	HB12	N	HB15
1	525	93.963818	420	96.154243
2	1331	94.109622	1028	96.306452
3	2645	94.113450	2020	96.308683
4	4467	94.114138	3396	96.308971
5	6797	94.114361	5156	96.309148
	$E\%$	0.22%	$E\%$	0.19%

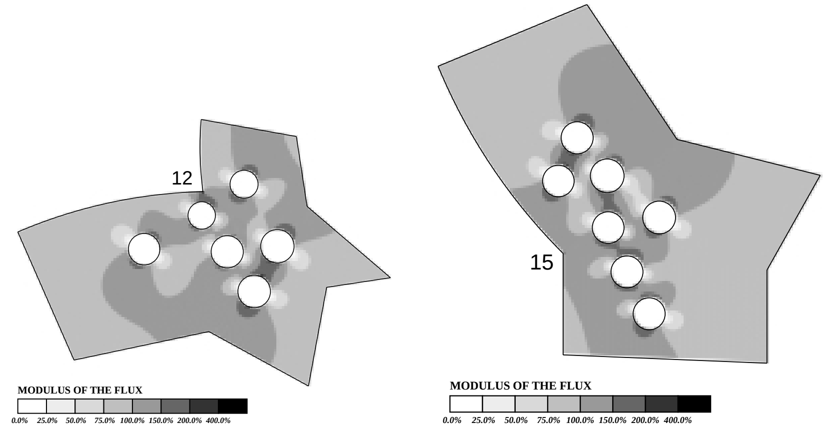

(a) (b)

Figure 3.28. Relative modulus of the gradient of the first handbook functions of (a). HB12 and (b). HB15 for $p = 5$.

Let us now use the GFEM with bi-p FE basis on mesh $\Delta_h^{(1)}$ enriched by vertex handbook functions to solve the Neumann model problem IV. Table 3.14 reports the p-convergence of the energy norm $||u^{\text{GFEM}}(\Delta_h, p, p_{\text{hb}}; \gamma)||_{\mathsf{U}}$ of the computed GFEM solution, and Figure 3.29 shows the convergence graphs for the relative error $e_{\text{REL}}^{\text{GFEM}}(\Delta_h, p, p_{\text{hb}}; \gamma)$ as functions of the polynomial degree p.

Table 3.14. p convergence of the energy norm $||u^{\mathrm{GFEM}}(\Delta_h^{(1)}, p, p_{\mathrm{hb}}; \gamma)||_{\mathsf{U}}$ of the GFEM solution using mesh-based handbook functions on the mesh $\Delta_h^{(1)}$ for Problem IV. The percentage numbers are the corresponding relative errors of the GFEM solutions. The numbers in the brackets are the number of the degree of freedom.

	$\gamma = 1.0$	$\gamma = 1.125$	$\gamma = 1.25$	$\gamma = 1.375$
$p = 1$	479.656465 6.77% (1097)	519.961694 7.92% (1099)	575.995036 10.42% (1097)	667.587412 14.04% (1099)
$p = 2$	480.285351 4.44% (2073)	520.844755 5.38% (2075)	577.937943 6.46% (2073)	671.576264 8.93% (2075)
$p = 3$	480.384261 3.95% (3657)	520.926706 5.08% (3659)	578.012347 6.26% (3657)	672.195136 7.84% (3659)
$p = 4$	480.540174 3.02% (5849)	521.250698 3.66% (5851)	578.445133 4.92% (5849)	673.014927 6.10% (5851)
$p = 5$	480.569616 2.81% (8649)	521.307407 3.35% (8651)	578.485281 4.78% (8649)	673.214251 5.59% (8651)

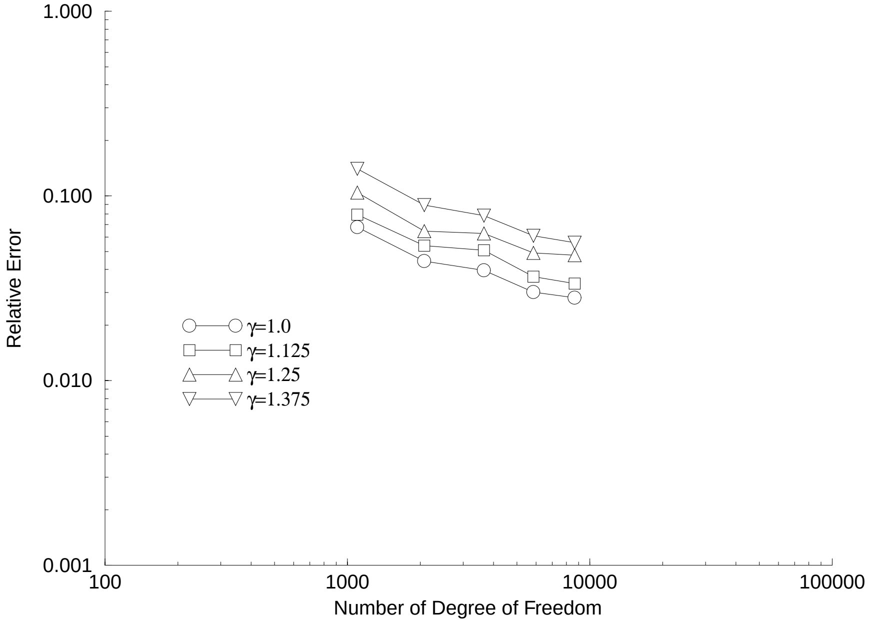

Figure 3.29. The convergence graphs of the relative error $e_{\mathrm{REL}}^{\mathrm{GFEM}}(\Delta_h, p, p_{\mathrm{hb}}; \gamma)$ for Problems IV(a)-IV(d) solved on mesh $\Delta_h^{(1)}$.

3.2.4.2 GFEM using handbooks on the mesh of squares $\Delta_h^{(2)}$

Let us also report the GFEM solution of the model problem IV using the mesh $\Delta_h^{(2)}$ shown in Figure 3.25(b).

Let us first investigate the accuracy of the handbook functions $\psi_j^{X;1}$ for the typical handbook domains $\tilde{\omega}_X^{(1);1}$ for two vertices near the singular points X_{12} and X_{15},as shown in Figure 3.30; below we will refer to these handbooks by HB12-G3 and HB15-G3. We will investigate the accuracy of the numerical construction of the handbook functions $\psi_1^{X;1}$ for these two handbooks.

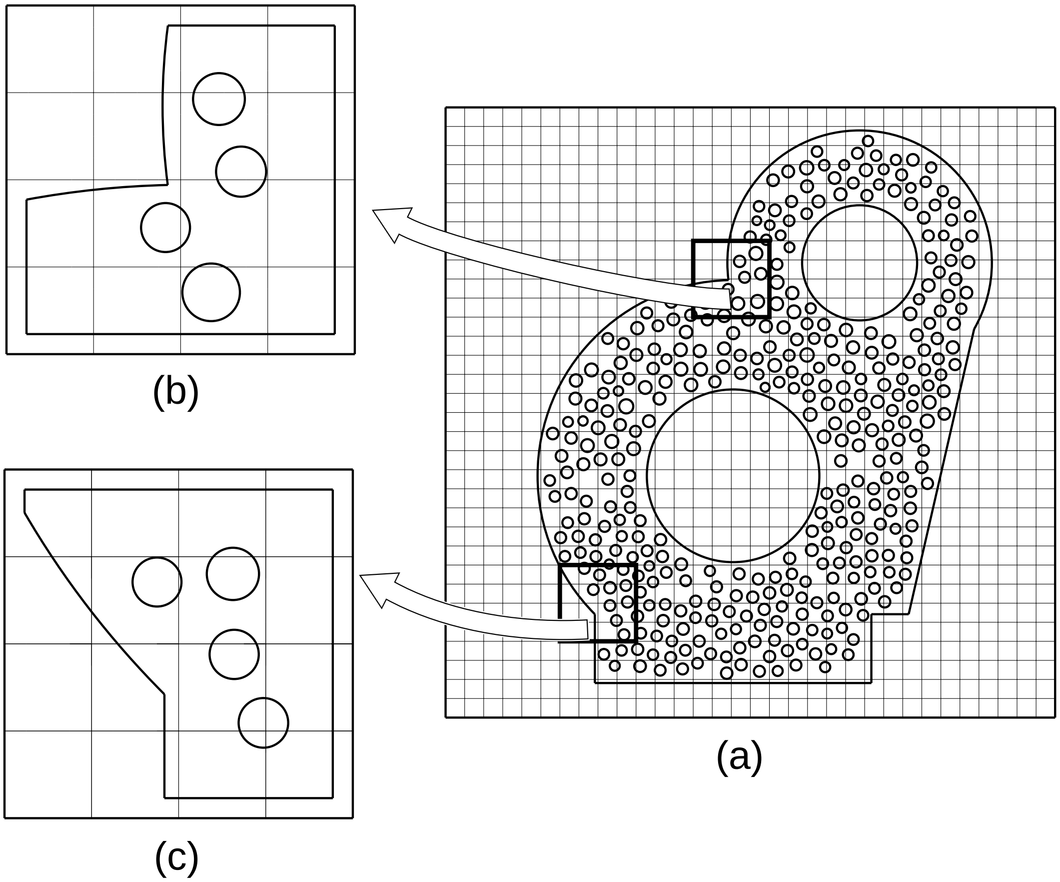

Figure 3.30. Creation of typical handbooks on the mesh $\Delta_h^{(2)}$. (a) Mesh of squares $\Delta_h^{(2)}$ employed for the GFEM solution. (b) and (c) Handbook domains $\tilde{\omega}_X^{(1);1}$ for the two vertices, respectively, near the singular points X_{12} and X_{15}. The corresponding handbooks are denoted by HB12-G3 and HB15-G3, respectively.

As in the previous examples, the handbook functions $\psi_j^{X;1}$ were constructed numerically by employing the bi-p FE basis, enriched by the analytical void functions of degree $p_{\text{voids}} = 1$ added at $n_{\text{layers}} = 0$ around each void. Table 3.15 reports the p-convergence of the energy norms of the first handbook functions $\psi_1^{X;1}$ of the two typical handbooks near singular points, HB12-G3 and HB15-G3. Note that the relative difference between the last two solutions of each sequence of the solutions, is less than 0.2%. Figure 3.31 shows the relative modulus of the gradient of the solutions $\psi_1^{X;1}$ for HB12-G3, and HB15-G3, computed using $p = 5$.

Table 3.15. p-convergence of the energy norms of the handbook functions $\|\psi_1^{X;1}\|_{\mathsf{U}(\tilde{\omega}_X^{(1);1})}$ for the typical handbooks HB12-G3 and HB15-G3.

p	N_{dof}	HB12-G3	N_{dof}	HB15-G3
1	415	64.695365	404	62.434781
2	1041	65.163043	1006	62.703023
3	2057	65.172630	1984	62.711533
4	3463	65.173167	3338	62.712027
5	5259	65.173239	5068	62.712046
	$E\%$	0.15%	$E\%$	0.08%

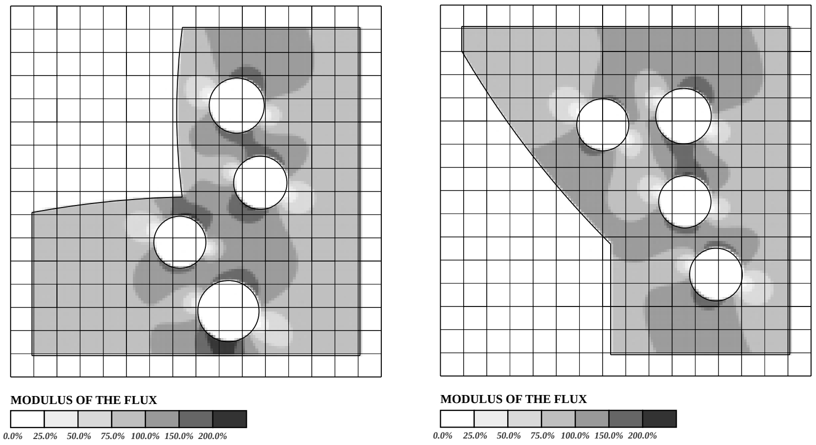

(a) (b)

Figure 3.31. Relative modulus of the gradient of the first handbook functions of (a). HB12-G3 and (b). HB15-G3 for $p = 5$

Using the GFEM with bi-p FE basis on mesh $\Delta_h^{(2)}$ enriched by vertex handbook functions to solve the Neumann model problem IV, we obtain Table 3.14 which reports the p-convergence of the energy norm $||u^{\text{GFEM}}(\Delta_h, p, p_{\text{hb}}; \gamma)||_{\mathsf{U}}$ of the computed GFEM solution, and Figure 3.32 shows the convergence graphs for the relative error $e_{\text{REL}}^{\text{GFEM}}(\Delta_h, p, p_{\text{hb}}; \gamma)$ as functions of the polynomial degree p.

Table 3.16. p-convergence of the energy norm $||u^{\mathrm{GFEM}}(\Delta_h, p, p_{\mathrm{hb}}; \gamma)||_{\mathsf{U}}$ of the GFEM solutions using mesh-based handbook functions on the mesh $\Delta_h^{(2)}$ for Problem IV. The percentage numbers are the corresponding relative errors of the GFEM solutions. The numbers in the brackets are the number of the degree of freedom.

	$\gamma = 1.0$	$\gamma = 1.125$	$\gamma = 1.25$	$\gamma = 1.375$
$p = 1$	480.159288 5.00% (1495)	520.833245 5.42% (1511)	578.072944 6.09% (1527)	672.214423 7.80% (1547)
$p = 2$	480.652936 2.10% (3025)	521.441730 2.46% (3041)	578.861839 3.14% (3057)	673.617593 4.39% (3077)
$p = 3$	480.716567 1.34% (5521)	521.545126 1.45% (5537)	579.056276 1.77% (5553)	674.055155 2.52% (5573)
$p = 4$	480.733221 1.04% (8983)	521.572557 1.03% (8999)	579.106961 1.18% (9015)	674.175119 1.67% (9035)
$p = 5$	480.742154 0.85% (13411)	521.581610 0.84% (13427)	579.124522 0.88% (13443)	674.217921 1.23% (13463)

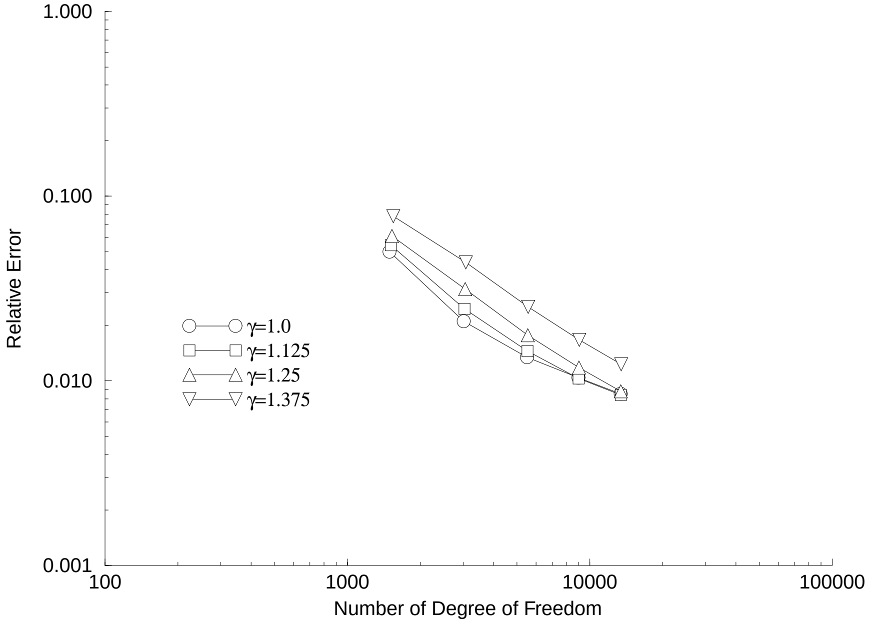

Figure 3.32. The convergence graphs of the relative error $e_{\mathrm{REL}}^{\mathrm{GFEM}}(\Delta_h, p, p_{\mathrm{hb}}; \gamma)$ for Problems IV(a)-IV(d) solved on mesh $\Delta_h^{(2)}$.

3.3 p_{handbook}-version of the Generalized FEM

In previous examples, we employed the GFEM with bi-p FE basis enriched only by the handbook functions of degree one, $p_{\text{hb}} = 1$, and explored the convergence of the GFEM with p, the polynomial degree of the FE basis. In this section, we will investigate the p_{hb}-version of the GFEM, namely the convergence of the method as p_{hb}, the degree of the handbook functions, is increased. We will also underline the importance of the accuracy of the numerical construction of the handbook functions in achieving the optimal convergence rate.

Let us consider, once more, the model Problem II. Table 3.17 gives the energy norm of the overkill solution $||u_{\text{ov}}||_{\mathsf{U}}$, computed using the GFEM on the overkill 64×64 mesh shown in Figure 3.33(d) with bi-quartic ($p = 4$) FE basis enriched by analytical void functions of degree one, $p_{\text{voiods}} = 1$, applied at $n_{\text{layers}} = 0$ around each void

Table 3.17. Energy norm and number of degree of freedom of the overkill solutions.

	$\gamma = 1.0$	$\gamma = 1.125$	$\gamma = 1.25$	$\gamma = 1.375$
$\vert\vert u_{\text{ov}}\vert\vert_{\mathsf{U}}$	597.413841	653.089387	733.086793	870.712149
N_{dof}	75498	76546	77351	77824

Let us solve the model Problem II again by using the three meshes shown in Figure 3.33(a), (b) and (c). On each of the three meshes, the GFEM solution was obtained by using the bi-p FE basis (p = 1, 2, 3, 4, and 5) enriched by the mesh-based handbook functions with order p_{hb} = 1, 2, 3, 4 and 5.

In order to investigate the influence of the accuracy of the numerical construction of handbook functions $\psi_j^{X;1}$, we employed three choices of mesh size for the handbook problems. Figure 3.34 illustrate the handbook meshes by using a corner handbook extracted from the global mesh, Mesh I, II, and III, respectively. For convenience, we call the handbook meshes with the three choices of mesh size, Type I, II, and III, respectively. Note that each type of the handbook mesh has the same mesh size, no matter how large or small the handbook domain is. We also note that the Type II handbook mesh has the same mesh size as the overkill mesh shown in Figure 3.33(d). The numerical construction of the handbook functions $\psi_j^{X;1}$ was done using bi-p FEM ($p = 5$) enriched by the analytical void functions with $p_{\text{voids}} = 1$ at the zeroth layer $n_{\text{layers}} = 0$ around each void.

Let us proceed with the analysis of the results.

Tables 3.18-3.23 report the energy norm of the GFEM solution computed by using the bi-p FE basis enriched by the numerically constructed vertex handbook functions of degree p_{hb} versus the number of degree of freedom for each solution, and the corresponding relative

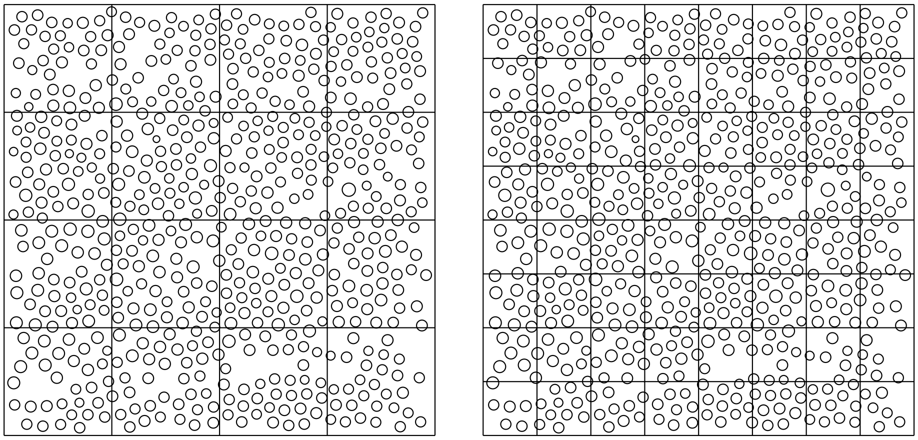

(a). Mesh I (4 × 4 elements) (b). Mesh II (8 × 8 elements)

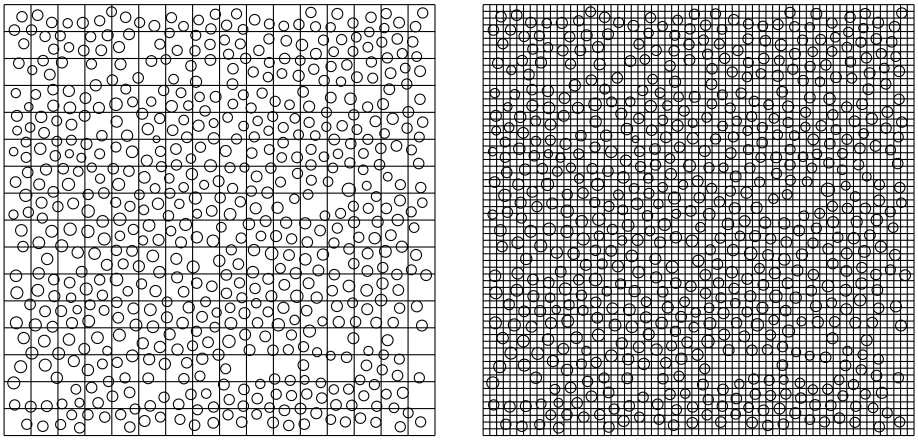

(c). Mesh III (16 × 16 elements) (d). Overkill Mesh (64 × 64 elements)

Figure 3.33. Meshes used for Model Problem II for $\gamma = 1.0$.

error in the energy norm, i.e. $\sqrt{||u_{\text{ov}}||_{\mathsf{U}}^2 - ||u_{\text{GFEM}}||_{\mathsf{U}}^2}/||u_{\text{ov}}||_{\mathsf{U}}$, for $\gamma = 1.0$ and $\gamma = 1.375$. The handbook functions, $\psi_j^{X;1}$, are numerically constructed on handbook mesh Type I. As a comparison, we also computed the GFEM solution with $p_{\text{hb}} = 0$, i.e. only bi-p FE basis were employed in the GFEM solution. By comparing the first two columns in Tables 3.18-3.23, we see that there is a big improvement by using handbook functions, rather than not using any handbook function. From these tables we can see that, the GFEM solution does not converge either by increasing the degree of the polynomials or by increasing the order of the handbook functions. For each choice of γ, comparing the corresponding three tables, we also observe that the GFEM solution does not converge either by decreasing the global mesh size, although we can achieve better accuracy by using less degree of freedom. This can also be seen from the convergence graphs given in Figures 3.35 and 3.36.

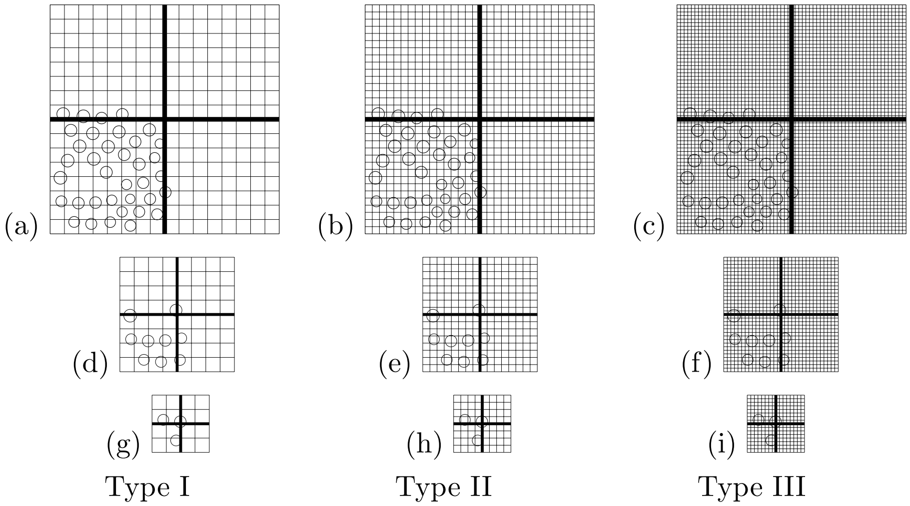

Figure 3.34. Examples of handbook meshes used for the numerical construction of the handbook functions, for a corner handbook problem extracted from the: (a), (b) and (c) Mesh I (4×4 elements); (d), (e) and (f) Mesh II (8×8 elements); (g), (h) and (i) Mesh III (16×16 elements), shown here for $\gamma = 1.0$.

Table 3.18. Energy norm of the GFEM solution using mesh-based handbooks for $\gamma = 1.0$ on Mesh I with 4×4 elements. The numbers in the brackets are the number of degree of freedom, and the percentage numbers are the relative error in the energy norm.

	$p_{\text{hb}} = 0$	$p_{\text{hb}} = 1$	$p_{\text{hb}} = 2$	$p_{\text{hb}} = 3$	$p_{\text{hb}} = 4$	$p_{\text{hb}} = 5$
$p = 1$	526.047756 (25) 47.40%	596.354559 (75) 5.95%	596.480454 (109) 5.58%	596.533200 (143) 5.42%	596.544491 (177) 5.39%	596.546671 (211) 5.38%
$p = 2$	526.460025 (81) 47.27%	596.508418 (131) 5.50%	596.526307 (165) 5.44%	596.540071 (199) 5.40%	596.546791 (233) 5.38%	596.549024 (267) 5.37%
$p = 3$	527.076526 (169) 47.07%	596.524964 (219) 5.45%	596.537184 (253) 5.41%	596.545325 (287) 5.39%	596.551592 (321) 5.37%	596.553526 (355) 5.36%
$p = 4$	527.663025 (289) 46.89%	596.530891 (339) 5.43%	596.542672 (373) 5.39%	596.549636 (407) 5.37%	596.555978 (441) 5.36%	596.558075 (475) 5.35%
$p = 5$	528.168569 (441) 46.73%	596.532039 (491) 5.43%	596.543858 (525) 5.39%	596.550861 (559) 5.37%	596.557549 (593) 5.35%	596.559776 (627) 5.34%

Table 3.19. Energy norm of the GFEM solution using mesh-based handbooks for $\gamma = 1.0$ on Mesh II with 8×8 elements. The numbers in the brackets are the number of degree of freedom, and the percentage numbers are the relative error in the energy norm.

	$p_{\text{hb}} = 0$	$p_{\text{hb}} = 1$	$p_{\text{hb}} = 2$	$p_{\text{hb}} = 3$	$p_{\text{hb}} = 4$	$p_{\text{hb}} = 5$
$p = 1$	526.349745 (81) 47.30%	596.374122 (243) 5.90%	596.497764 (373) 5.53%	596.546818 (503) 5.38%	596.558071 (633) 5.35%	596.561965 (763) 5.34%
$p = 2$	527.500512 (289) 46.94%	596.507229 (451) 5.51%	596.522092 (581) 5.46%	596.551603 (711) 5.37%	596.559456 (841) 5.34%	596.562965 (971) 5.33%
$p = 3$	528.905577 (625) 46.50%	596.543029 (787) 5.39%	596.553681 (917) 5.36%	596.559894 (1047) 5.34%	596.563319 (1177) 5.33%	596.565375 (1307) 5.33%
$p = 4$	531.392559 (1089) 45.69%	596.549570 (1251) 5.37%	596.559981 (1381) 5.34%	596.565254 (1511) 5.32%	596.567341 (1641) 5.32%	596.568640 (1771) 5.32%
$p = 5$	535.140625 (1681) 44.45%	596.553077 (1843) 5.36%	596.562254 (1973) 5.33%	596.567341 (2103) 5.32%	596.569557 (2233) 5.31%	596.570587 (2363) 5.31%

Table 3.20. Energy norm of the GFEM solution using mesh-based handbooks for $\gamma = 1.0$ on Mesh III with 16×16 elements. The numbers in the brackets are the number of degree of freedom, and the percentage numbers are the relative error in the energy norm.

	$p_{\text{hb}} = 0$	$p_{\text{hb}} = 1$	$p_{\text{hb}} = 2$	$p_{\text{hb}} = 3$	$p_{\text{hb}} = 4$	$p_{\text{hb}} = 5$
$p = 1$	527.206120 (289) 47.03%	596.367579 (867) 5.91%	596.481838 (1381) 5.58%	596.541779 (1895) 5.40%	596.557674 (2409) 5.35%	596.566524 (2923) 5.32%
$p = 2$	531.284898 (1089) 45.73%	596.478734 (1667) 5.59%	596.509660 (2181) 5.50%	596.549230 (2695) 5.38%	596.562569 (3209) 5.34%	596.570355 (3723) 5.31%
$p = 3$	541.855531 (2401) 42.11%	596.540586 (2979) 5.40%	596.556918 (3493) 5.35%	596.566336 (4007) 5.32%	596.573090 (4521) 5.30%	596.579247 (5035) 5.28%
$p = 4$	558.050844 (4225) 35.70%	596.556949 (4803) 5.35%	596.569200 (5317) 5.31%	596.577328 (5831) 5.29%	596.586096 (6345) 5.26%	596.596171 (6859) 5.23%
$p = 5$	573.850349 (6561) 27.81%	596.565782 (7139) 5.32%	596.576615 (7653) 5.29%	596.586054 (8167) 5.26%	596.598127 (8681) 5.22%	596.615491 (9195) 5.17%

Table 3.21. Energy norm of the GFEM solution using mesh-based handbooks for $\gamma = 1.375$ on Mesh I with 4×4 elements. The numbers in the brackets are the number of degree of freedom, and the percentage numbers are the relative error in the energy norm.

	$p_{\text{hb}} = 0$	$p_{\text{hb}} = 1$	$p_{\text{hb}} = 2$	$p_{\text{hb}} = 3$	$p_{\text{hb}} = 4$	$p_{\text{hb}} = 5$
$p = 1$	649.928012 (25) 66.55%	866.207641 (75) 10.15%	869.313172 (109) 5.66%	869.825951 (143) 4.51%	869.925680 (177) 4.25%	869.951239 (211) 4.18%
$p = 2$	653.693332 (81) 66.06%	869.372547 (131) 5.54%	869.599520 (165) 5.05%	869.888974 (199) 4.34%	869.939700 (233) 4.21%	869.957359 (267) 4.16%
$p = 3$	658.158124 (169) 65.47%	869.531259 (219) 5.20%	869.804683 (253) 4.56%	869.922548 (287) 4.25%	869.954411 (321) 4.17%	869.968707 (355) 4.13%
$p = 4$	662.758452 (289) 64.86%	869.615335 (339) 5.01%	869.848876 (373) 4.45%	869.952899 (407) 4.17%	869.974243 (441) 4.12%	869.982158 (475) 4.09%
$p = 5$	665.710613 (441) 64.45%	869.641052 (491) 4.95%	869.861371 (525) 4.42%	869.960081 (559) 4.15%	869.980568 (593) 4.10%	869.989448 (627) 4.07%

Table 3.22. Energy norm of the GFEM solution using mesh-based handbooks for $\gamma = 1.375$ on Mesh II with 8×8 elements. The numbers in the brackets are the number of degree of freedom, and the percentage numbers are the relative error in the energy norm.

	$p_{\text{hb}} = 0$	$p_{\text{hb}} = 1$	$p_{\text{hb}} = 2$	$p_{\text{hb}} = 3$	$p_{\text{hb}} = 4$	$p_{\text{hb}} = 5$
$p = 1$	652.676494 (81) 66.19%	866.933323 (243) 9.30%	869.226983 (373) 5.83%	869.723921 (503) 4.76%	869.826274 (633) 4.51%	869.872362 (763) 4.39%
$p = 2$	661.620399 (289) 65.01%	869.168711 (451) 5.95%	869.436589 (581) 5.41%	869.762309 (711) 4.67%	869.838250 (841) 4.48%	869.877619 (971) 4.38%
$p = 3$	669.885357 (625) 63.88%	869.473457 (787) 5.33%	869.719395 (917) 4.77%	869.828961 (1047) 4.50%	869.866487 (1177) 4.41%	869.890491 (1307) 4.34%
$p = 4$	683.265951 (1089) 61.98%	869.568282 (1251) 5.12%	869.780699 (1381) 4.62%	869.869939 (1511) 4.39%	869.895428 (1641) 4.33%	869.911655 (1771) 4.29%
$p = 5$	701.572246 (1681) 59.22%	869.638176 (1843) 4.96%	869.813417 (1973) 4.54%	869.889643 (2103) 4.34%	869.912153 (2233) 4.28%	869.924951 (2363) 4.25%

Table 3.23. Energy norm of the GFEM solution using mesh-based handbooks for $\gamma = 1.375$ on Mesh III with 16×16 elements. The numbers in the brackets are the number of degree of freedom, and the percentage numbers are the relative error in the energy norm.

	$p_{\rm hb} = 0$	$p_{\rm hb} = 1$	$p_{\rm hb} = 2$	$p_{\rm hb} = 3$	$p_{\rm hb} = 4$	$p_{\rm hb} = 5$
$p = 1$	659.542408 (289) 65.29%	867.705374 (867) 8.30%	869.225227 (1381) 5.84%	869.781897 (1895) 4.62%	869.892030 (2409) 4.34%	869.931591 (2923) 4.23%
$p = 2$	681.999515 (1089) 62.17%	869.071590 (1667) 6.13%	869.497292 (2181) 5.28%	869.820117 (2695) 4.52%	869.905044 (3209) 4.30%	869.936415 (3723) 4.22%
$p = 3$	731.526290 (2401) 54.23%	869.577840 (2979) 5.10%	869.801825 (3493) 4.57%	869.899300 (4007) 4.32%	869.929196 (4521) 4.24%	869.945152 (5035) 4.20%
$p = 4$	789.461509 (4225) 42.18%	869.761067 (4803) 4.67%	869.881539 (5317) 4.36%	869.932995 (5831) 4.23%	869.949330 (6345) 4.18%	869.957898 (6859) 4.16%
$p = 5$	831.372912 (6561) 29.72%	869.852335 (7139) 4.44%	869.919664 (7653) 4.26%	869.948578 (8167) 4.18%	869.962310 (8681) 4.15%	869.970887 (9195) 4.12%

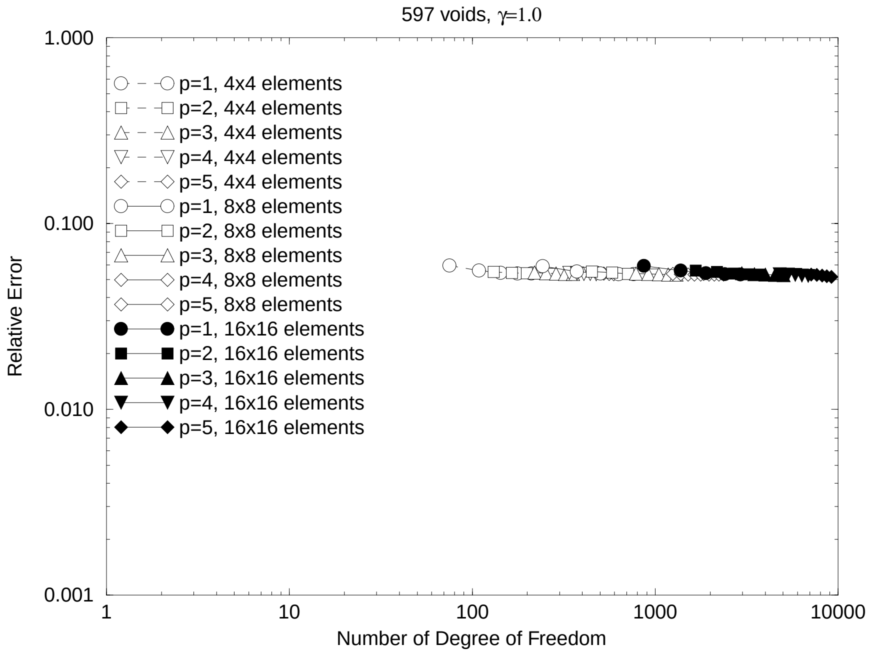

Figure 3.35. Convergence of the GFEM solution of model Problem II with $\gamma = 1.0$ on Mesh I, II and III using mesh-based handbook functions obtained on the meshes shown in Figure 3.34.

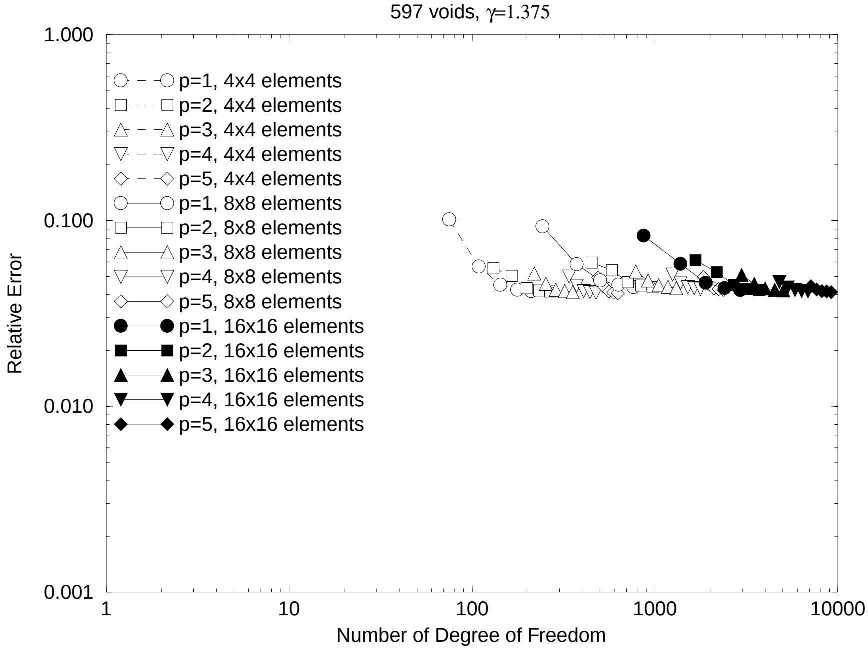

Figure 3.36. Convergence of the GFEM solution of model Problem II with $\gamma = 1.375$ on Mesh I, II and III using mesh-based handbook functions obtained on the meshes shown in Figure 3.34.

Let us solve the Model Problem II again, using finer meshes, handbook mesh Type II shown in Figure 3.34, for the numerical construction of the handbook functions $\psi_j^{X;1}$. Note that these meshes are the same as the restrictions of the overkill mesh shown in Figure 3.33(d) to the handbook domains. Tables 3.24-3.35 report the energy norm of the GFEM solutions of Model Problem II on Mesh I (with 4×4 elements), Mesh II (with 8×8 elements) and Mesh III (with 16×16 elements) using the mesh-based handbook functions for $\gamma = 1.0$, 1.125, 1.25 and 1.375, respectively. In the tables, we see that some of the computed GFEM solutions are more accurate than the overkill solutions; for this reason in each table we used the solution with $p = 5$ and $p_{\text{hb}} = 5$ as the new overkill solution to compute the relative error. We observe, once more, that we can achieve better accuracy by using less degree of freedom. Figures 3.37-3.40 show the exponential convergence of the GFEM solutions. From Tables 3.24-3.35 and Figures 3.37-3.40, we also observe that the GFEM solution has much similar convergence behavior on the three meshes, Mesh I, II, and III, and the decease of the global mesh size does not make the GFEM solution converge.

Table 3.24. Energy norm of the solution of Model Problem II on Mesh I (with 4 × 4 elements) for $\gamma = 1.0$ using the mesh-based handbook functions obtained on handbook mesh Type II. The numbers in bracket are the number of degree of freedom, and the percentage numbers are the relative error of the solution. Here the solution for $p = 5$ and $p_{\text{hb}} = 5$ is used as overkill solution in the computation of the relative error.

	$p_{\text{hb}} = 1$	$p_{\text{hb}} = 2$	$p_{\text{hb}} = 3$	$p_{\text{hb}} = 4$	$p_{\text{hb}} = 5$
$p = 1$	597.223463 (75) 2.66%	597.352380 (109) 1.66%	597.405799 (143) 0.98%	597.417457 (177) 0.75%	597.419870 (211) 0.69%
$p = 2$	597.379945 (131) 1.35%	597.398663 (165) 1.09%	597.413286 (199) 0.84%	597.420154 (233) 0.69%	597.422822 (267) 0.62%
$p = 3$	597.397113 (219) 1.11%	597.410107 (253) 0.90%	597.418923 (287) 0.72%	597.425465 (321) 0.54%	597.427684 (355) 0.47%
$p = 4$	597.403085 (339) 1.02%	597.415649 (373) 0.79%	597.423456 (407) 0.60%	597.429948 (441) 0.38%	597.432449 (475) 0.24%
$p = 5$	597.404253 (491) 1.00%	597.416764 (525) 0.76%	597.424505 (559) 0.57%	597.431349 (593) 0.31%	597.434226 (627)

Table 3.25. Energy norm of the solution of Model Problem II on Mesh II (with 8 × 8 elements) for $\gamma = 1.0$ using the mesh-based handbook functions obtained on handbook mesh Type II. The numbers in bracket are the number of degree of freedom, and the percentage numbers are the relative error of the solution. Here the solution for $p = 5$ and $p_{\text{hb}} = 5$ is used as overkill solution in the computation of the relative error.

	$p_{\text{hb}} = 1$	$p_{\text{hb}} = 2$	$p_{\text{hb}} = 3$	$p_{\text{hb}} = 4$	$p_{\text{hb}} = 5$
$p = 1$	597.223977 (243) 2.58%	597.350383 (373) 1.56%	597.400110 (503) 0.88%	597.411934 (633) 0.62%	597.415788 (763) 0.50%
$p = 2$	597.359292 (451) 1.46%	597.374917 (581) 1.27%	597.404901 (711) 0.79%	597.413183 (841) 0.58%	597.416523 (971) 0.48%
$p = 3$	597.395585 (787) 0.96%	597.406892 (917) 0.74%	597.413137 (1047) 0.58%	597.416783 (1177) 0.47%	597.418703 (1307) 0.39%
$p = 4$	597.402057 (1251) 0.84%	597.412927 (1381) 0.59%	597.418541 (1511) 0.40%	597.420530 (1641) 0.31%	597.421461 (1771) 0.25%
$p = 5$	597.405660 (1843) 0.77%	597.415578 (1973) 0.51%	597.420707 (2103) 0.30%	597.422540 (2233) 0.16%	597.423341 (2363)

Table 3.26. Energy norm of the solution of Model Problem II on Mesh III (with 16 × 16 elements) for $\gamma = 1.0$ using the mesh-based handbook functions obtained on handbook mesh Type II. The numbers in bracket are the number of degree of freedom, and the percentage numbers are the relative error of the solution. Here the solution for $p = 5$ and $p_{\mathrm{hb}} = 5$ is used as overkill solution in the computation of the relative error.

	$p_{\mathrm{hb}} = 1$	$p_{\mathrm{hb}} = 2$	$p_{\mathrm{hb}} = 3$	$p_{\mathrm{hb}} = 4$	$p_{\mathrm{hb}} = 5$
$p = 1$	597.217498 (867) 2.66%	597.333781 (1381) 1.78%	597.395365 (1895) 1.05%	597.411471 (2409) 0.75%	597.418804 (2923) 0.56%
$p = 2$	597.330451 (1667) 1.81%	597.361503 (2181) 1.49%	597.401769 (2695) 0.94%	597.414104 (3209) 0.69%	597.420222 (3723) 0.52%
$p = 3$	597.393083 (2979) 1.09%	597.408376 (3493) 0.82%	597.416892 (4007) 0.62%	597.420647 (4521) 0.50%	597.423184 (5035) 0.41%
$p = 4$	597.409219 (4803) 0.80%	597.419165 (5317) 0.55%	597.424210 (5831) 0.37%	597.425781 (6345) 0.29%	597.426591 (6859) 0.24%
$p = 5$	597.417730 (7139) 0.59%	597.424005 (7653) 0.38%	597.426764 (8167) 0.22%	597.427723 (8681) 0.13%	597.428250 (9195)

Table 3.27. Energy norm of the solution of Model Problem II on Mesh I (with 4 × 4 elements) for $\gamma = 1.125$ using the mesh-based handbook functions obtained on handbook mesh Type II. The numbers in bracket are the number of degree of freedom, and the percentage numbers are the relative error of the solution. Here the solution for $p = 5$ and $p_{\text{hb}} = 5$ is used as overkill solution in the computation of the relative error.

	$p_{\text{hb}} = 1$	$p_{\text{hb}} = 2$	$p_{\text{hb}} = 3$	$p_{\text{hb}} = 4$	$p_{\text{hb}} = 5$
$p = 1$	652.652451 (75) 3.79%	652.976786 (109) 2.11%	653.080604 (143) 1.13%	653.100483 (177) 0.82%	653.105028 (211) 0.73%
$p = 2$	653.025819 (131) 1.72%	653.061700 (165) 1.36%	653.094900 (199) 0.92%	653.104829 (233) 0.73%	653.108827 (267) 0.64%
$p = 3$	653.057134 (219) 1.41%	653.086504 (253) 1.05%	653.103318 (287) 0.76%	653.110924 (321) 0.59%	653.114566 (355) 0.48%
$p = 4$	653.069924 (339) 1.27%	653.097561 (373) 0.87%	653.112773 (407) 0.54%	653.117708 (441) 0.37%	653.120216 (475) 0.25%
$p = 5$	653.072400 (491) 1.24%	653.099400 (525) 0.84%	653.114321 (559) 0.49%	653.119398 (593) 0.30%	653.122245 (627)

Table 3.28. Energy norm of the solution of Model Problem II on Mesh II (with 8 × 8 elements) for $\gamma = 1.125$ using the mesh-based handbook functions obtained on handbook mesh Type II. The numbers in bracket are the number of degree of freedom, and the percentage numbers are the relative error of the solution. Here the solution for $p = 5$ and $p_{\text{hb}} = 5$ is used as overkill solution in the computation of the relative error.

	$p_{\text{hb}} = 1$	$p_{\text{hb}} = 2$	$p_{\text{hb}} = 3$	$p_{\text{hb}} = 4$	$p_{\text{hb}} = 5$
$p = 1$	652.666608 (243) 3.61%	652.956735 (373) 2.03%	653.051213 (503) 1.11%	653.072061 (633) 0.77%	653.078476 (763) 0.63%
$p = 2$	652.972363 (451) 1.91%	653.000794 (581) 1.67%	653.060017 (711) 0.98%	653.074214 (841) 0.73%	653.079750 (971) 0.60%
$p = 3$	653.034684 (787) 1.32%	653.060628 (917) 0.97%	653.073948 (1047) 0.73%	653.080631 (1177) 0.58%	653.083764 (1307) 0.49%
$p = 4$	653.046622 (1251) 1.17%	653.070915 (1381) 0.80%	653.082886 (1511) 0.52%	653.086570 (1641) 0.39%	653.088367 (1771) 0.31%
$p = 5$	653.054901 (1843) 1.06%	653.076218 (1973) 0.69%	653.086953 (2103) 0.38%	653.090224 (2233) 0.20%	653.091556 (2363)

Table 3.29. Energy norm of the solution of Model Problem II on Mesh III (with 16 × 16 elements) for $\gamma = 1.125$ using the mesh-based handbook functions obtained on handbook mesh Type II. The numbers in bracket are the number of degree of freedom, and the percentage numbers are the relative error of the solution. Here the solution for $p = 5$ and $p_{\mathrm{hb}} = 5$ is used as overkill solution in the computation of the relative error.

	$p_{\mathrm{hb}} = 1$	$p_{\mathrm{hb}} = 2$	$p_{\mathrm{hb}} = 3$	$p_{\mathrm{hb}} = 4$	$p_{\mathrm{hb}} = 5$
$p = 1$	652.688806 (867) 3.54%	652.928325 (1381) 2.28%	653.043198 (1895) 1.29%	653.071845 (2409) 0.88%	653.085890 (2923) 0.59%
$p = 2$	652.917880 (1667) 2.34%	652.980762 (2181) 1.89%	653.054591 (2695) 1.15%	653.076665 (3209) 0.80%	653.087706 (3723) 0.55%
$p = 3$	653.030333 (2979) 1.43%	653.062333 (3493) 1.04%	653.079455 (4007) 0.74%	653.086525 (4521) 0.58%	653.091249 (5035) 0.43%
$p = 4$	653.062043 (4803) 1.04%	653.081536 (5317) 0.70%	653.090870 (5831) 0.45%	653.093779 (6345) 0.33%	653.095432 (6859) 0.25%
$p = 5$	653.078788 (7139) 0.76%	653.089946 (7653) 0.48%	653.094669 (8167) 0.29%	653.096426 (8681) 0.17%	653.097420 (9195)

Table 3.30. Energy norm of the solution of Model Problem II on Mesh I (with 4 × 4 elements) for $\gamma = 1.25$ using the mesh-based handbook functions obtained on handbook mesh Type II. The numbers in bracket are the number of degree of freedom, and the percentage numbers are the relative error of the solution. Here the solution for $p = 5$ and $p_{\rm hb} = 5$ is used as overkill solution in the computation of the relative error.

	$p_{\rm hb} = 1$	$p_{\rm hb} = 2$	$p_{\rm hb} = 3$	$p_{\rm hb} = 4$	$p_{\rm hb} = 5$
$p = 1$	731.926327 (75) 5.65%	732.811954 (109) 2.79%	733.027643 (143) 1.39%	733.072390 (177) 0.84%	733.080795 (211) 0.69%
$p = 2$	732.891882 (131) 2.37%	732.963477 (165) 1.92%	733.055477 (199) 1.08%	733.077159 (233) 0.76%	733.083498 (267) 0.64%
$p = 3$	732.956631 (219) 1.97%	733.030375 (253) 1.36%	733.069654 (287) 0.88%	733.083897 (321) 0.63%	733.089161 (355) 0.50%
$p = 4$	732.984454 (339) 1.76%	733.049134 (373) 1.16%	733.083833 (407) 0.63%	733.091607 (441) 0.43%	733.094840 (475) 0.31%
$p = 5$	732.991904 (491) 1.70%	733.054318 (525) 1.10%	733.087260 (559) 0.55%	733.094818 (593) 0.31%	733.098324 (627)

Table 3.31. Energy norm of the solution of Model Problem II on Mesh II (with 8 × 8 elements) for $\gamma = 1.25$ using the mesh-based handbook functions obtained on handbook mesh Type II. The numbers in bracket are the number of degree of freedom, and the percentage numbers are the relative error of the solution. Here the solution for $p = 5$ and $p_{\text{hb}} = 5$ is used as overkill solution in the computation of the relative error.

	$p_{\text{hb}} = 1$	$p_{\text{hb}} = 2$	$p_{\text{hb}} = 3$	$p_{\text{hb}} = 4$	$p_{\text{hb}} = 5$
$p = 1$	732.074846 (243) 5.24%	732.801790 (373) 2.76%	732.999698 (503) 1.49%	733.041437 (633) 1.04%	733.057930 (763) 0.79%
$p = 2$	732.809490 (451) 2.72%	732.885720 (581) 2.31%	733.016047 (711) 1.33%	733.045390 (841) 0.98%	733.059923 (971) 0.75%
$p = 3$	732.939326 (787) 1.96%	733.011213 (917) 1.38%	733.044770 (1047) 0.99%	733.058362 (1177) 0.78%	733.066228 (1307) 0.63%
$p = 4$	732.968200 (1251) 1.75%	733.033266 (1381) 1.14%	733.062554 (1511) 0.70%	733.070763 (1641) 0.52%	733.075755 (1771) 0.37%
$p = 5$	732.988270 (1843) 1.59%	733.043957 (1973) 1.00%	733.069576 (2103) 0.55%	733.076673 (2233) 0.33%	733.080726 (2363)

Table 3.32. Energy norm of the solution of Model Problem II on Mesh III (with 16 × 16 elements) for $\gamma = 1.25$ using the mesh-based handbook functions obtained on handbook mesh Type II. The numbers in bracket are the number of degree of freedom, and the percentage numbers are the relative error of the solution. Here the solution for $p = 5$ and $p_{\text{hb}} = 5$ is used as overkill solution in the computation of the relative error.

	$p_{\text{hb}} = 1$	$p_{\text{hb}} = 2$	$p_{\text{hb}} = 3$	$p_{\text{hb}} = 4$	$p_{\text{hb}} = 5$
$p = 1$	732.264105 (867) 4.75%	732.796958 (1381) 2.84%	733.008461 (1895) 1.52%	733.059271 (2409) 0.96%	733.079408 (2923) 0.61%
$p = 2$	732.748354 (1667) 3.07%	732.895954 (2181) 2.32%	733.027777 (2695) 1.34%	733.065829 (3209) 0.86%	733.081828 (3723) 0.56%
$p = 3$	732.957686 (2979) 1.92%	733.033474 (3493) 1.28%	733.066764 (4007) 0.85%	733.078599 (4521) 0.63%	733.086138 (5035) 0.44%
$p = 4$	733.022459 (4803) 1.39%	733.065285 (5317) 0.87%	733.082786 (5831) 0.53%	733.088169 (6345) 0.37%	733.090893 (6859) 0.25%
$p = 5$	733.056745 (7139) 1.00%	733.079666 (7653) 0.61%	733.088473 (8167) 0.36%	733.091674 (8681) 0.20%	733.093201 (9195)

Table 3.33. Energy norm of the solution of Model Problem II on Mesh I (with 4 × 4 elements) for $\gamma = 1.375$ using the mesh-based handbook functions obtained on handbook mesh Type II. The numbers in bracket are the number of degree of freedom, and the percentage numbers are the relative error of the solution. Here the solution for $p = 5$ and $p_{\text{hb}} = 5$ is used as overkill solution in the computation of the relative error.

	$p_{\text{hb}} = 1$	$p_{\text{hb}} = 2$	$p_{\text{hb}} = 3$	$p_{\text{hb}} = 4$	$p_{\text{hb}} = 5$
$p = 1$	866.961277 (75) 9.33%	870.087384 (109) 3.94%	870.604358 (143) 1.91%	870.702394 (177) 1.18%	870.728011 (211) 0.89%
$p = 2$	870.146407 (131) 3.76%	870.374976 (165) 2.98%	870.667769 (199) 1.48%	870.716137 (233) 1.03%	870.733701 (267) 0.82%
$p = 3$	870.306237 (219) 3.24%	870.581729 (253) 2.04%	870.702083 (287) 1.18%	870.730464 (321) 0.86%	870.744585 (355) 0.65%
$p = 4$	870.390943 (339) 2.92%	870.626234 (373) 1.77%	870.732334 (407) 0.84%	870.748937 (441) 0.56%	870.756711 (475) 0.37%
$p = 5$	870.417031 (491) 2.82%	870.638864 (525) 1.69%	870.739671 (559) 0.73%	870.755134 (593) 0.42%	870.762744 (627)

Table 3.34. Energy norm of the solution of Model Problem II on Mesh II (with 8 × 8 elements) for $\gamma = 1.375$ using the mesh-based handbook functions obtained on handbook mesh Type II. The numbers in bracket are the number of degree of freedom, and the percentage numbers are the relative error of the solution. Here the solution for $p = 5$ and $p_{\text{hb}} = 5$ is used as overkill solution in the computation of the relative error.

	$p_{\text{hb}} = 1$	$p_{\text{hb}} = 2$	$p_{\text{hb}} = 3$	$p_{\text{hb}} = 4$	$p_{\text{hb}} = 5$
$p = 1$	867.688241 (243) 8.31%	869.999631 (373) 4.01%	870.500115 (503) 2.15%	870.604599 (633) 1.49%	870.650687 (763) 1.08%
$p = 2$	869.938487 (451) 4.18%	870.209379 (581) 3.36%	870.538768 (711) 1.93%	870.616479 (841) 1.40%	870.655468 (971) 1.03%
$p = 3$	870.245297 (787) 3.24%	870.494899 (917) 2.18%	870.604916 (1047) 1.49%	870.644146 (1177) 1.15%	870.667705 (1307) 0.88%
$p = 4$	870.340969 (1251) 2.88%	870.556222 (1381) 1.83%	870.646109 (1511) 1.13%	870.673313 (1641) 0.80%	870.688765 (1771) 0.54%
$p = 5$	870.411196 (1843) 2.58%	870.589516 (1973) 1.60%	870.665962 (2103) 0.90%	870.689529 (2233) 0.52%	870.701238 (2363)

Table 3.35. Energy norm of the solution of Model Problem II on Mesh III (with 16 × 16 elements) for $\gamma = 1.375$ using the mesh-based handbook functions obtained on handbook mesh Type II. The numbers in bracket are the number of degree of freedom, and the percentage numbers are the relative error of the solution. Here the solution for $p = 5$ and $p_{\text{hb}} = 5$ is used as overkill solution in the computation of the relative error.

	$p_{\text{hb}} = 1$	$p_{\text{hb}} = 2$	$p_{\text{hb}} = 3$	$p_{\text{hb}} = 4$	$p_{\text{hb}} = 5$
$p = 1$	868.462359 (867) 7.21%	869.994193 (1381) 4.11%	870.558307 (1895) 1.98%	870.669129 (2409) 1.17%	870.709291 (2923) 0.67%
$p = 2$	869.836827 (1667) 4.53%	870.267733 (2181) 3.25%	870.596143 (2695) 1.75%	870.680995 (3209) 1.05%	870.712746 (3723) 0.61%
$p = 3$	870.347330 (2979) 2.96%	870.575043 (3493) 1.88%	870.675107 (4007) 1.11%	870.703477 (4521) 0.77%	870.718933 (5035) 0.48%
$p = 4$	870.530751 (4803) 2.13%	870.652409 (5317) 1.33%	870.706031 (5831) 0.73%	870.719249 (6345) 0.47%	870.725460 (6859) 0.29%
$p = 5$	870.622212 (7139) 1.57%	870.688329 (7653) 0.97%	870.716977 (8167) 0.53%	870.725120 (8681) 0.30%	870.728997 (9195)

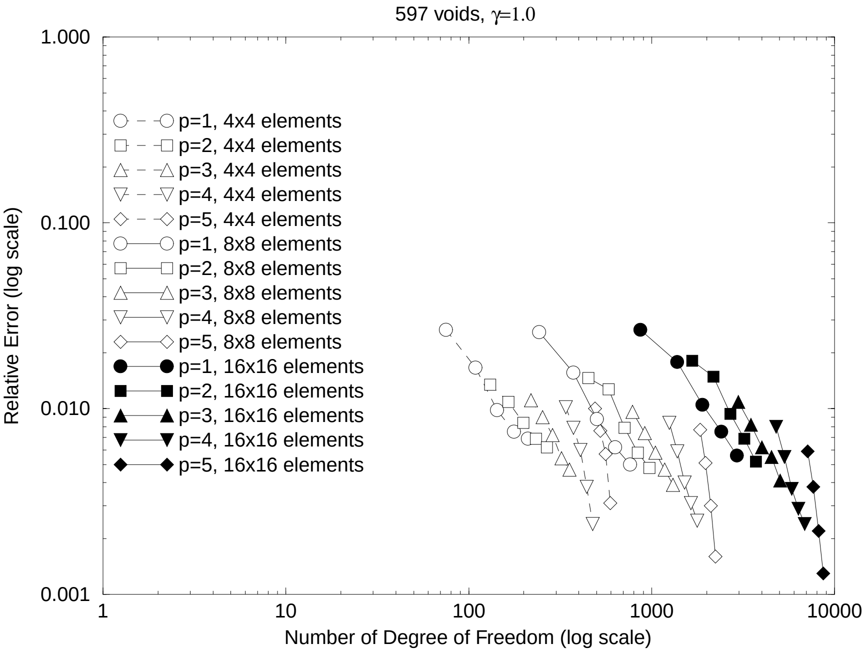

Figure 3.37. Convergence of GFEM solution of Model Problem II with $\gamma = 1.0$ using mesh-based handbook functions obtained on handbook mesh Type II.

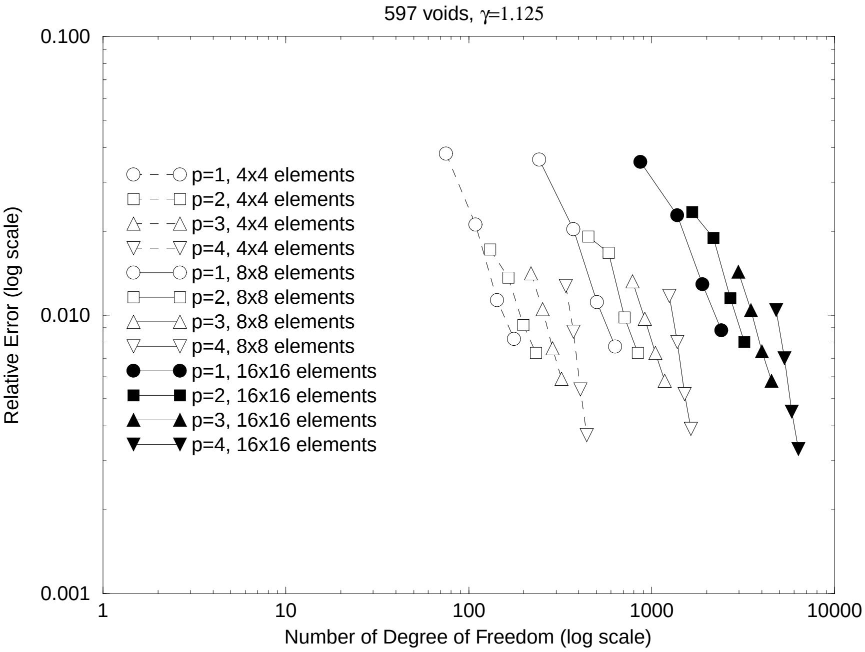

Figure 3.38. Convergence of GFEM solution of Model Problem II with $\gamma = 1.125$ using mesh-based handbook functions obtained on handbook mesh Type II.

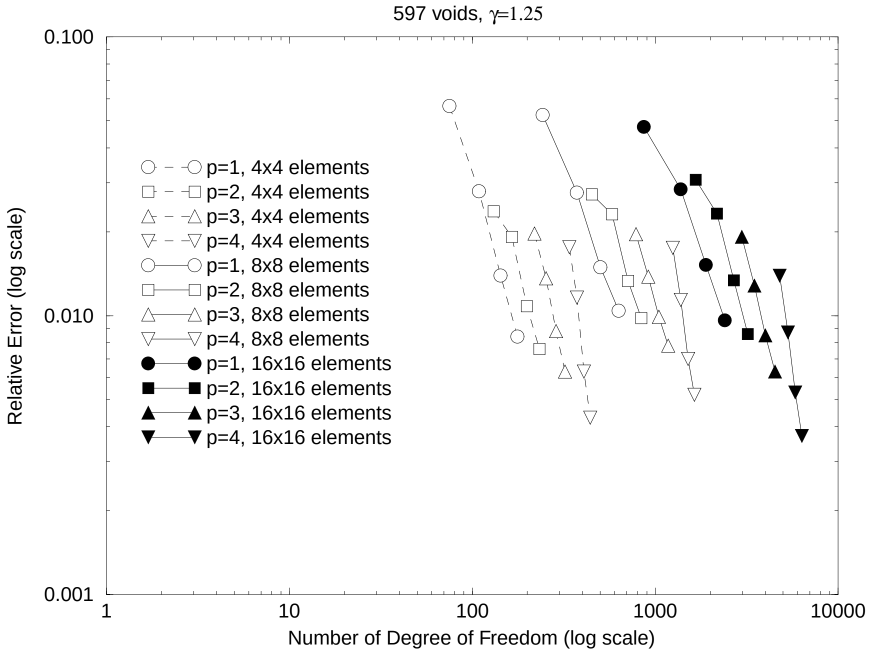

Figure 3.39. Convergence of GFEM solution of Model Problem II with $\gamma = 1.25$ using mesh-based handbook functions obtained on handbook mesh Type II.

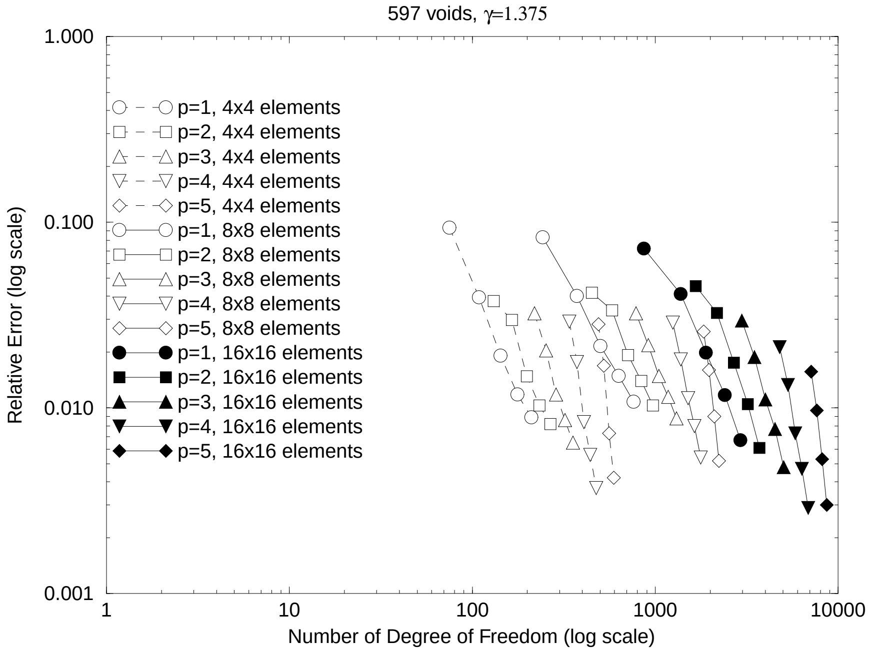

Figure 3.40. Convergence of GFEM solution of Model Problem II with $\gamma = 1.375$ using mesh-based handbook functions obtained on handbook mesh Type II.

Now, let us solve the Model Problem II by using handbook mesh Type III shown in Figure 3.34 for the numerical construction of the handbook functions $\psi_j^{X;1}$. Note that these meshes have smaller mesh size than the overkill mesh shown in Figure 3.33(d). Table 3.36 reports the energy norm of the GFEM solutions for $\gamma = 1.0$ of Model Problem II on Mesh III (with 16×16 elements) using the mesh-based handbook functions. Comparing Tables 3.36 with Table 3.26, there is no difference in the relative error. This means that further refinement of the handbook mesh does not bring any benefit in the GFEM solution. The results for other choices of γ and other choices of mesh, Mesh I and II, are omitted here, because they give the same conclusion.

Table 3.36. Energy norm of the solution of Model Problem II on Mesh III (with 16×16 elements) for $\gamma = 1.0$ using the mesh-based handbook functions solved on handbook mesh Type III shown in Figure 3.34. The numbers in bracket are the number of degree of freedom, and the percentage numbers are the relative error of the solution. Here the solution for $p = 5$ and $p_{\text{hb}} = 5$ is used as overkill solution in the computation of the relative error.

	$p_{\text{hb}} = 1$	$p_{\text{hb}} = 2$	$p_{\text{hb}} = 3$	$p_{\text{hb}} = 4$	$p_{\text{hb}} = 5$
$p = 1$	597.219242 (867) 2.66%	597.335528 (1381) 1.78%	597.397113 (1895) 1.05%	597.412889 (2409) 0.76%	597.420545 (2923) 0.56%
$p = 2$	597.332200 (1667) 1.81%	597.363249 (2181) 1.50%	597.403513 (2695) 0.94%	597.415845 (3209) 0.69%	597.421964 (3723) 0.52%
$p = 3$	597.394837 (2979) 1.09%	597.410137 (3493) 0.82%	597.418644 (4007) 0.62%	597.422395 (4521) 0.51%	597.424929 (5035) 0.41%
$p = 4$	597.410972 (4803) 0.80%	597.420931 (5317) 0.55%	597.425966 (5831) 0.37%	597.427536 (6345) 0.29%	597.428345 (6859) 0.24%
$p = 5$	597.419499 (7139) 0.59%	597.425778 (7653) 0.38%	597.428536 (8167) 0.22%	597.429493 (8681) 0.13%	597.430022 (9195)

In above examples, we see that the accuracy of the handbook functions $\psi_j^{X;1}$ plays the significant role in the global GFEM solution, and the exponential convergence of the global GFEM solution can be achieved by using accurate handbook functions. Similar conclusions can also be observed in bigger problem.

Let us solve Problem III again on three meshes shown in Figure 3.41, by using the handbook functions which are numerically constructed on the handbook mesh Type II. Tables 3.37-3.39 report the energy norm of the GFEM solutions of Model Problem III on Mesh I (with 8×8 elements), Mesh II (with 16×16 elements) and Mesh III (with 32×32

elements) using the mesh-based handbook functions for $\gamma = 1.0$. In each table we used the solution with $p = 5$ and $p_{\text{hb}} = 5$ as the overkill solution to compute the relative error. We observe, once more, that we can achieve better accuracy by using less degree of freedom. Figure 3.42 shows the exponential convergence of the GFEM solutions. Like in Model Problem II, from Tables 3.37-3.39 and Figure 3.42, we also observe that the GFEM solution has much similar convergence behavior on the three meshes, Mesh I, II, and III, and the decease of the global mesh size does not make the GFEM solution converge.

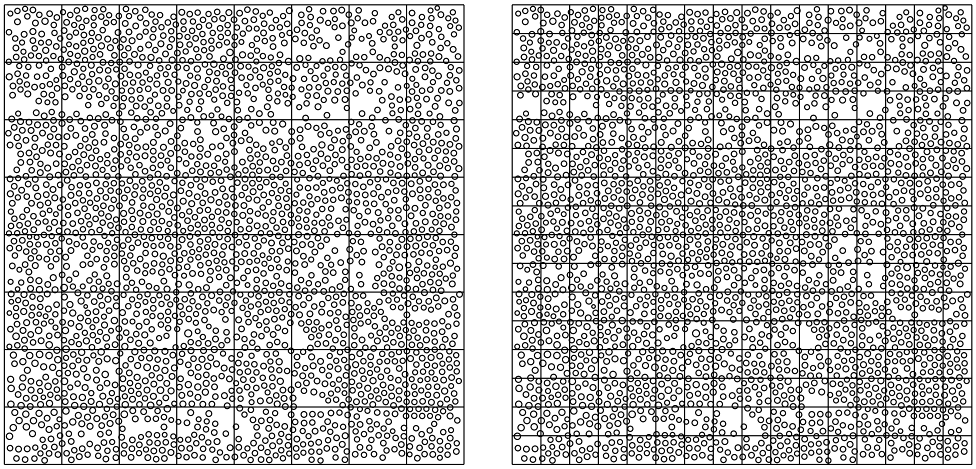

(a). Mesh I (8 × 8 elements)

(b). Mesh II (16 × 16 elements)

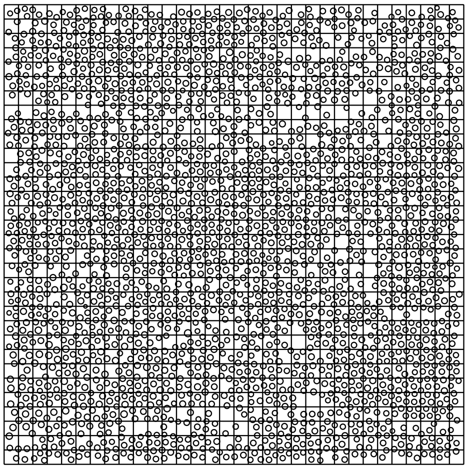

(c). Mesh III (32 × 32 elements)

Figure 3.41. Meshes used for Model Problem III for $\gamma = 1.0$.

We have seen, in this paper, that the GFEM solution can be polluted by two errors: the error in the handbook model and the error in the numerical construction of the handbook functions. More results will be presented in the forthcoming paper.

Table 3.37. Energy norm of the solution of Model Problem III on Mesh I (with 8 × 8 elements) for $\gamma = 1.0$ using the mesh-based handbook functions obtained on handbook mesh Type II. The numbers in bracket are the number of degree of freedom, and the percentage numbers are the relative error of the solution. Here the solution for $p = 5$ and $p_{\text{hb}} = 5$ is used as overkill solution in the computation of the relative error.

	$p_{\text{hb}} = 1$	$p_{\text{hb}} = 2$	$p_{\text{hb}} = 3$	$p_{\text{hb}} = 4$	$p_{\text{hb}} = 5$
$p = 1$	1198.149029 (243) 2.75%	1198.452264 (373) 1.59%	1198.561998 (503) 0.83%	1198.579842 (633) 0.63%	1198.582830 (763) 0.59%
$p = 2$	1198.497620 (451) 1.33%	1198.535042 (581) 1.07%	1198.573962 (711) 0.71%	1198.584115 (841) 0.57%	1198.586820 (971) 0.53%
$p = 3$	1198.554766 (787) 0.90%	1198.570465 (917) 0.75%	1198.582064 (1047) 0.60%	1198.591289 (1177) 0.46%	1198.593604 (1307) 0.41%
$p = 4$	1198.562860 (1251) 0.83%	1198.578701 (1381) 0.65%	1198.590770 (1511) 0.47%	1198.597901 (1641) 0.31%	1198.600744 (1771) 0.22%
$p = 5$	1198.565004 (1843) 0.80%	1198.580865 (1973) 0.62%	1198.592811 (2103) 0.43%	1198.600732 (2233) 0.22%	1198.603758 (2363)

Table 3.38. Energy norm of the solution of Model Problem III on Mesh II (with 16 × 16 elements) for $\gamma = 1.0$ using the mesh-based handbook functions obtained on handbook mesh Type II. The numbers in bracket are the number of degree of freedom, and the percentage numbers are the relative error of the solution. Here the solution for $p = 5$ and $p_{\text{hb}} = 5$ is used as overkill solution in the computation of the relative error.

	$p_{\text{hb}} = 1$	$p_{\text{hb}} = 2$	$p_{\text{hb}} = 3$	$p_{\text{hb}} = 4$	$p_{\text{hb}} = 5$
$p = 1$	1198.238767 (867) 2.45%	1198.453314 (1381) 1.56%	1198.557050 (1895) 0.83%	1198.576213 (2409) 0.61%	1198.583690 (2923) 0.50%
$p = 2$	1198.466525 (1667) 1.49%	1198.489158 (2181) 1.35%	1198.564479 (2695) 0.76%	1198.578430 (3209) 0.58%	1198.585106 (3723) 0.48%
$p = 3$	1198.551529 (2979) 0.89%	1198.566935 (3493) 0.73%	1198.578946 (4007) 0.57%	1198.585328 (4521) 0.47%	1198.589097 (5035) 0.40%
$p = 4$	1198.563851 (4803) 0.76%	1198.578242 (5317) 0.58%	1198.589808 (5831) 0.39%	1198.593110 (6345) 0.31%	1198.595082 (6859) 0.25%
$p = 5$	1198.570206 (7139) 0.69%	1198.583200 (7653) 0.51%	1198.593968 (8167) 0.28%	1198.597048 (8681) 0.17%	1198.598698 (9195)

Table 3.39. Energy norm of the solution of Model Problem III on Mesh III (with 32 × 32 elements) for $\gamma = 1.0$ using the mesh-based handbook functions obtained on handbook mesh Type II. The numbers in bracket are the number of degree of freedom, and the percentage numbers are the relative error of the solution. Here the solution for $p = 5$ and $p_{\mathrm{hb}} = 5$ is used as overkill solution in the computation of the relative error.

	$p_{\mathrm{hb}} = 1$	$p_{\mathrm{hb}} = 2$	$p_{\mathrm{hb}} = 3$	$p_{\mathrm{hb}} = 4$	$p_{\mathrm{hb}} = 5$
$p = 1$	1198.213817 (3267) 2.55%	1198.417531 (5317) 1.76%	1198.540127 (7367) 1.03%	1198.571257 (9417) 0.74%	1198.585571 (11467) 0.55%
$p = 2$	1198.406894 (6403) 1.81%	1198.467037 (8453) 1.51%	1198.552107 (10503) 0.93%	1198.576567 (12553) 0.67%	1198.588333 (14603) 0.51%
$p = 3$	1198.536782 (11587) 1.06%	1198.564533 (13637) 0.81%	1198.581400 (15687) 0.61%	1198.588820 (17737) 0.50%	1198.593930 (19787) 0.40%
$p = 4$	1198.566874 (18819) 0.78%	1198.585075 (20869) 0.56%	1198.595595 (22919) 0.37%	1198.598758 (24969) 0.29%	1198.600426 (27019) 0.23%
$p = 5$	1198.582838 (28099) 0.59%	1198.594616 (30149) 0.39%	1198.600741 (32199) 0.22%	1198.602702 (34249) 0.13%	1198.603704 (36299)

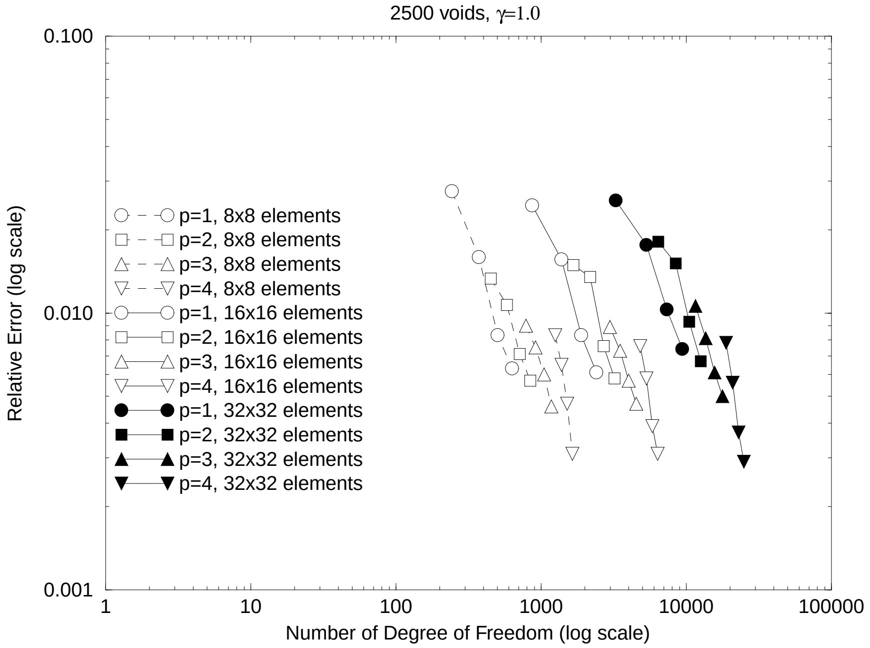

Figure 3.42. Convergence of the GFEM solution of Model Problem III with $\gamma = 1.0$ using mesh-based handbook functions with finer meshes for handbook problems.

CHAPTER IV

FURTHER STUDY OF THE p-HANDBOOK VERSION OF THE GENERALIZED FEM

4.1 Introduction

In this section we briefly re-describe the Generalized FEM using mesh-based handbooks, in order to introduce the new notions for the further study presented in the following sections.

We will describe the method by employing the Neumann problem for the Laplacian in a domain with 597 internal voids as our model problem, namely:

$$\begin{cases} -\Delta u &= 0, \quad \text{in} \quad \Omega_\gamma, \\ \dfrac{\partial u}{\partial n} &= g, \quad \text{on} \quad \Gamma_{\text{outer}}, \\ \dfrac{\partial u}{\partial n} &= 0, \quad \text{on} \quad \partial\Omega_\gamma \backslash \Gamma_{\text{outer}}. \end{cases} \tag{4.1}$$

Here Ω_γ is the problem domain which includes 597 circular voids in its interior the size of which is controlled by a parameter γ, $1.0 \leq \gamma \leq 1.375$, as shown in Figure 4.1, Γ_{outer} denotes the square outer boundary of the domain, $\partial\Omega_\gamma \backslash \Gamma_{\text{outer}}$ is the boundary of the voids, and $g = \nabla(2x - y) \cdot \mathbf{n}$, where $\mathbf{n}$ is the exterior unit normal, is the non-zero Neumann boundary condition imposed only on Γ_{outer}. On the boundaries of the voids, $\partial\Omega_\gamma \backslash \Gamma_{\text{outer}}$, we impose zero Neumann boundary condition.

We will illustrate the robustness of the method by varying the parameter γ which controls the closeness of the voids. Figure 4.1(a) (resp. Figure 4.1(b)) shows the domain Ω_γ for $\gamma = 1.0$ (resp. $\gamma = 1.375$) in which the voids are relatively far apart and it is relatively easy (resp. are almost touching and is more difficult) to approximate the solution of (4.1) with good accuracy.

To construct a Generalized FEM approximation of the solution of (4.1) we will employ a uniform mesh of squares Δ_h as shown in Figure 4.2(a). We will often call Δ_h the GFEM mesh to underline that Δ_h may overlap part of the boundary of the domain and hence it is not a classical FEM mesh; in particular here Δ_h overlaps all the voids. We will denote the elements by τ, the vertices by X_i, $i = 1, 2, ..., n_{\text{vert}}$, and the corresponding element-wise bilinear basis functions (the standard hat-functions) by ϕ_i^h, $i = 1, 2, ..., n_{\text{vert}}$. With each vertex X_i we will associate the vertex patch $\omega_{X_i}^{(0)}$, defined as the zeroth layer patch of elements,

$$\Omega_i^h = \omega_{X_i}^{(0)} \overset{\text{def}}{=} \operatorname{supp}(\phi_i^h) = \bigcup_{\substack{\tau\in\Delta_h \\ X_i\in\partial\tau}} \tau \tag{4.2}$$

Then $\{\phi_i^h\}_{i=1}^{n_{\text{vert}}}$ is a Partition of Unity subordinate to the *covering* $\{\Omega_i^h\}_{i=1}^{n_{\text{vert}}}$ satisfying

$$\phi_i^h \geq 0, \qquad \sum_{i=1}^{n_{\text{vert}}} \phi_i^h \equiv 1, \quad \text{on} \quad \Omega, \tag{4.3}$$

$$\|\phi_i^h\|_{L^\infty(\Omega)} \leq 1, \qquad \|\nabla\phi_i^h\|_{L^\infty(\Omega)} \leq \frac{\mathsf{C}}{h}, \tag{4.4}$$

and, in addition, the covering $\{\Omega_i^h\}_{i=1}^{n_{\text{vert}}}$ satisfies the *overlap* condition

$$\operatorname{card}\{i | x \in \Omega_i^h\} \leq 4. \tag{4.5}$$

Given the mesh Δ_h, and a positive integer p_{hb}, and a parameter $d \in (0, 2]$, we will introduce the *space of mesh-based handbook functions of degree* p_{hb} by

$$V_{\Delta_h}^{p_{\text{hb}};d} = \left\{ v \in H^1(\Omega) \middle| \quad v = \sum_{i=1}^{n_{\text{vert}}} \phi_i^h v_i, \quad v_i \in V_{\text{loc}}^{p_{\text{hb}};d}(\Omega_i^h) \right\}, \tag{4.6}$$

where $V_{\text{loc}}^{p_{\text{hb}};d}(\Omega_i^h)$ is the local space of the handbook functions of degree p_{hb}

$$V_{\text{loc}}^{p_{\text{hb}};d}(\Omega_i^h) = \left\{ v \in H^1(\Omega_i^h) \middle| \quad v = \sum_{j=1}^{n_{\text{hb}}} a_j \psi_j^{X_i;d} \right\}, \tag{4.7}$$

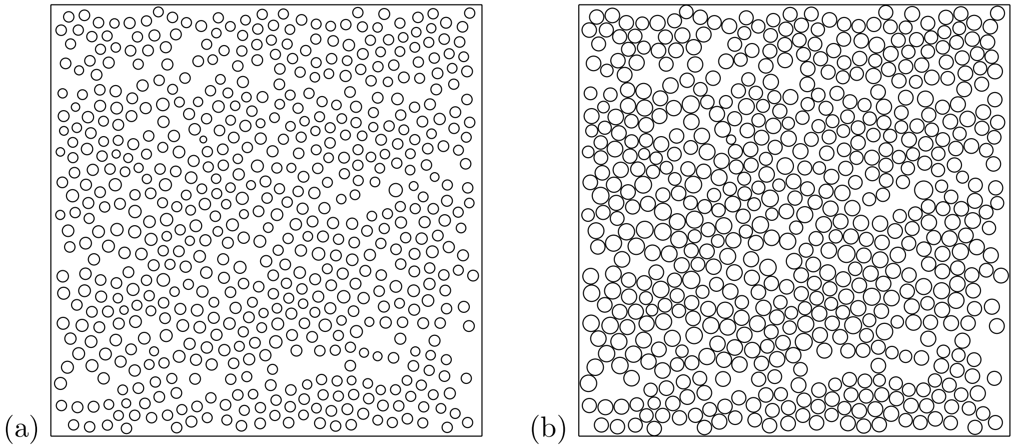

Figure 4.1. The problem domain which includes 597 voids in its interior is shown here for (a) $\gamma = 1.0$, and (b) $\gamma = 1.375$.

where n_{hb} is the dimension of the handbook space $V_{\text{loc}}^{p_{\text{hb}};d}(\Omega_i^h)$, and $\psi_j^{X_i;d}$ is the jth handbook function associated with the vertex patch Ω_i^h and the parameter d, defined as the exact solution of the following local Neumann problem:

$$\begin{aligned}
\Delta\psi_j^{X_i;d} &= 0, \qquad \text{in} \quad \tilde{\omega}_{X_i}^{(1);d}, && (4.8)\\
\frac{\partial}{\partial n}\big(\psi_j^{X_i;d}\big) &= \begin{cases} \nabla(\Re(z^{p_{\text{hb}}}))\cdot\mathbf{n}, & \text{if} \quad j = 2p_{\text{hb}}-1,\\ \nabla(\Im(z^{p_{\text{hb}}}))\cdot\mathbf{n}, & \text{if} \quad j = 2p_{\text{hb}}, \end{cases} \qquad \text{on} \quad \partial\omega_{X_i}^{(1)}, && (4.9)\\
\frac{\partial}{\partial n}\big(\psi_j^{X_i;d}\big) &= 0, \qquad \text{on} \quad \partial\tilde{\omega}_{X_i}^{(1);d} - \partial\omega_{X_i}^{(1)}. && (4.10)
\end{aligned}$$

Here $\omega_{X_i}^{(1)}$ is the one-layer patch of elements around X_i, namely

$$\omega_{X_i}^{(1)} = \bigcup_{\substack{\tau\in\Delta_h\\ \partial\tau\bigcap\omega_{X_i}^{(0)}\neq 0}} \tau. \tag{4.11}$$

$\tilde{\omega}_{X_i}^{1;d}$ is the *handbook* domain obtained from $\omega_{X_i}^{(1)}\bigcap\Omega_\gamma$ by eliminating the voids which do not intersect a neighborhood of X_i controlled by the parameter $d\in(0,2]$. Figure 4.2(c) shows the domain $\tilde{\omega}_X^{(1);1}$, obtained for $d=1$ which we will use throughout this and the next section. In [53] we also employed handbook domains with $d=1/2$.

Figures 4.3 and 4.4 show the shades of the gradient for $\psi_j^{X;1}$, the handbook functions of degree one and two for $\gamma=1.0$ and 1.375, for the patch shown in Figure 4.2. We refer the reader to [53] for more details of the definition of the handbook functions for boundary patches and curvilinear domains.

The $\big(p;(p_{\text{hb}},d)\big)$ Generalized FEM approximation of the solution of (4.1) is given by

$$u_{\Delta_h}^{p;(p_{\text{hb}},d)} = \sum_{k=1}^{n_{\text{FEM}}} b_k\tilde{\psi}_k + \sum_{i=1}^{n_{\text{vert}}} \phi_i^h\Big(\sum_{j=1}^{n_{\text{hb}}} a_j^{(i)}\psi_j^{X_i;d}\Big) \in S_{\Delta_h}^p \oplus V_{\Delta_h}^{p_{\text{hb}};d}, \tag{4.12}$$

where $\tilde{\psi}_k$ (resp. $S_{\Delta_h}^p$) are the standard bi-p finite element basis functions (resp. bi-p finite element space) of degree p defined over the mesh Δ_h, and b_k, $k=1,...,n_{\text{FEM}}$, $a_j^{(i)}$, $j=1,...,n_{\text{hb}}$, $i=1,...,n_{\text{vert}}$, are the Generalized FEM degrees of freedom which are determined to be such that (4.12) satisfies the standard discrete variational problem:

$$\int_\Omega \nabla u_{\Delta_h}^{p;(p_{\text{hb}},d)}\cdot\nabla v\, d\Omega = \oint_{\Gamma_{\text{outer}}} gv\, ds, \qquad \forall v\in S_{\Delta_h}^p\oplus V_{\Delta_h}^{p_{\text{hb}};d}. \tag{4.13}$$

In [53] we analyzed the $\big(p;(p_{\text{hb}},d)\big)$ convergence of the Generalized FEM approximation on the uniform 4×4, 8×8, and 16×16 meshes of squares shown in Figure 4.5 for several values of the parameter γ, $1\leq\gamma\leq1.375$. Tables 4.1, 4.2 and 4.3 give the p, and p-handbook (p_{hb}) convergence of the error

$$\frac{\|e_{\text{GFEM}}\|_{\mathsf{U}}}{\|u_{\text{EX}}\|_{\mathsf{U}}} = \frac{\sqrt{\|u_{\text{EX}}\|_{\mathsf{U}}^2 - \|u_{\text{GFEM}}\|_{\mathsf{U}}^2}}{\|u_{\text{EX}}\|_{\mathsf{U}}},$$

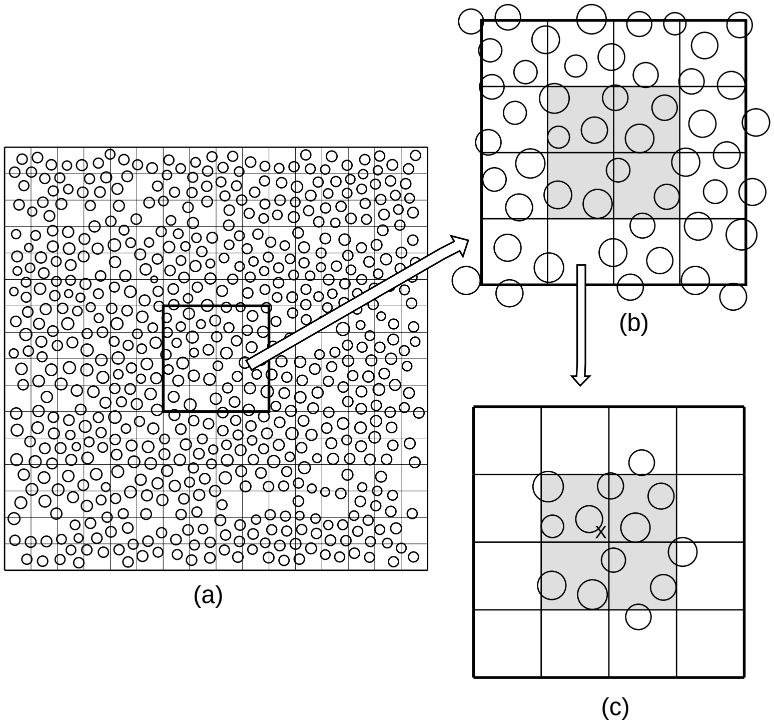

Figure 4.2. Creation of handbook domains $\tilde{\omega}_X^{(1);1}$ associated with a vertex X. (a) The domain Ω_γ covered by a uniform 16×16 mesh Δ_h of square elements; (b) A typical vertex patch $\omega_X^{(1)}$ with the voids intersecting it; (c) The handbook domain $\tilde{\omega}_X^{(1);1}$ obtained from $\omega_X^{(1)} \bigcap \Omega_\gamma$ by eliminating all the voids outside $\omega_X^{(0)}$.

respectively for the 4×4, 8×8, and 16×16 meshes for $\gamma = 1.0$. Each column gives the p-convergence for fixed p_{hb} order, while each row gives the p_{hb}-convergence for fixed p. In each case the handbook functions were constructed numerically with sufficient accuracy so that *the errors in their numerical construction do not affect significantly the accuracy of the Generalized FEM solution.* We will address the effect of the accuracy of the numerical construction of the handbook functions on the accuracy of the Generalized FEM in the next section. The first column of each table corresponds to $p_{\mathrm{hb}} = 0$, i.e. to the case that no handbook functions are used in the GFEM solution. Comparing the relative errors for $p_{\mathrm{hb}} = 0$ (first column) and $p_{\mathrm{hb}} = 1$ (second column) we can see clearly that there is very significant improvement in accuracy when we employ $p_{\mathrm{hb}} = 1$, i.e. *the enrichment of the approximation by handbook functions leads to significant improvement of its accuracy.* Further, from Figure 4.6, which gives the p_{hb} (abbreviation for p-handbook)-convergence when the 4×4 mesh is employed for $\gamma = 1.0$ and $\gamma = 1.375$, it appears that the error decreases exponentially with p and p_{hb}, similarly as in the classical p-version of the FEM for heat-conduction and elasticity problems in polygonal domains (see [71]) and that the

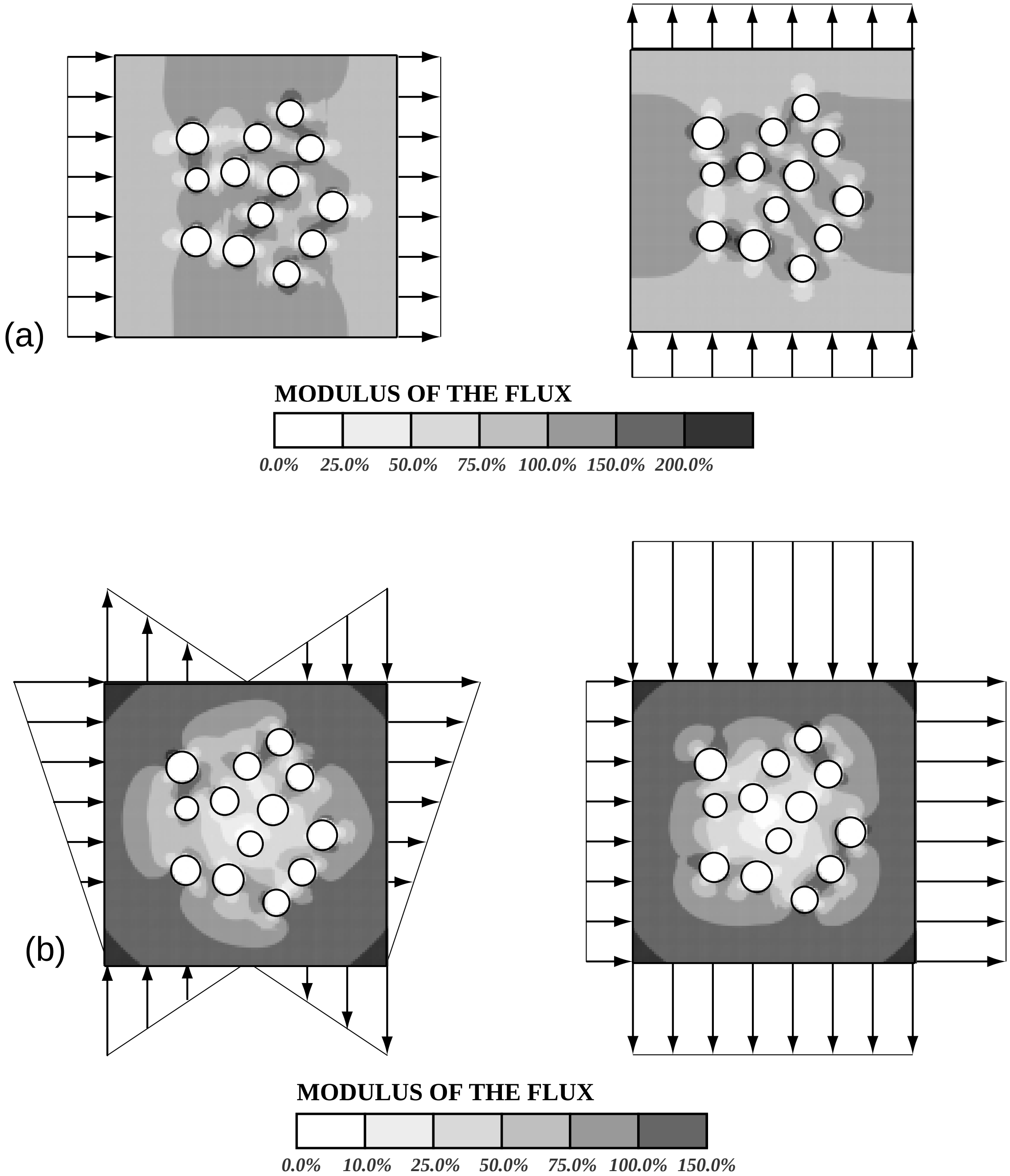

Figure 4.3. Examples of the handbook functions $\psi_j^{X;1}$ for $d = 1$, $j = 1, ..., 4$, for the handbook domain $\tilde{\omega}_X^{(1);1}$ shown in Figure 4.2(c). Shades of the gradient of the pairs of handbook functions of degrees one and two for (c) $\gamma = 1.0$, with the boundary conditions for the handbook functions of degree (a) $p_{\mathrm{hb}} = 1$ ($\nabla(\Re(z)) \cdot \mathbf{n}$ and $\nabla(\Im(z)) \cdot \mathbf{n}$), and (b) $p_{\mathrm{hb}} = 2$ ($\nabla(\Re(z^2)) \cdot \mathbf{n}$ and $\nabla(\Im(z^2)) \cdot \mathbf{n}$).

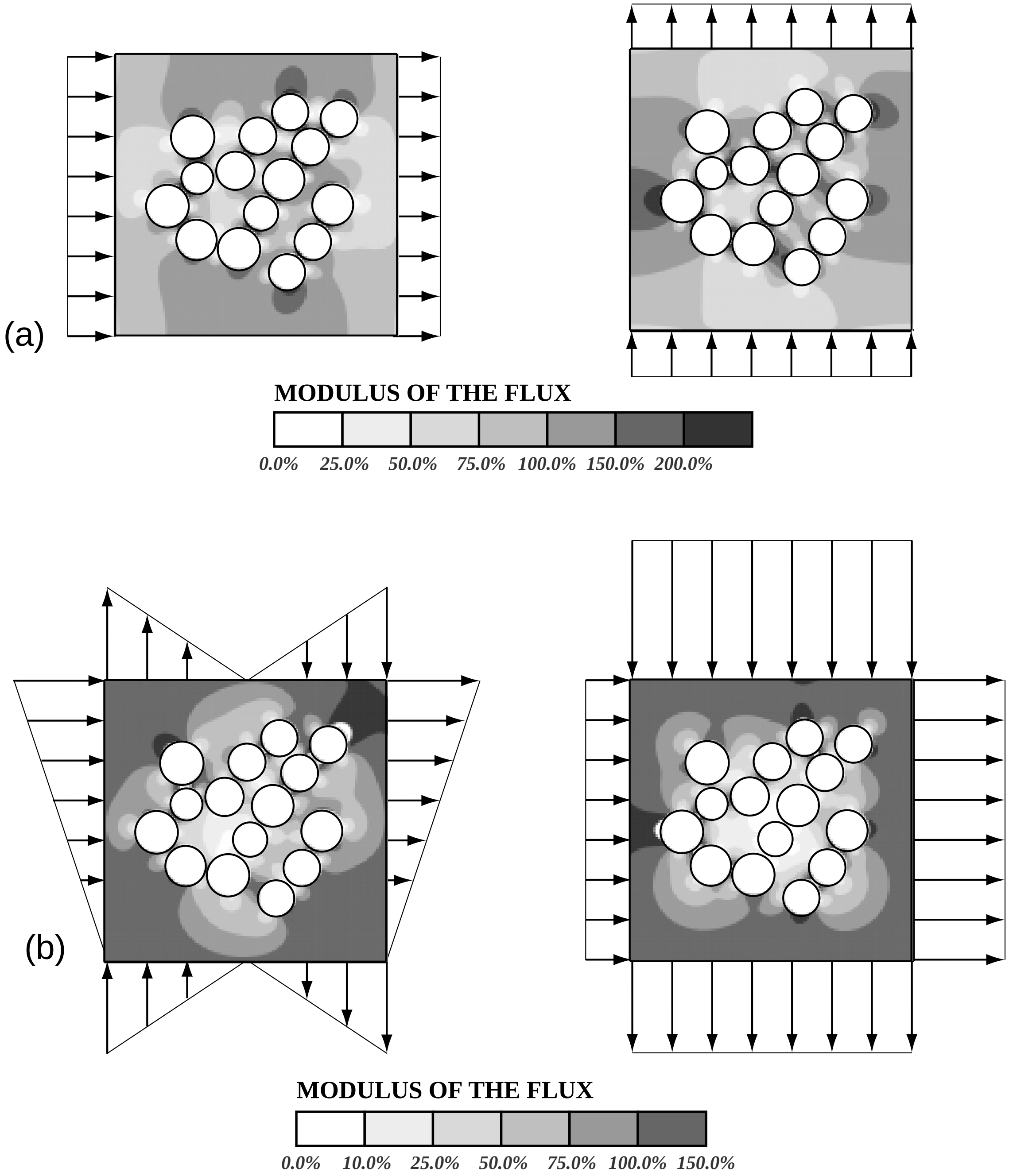

Figure 4.4. Examples of the handbook functions $\psi_j^{X;1}$ for $d = 1$, $j = 1, ..., 4$, for the handbook domain $\tilde{\omega}_X^{(1);1}$ shown in Figure 4.2(c). Shades of the gradient of the pairs of handbook functions of degrees one and two for (c) $\gamma = 1.375$, with the boundary conditions for the handbook functions of degree (a) $p_{\text{hb}} = 1$ ($\nabla(\Re(z)) \cdot \mathbf{n}$ and $\nabla(\Im(z)) \cdot \mathbf{n}$), and (b) $p_{\text{hb}} = 2$ ($\nabla(\Re(z^2)) \cdot \mathbf{n}$ and $\nabla(\Im(z^2)) \cdot \mathbf{n}$).

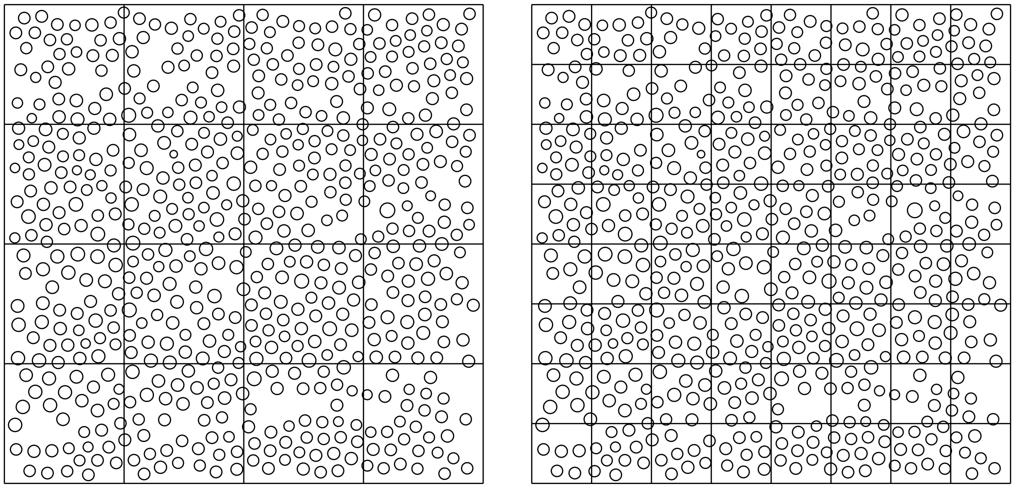

(a). Mesh I (4 × 4 elements) (b). Mesh II (8 × 8 elements)

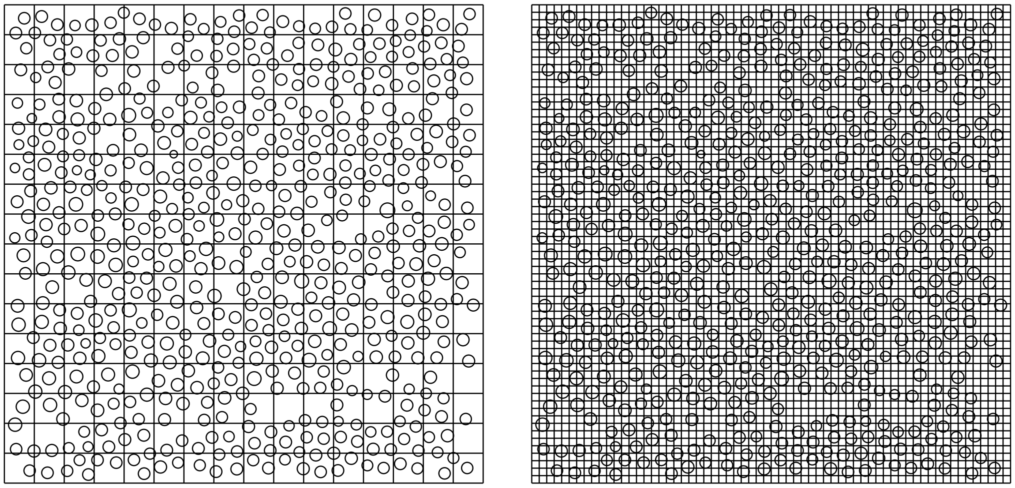

(c). Mesh III (16 × 16 elements) (d). Mesh V (64 × 64 elements)

Figure 4.5. Uniform meshes of squares used for the Generalized FEM solution of model problem (4.1) shown here over the problem domain for $\gamma = 1.0$.

Generalized FEM is robust with respect to the γ, except for the case when $p_{\mathrm{hb}} = 0$, i.e. when no handbook functions are employed.

In order to compare the p-convergence with $p_{\mathrm{hb}} > 1$, with the convergence of the h and p-version of the Generalized FEM with $p_{\mathrm{hb}} = 0$, when no handbook functions are added, we computed the bi-p GFEM solutions on the 4×4, 8×8, 16×16, 32×32, 64×64, and 128×128 meshes for $\gamma = 1.0$, for $p = 1,...,5$, using $p_{\mathrm{hb}} = 0$. Table 4.4 reports the energy norms and the corresponding relative errors of the GFEM solution for $p = 1,...,5$ ($p_{\mathrm{hb}} = 0$), $h = L/4, ..., L/128$ (L denotes the length of the side of the outer square of Ω), and Figure 4.7 compares its convergence versus the p-handbook convergence of the method for $p_{\mathrm{hb}} = 1, ..., 5$, $p = 1, ..., 5$, on the 4×4, 8×8 and 16×16 meshes. *Note the very significant improvement in the accuracy due to the employment of the handbook functions and that the p-handbook version of the method appears to converge exponentially.* Let us also remark that linear convergence is at best the convergence to be expected from the X-FEM of Belytschko *et al.* (see [30, 34]), because it does not include enrichment by handbook functions. The level set functions employed to enrich the $p = 1$ FE basis in the X-FEM have different character than our handbook functions and most likely do not contribute significantly in the improvement of the accuracy of the X-FEM. Their main use is related with the description of the problem domain in the elements overlapping a boundary.

Let us also examine the effect of enrichment by handbook functions in the pointwise accuracy. Figure 4.8 compares the pointwise error of the GFEM solution computed using: $p = 1$ and $p_{\mathrm{hb}} = 1$ on the mesh with 4×4 elements, with the GFEM solution computed using $p = 1$ and $p_{\mathrm{hb}} = 0$ on the mesh with 128×128 elements. It is clear that the handbook function are responsible for very significant improvement in the pointwise accuracy of the GFEM solution.

Table 4.1. p and p_{hb} convergence of the energy norm of the solution of the model problem on the mesh with 4×4 elements for $\gamma = 1.0$. The numbers in bracket are the number of degrees of freedom, and the percentage numbers are the relative error of the solution. Here we used the solution for $p = 5$ and $p_{\mathrm{hb}} = 5$ as overkill solution to compute the relative error for all the other entries in the Table. The first column shows the p-convergence for the case $p_{\mathrm{hb}} = 0$ (no handbook functions), in which the error is very high for the entire range of p.

	$p_{\mathrm{hb}} = 0$	$p_{\mathrm{hb}} = 1$	$p_{\mathrm{hb}} = 2$	$p_{\mathrm{hb}} = 3$	$p_{\mathrm{hb}} = 4$	$p_{\mathrm{hb}} = 5$
$p = 1$	526.047756 (25) 47.40%	597.223463 (75) 2.66%	597.352380 (109) 1.66%	597.405799 (143) 0.98%	597.417457 (177) 0.75%	597.419870 (211) 0.69%
$p = 2$	526.460025 (81) 47.27%	597.379945 (131) 1.35%	597.398663 (165) 1.09%	597.413286 (199) 0.84%	597.420154 (233) 0.69%	597.422822 (267) 0.62%
$p = 3$	527.076526 (169) 47.07%	597.397113 (219) 1.11%	597.410107 (253) 0.90%	597.418923 (287) 0.72%	597.425465 (321) 0.54%	597.427684 (355) 0.47%
$p = 4$	527.663025 (289) 46.89%	597.403085 (339) 1.02%	597.415649 (373) 0.79%	597.423456 (407) 0.60%	597.429948 (441) 0.38%	597.432449 (475) 0.24%
$p = 5$	528.168569 (441) 46.73%	597.404253 (491) 1.00%	597.416764 (525) 0.76%	597.424505 (559) 0.57%	597.431349 (593) 0.31%	597.434226 (627)

Table 4.2. p and p_{hb} convergence of the energy norm of the solution of the model problem on the mesh with 8×8 elements for $\gamma = 1.0$. The numbers in bracket are the number of degrees of freedom, and the percentage numbers are the relative error of the solution. Here we used the solution for $p = 5$ and $p_{\text{hb}} = 5$ as overkill solution to compute the relative error for all the other entries in the Table. The first column shows the p-convergence for the case $p_{\text{hb}} = 0$ (no handbook functions), in which the error is very high for the entire range of p.

	$p_{\text{hb}} = 0$	$p_{\text{hb}} = 1$	$p_{\text{hb}} = 2$	$p_{\text{hb}} = 3$	$p_{\text{hb}} = 4$	$p_{\text{hb}} = 5$
$p = 1$	526.349745 (81) 47.30%	597.223977 (243) 2.58%	597.350383 (373) 1.56%	597.400110 (503) 0.88%	597.411934 (633) 0.62%	597.415788 (763) 0.50%
$p = 2$	527.500512 (289) 46.94%	597.359292 (451) 1.46%	597.374917 (581) 1.27%	597.404901 (711) 0.79%	597.413183 (841) 0.58%	597.416523 (971) 0.48%
$p = 3$	528.905577 (625) 46.50%	597.395585 (787) 0.96%	597.406892 (917) 0.74%	597.413137 (1047) 0.58%	597.416783 (1177) 0.47%	597.418703 (1307) 0.39%
$p = 4$	531.392559 (1089) 45.69%	597.402057 (1251) 0.84%	597.412927 (1381) 0.59%	597.418541 (1511) 0.40%	597.420530 (1641) 0.31%	597.421461 (1771) 0.25%
$p = 5$	535.140625 (1681) 44.45%	597.405660 (1843) 0.77%	597.415578 (1973) 0.51%	597.420707 (2103) 0.30%	597.422540 (2233) 0.16%	597.423341 (2363)

Table 4.3. p and p_{hb} convergence of the energy norm of the solution of the model problem on the mesh with 16×16 elements for $\gamma = 1.0$. The numbers in bracket are the number of degrees of freedom, and the percentage numbers are the relative error of the solution. Here we used the solution for $p = 5$ and $p_{\mathrm{hb}} = 5$ as overkill solution to compute the relative error for all the other entries in the Table. The first column shows the p-convergence for the case $p_{\mathrm{hb}} = 0$ (no handbook functions), in which the error is very high for the entire range of p.

	$p_{\mathrm{hb}} = 0$	$p_{\mathrm{hb}} = 1$	$p_{\mathrm{hb}} = 2$	$p_{\mathrm{hb}} = 3$	$p_{\mathrm{hb}} = 4$	$p_{\mathrm{hb}} = 5$
$p = 1$	527.206120 (289) 47.03%	597.217498 (867) 2.66%	597.333781 (1381) 1.78%	597.395365 (1895) 1.05%	597.411471 (2409) 0.75%	597.418804 (2923) 0.56%
$p = 2$	531.284898 (1089) 45.73%	597.330451 (1667) 1.81%	597.361503 (2181) 1.49%	597.401769 (2695) 0.94%	597.414104 (3209) 0.69%	597.420222 (3723) 0.52%
$p = 3$	541.855531 (2401) 42.11%	597.393083 (2979) 1.09%	597.408376 (3493) 0.82%	597.416892 (4007) 0.62%	597.420647 (4521) 0.50%	597.423184 (5035) 0.41%
$p = 4$	558.050844 (4225) 35.70%	597.409219 (4803) 0.80%	597.419165 (5317) 0.55%	597.424210 (5831) 0.37%	597.425781 (6345) 0.29%	597.426591 (6859) 0.24%
$p = 5$	573.850349 (6561) 27.81%	597.417730 (7139) 0.59%	597.424005 (7653) 0.38%	597.426764 (8167) 0.22%	597.427723 (8681) 0.13%	597.428250 (9195)

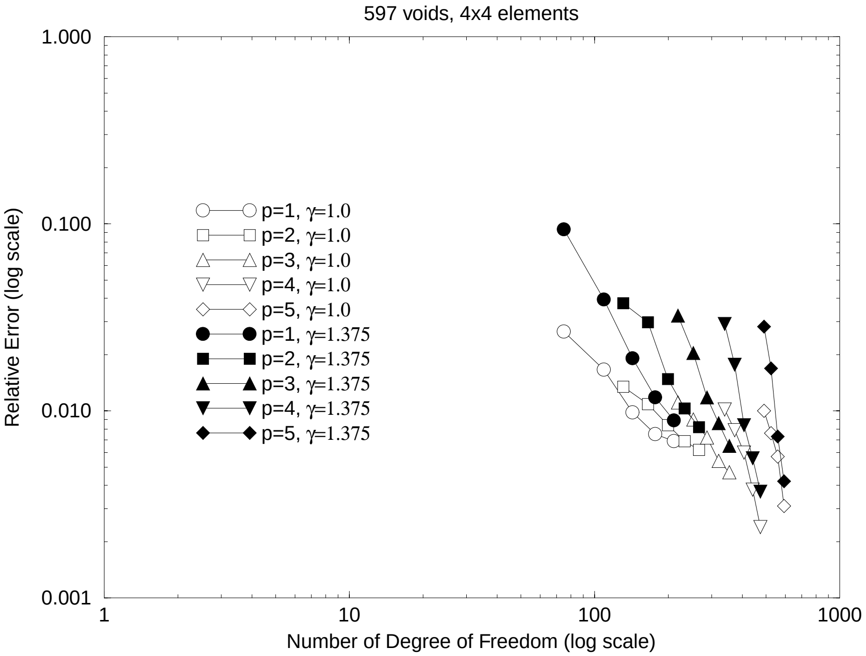

Figure 4.6. p_{hb}-convergence of the GFEM solution for $\gamma = 1.0$ and $\gamma = 1.375$ on the 4×4 mesh. Note that the character of the convergence does not depend on γ.

Table 4.4. h and p convergence of the bi-p GFEM solution when no handbook functions are used ($p_{\text{hb}} = 0$). The numbers in brackets are the corresponding numbers of degrees of freedom, and the percentage numbers are the relative error of the FEM solutions, for the case $\gamma = 1.0$. Here, we used the $p = 5$ and $p_{\text{hb}} = 5$ GFEM solution on the 4×4 mesh to compute the relative errors.

	$p = 1$	$p = 2$	$p = 3$	$p = 4$	$p = 5$
4×4 mesh	526.047757 (25) 47.40%	526.460025 (81) 47.27%	527.076526 (169) 47.08%	527.663025 (289) 46.90%	528.168570 (441) 46.74%
8×8 mesh	526.349746 (81) 47.31%	527.500513 (289) 46.95%	528.905577 (625) 46.50%	531.392559 (1089) 45.70%	535.140624 (1681) 44.46%
16×16 mesh	527.206120 (289) 47.04%	531.284899 (1089) 45.74%	541.855520 (2401) 42.12%	558.050857 (4225) 35.71%	573.850334 (6561) 27.82%
32×32 mesh	530.863334 (1089) 45.87%	561.402890 (4225) 34.20%	585.185212 (9409) 20.15%	593.588735 (16641) 11.33%	596.252541 (25921) 6.29%
64×64 mesh	563.133352 (4225) 33.40%	593.801073 (16616) 11.01%	597.101554 (37149) 3.34%	597.269237 (65824) 2.35%	597.427011 (102641) 0.49%
128×128 mesh	591.321915 (16558) 14.27%	597.232113 (63468) 2.60%	597.424852 (140136) 0.56%	597.430807 (246562) 0.34%	

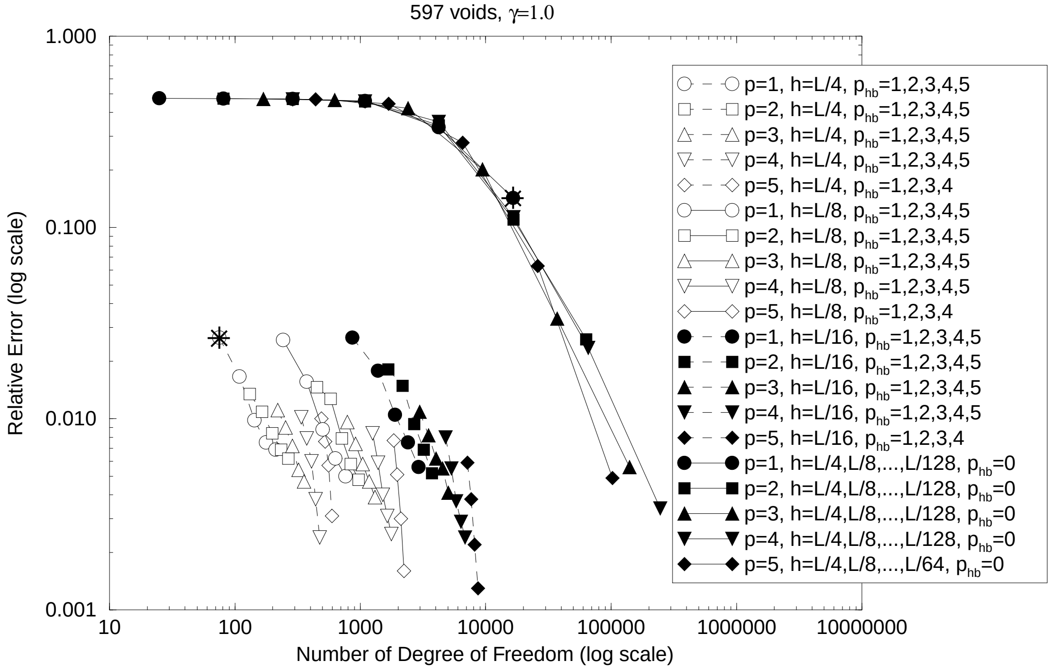

Figure 4.7. Comparison of the h-convergence of the FEM solutions and the $p_{\rm hb}$- convergence of the GFEM solutions. Note the very different character of the method when $p_{\rm hb} = 0$ (no enrichment) and $p_{\rm hb} \geq 1$! The $*$ symbol indicates the solutions which are compared in Figure 4.8.

4.2 Effect of the error in the numerical construction of the handbook functions

In the computational implementation of the Generalized FEM the handbook functions $\psi_j^{X;d}$ are replaced by numerical constructions $\mathsf{A}^{p;(p_{\rm void},n_{\rm layers})}_{T_{h/2^n}}\psi_j^{X;d}$ obtained by employing the GFEM on mesh discretization $T_{h/2^n}(\omega_X^{(1)})$ of the handbook subdomains $\tilde\omega_X^{(1);d}$ using bi-p FE basis of degree p, and special functions of degree $p_{\rm void}$ which are applied at $n_{\rm layers}$ of vertices around each void (see [49–52]). Here $T_{h/2^n}(\omega_X^{(1)})$ is the mesh obtained by refining n-times the restriction of the mesh Δ_h in the handbook domain $\tilde\omega_X^{(1);d}$. We will call $T_{h/2^n}(\omega_X^{(1)})$ the employed *handbook mesh*.

Using the numerically constructed handbook functions $\mathsf{A}^{p;p_{\rm sp}}_{T_{h/2^n}}\psi_j^{X;d}$, where $p_{\rm sp}$ is used as an abbreviation of $(p_{\rm void}, n_{\rm layers})$, we obtain the *computed* GFEM solution

$$u^{p;(p_{\rm hb},d)}_{\Delta_h;\mathsf{A}} = \sum_{k=1}^{n_{\rm FEM}} \bar{b}_k\tilde{\psi}_k + \sum_{i=1}^{n_{\rm vert}} \phi_i^h \Big(\sum_{j=1}^{n_{\rm hb}} \bar{a}_j^{(i)} \mathsf{A}^{p;p_{\rm sp}}_{T_{h/2^n}} \psi_j^{X_i;d} \Big) \in S^p_{\Delta_h} \oplus V^{p_{\rm hb};d}_{\Delta_h;\mathsf{A}}, \qquad (4.14)$$

where $V^{p_{\rm hb};d}_{\Delta_h;\mathsf{A}}$ is the global space of numerically constructed handbook functions which is defined as in (4.6) and (4.7) by replacing the handbook functions $\psi_j^{X;d}$ by their numerical constructions $\mathsf{A}^{p;(p_{\rm void},n_{\rm layers})}_{T_{h/2^n}}\psi_j^{X;d}$, and the degrees of freedom $\bar{b}_k$ and $\bar{a}_j^{(i)}$ are determined to

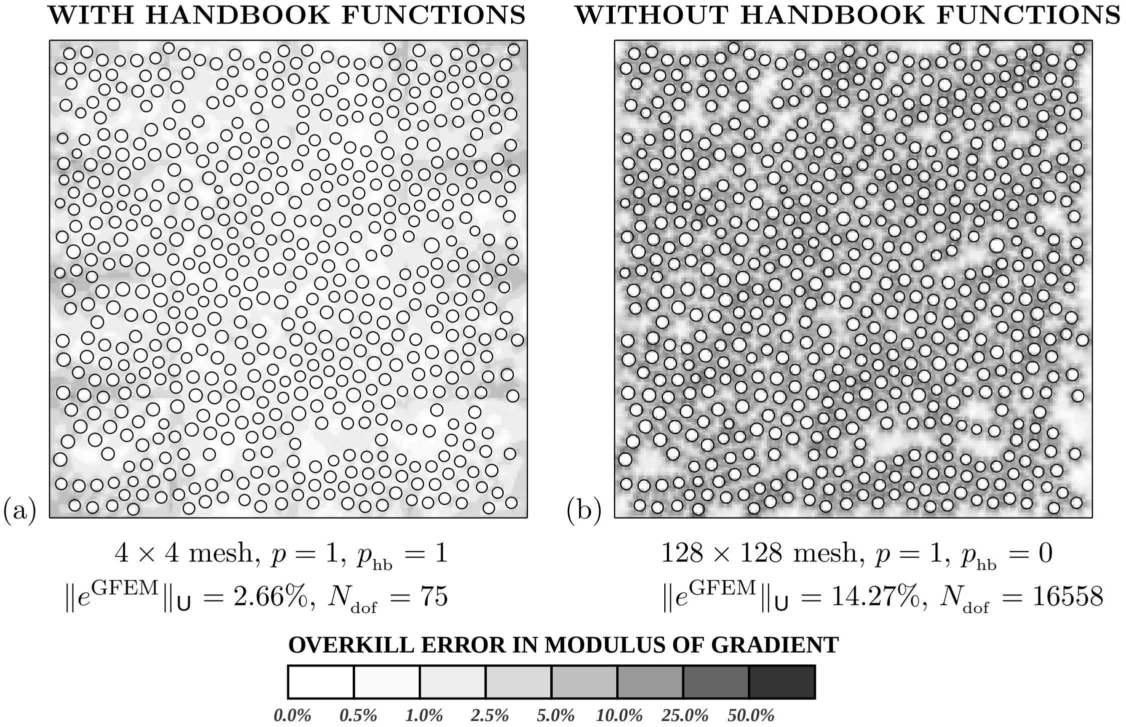

(a) 4×4 mesh, $p = 1$, $p_{\mathrm{hb}} = 1$
$\|e^{\mathrm{GFEM}}\|_{\mathsf{U}} = 2.66\%$, $N_{\mathrm{dof}} = 75$

(b) 128×128 mesh, $p = 1$, $p_{\mathrm{hb}} = 0$
$\|e^{\mathrm{GFEM}}\|_{\mathsf{U}} = 14.27\%$, $N_{\mathrm{dof}} = 16558$

Figure 4.8. Relative modulus of the error of gradient for: (a). the $p = 1$, $p_{\mathrm{hb}} = 1$ GFEM solution on the 4×4 mesh using only 75 degrees of freedom; and (b) the $p = 1$, $p_{\mathrm{hb}} = 0$ GFEM solution on the 128×128 mesh using 16558 degrees of freedom.

satisfy the discrete variational problem

$$\int_\Omega \nabla u^{p;(p_{\mathrm{hb}},d)}_{\Delta_h;\mathsf{A}} \cdot \nabla v \, d\Omega = \oint_{\Gamma_{\mathrm{outer}}} gv \, ds, \qquad \forall v \in S^p_{\Delta_h} \oplus V^{p_{\mathrm{hb}};d}_{\Delta_h;\mathsf{A}}, \tag{4.15}$$

We call $u^{p;(p_{\mathrm{hb}},d)}_{\Delta_h;\mathsf{A}}$ the *computed* GFEM solution to underline the fact that it is different from the GFEM solution $u^{p;(p_{\mathrm{hb}},d)}_{\Delta_h}$ defined in terms of the exact handbook functions $\psi^{X;d}_j$.

In [53], we have seen that large errors, $\psi^{X;d}_j - \mathsf{A}^{p;(p_{\mathrm{void}},n_{\mathrm{layers}})}_{T_{h/2^n}} \psi^{X;d}_j$, in the numerical constructions of the handbook function can degrade the accuracy of the computed GFEM solution $u^{p;(p_{\mathrm{hb}},d)}_{\Delta_h;\mathsf{A}}$, in comparison with the accuracy of $u^{p;(p_{\mathrm{hb}},d)}_{\Delta_h}$, the GFEM solution based on the exact handbook functions $\psi^{X;d}_j$. To underline this point, let us, once more, consider the model example in the domain with 597 voids, and let us determine the computed GFEM solution $u^{p;(p_{\mathrm{hb}},d)}_{\Delta_h;\mathsf{A}}$ using $p, p_{\mathrm{hb}} = 1, ..., 5$ on the 16×16 mesh Δ_h using the computed handbook functions $\mathsf{A}^{5;(1,0)}_{T_{h/2}} \psi^{X;1}_j$ (resp. $\mathsf{A}^{5;(1,0)}_{T_{h/4}} \psi^{X;1}_j$) which are constructed numerically using the bi-p FEM approximation enriched by analytical void functions of degree $p_{\mathrm{void}} = 1$ at $n_{\mathrm{layers}} = 0$ on the handbook mesh $T_{h/2}(\omega^{(1)}_X)$ (resp. $T_{h/4}(\omega^{(1)}_X)$), which are shown in Figure 4.9(b) (resp. Figure 4.9(c))

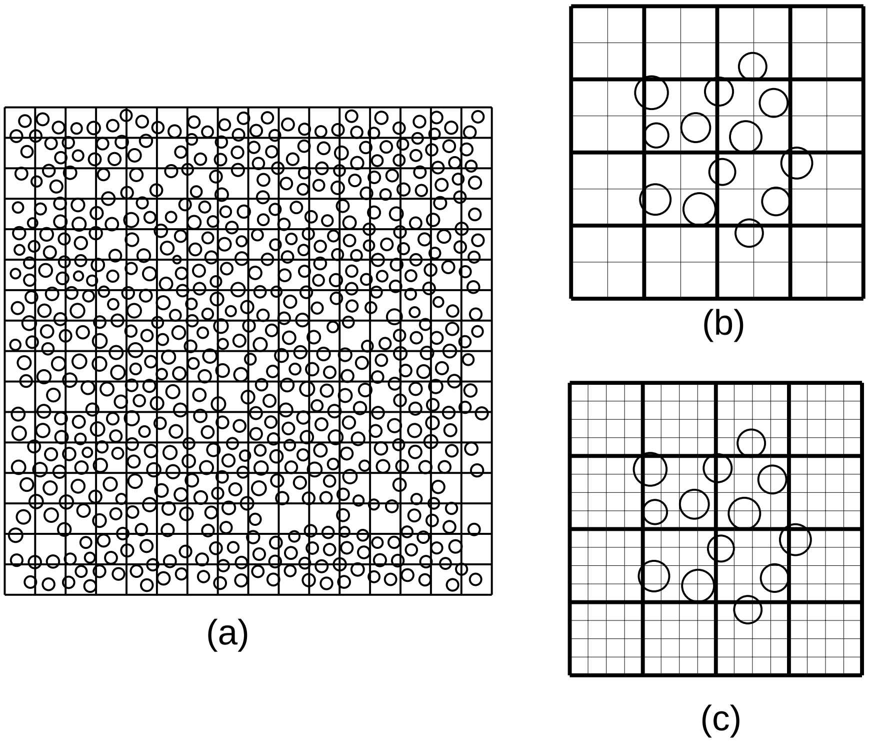
(a)

(b)

(c)

Figure 4.9. (a) The problem domain which includes 597 voids covered by the 16×16 mesh Δ_h. (b) The meshes $T_{h/2}(\omega_X^{(1)})$, and (c) $T_{h/4}(\omega_X^{(1)})$, for a typical handbook domain $\tilde{\omega}_X^{(1);1}$ already shown in Figure 4.2 above. The mesh shown with thick lines is $T_h(\omega_X^{(1)})$, the restriction of the mesh Δ_h in $\omega_X^{(1)}$.

Table 4.5 (resp. Table 4.6) gives the relative errors of the computed GFEM solution $u_{\Delta_h;\mathsf{A}}^{p;(p_{\text{hb}},d)}$ obtained using the $\mathsf{A}_{T_{h/2}}^{5;(1,0)}\psi_j^{X;1}$ (resp. $\mathsf{A}_{T_{h/4}}^{5;(1,0)}\psi_j^{X;1}$) handbook functions, and Figure 4.10 compares the p_{hb} convergence in the two cases. Note that when the $\mathsf{A}_{T_{h/2}}^{5;(1,0)}\psi_j^{X;1}$ handbook functions are employed only up to 5% accuracy can be achieved, while by using the $\mathsf{A}_{T_{h/4}}^{5;(1,0)}\psi_j^{X;1}$ handbook functions better than 0.5% accuracy can be attained!

Let us now see in more detail the accuracy of the numerical construction of the handbook functions. The above example employs 289 handbooks (225 interior handbooks and 64 boundary handbooks). Let us solve the handbook problems for the handbook functions $\psi_j^{X;1}$, $j = 1,...,10$, using the meshes $T_{h/2}(\omega_X^{(1)})$, $T_{h/4}(\omega_X^{(1)})$ and $T_{h/8}(\omega_X^{(1)})$, (shown in Figure 4.11 for a typical handbook domain $\tilde{\omega}_X^{(1);1}$, obtained respectively from one, two and three uniform subdivisions of the restriction of the GFEM mesh Δ_h in $\omega_X^{(1)}$. Using these meshes we constructed the handbook functions $\psi_j^{X;1}$, employing bi-quintic ($p = 5$) basis with void functions of degree one ($p_{\text{voids}} = 1$) at $n_{\text{layers}} = 0$, namely $\mathsf{A}_{T_{h/2^n}}^{5;(1,0)}\psi_j^{X;1}$ for $j = 1, ..., 10$, $n = 1,2,3$. Using $\mathsf{A}_{T_{h/8}}^{5;(1,0)}\psi_j^{X;1}$ as the reference solution we computed the relative errors

Table 4.5. p and p_{hb} convergence of the energy norm of the computed GFEM solution $u^{\text{GFEM}}_{\mathsf{A}^{5;(1,0)}_{T_{h/2}}}(\Delta_h, p, p_{\text{hb}})$ using the numerically constructed handbook functions $\mathsf{A}^{5;(1,0)}_{T_{h/2}}\psi_j^{X;1}$ for $\gamma = 1.0$ on the mesh with 16 × 16 elements. The numbers in the brackets are the number of degree of freedom, and the percentage numbers are the relative error in the energy norm. Note that due to the large errors in the numerical construction of the handbook functions, the GFEM converges very slowly and only 5% accuracy can be achieved. Here we used the $p = 5$ and $p_{\text{hb}} = 5$ solution from the next Table to compute all the relative errors.

	$p_{\text{hb}} = 0$	$p_{\text{hb}} = 1$	$p_{\text{hb}} = 2$	$p_{\text{hb}} = 3$	$p_{\text{hb}} = 4$	$p_{\text{hb}} = 5$
$p = 1$	527.206120 (289) 47.03%	596.367579 (867) 5.91%	596.481838 (1381) 5.58%	596.541779 (1895) 5.40%	596.557674 (2409) 5.35%	596.566524 (2923) 5.32%
$p = 2$	531.284898 (1089) 45.73%	596.478734 (1667) 5.59%	596.509660 (2181) 5.50%	596.549230 (2695) 5.38%	596.562569 (3209) 5.34%	596.570355 (3723) 5.31%
$p = 3$	541.855531 (2401) 42.11%	596.540586 (2979) 5.40%	596.556918 (3493) 5.35%	596.566336 (4007) 5.32%	596.573090 (4521) 5.30%	596.579247 (5035) 5.28%
$p = 4$	558.050844 (4225) 35.70%	596.556949 (4803) 5.35%	596.569200 (5317) 5.31%	596.577328 (5831) 5.29%	596.586096 (6345) 5.26%	596.596171 (6859) 5.23%
$p = 5$	573.850349 (6561) 27.81%	596.565782 (7139) 5.32%	596.576615 (7653) 5.29%	596.586054 (8167) 5.26%	596.598127 (8681) 5.22%	596.615491 (9195) 5.17%

$$e^{\text{h/2}}_{\text{REL}}(\omega^{(0)}_X) = \frac{\|\mathsf{A}^{5;(1,0)}_{T_{h/8}}\psi_j^{X;1} - \mathsf{A}^{5;(1,0)}_{T_{h/2}}\psi_j^{X;1}\|_{\mathsf{U}(\omega^{(0)}_X)}}{\|\mathsf{A}^{5;(1,0)}_{T_{h/8}}\psi_j^{X;1}\|_{\mathsf{U}(\omega^{(0)}_X)}}, \qquad j = 1, ..., 10$$

$$e^{\text{h/4}}_{\text{REL}}(\omega^{(0)}_X) = \frac{\|\mathsf{A}^{5;(1,0)}_{T_{h/8}}\psi_j^{X;1} - \mathsf{A}^{5;(1,0)}_{T_{h/4}}\psi_j^{X;1}\|_{\mathsf{U}(\omega^{(0)}_X)}}{\|\mathsf{A}^{5;(1,0)}_{T_{h/8}}\psi_j^{X;1}\|_{\mathsf{U}(\omega^{(0)}_X)}}, \qquad j = 1, ..., 10$$

in $\omega^{(0)}_X \bigcap \tilde{\omega}^{(1);1}_X$ where the handbook functions are used in the approximation. Figure 4.12 shows the maximum relative error of the ten handbook functions $\mathsf{A}^{5;(1,0)}_{T_{h/2}}\psi_j^{X;1}$ (resp. $\mathsf{A}^{5;(1,0)}_{T_{h/4}}\psi_j^{X;1}$), $j = 1, ..., 10$, for the 289 handbook problems shown with bars (resp. shown with solid black bars). We note that the average error is around 10% (resp. 1%), the error distribution is more or less uniform over the handbooks, and the biggest errors occur in the boundary handbooks. As we have seen from Figures 4.10 and 4.12 and Tables 4.5 and 4.6 when using the numerically constructed handbook functions with about 10% (resp. 1%) error we can achieve only 5% (resp. better than 1%) accuracy in the GFEM solution.

Table 4.6. p and p_{hb} convergence of the energy norm of the computed GFEM solution $u^{\text{GFEM}}_{\mathsf{A}^{5;(1,0)}_{T_{h/4}}}(\Delta_h, p, p_{\text{hb}})$ using the numerically constructed handbook functions $\mathsf{A}^{5;(1,0)}_{T_{h/4}}\psi_j^{X;1}$ for $\gamma = 1.0$ on the mesh with 16×16 elements. Here we used the solution for $p = 5$ and $p_{\text{hb}} = 5$ as overkill solution to compute the relative error for all the other entries in the Table. In this case there is no pollution of the accuracy of the GFEM solution due to the numerical construction of the handbook functions.

	$p_{\text{hb}} = 0$	$p_{\text{hb}} = 1$	$p_{\text{hb}} = 2$	$p_{\text{hb}} = 3$	$p_{\text{hb}} = 4$	$p_{\text{hb}} = 5$
$p = 1$	527.206120 (289) 47.03%	597.217498 (867) 2.66%	597.333781 (1381) 1.78%	597.395365 (1895) 1.05%	597.411471 (2409) 0.75%	597.418804 (2923) 0.56%
$p = 2$	531.284898 (1089) 45.73%	597.330451 (1667) 1.81%	597.361503 (2181) 1.49%	597.401769 (2695) 0.94%	597.414104 (3209) 0.69%	597.420222 (3723) 0.52%
$p = 3$	541.855531 (2401) 42.11%	597.393083 (2979) 1.09%	597.408376 (3493) 0.82%	597.416892 (4007) 0.62%	597.420647 (4521) 0.50%	597.423184 (5035) 0.41%
$p = 4$	558.050844 (4225) 35.70%	597.409219 (4803) 0.80%	597.419165 (5317) 0.55%	597.424210 (5831) 0.37%	597.425781 (6345) 0.29%	597.426591 (6859) 0.24%
$p = 5$	573.850349 (6561) 27.81%	597.417730 (7139) 0.59%	597.424005 (7653) 0.38%	597.426764 (8167) 0.22%	597.427723 (8681) 0.13%	597.428250 (9195)

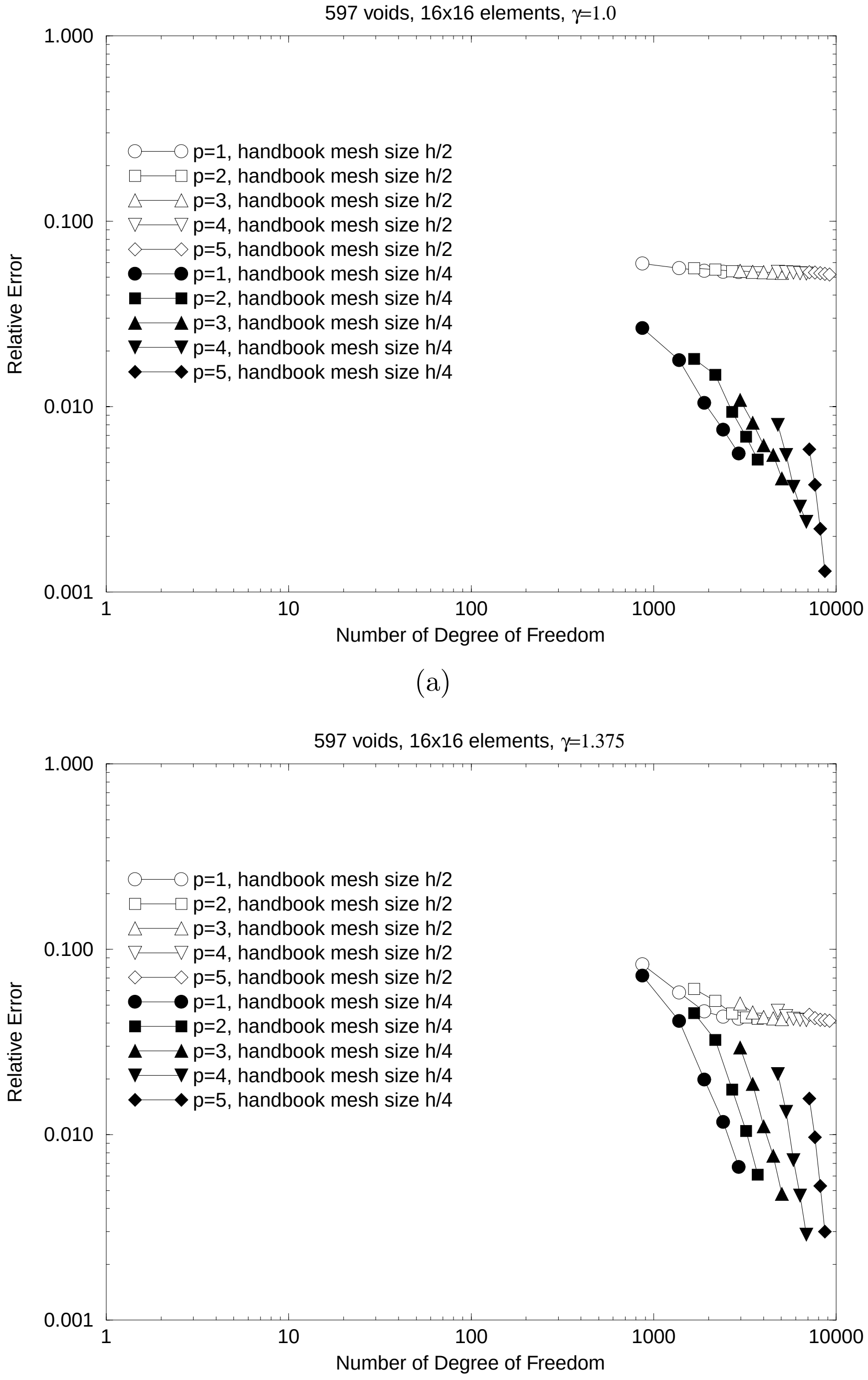

(a)

(b)

Figure 4.10. Comparison of the convergence of the computed GFEM solutions $u^{p;(p_{\mathrm{hb}},d)}_{\Delta_h;\mathsf{A}_{T_{h/2}}}$ by employing the numerical constructions $\mathsf{A}^{5;(1,0)}_{T_{h/2}}\psi^{X;1}_j$ and $\mathsf{A}^{5;(1,0)}_{T_{h/4}}\psi^{X;1}_j$ of the handbook functions $\psi^{X;1}_j$ for (a) $\gamma = 1.0$; (b) $\gamma = 1.375$. Note that, unless the handbook functions are constructed with sufficient accuracy the exponential convergence characteristics of the method are lost.

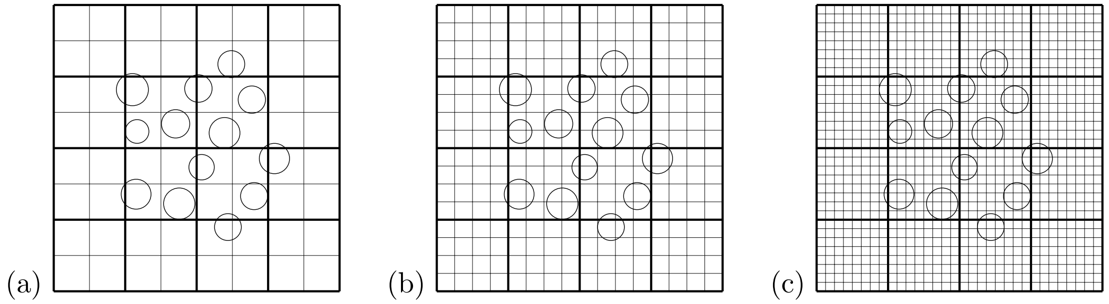

Figure 4.11. Meshes used for the handbook problem shown for a typical interior handbook, (a) $T_{h/2}$ with 8×8 elements, (b) $T_{h/4}$ with 16×16 elements, (c) $T_{h/8}$ with 32×32 elements. Squares with thicker lines are the elements of the global mesh Δ_h.

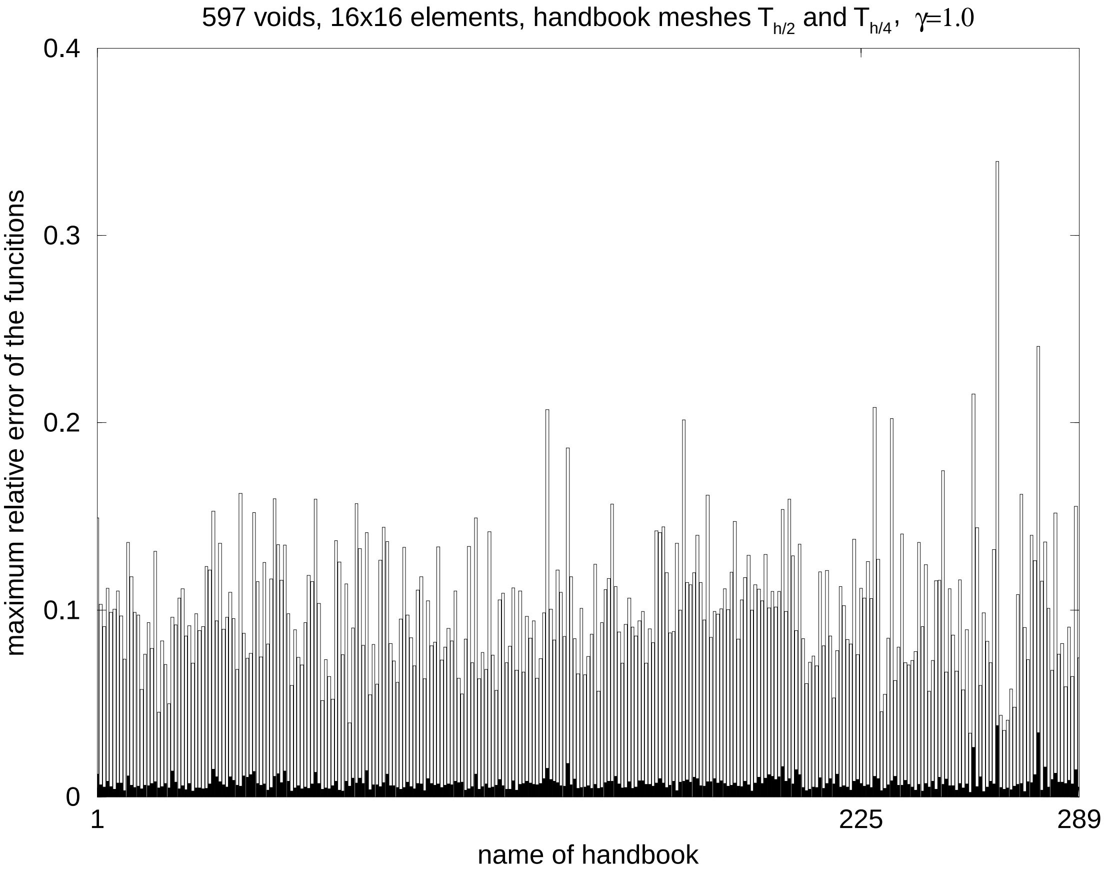

Figure 4.12. Maximum relative error in the numerical construction of the ten handbook functions $\mathsf{A}^{5;(1,0)}_{T_{h/2}}\psi^{X;1}_j$, $j = 1, ..., 10$, compared with the corresponding error in $\mathsf{A}^{5;(1,0)}_{T_{h/4}}\psi^{X;1}_j$ shown with black bars.

Let us look into the details of the error in the GFEM solution, $u_{\mathsf{A}}^{\mathrm{GFEM}}(\Delta_h, p, p_{\mathrm{hb}})$, where the subscript A underlines the dependence of the GFEM solution $u_{\mathsf{A}}^{\mathrm{GFEM}}(\Delta_h, p, p_{\mathrm{hb}})$ on the precise numerical construction of the handbook functions $\mathsf{A}_{T_{h/2^n}}^{p;(p_{\mathrm{hb}},d)}\psi_j^{X;1}$. We solved for the global GFEM solution, $u_{\mathsf{A}}^{\mathrm{GFEM}}(\Delta_h, p, p_{\mathrm{hb}})$, of the example problem using the numerical constructions: (1). $\mathsf{A}_{T_{h/2}}^{5;(1,0)}\psi_j^{X;1}$; (2). $\mathsf{A}_{T_{h/4}}^{5;(1,0)}\psi_j^{X;1}$; of the handbook functions $\psi_j^{X;1}$, and obtained the GFEM solutions $u_{\mathsf{A}_{T_{h/2}}^{5;(1,0)}}^{\mathrm{GFEM}}(\Delta_h, p, p_{\mathrm{hb}})$ and $u_{\mathsf{A}_{T_{h/4}}^{5;(1,0)}}^{\mathrm{GFEM}}(\Delta_h, p, p_{\mathrm{hb}})$, respectively. Figure 4.13 shows the relative modulus of the error of the gradient of $u_{\mathsf{A}_{T_{h/2}}^{5;(1,0)}}^{\mathrm{GFEM}}(\Delta_h, p = 5, p_{\mathrm{hb}} = 1)$ and $u_{\mathsf{A}_{T_{h/4}}^{5;(1,0)}}^{\mathrm{GFEM}}(\Delta_h, p = 5, p_{\mathrm{hb}} = 1)$, which for the solution $u_{\mathsf{A}_{T_{h/2}}^{5;(1,0)}}^{\mathrm{GFEM}}(\Delta_h, p = 5, p_{\mathrm{hb}} = 1)$, was computed by using the overkill solution u_{ov} obtained by using $p = 4$ and $p_{\mathrm{voids}} = 1$, $n_{\mathrm{layers}} = 0$, on the uniform overkill mesh with 64×64 elements (the energy norm is $\|u_{\mathrm{ov}}\|_{\mathsf{U}}$ $= 597.413841$ with the number of degree of freedom $N_{\mathrm{dof}} = 75498$), while the relative error of $u_{\mathsf{A}_{T_{h/4}}^{5;(1,0)}}^{\mathrm{GFEM}}(\Delta_h, p = 5, p_{\mathrm{hb}} = 1)$ was computed by using the GFEM solution $u_{\mathsf{A}_{T_{h/4}}^{5;(1,0)}}^{\mathrm{GFEM}}(\Delta_h, p = 5, p_{\mathrm{hb}} = 5)$ as the overkill solution ($\|u_{\mathsf{A}_{T_{h/4}}^{5;(1,0)}}^{\mathrm{GFEM}}(\Delta_h, p = 5, p_{\mathrm{hb}} = 5)\|_{\mathsf{U}} = 597.428250$ with the number of degree of freedom $N_{\mathrm{dof}} = 9195$). From Figure 4.13, it can be seen that the pointwise relative error in $u_{\mathsf{A}_{T_{h/4}}^{5;(1,0)}}^{\mathrm{GFEM}}(\Delta_h, p = 5, p_{\mathrm{hb}} = 1)$ is much reduced compared with the one in $u_{\mathsf{A}_{T_{h/2}}^{5;(1,0)}}^{\mathrm{GFEM}}(\Delta_h, p = 5, p_{\mathrm{hb}} = 1)$, and hence the error in the numerical construction of the handbook functions can play a very important role in the global GFEM solution. The above results indicate that *errors in the microscale can significantly pollute the accuracy of macroscale computations in multiscale analysis* (see e.g. [72]) especially when many scales are involved.

4.3 Effect of the local data and the buffer included in the handbooks

Above we described the convergence of the computed Generalized FEM solution $u_{\mathsf{A}}^{\mathrm{GFEM}}(\Delta_h,$ $p, p_{\mathrm{hb}})$ constructed as a bi-p FE solution enriched by the numerically constructed handbook functions $\mathsf{A}\psi_j^{X;d}$ pasted into the approximation by the Partition of Unity Method. We employed numerical constructions $\mathsf{A}_{T_{h/2^n}}^{p;(p_{\mathrm{hb}},d)}\psi_j^{X;1}$ of the handbook functions $\psi_j^{X;1}$, $j = 1, ..., n_{\mathrm{hb}}$, defined as the exact solutions of the Neumann problems (4.8)-(4.10) in the handbook domain $\tilde{\omega}_X^{(1);1}$ which is enclosed by $\partial\omega_X^{(1)}$ and includes only the voids intersecting the neighborhood $\omega_X^{(0)}$ of X, as shown in Figure 4.9 above. The voids included in $\tilde{\omega}_X^{(1);1}$ are the *local data* included in the handbook, while the region $\omega_X^{(1)} \backslash \omega_X^{(0)}$ is the *buffer* of the handbook domain. In [53] we also considered the handbooks $\tilde{\omega}_X^{(1);1/2}$ which we called *simple* handbooks. Here we will generalize further the definition of the handbooks and we will study its effect in the accuracy of the GFEM solution $u_{\mathsf{A}}^{\mathrm{GFEM}}(\Delta_h, p, p_{\mathrm{hb}})$.

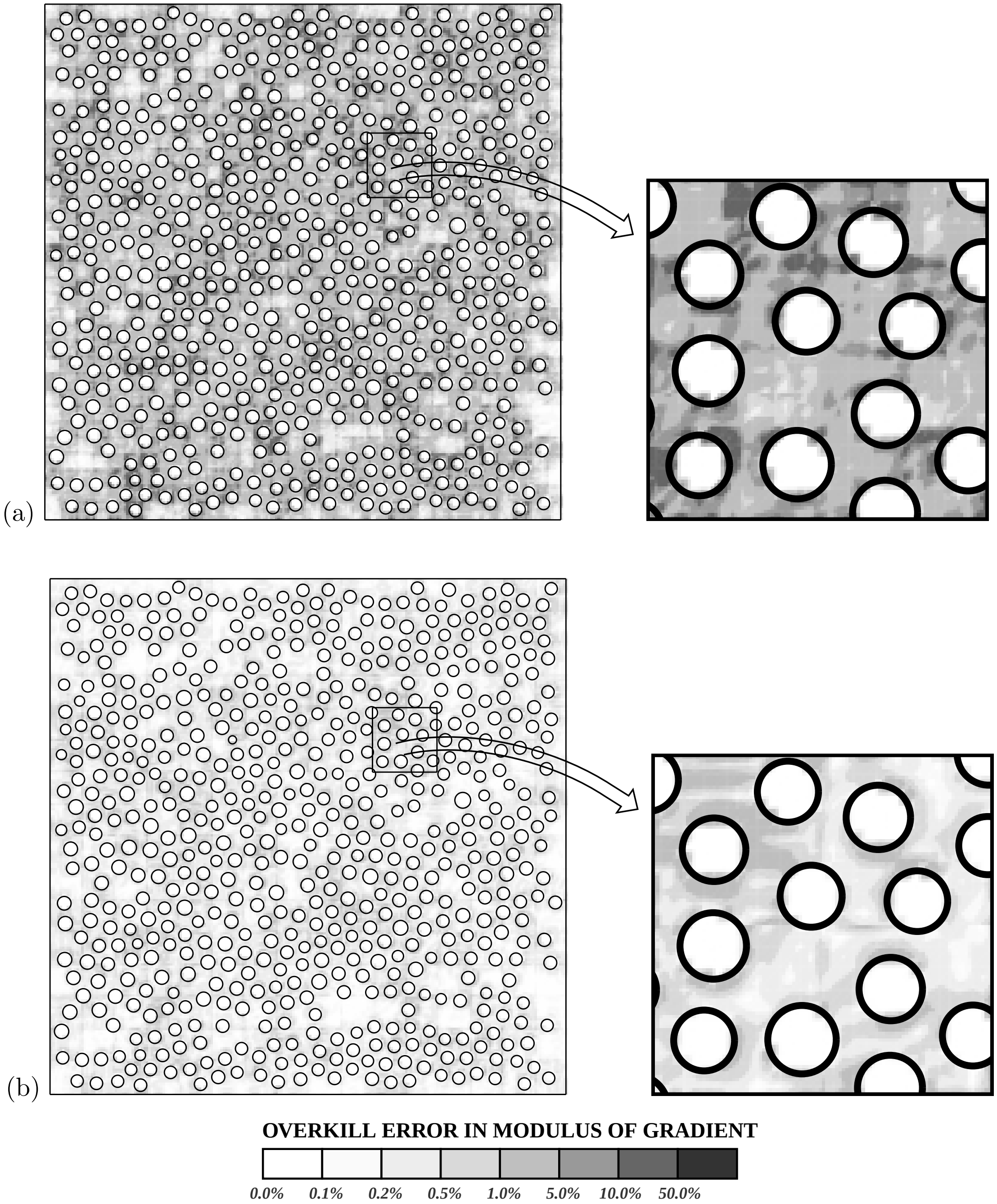

Figure 4.13. Relative modulus of the error of gradient of two GFEM solutions employing the numerically constructed handbook functions $\mathsf{A}^{5;(1,0)}_{T_{h/2}}\psi_j^{X;1}$ versus $\mathsf{A}^{5;(1,0)}_{T_{h/4}}\psi_j^{X;1}$ for the model problem (4.1) with $\gamma = 1.0$ on the mesh Δ_h with 16×16 elements. (a). $u^{\mathrm{GFEM}}_{\mathsf{A}^{5;(1,0)}_{T_{h/2}}}(\Delta_h, p = 5, p_{\mathrm{hb}} = 1)$; (b). $u^{\mathrm{GFEM}}_{\mathsf{A}^{5;(1,0)}_{T_{h/4}}}(\Delta_h, p = 5, p_{\mathrm{hb}} = 1)$. The difference between the two error is due to errors in the numerical construction of the handbook functions which is visible in (a).

Let us denote by $\tilde{\omega}_X^{(k);d}$, the region enclosed by the outer boundary of the k-layered mesh patch around X, which includes only the voids intersecting the patch $\omega_X^{(d-1)}$. We will employ $\tilde{\omega}_X^{(k);d}$ as the handbook domain associated with the vertex X, and we will write $\psi_j(\tilde{\omega}_X^{(k);d})$ to underline the dependence of the handbook functions ψ_j on the employed handbook domain $\tilde{\omega}_X^{(k);d}$. For the handbook functions $\psi_j^{X;1}$ employed in the previous sections, we have

$$\psi_j^{X;1} \equiv \psi_j(\tilde{\omega}_X^{(1);1}).$$

Below we will study the accuracy of the GFEM solution $u_{\mathsf{A}}^{\mathrm{GFEM}}(\Delta_h, p, p_{\mathrm{hb}})$ for the following choices of handbook domains which are illustrated in Figure 4.14;

a). $\tilde{\omega}_X^{(0);1}$: Handbook domain enclosed by $\partial\omega_X^{(0)}$ including all the voids in the interior of $\omega_X^{(0)}$. This handbook domain has no buffer.

b). $\tilde{\omega}_X^{(1);1}$: Handbook domain enclosed by $\partial\omega_X^{(1)}$ including all the voids intersecting $\omega_X^{(0)}$.

c). $\tilde{\omega}_X^{(1);2}$: Handbook domain enclosed by $\partial\omega_X^{(1)}$ including all voids in its interior.

d). $\tilde{\omega}_X^{(2);2}$: Handbook domain enclosed by $\partial\omega_X^{(2)}$ with all the voids intersecting $\omega_X^{(1)}$.

We will write $u_{\mathsf{A}}^{\mathrm{GFEM}}(\Delta_h, p, p_{\mathrm{hb}}; \tilde{\omega}_X^{(k);d})$ to underline the dependence of the GFEM solution on the choice of the handbook domains. Further in all the computations below we will employ the computed handbook functions $\mathsf{A}_{T_{h/4}}^{5;(1,0)}\psi_j(\tilde{\omega}_X^{(k);d})$ for which, as we have seen in previous sections, the effect of the numerical construction in the accuracy of the GFEM solution $u_{\mathsf{A}}^{\mathrm{GFEM}}(\Delta_h, p, p_{\mathrm{hb}}; \tilde{\omega}_X^{(k);d})$ for p, $p_{\mathrm{hb}} = 1,...,5$, is negligible and hence we can omit the dependence on A.

Tables 4.7-4.9 report the energy norm of the GFEM solution employing the $\tilde{\omega}_X^{(0);1}$ handbook functions for $\gamma = 1.375$, on three meshes Δ_h, Mesh I (4×4 mesh), Mesh II (8×8 mesh) and Mesh III (16×16 mesh), respectively. Figures 4.15 and 4.16 show the p_{hb} convergence of the GFEM solution $u^{\mathrm{GFEM}}(\Delta_h, p, p_{\mathrm{hb}}; \tilde{\omega}_X^{(0);1})$ for $\gamma = 1.0$, 1.125, 1.25 and 1.375, respectively. We see that the error is increasing with increasing γ as the voids get closer together. However the character of the convergence is independent of γ. Comparing these Tables and Figures with the ones given above and in [53] for $\tilde{\omega}_X^{(1);1}$, we see that the accuracy of the method is rather poor when $\tilde{\omega}_X^{(0);1}$ is employed as the handbook domain, and we always have

$$\|u_{\mathrm{EX}} - u^{\mathrm{GFEM}}(\Delta_h, p, p_{\mathrm{hb}}; \tilde{\omega}_X^{(1);1})\|_{\mathsf{U}} < \|u_{\mathrm{EX}} - u^{\mathrm{GFEM}}(\Delta_h, p, p_{\mathrm{hb}}; \tilde{\omega}_X^{(0);1})\|_{\mathsf{U}}.$$

Another point is that for the GFEM solution which uses $\omega_X^{(0);1}$ handbooks the error is increasing as the mesh is refined! This is because as the mesh is refined the number of voids included in the handbooks $\tilde{\omega}_X^{(0);1}$ is drastically reduced since we omit any voids intersecting the boundary of $\omega_X^{(0)}$. Also, in contrast with the GFEM solution which employs $\tilde{\omega}_X^{(1);1}$ handbooks for which as we have seen above we get exponential convergence, we do not get exponential convergence when using the $\tilde{\omega}_X^{(0);1}$ handbooks!

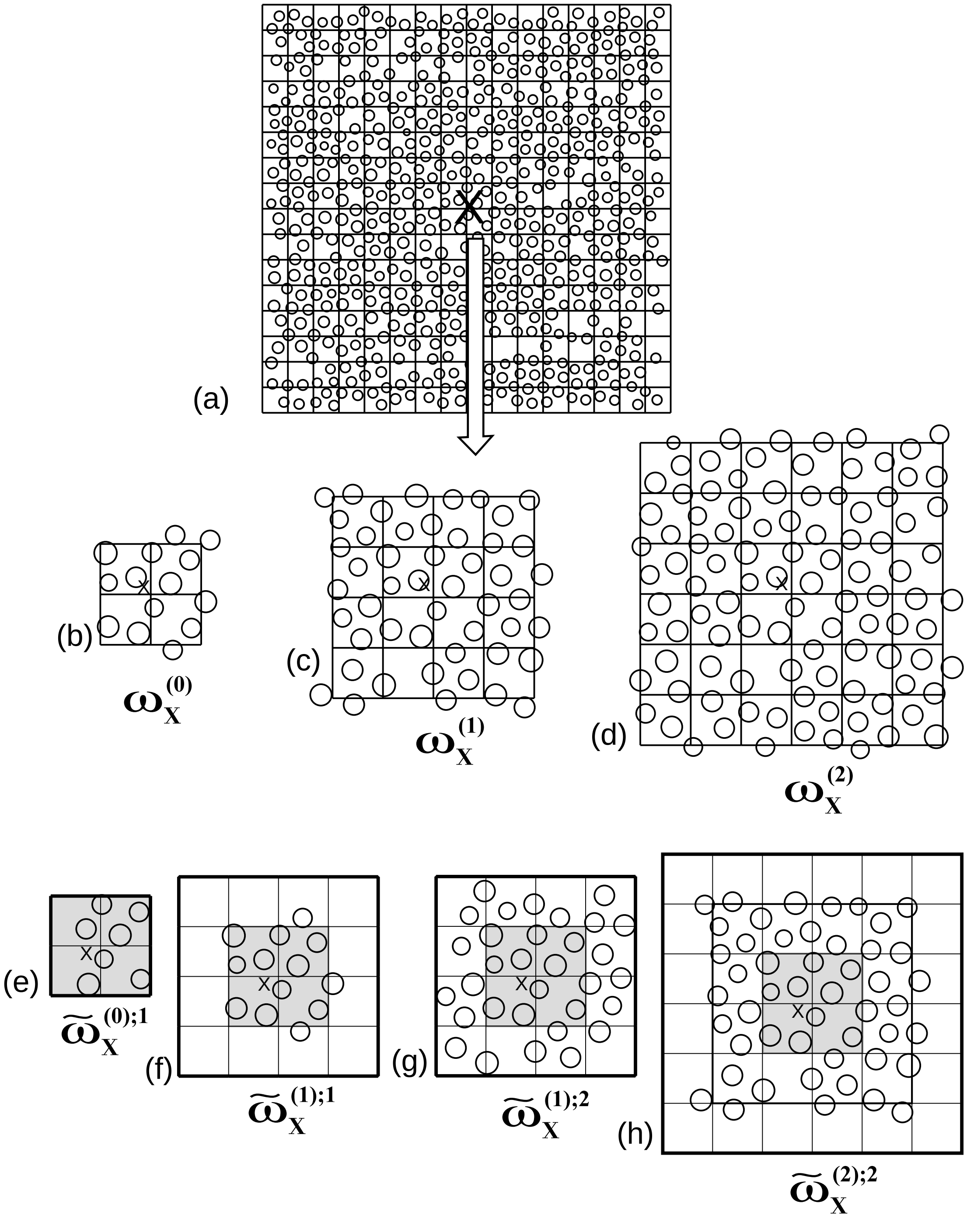

Figure 4.14. Four choices for the handbook domains associated with a vertex X. (a) The problem domain Ω covered by the 16×16 mesh Δ_h; (b)-(d) The neighborhoods $\omega_X^{(0)}$, $\omega_X^{(1)}$ and $\omega_X^{(2)}$ with voids intersecting them; (e)-(h) The handbook domains $\tilde{\omega}_X^{(0);1}$, $\tilde{\omega}_X^{(1);1}$, $\tilde{\omega}_X^{(1);2}$ and $\tilde{\omega}_X^{(2);2}$. The shaded area is the "useful" region of the handbooks, i.e. the region where the handbook functions are used in the computation of the GFEM solution.

Table 4.7. p and p_{hb} convergence of the energy norm of the solution of the model problem on the 4×4 mesh for $\gamma = 1.375$ using the $\tilde{\omega}_X^{(0);1}$ mesh-based handbook functions. Here we used the GFEM solution on 64×64 mesh with $p = 4$ and $p_{\text{voids}} = 1$ as the overkill solution for computing the relative error.

	$p_{\text{hb}} = 1$	$p_{\text{hb}} = 2$	$p_{\text{hb}} = 3$	$p_{\text{hb}} = 4$	$p_{\text{hb}} = 5$
$p = 1$	869.445297 (75) 5.39%	869.731126 (109) 4.75%	869.856635 (143) 4.43%	870.007459 (177) 4.02%	870.069299 (211) 3.84%
$p = 2$	869.719094 (131) 4.77%	869.833737 (165) 4.49%	869.937975 (199) 4.22%	870.047746 (233) 3.91%	870.110426 (267) 3.72%
$p = 3$	869.914637 (219) 4.28%	870.000204 (253) 4.04%	870.079070 (287) 3.81%	870.138277 (321) 3.63%	870.176895 (355) 3.51%
$p = 4$	870.006606 (339) 4.02%	870.085126 (373) 3.79%	870.149946 (407) 3.59%	870.200931 (441) 3.43%	870.240250 (475) 3.29%
$p = 5$	870.098715 (491) 3.75%	870.181332 (525) 3.49%	870.239347 (559) 3.30%	870.285171 (593) 3.13%	870.314502 (627) 3.02%

Table 4.8. p and p_{hb} convergence of the energy norm of the solution of the model problem on the 8×8 mesh for $\gamma = 1.375$ using the $\tilde{\omega}_X^{(0);1}$ mesh-based handbook functions. Here we used the GFEM solution on 64×64 mesh with $p = 4$ and $p_{\text{voids}} = 1$ as the overkill solution for computing the relative error.

	$p_{\text{hb}} = 1$	$p_{\text{hb}} = 2$	$p_{\text{hb}} = 3$	$p_{\text{hb}} = 4$	$p_{\text{hb}} = 5$
$p = 1$	864.640258 (243) 11.79%	866.231728 (373) 10.13%	867.087801 (503) 9.11%	867.556158 (633) 8.51%	867.920672 (763) 8.00%
$p = 2$	865.963175 (451) 10.43%	866.897018 (581) 9.35%	867.538498 (711) 8.53%	867.912262 (841) 8.01%	868.219004 (971) 7.56%
$p = 3$	867.049725 (787) 9.16%	867.816599 (917) 8.15%	868.229485 (1047) 7.55%	868.489999 (1177) 7.14%	868.803327 (1307) 6.62%
$p = 4$	867.645157 (1251) 8.39%	868.331152 (1381) 7.39%	868.704469 (1511) 6.79%	868.920751 (1641) 6.41%	869.183193 (1771) 5.92%
$p = 5$	868.322918 (1843) 7.40%	868.922825 (1973) 6.41%	869.220537 (2103) 5.85%	869.381863 (2233) 5.53%	869.561721 (2363) 5.14%

Table 4.9. p and p_{hb} convergence of the energy norm of the solution of the model problem on the 16×16 mesh for $\gamma = 1.375$ using the $\tilde{\omega}_X^{(0);1}$ mesh-based handbook functions. Here we used the GFEM solution on 64×64 mesh with $p = 4$ and $p_{\mathrm{voids}} = 1$ as the overkill solution for computing the relative error.

	$p_{\mathrm{hb}} = 1$	$p_{\mathrm{hb}} = 2$	$p_{\mathrm{hb}} = 3$	$p_{\mathrm{hb}} = 4$	$p_{\mathrm{hb}} = 5$
$p = 1$	847.677749 (863) 22.85%	853.815010 (1375) 19.61%	858.642683 (1887) 16.59%	860.996417 (2399) 14.90%	862.569177 (2911) 13.64%
$p = 2$	854.346453 (1663) 19.30%	858.028061 (2175) 17.01%	861.690961 (2687) 14.36%	863.413011 (3199) 12.92%	864.720878 (3711) 11.71%
$p = 3$	861.260374 (2975) 14.69%	863.452970 (3487) 12.89%	864.930626 (3999) 11.50%	866.113364 (4511) 10.26%	867.171386 (5023) 9.01%
$p = 4$	864.921996 (4799) 11.51%	866.339432 (5311) 10.01%	867.340953 (5823) 8.79%	868.076988 (6335) 7.77%	868.665387 (6847) 6.85%
$p = 5$	867.325832 (7135) 8.81%	868.163567 (7647) 7.65%	868.711882 (8159) 6.77%	869.157084 (8671) 5.97%	869.531566 (9183) 5.21%

Let us now employ the $\tilde{\omega}_X^{(1);2}$ handbooks. These handbooks are obtained from the $\tilde{\omega}_X^{(1);1}$ handbooks by including all the voids in the buffer which do not intersect the handbook boundary. Table 4.10 reports the energy norm of the GFEM solution $u^{\mathrm{GFEM}}(\Delta_h, p, p_{\mathrm{hb}}; \tilde{\omega}_X^{(1);2})$ and its relative error, together with the number of degree of freedom, for $\gamma = 1.375$, on Mesh III (the 16×16 mesh). Figures 4.17 and 4.18 give the convergence graphs of the GFEM solution $u^{\mathrm{GFEM}}(\Delta_h, p, p_{\mathrm{hb}}; \tilde{\omega}_X^{(1);2})$ for $\gamma = 1.0$, 1.125, 1.25 and 1.375. We see that higher accuracy is obtained, in comparison with the GFEM solution which uses the handbooks $\tilde{\omega}_X^{(1);1}$, namely

$$\|u_{\mathrm{EX}} - u^{\mathrm{GFEM}}(\Delta_h, p, p_{\mathrm{hb}}; \tilde{\omega}_X^{(1);2})\|_{\mathsf{U}} < \|u_{\mathrm{EX}} - u^{\mathrm{GFEM}}(\Delta_h, p, p_{\mathrm{hb}}; \tilde{\omega}_X^{(1);1})\|_{\mathsf{U}}.$$

and that the character of the convergence does not depend on γ.

Further, Table 4.11 reports the results for the error in $u^{\mathrm{GFEM}}(\Delta_h, p, p_{\mathrm{hb}}; \tilde{\omega}_X^{(2);2})$ on Mesh III (the 16×16 mesh), for $\gamma = 1.375$, while Figures 4.19 and 4.20 give the convergence graphs for $\gamma = 1.0$, 1.125, 1.25, and 1.375. Once more, we see that the accuracy of global GFEM solution is increased by including more data in the handbook and by adding a buffer, namely

$$\|u_{\mathrm{EX}} - u^{\mathrm{GFEM}}(\Delta_h, p, p_{\mathrm{hb}}; \tilde{\omega}_X^{(2);2})\|_{\mathsf{U}} < \|u_{\mathrm{EX}} - u^{\mathrm{GFEM}}(\Delta_h, p, p_{\mathrm{hb}}; \tilde{\omega}_X^{(1);2})\|_{\mathsf{U}}.$$

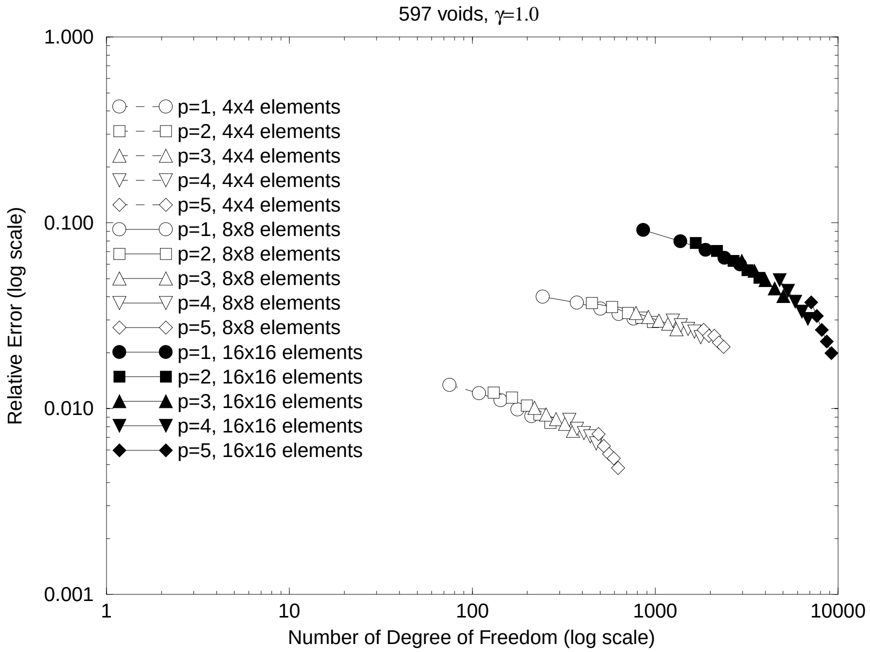

(a)

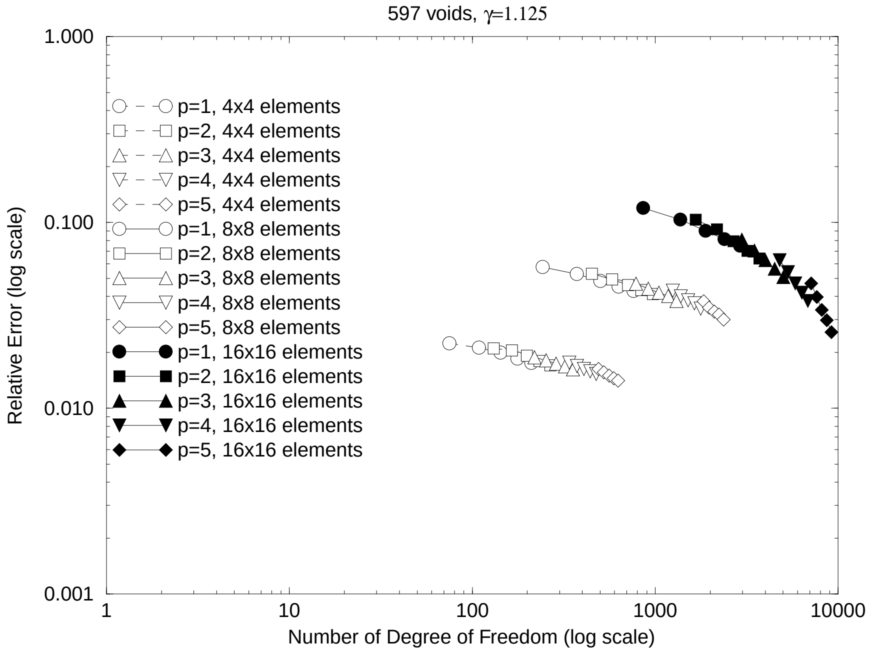

(b)

Figure 4.15. Convergence of the GFEM solution of the model problem using the *zero layer handbooks without buffer* $\tilde{\omega}_X^{(0);1}$ for: (a) $\gamma = 1.0$, and (b) $\gamma = 1.125$. Note the slow convergence of the GFEM solution for this choice of handbooks, and that the character of the error convergence is independent of γ.

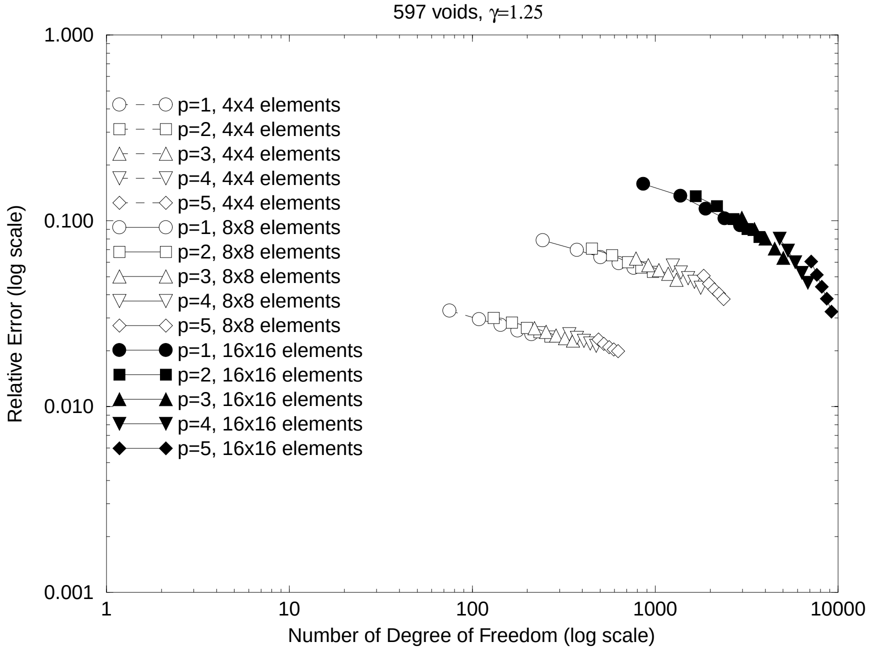

(a)

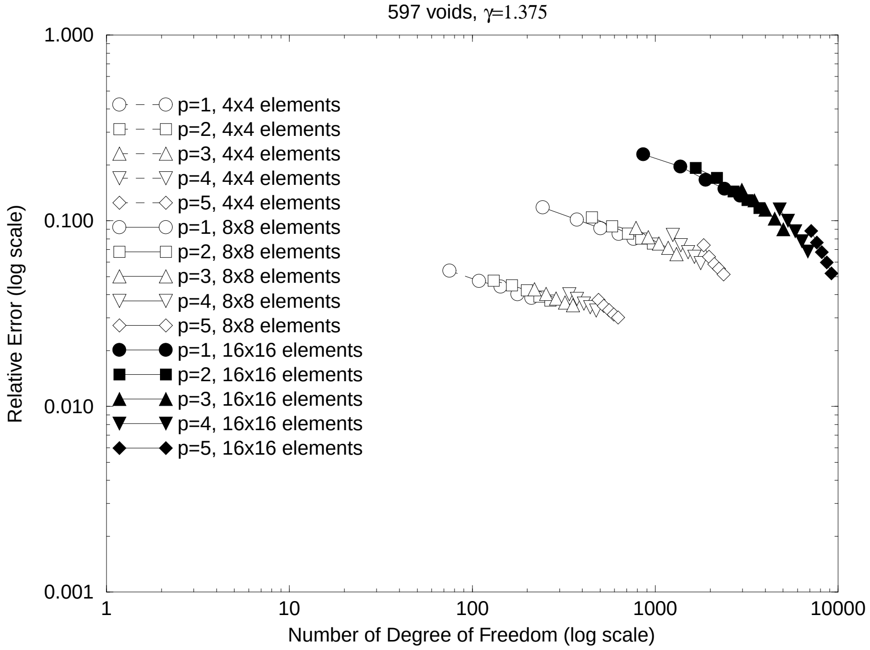

(b)

Figure 4.16. Convergence of the GFEM solution of the model problem using the *zero layer handbooks without buffer* $\tilde{\omega}_X^{(0);1}$ for: (a) $\gamma = 1.25$, and (b) $\gamma = 1.375$. Note the slow convergence of the GFEM solution for this choice of handbooks, and that the character of the error convergence is independent of γ.

Table 4.10. p and p_{hb} convergence of the energy norm of the solution of the model problem on the 16×16 mesh for $\gamma = 1.375$ using the $\tilde{\omega}_X^{(1);2}$ mesh-based handbook functions. The numbers in bracket are the number of degree of freedom, and the percentage numbers are the relative error of the solution. Here the solution for $p = 5$ and $p_{\mathrm{hb}} = 5$ is used as overkill solution in the computation of the relative error.

	$p_{\mathrm{hb}} = 1$	$p_{\mathrm{hb}} = 2$	$p_{\mathrm{hb}} = 3$	$p_{\mathrm{hb}} = 4$	$p_{\mathrm{hb}} = 5$
$p = 1$	868.666825 (867) 6.88%	870.026857 (1381) 4.01%	870.558593 (1895) 1.98%	870.669621 (2409) 1.17%	870.709427 (2923) 0.67%
$p = 2$	869.890855 (1667) 4.39%	870.287721 (2181) 3.18%	870.596562 (2695) 1.74%	870.681445 (3209) 1.04%	870.712907 (3723) 0.61%
$p = 3$	870.373079 (2979) 2.86%	870.579818 (3493) 1.85%	870.675105 (4007) 1.11%	870.703684 (4521) 0.76%	870.719011 (5035) 0.48%
$p = 4$	870.542634 (4803) 2.07%	870.654283 (5317) 1.31%	870.705965 (5831) 0.73%	870.719285 (6345) 0.47%	870.725505 (6859) 0.28%
$p = 5$	870.628589 (7139) 1.52%	870.689089 (7653) 0.96%	870.716831 (8167) 0.53%	870.725057 (8681) 0.30%	870.728930 (9195)

Table 4.11. p and p_{hb} convergence of the energy norm of the solution of the model problem on the 16×16 mesh for $\gamma = 1.375$ using the $\tilde{\omega}_X^{(2);2}$ mesh-based handbook functions. The numbers in bracket are the number of degree of freedom, and the percentage numbers are the relative error of the solution. Here we used the $p = 5$ and $p_{\text{hb}} = 5$ GFEM solution as overkill solution in the computation of the relative error.

	$p_{\text{hb}} = 1$	$p_{\text{hb}} = 2$	$p_{\text{hb}} = 3$	$p_{\text{hb}} = 4$	$p_{\text{hb}} = 5$
$p = 1$	870.424322 (867) 2.45%	870.581830 (1381) 1.55%	870.651943 (1895) 0.89%	870.672775 (2409) 0.56%	870.681094 (2923) 0.35%
$p = 2$	870.565006 (1667) 1.67%	870.615097 (2181) 1.28%	870.660615 (2695) 0.77%	870.676397 (3209) 0.48%	870.681686 (3723) 0.33%
$p = 3$	870.624776 (2979) 1.19%	870.654973 (3493) 0.85%	870.669148 (4007) 0.63%	870.678378 (4521) 0.43%	870.682243 (5035) 0.31%
$p = 4$	870.650375 (4803) 0.91%	870.668034 (5317) 0.65%	870.677999 (5831) 0.44%	870.682243 (6345) 0.31%	870.684507 (6859) 0.21%
$p = 5$	870.664481 (7139) 0.71%	870.674198 (7653) 0.53%	870.679805 (8167) 0.39%	870.684124 (8681) 0.23%	870.686427 (9195)

Figures 4.21 and 4.22 compare the convergence of the GFEM solution $u^{\text{GFEM}}(\Delta_h, p, p_{\text{hb}}; \tilde{\omega}_X^{(k);d})$ for the four choices of the handbook domains: $\tilde{\omega}_X^{(0);1}$, $\tilde{\omega}_X^{(1);1}$, $\tilde{\omega}_X^{(1);2}$, and $\tilde{\omega}_X^{(2);2}$, for the case $\gamma = 1.0$. We see that the method achieves high accuracy through exponential convergence except for the GFEM solution $u^{\text{GFEM}}(\Delta_h, p, p_{\text{hb}}; \tilde{\omega}_X^{(0);1})$ which employs the $\tilde{\omega}_X^{(0);1}$ handbooks, namely the zero layer handbooks which has no buffer. In general we should expect that the accuracy of the GFEM solution $u^{\text{GFEM}}(\Delta_h, p, p_{\text{hb}}; \tilde{\omega}_X^{(k);d})$ increases as k and d are increased.

Let us also illustrate the influence of the choice of handbook on the pointwise accuracy. Figures 4.23 and 4.24 show the pointwise modulus of the error gradient of the GFEM solution $u^{\text{GFEM}}(\Delta_h, p, p_{\text{hb}}; \tilde{\omega}_X^{(k);d})$ for $p = 5$ and $p_{\text{hb}} = 1$ with the four choices of handbooks: $\tilde{\omega}_X^{(0);1}$, $\tilde{\omega}_X^{(1);1}$, $\tilde{\omega}_X^{(1);2}$ and $\tilde{\omega}_X^{(2);2}$. We note that the pointwise accuracy of the GFEM solution $u^{\text{GFEM}}(\Delta_h, p, p_{\text{hb}}; \tilde{\omega}_X^{(k);d})$ is also increased as the handbook domain $\tilde{\omega}_X^{(k);d}$ includes more data and also includes a buffer zone.

Let us explain the above results. Recall the Theorem 2.1 from [53], we have the following estimate

$$\|\nabla(u_{\text{EX}} - u^{\text{GFEM}}(\Delta_h, p, p_{\text{hb}}; \tilde{\omega}_X^{(k);d}))\|_{L^2(\Omega)} \leq \sqrt{2}M \max_i \left(\frac{C_G \epsilon_1}{\text{diam}(\Omega \bigcap \Omega_i^h)} + C_\infty \epsilon_2 \right) \|u\|_{H^k(\Omega)},$$

where ϵ_1 and ϵ_2 are the local approximation error in L^2 and H^1 norm, respectively, i.e.

$$\epsilon_i = \min_{\alpha_j^{(i)}} \|u_{\text{EX}} - \sum_{i,j} \alpha_j^{(i)} \psi_j^{X;d}(\tilde{\omega}_X^{(k);d})\|_{H_i},$$

where $H_1 = L^2(\omega_X^{(0)})$, and $H_2 = H^1(\omega_X^{(0)})$. As we increase the number of layers k and the data included in the handbooks $\tilde{\omega}_X^{(k);d}$ by increasing d, the magnitudes of ϵ_1 and ϵ_2 decrease because of the better approximability of u_{EX} by the set of employed handbook functions $\psi_j(\tilde{\omega}_X^{(k);d})$ in the vertex patch $\omega_X(0)$ and hence the accuracy of the GFEM solution $u^{\text{GFEM}}(\Delta_h, p, p_{\text{hb}}; \tilde{\omega}_X^{(k);d})$ also improves.

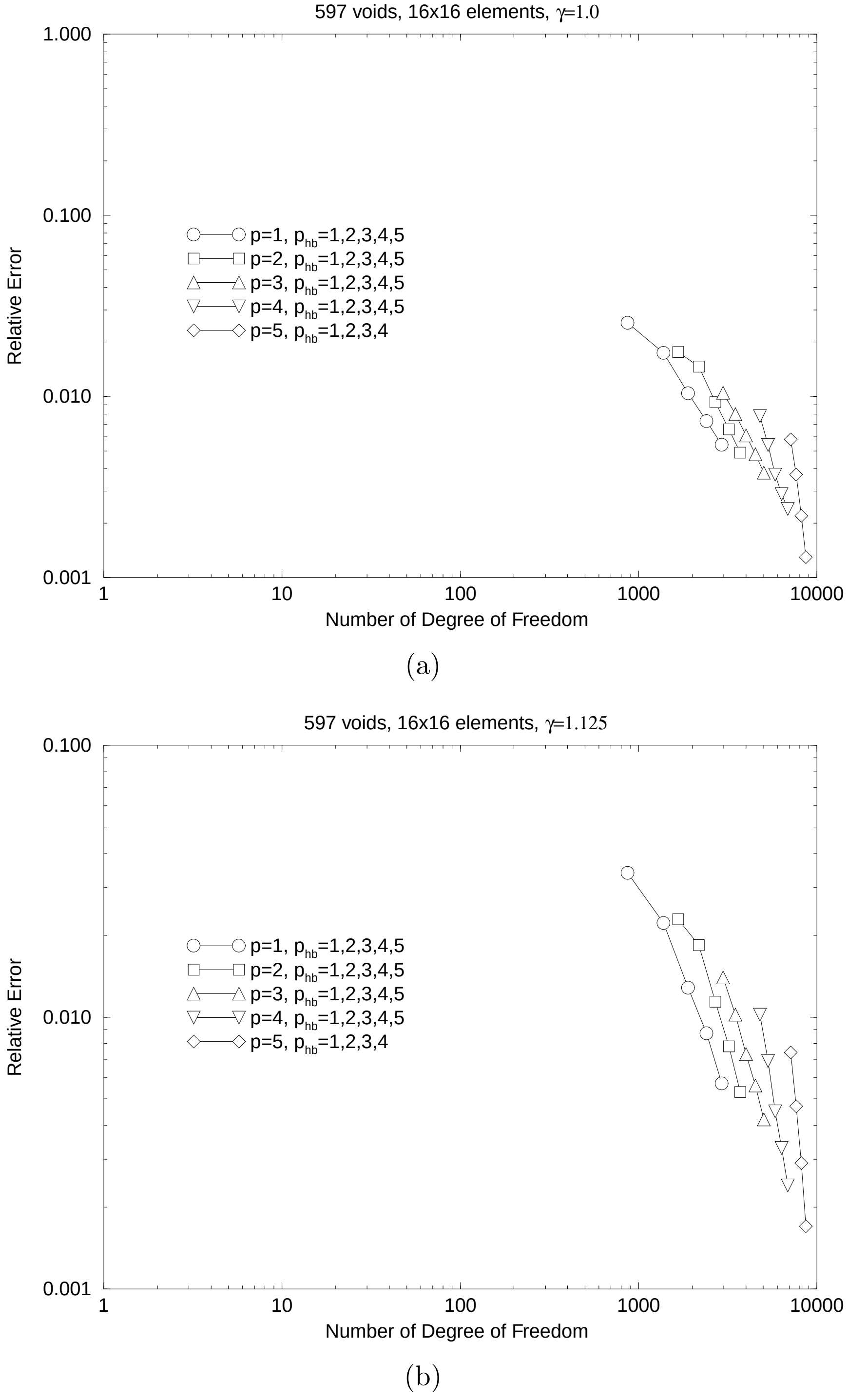

Figure 4.17. Convergence of the GFEM solution of the model problem using the two-layer handbooks without buffer $\tilde{\omega}_X^{(1);2}$ for: (a) $\gamma = 1.0$, and (b) $\gamma = 1.125$. Note the dramatic improvement in the convergence in comparison with Figure 4.15, and that the character of the error convergence is independent of γ.

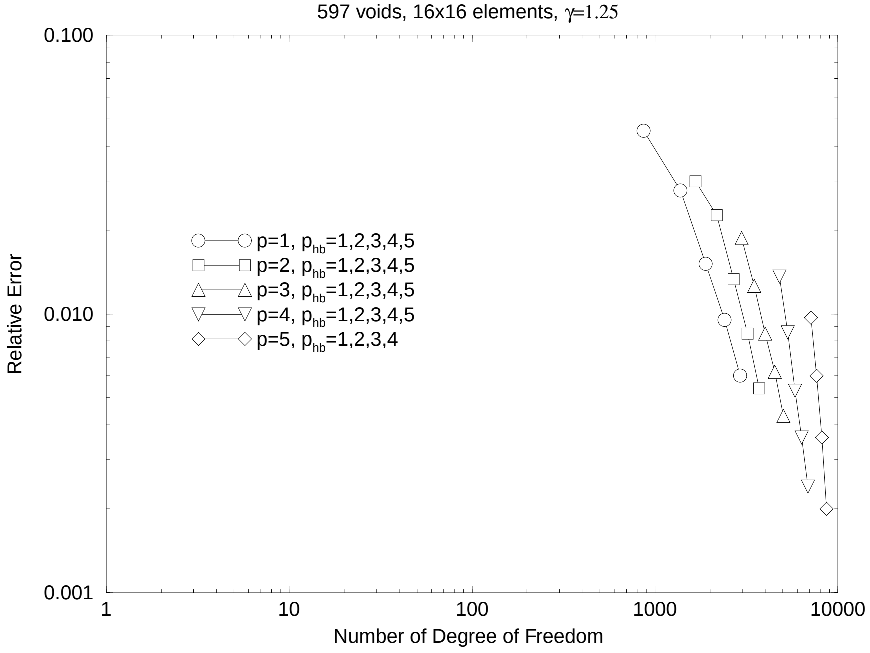

(a)

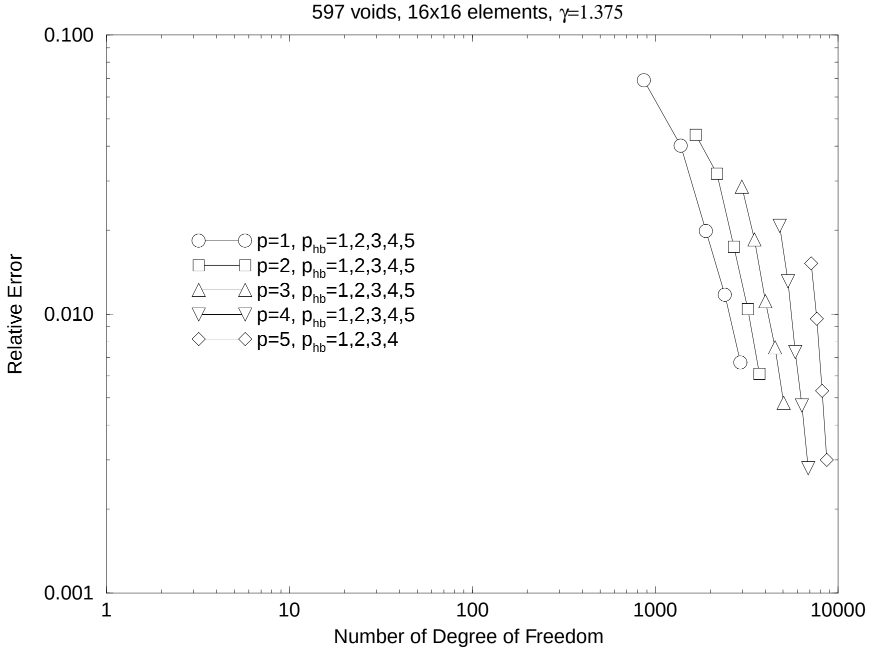

(b)

Figure 4.18. Convergence of the GFEM solution of the model problem using the two-layer handbooks without buffer $\tilde{\omega}_X^{(1);2}$ for: (a) $\gamma = 1.25$, and (b) $\gamma = 1.375$. Note the dramatic improvement in the convergence in comparison with Figure 4.16, and that the character of the error convergence is independent of γ.

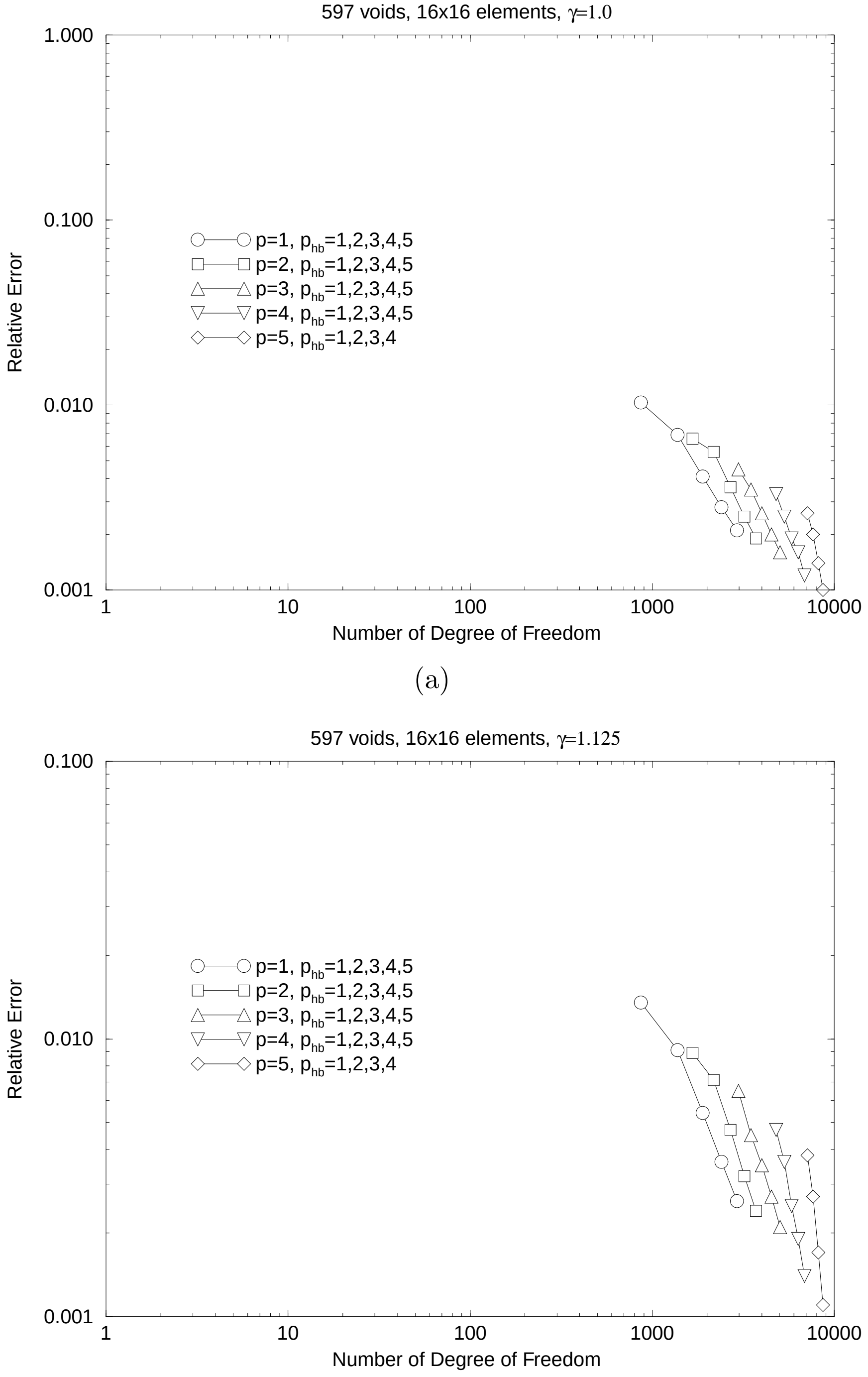

(a)

(b)

Figure 4.19. Convergence of the GFEM solution of the model problem using the two-layer handbooks with buffer $\tilde{\omega}_X^{(2);2}$ for: (a) $\gamma = 1.0$, and (b) $\gamma = 1.125$, and that the character of the error convergence is independent of γ.

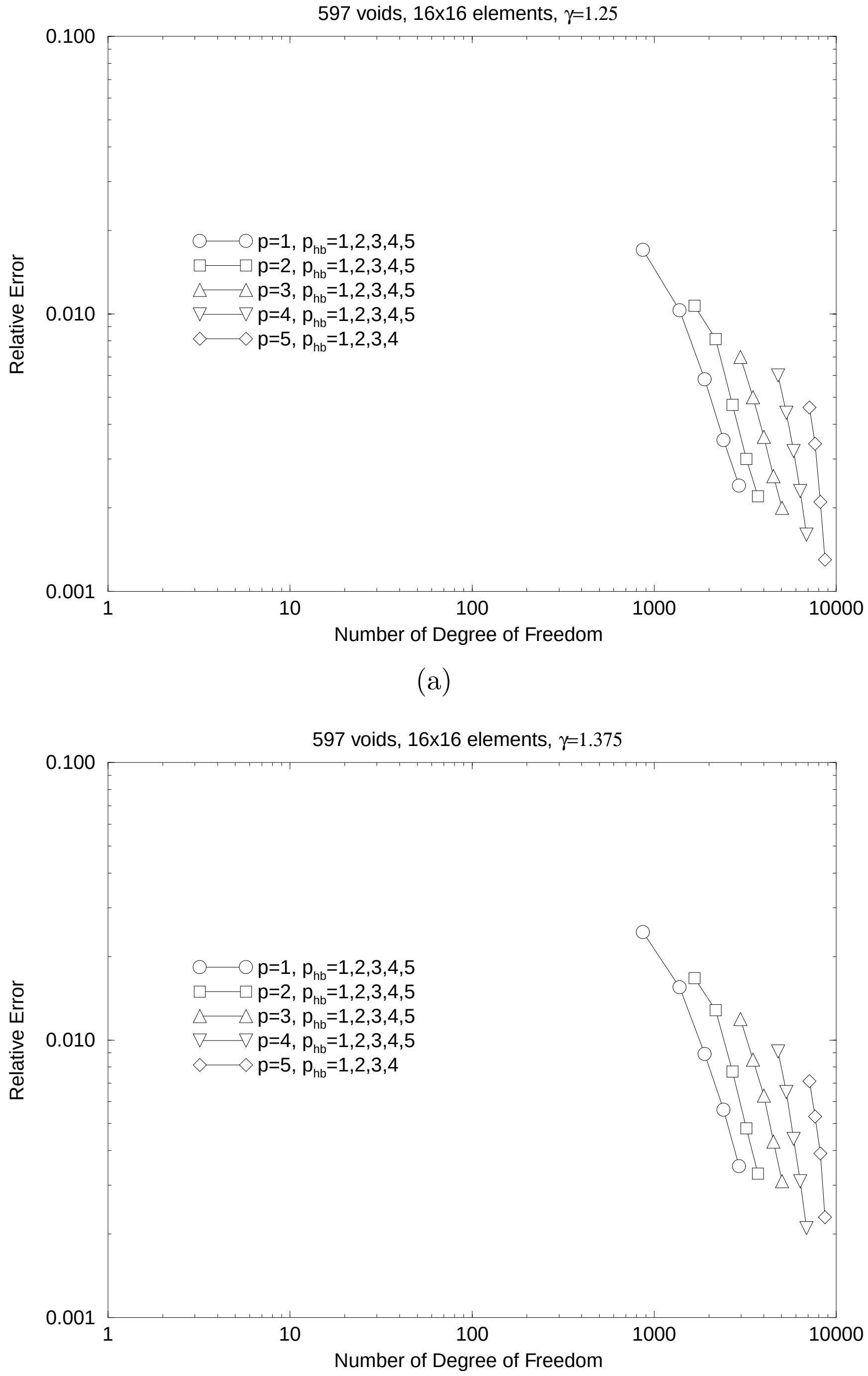

(a)

(b)

Figure 4.20. Convergence of the GFEM solution of the model problem using the two-layer handbooks with buffer $\tilde{\omega}_X^{(2);2}$ for: (a) $\gamma = 1.25$, and (b) $\gamma = 1.375$, and that the character of the error convergence is independent of γ.

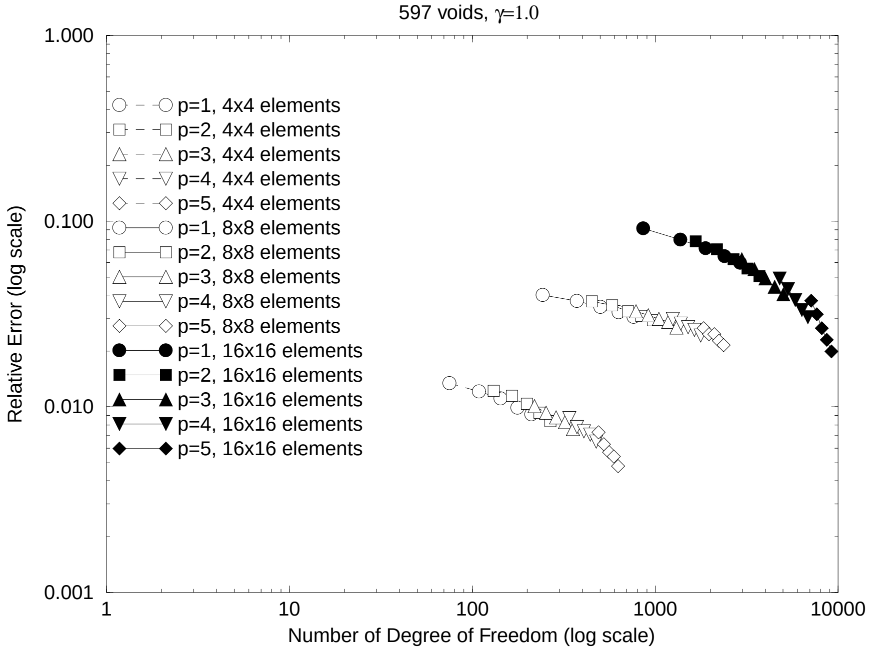

(a)

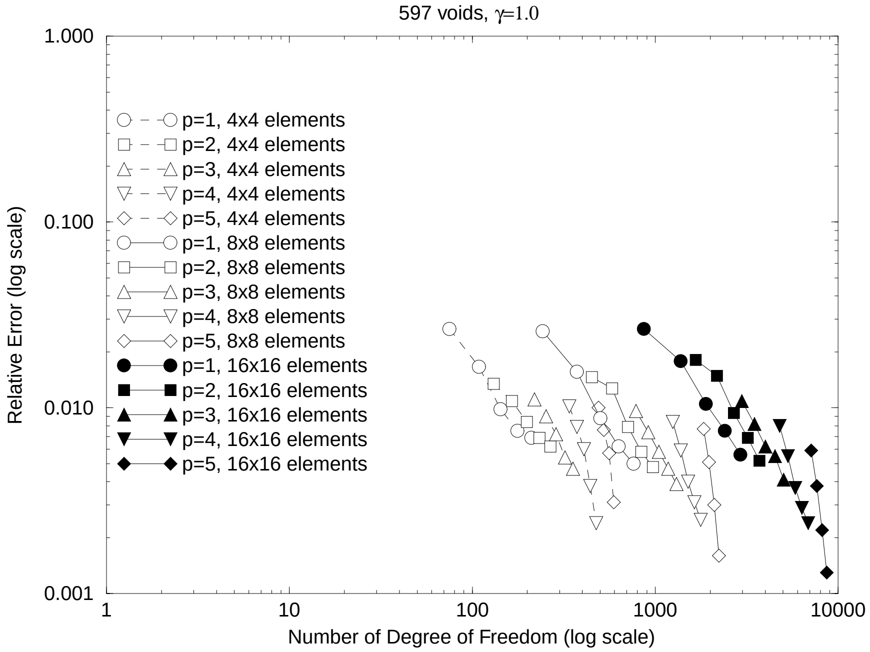

(b)

Figure 4.21. Comparison of the convergence of the GFEM solution of the model problem elements using the handbooks: (a) $\tilde{\omega}_X^{(0);1}$, and (b) $\tilde{\omega}_X^{(1);1}$, for $\gamma = 1.0$. Note that, except for the case of the $\tilde{\omega}_X^{(0);1}$, we get exponential convergence, and the accuracy improves as the amount of local data included in the handbooks is increased.

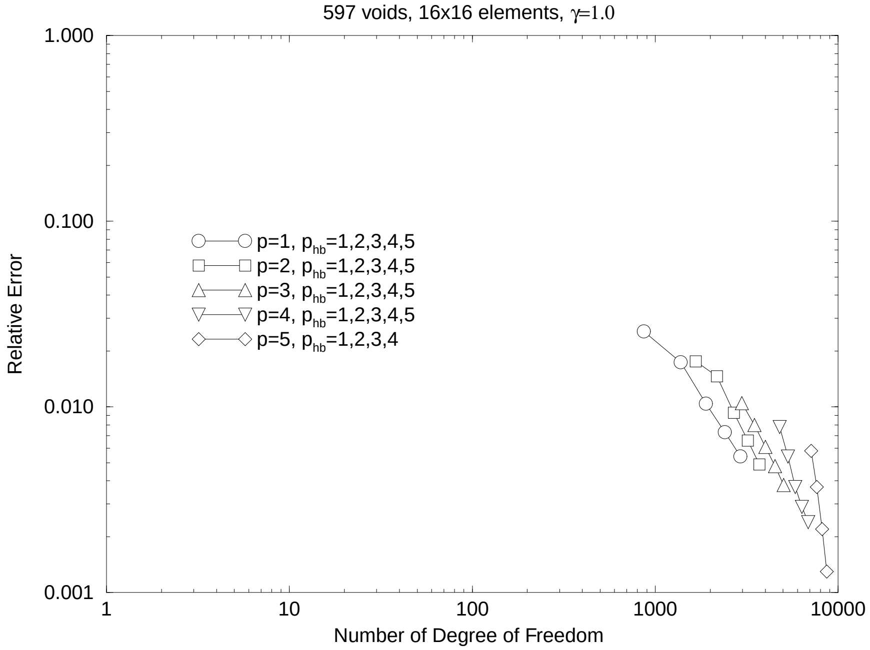

(a)

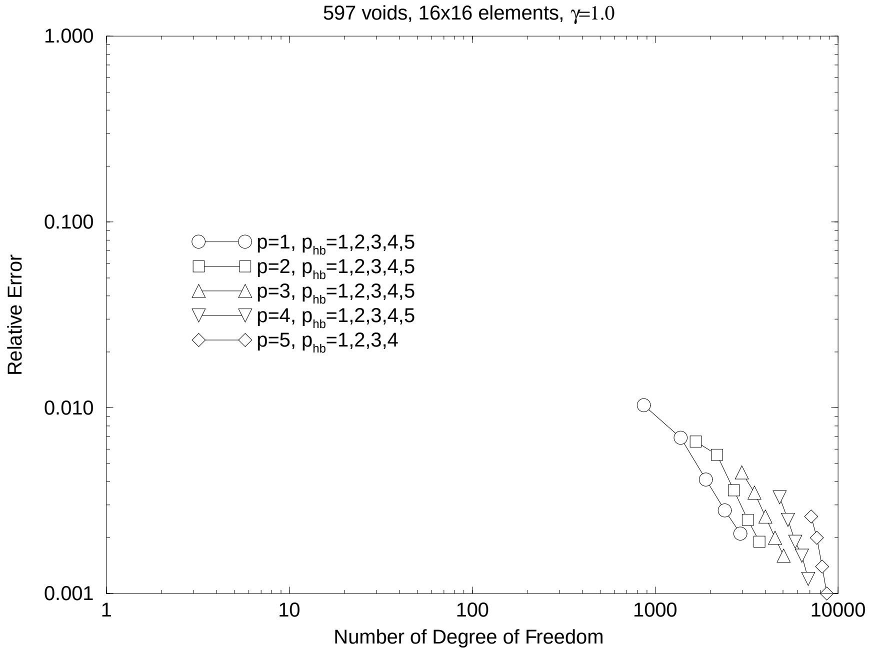

(b)

Figure 4.22. Comparison of the convergence of the GFEM solution of the model problem elements using the handbooks: (a) $\tilde{\omega}_X^{(1);2}$, and (b) $\tilde{\omega}_X^{(2);2}$, for $\gamma = 1.0$. Note that, except for the case of the $\tilde{\omega}_X^{(0);1}$, we get exponential convergence, and the accuracy improves as the amount of local data included in the handbooks is increased.

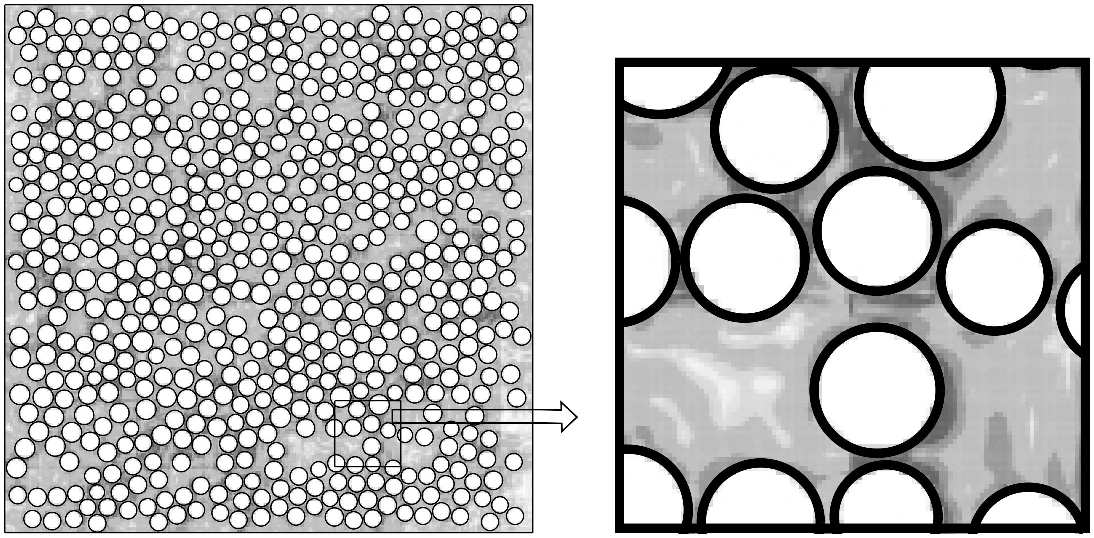

(a) Handbook $\tilde{\omega}_X^{(0);1}$

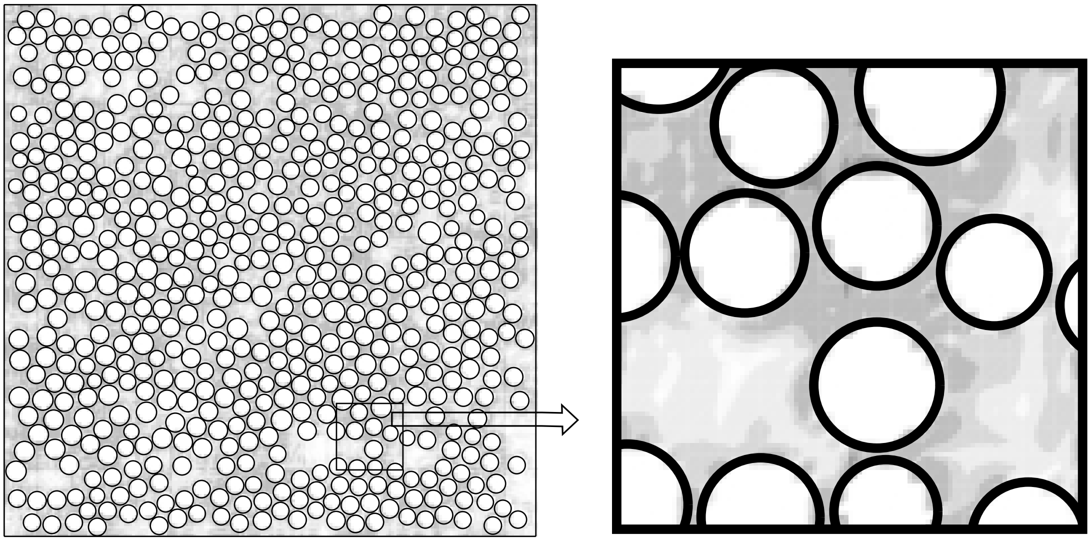

(b) Handbook $\tilde{\omega}_X^{(1);1}$

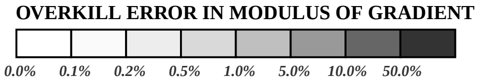

Figure 4.23. Relative modulus of the error of gradient of GFEM solutions for $p = 5$ and $p_{\mathrm{hb}} = 1$ on the mesh with 16×16 elements. $\gamma = 1.375$, for (a) Handbook $\tilde{\omega}_X^{(0);1}$; (b) Handbook $\tilde{\omega}_X^{(1);1}$

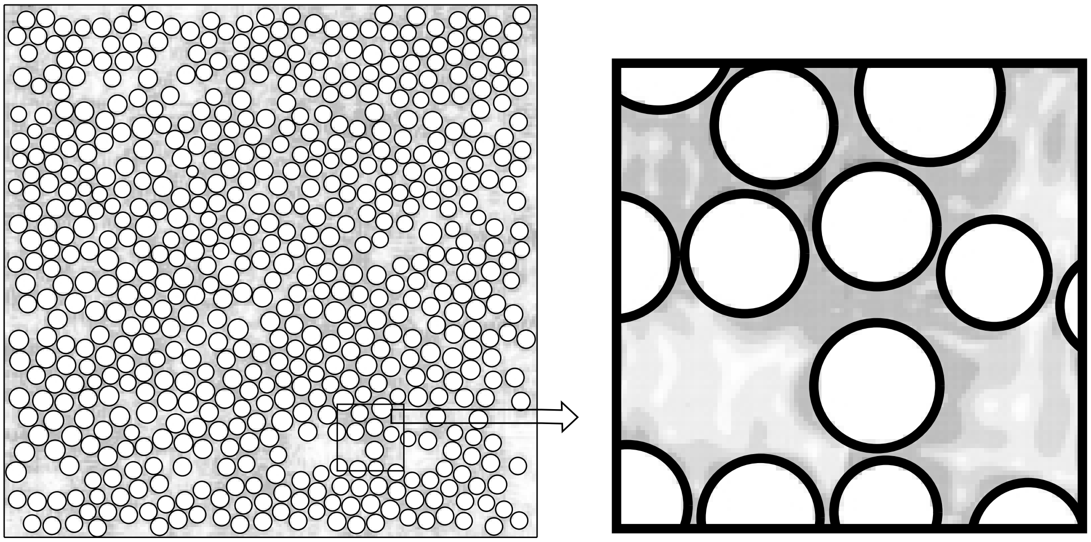

(a) Handbook $\tilde{\omega}_X^{(1);2}$

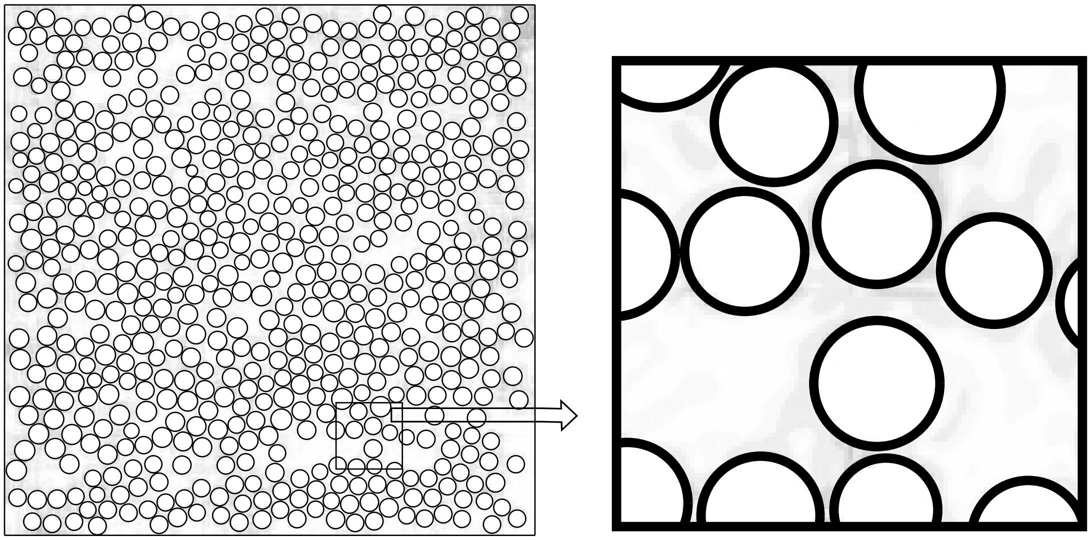

(b) Handbook $\tilde{\omega}_X^{(2);2}$

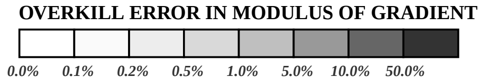

Figure 4.24. Relative modulus of the error of gradient of GFEM solutions for $p = 5$ and $p_{\text{hb}} = 1$ on the mesh with 16×16 elements. $\gamma = 1.375$, for (a) Handbook $\tilde{\omega}_X^{(1);2}$; (b) Handbook $\tilde{\omega}_X^{(2);2}$.

4.4 Analysis of the cost of Generalized FEM

In this section, we will investigate the cost of the GFEM employing mesh-based handbooks for the example problem of the Neumann problem for the Laplacian in a domain with 597 voids. Here we will measure the cost of the GFEM in terms of the CPU time. All the computation were performed on a PC, Dell Precision 450. We will use the results of these computations to estimate the cost in parallel implementations of the method.

The major part of the CPU time can be divided into two parts: (1) The time used for solving the handbook problems; and (2) The processing time starting from the computation of the elemental stiffness matrices to the end of the computation of the GFEM solution.

Let us first consider the case of the 16×16 mesh for $\gamma = 1.0$. Figure 4.25 shows the distribution of the CPU time in all the 289 handbooks, ranging from a few seconds to about one minute. The average CPU time used for the handbooks is 40.68 seconds. Table 4.12 reports the processing part of the CPU time for the GFEM solution. Here the major contribution of this part of CPU time comes from the adaptive integration of the entries of the elemental stiffness matrices, in particular for the entries involving of the handbook functions. Note that the increase of the handbook order p_{hb} causes a more substantial increase in the CPU time than the increase of the polynomial degree does. Similar conclusions can be obtained by analyzing the case of the 8×8 mesh, for which the results are given in Figure 4.26 and Table 4.13. Let us note that although the CPU time spent for integrating the GFEM stiffness coefficients is the major cost in the global phase of the method, it is still much smaller than the cost of numerical construction of the handbook functions!

Figure 4.27 shows the accuracy versus the cost of the GFEM solution for $\gamma = 1.0$ on the 16×16 and 8×8 meshes. We observe that the CPU time on 8×8 mesh is less than that of 16×16 mesh, while the accuracy of the GFEM solution on 8×8 mesh is higher than the one on 16×16 mesh.

As a comparison, let us also look into the CPU time for the case of $\gamma = 1.375$. Figure 4.28 and Figure 4.29 show the distribution of the CPU time in all the handbooks for the 16×16 and 8×8 meshes, respectively. The average CPU time used for the handbooks on the 16×16 mesh is 47.83 seconds, and 158.54 seconds for the case on the 8×8 mesh. Table 4.14 and Table 4.15 report the processing part of the CPU time for the GFEM solution on the 16×16 and 8×8 meshes, respectively. We observe that the CPU time increases as γ increases.

Figure 4.30 shows the accuracy versus the cost of the GFEM solution for $\gamma = 1.375$ on the 16×16 and 8×8 meshes. Similar to the case of $\gamma = 1.0$, we observe that the CPU time on 8×8 mesh is less than that of 16×16 mesh. But, unlike the case of $\gamma = 1.0$, the accuracy of the GFEM solution on 8×8 mesh is a little bit worse than the one on 16×16 mesh.

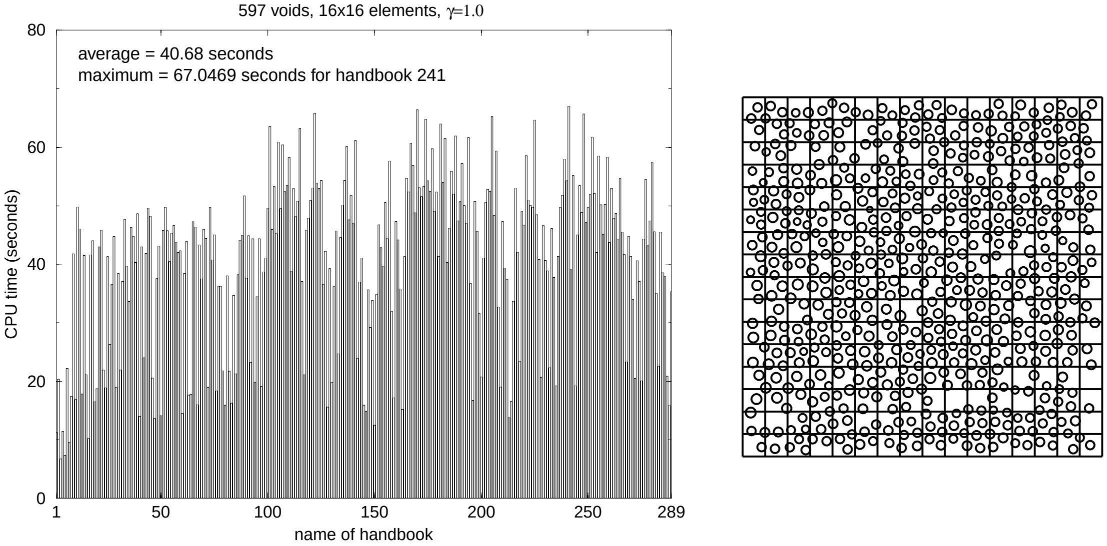

Figure 4.25. CPU time used for the handbook problems on the 16×16 mesh for $\gamma = 1.0$. These CPU costs is the main cost of the method.

Table 4.12. CPU time for the model problem (4.1) on the 16×16 mesh for $\gamma = 1.0$. Here one unit represents one second of CPU. The time shown here only includes processing time in the global phase of the method, starting from the computation of the elemental stiffness matrices to the end of the computation of the global GFEM solution. The number in the bracket is the corresponding number of degree of freedom, and the pairing numbers in the square bracket is the ratio of the CPU time of the computation of the stiffness matrix to the rest of the CPU time. Note that the main cost in the global phase is due to the numerical integrations, however the main cost of the method is due to the numerical construction of the handbook functions.

p	$p_{\text{hb}} = 1$	$p_{\text{hb}} = 2$	$p_{\text{hb}} = 3$	$p_{\text{hb}} = 4$	$p_{\text{hb}} = 5$
1	283.8594 [282.9844:0.8750] (867)	320.0469 [317.7031:2.3438] (1381)	419.0625 [414.5781:4.4844] (1895)	435.1406 [427.2031:7.9375] (2409)	504.4844 [492.0156:12.4688] (2923)
2	255.9531 [253.7813:2.1718] (1667)	287.7031 [282.9219:4.7812] (2181)	382.0781 [374.0313:8.0468] (2695)	393.9219 [381.5781:12.3438] (3209)	456.9844 [438.2656:18.7188] (3723)
3	239.5469 [235.3906:4.1563] (2979)	268.7969 [261.2969:7.5000] (3493)	352.4688 [341.4688:11.0000] (4007)	361.6719 [344.8125:16.8594] (4521)	416.6875 [392.9219:23.7656] (5035)
4	285.9531 [279.0313:6.9218] (4803)	321.2656 [310.9063:10.3593] (5317)	396.3125 [379.9531:16.3594] (5831)	417.2500 [393.4688:23.7812] (6345)	474.6094 [441.5938:33.0156] (6859)
5	418.2031 [406.9375:11.2656] (7139)	467.5313 [451.2188:16.3125] (7653)	533.3594 [510.5000:22.8594] (8167)	578.1094 [546.0938:32.0156] (8681)	642.5469 [597.6250:44.9219] (9195)

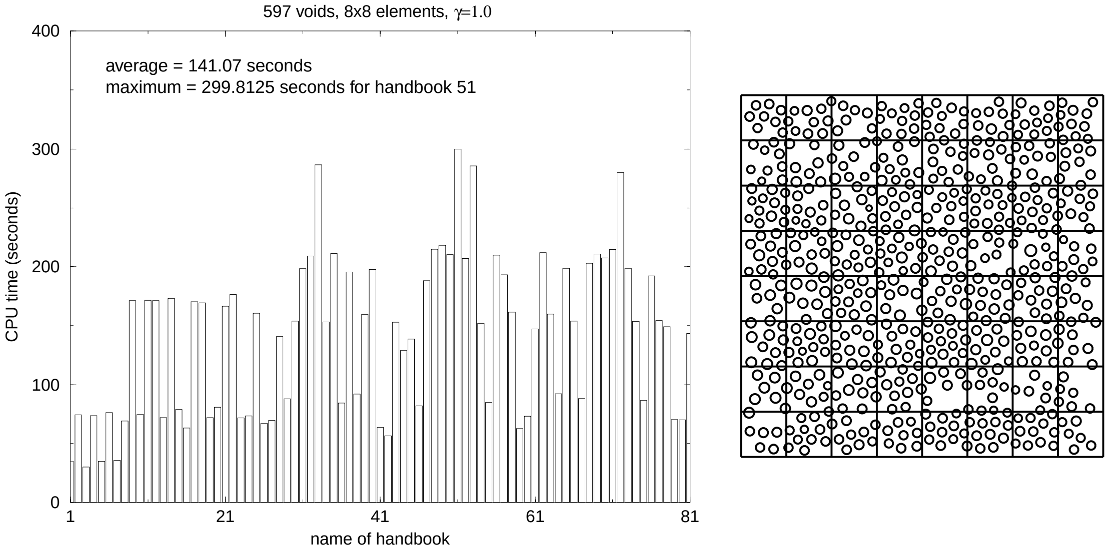

Figure 4.26. CPU time used for the handbook problems on the 8×8 mesh for $\gamma = 1.0$. These CPU costs is the main cost of the method.

Table 4.13. CPU time for the model problem (4.1) on the 8×8 mesh for $\gamma = 1.0$. Here one unit represents one second of CPU. The time shown here only includes processing time in the global phase of the method, starting from the computation of the elemental stiffness matrices to the end of the computation of the global GFEM solution. The number in the bracket is the corresponding number of degree of freedom, and the pairing numbers in the square bracket is the ratio of the CPU time of the computation of the stiffness matrix to the rest of the CPU time. Note that the main cost in the global phase is due to the numerical integrations, however the main cost of the method is due to the numerical construction of the handbook functions.

p	$p_{\mathrm{hb}} = 1$	$p_{\mathrm{hb}} = 2$	$p_{\mathrm{hb}} = 3$	$p_{\mathrm{hb}} = 4$	$p_{\mathrm{hb}} = 5$
1	614.5313 [614.3750:0.1563] (243)	632.1094 [631.6719:0.4375] (373)	722.0938 [721.2656:0.8282] (503)	700.9531 [699.7031:1.2500] (633)	767.1563 [765.2344:1.9219] (763)
2	563.8750 [563.5156:0.3594] (451)	577.8594 [577.1406:0.7188] (581)	665.2344 [664.0000:1.2344] (711)	641.9219 [640.1406:1.7813] (841)	703.7344 [701.2031:2.5313] (971)
3	535.8594 [535.1406:0.7188] (787)	550.9688 [549.8438:1.1250] (917)	636.7344 [634.9688:1.7656] (1047)	613.0938 [610.6719:2.4219] (1177)	672.5469 [669.2969:3.2500] (1307)
4	521.8594 [520.6250:1.2344] (1251)	537.8281 [535.9844:1.8437] (1381)	618.5781 [616.1250:2.4531] (1511)	595.6094 [592.0000:3.6094] (1641)	651.5938 [647.1563:4.4375] (1771)
5	574.2656 [572.2188:2.0468] (1843)	593.2344 [590.4688:2.7656] (1973)	666.0625 [662.4531:3.6094] (2103)	653.7031 [648.8125:4.8906] (2233)	704.6563 [698.2188:6.4375] (2363)

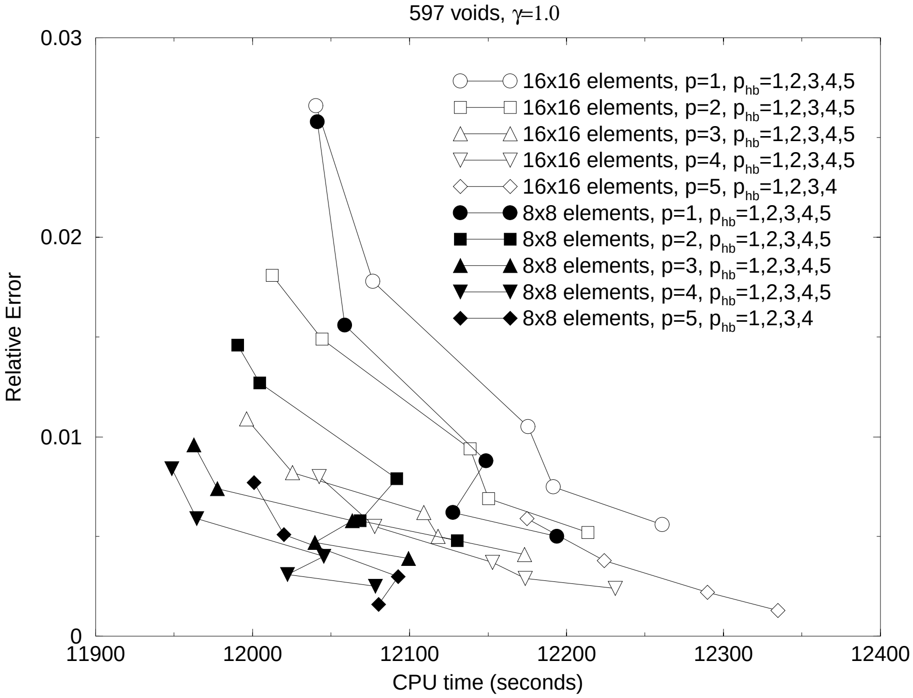

Figure 4.27. CPU time used for the GFEM solutions on the 16×16 and 8×8 meshes for $\gamma = 1.0$.

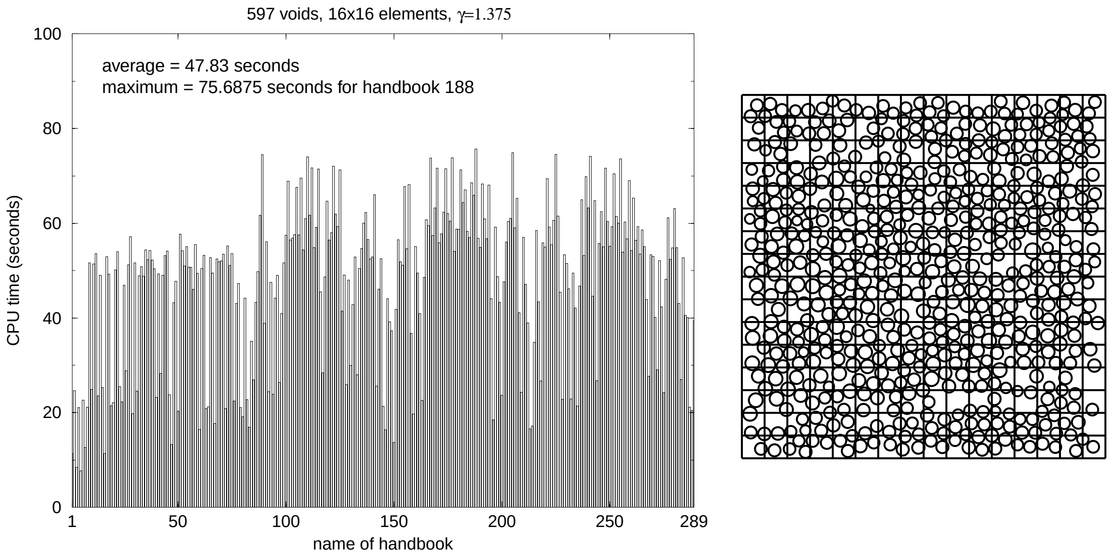

Figure 4.28. CPU time used for the handbook problems on the 16 × 16 mesh for $\gamma = 1.375$. These CPU costs is the main cost of the method.

Table 4.14. CPU time for the model problem (4.1) on the 16 × 16 mesh for $\gamma = 1.375$. Here one unit represents one second of CPU. The time shown here only includes processing time in the global phase of the method, starting from the computation of the elemental stiffness matrices to the end of the computation of the global GFEM solution. The number in the bracket is the corresponding number of degree of freedom, and the pairing numbers in the square bracket is the ratio of the CPU time of the computation of the stiffness matrix to the rest of the CPU time. Note that the main cost in the global phase is due to the numerical integrations, however the main cost of the method is due to the numerical construction of the handbook functions.

p	$p_{\mathrm{hb}} = 1$	$p_{\mathrm{hb}} = 2$	$p_{\mathrm{hb}} = 3$	$p_{\mathrm{hb}} = 4$	$p_{\mathrm{hb}} = 5$
1	432.5313 [431.6563:0.8750] (867)	476.1719 [473.7344:2.4375] (1381)	585.4063 [580.9219:4.4844] (1895)	596.6406 [588.7813:7.8593] (2409)	696.5938 [683.8750:12.7188] (2923)
2	388.6250 [386.4844:2.1406] (1667)	425.6094 [420.8125:4.7969] (2181)	526.1875 [518.3906:7.7969] (2695)	532.0313 [519.7344:12.2969] (3209)	622.4531 [603.4219:19.0312] (3723)
3	368.2031 [364.3281:3.8750] (2979)	397.0313 [389.9063:7.1250] (3493)	488.2031 [476.8594:11.3437] (4007)	496.4063 [479.2813:17.1250] (4521)	572.4375 [548.3594:24.0781] (5035)
4	418.8750 [412.4375:6.4375] (4803)	456.7969 [446.3906:10.4063] (5317)	541.9688 [525.7813:16.1875] (5831)	571.8125 [549.2031:22.6094] (6345)	647.5000 [614.5781:32.9219] (6859)
5	565.1094 [553.4375:11.6719] (7139)	623.5156 [607.2500:16.2656] (7653)	704.8750 [681.9219:22.9531] (8167)	766.4219 [734.5000:31.9219] (8681)	850.2031 [805.1563:45.0468] (9195)

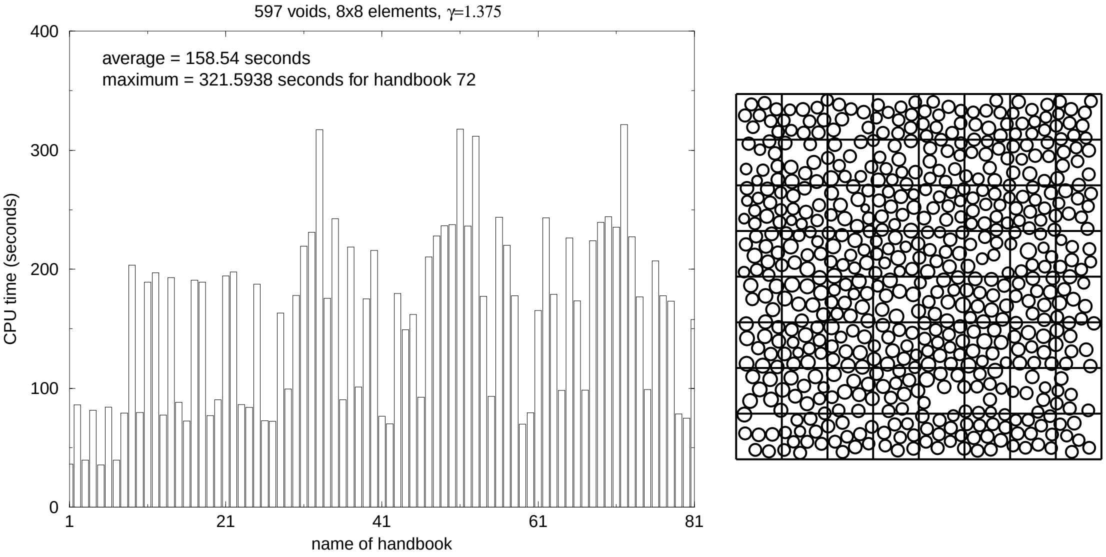

Figure 4.29. (a) CPU time used for the handbook problems on the mesh with 8 × 8 elements shown in (b) for $\gamma = 1.375$. These CPU costs is the main cost of the method.

Table 4.15. CPU time for the model problem (4.1) on the 8 × 8 mesh for $\gamma = 1.375$. Here one unit represents one second of CPU. The time shown here only includes processing time in the global phase of the method, starting from the computation of the elemental stiffness matrices to the end of the computation of the global GFEM solution. The number in the bracket is the corresponding number of degree of freedom, and the pairing numbers in the square bracket is the ratio of the CPU time of the computation of the stiffness matrix to the rest of the CPU time. Note that the main cost in the global phase is due to the numerical integrations, however the main cost of the method is due to the numerical construction of the handbook functions.

p	$p_{\text{hb}} = 1$	$p_{\text{hb}} = 2$	$p_{\text{hb}} = 3$	$p_{\text{hb}} = 4$	$p_{\text{hb}} = 5$
1	902.3750 [902.2344:0.1406] (243)	934.3750 [933.9531:0.4219] (373)	1061.9219 [1061.1406:0.7813] (503)	939.7344 [938.4219:1.3125] (633)	1065.1875 [1063.2813:1.9062] (763)
2	846.6406 [846.2656:0.3750] (451)	873.0781 [872.3750:0.7031] (581)	999.1250 [997.9219:1.2031] (711)	873.5156 [871.6563:1.8593] (841)	992.4219 [989.8594:2.5625] (971)
3	781.6406 [780.9063:0.7343] (787)	805.4219 [804.2813:1.1406] (917)	922.6719 [920.8906:1.7813] (1047)	808.1406 [805.4688:2.6718] (1177)	915.7500 [912.4688:3.2812] (1307)
4	770.5000 [769.1406:1.3594] (1251)	791.9219 [790.1094:1.8125] (1381)	908.9688 [906.5469:2.4219] (1511)	806.8750 [803.2188:3.6562] (1641)	901.6719 [897.3750:4.2969] (1771)
5	843.0000 [840.9844:2.0156] (1843)	867.6094 [864.8281:2.7813] (1973)	974.3281 [970.6875:3.6406] (2103)	907.7813 [902.5469:5.2344] (2233)	993.0625 [986.5313:6.5312] (2363)

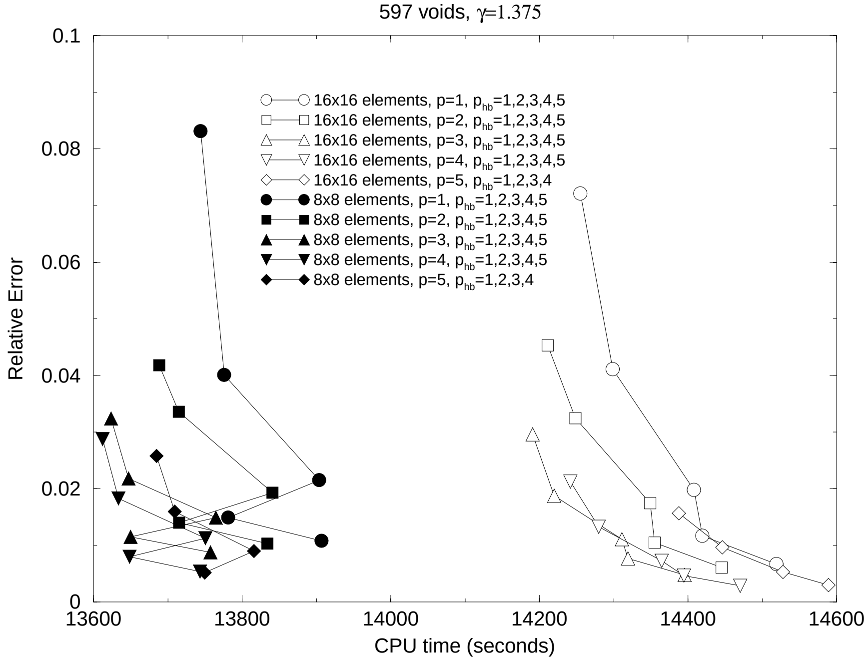

Figure 4.30. CPU time used for the GFEM solutions on the meshes with 16×16 and 8×8 elements for $\gamma = 1.375$.

Finally, let us give a rough analysis on how much the CPU time would be if we use a parallel computer. Assume we are using a parallel computer with 64 processors, each of which is a Dell Precision 450, and are solving for the GFEM solution with $p = 2$ and $p_{\text{hb}} = 1$ on the 16×16 mesh for $\gamma = 1.0$. Since the average time for solving one handbook is 40.68 seconds (see Figure 4.25), to solve the 289 handbooks by 64 processors will cost about 203 seconds. Further let us spread the computation of the element stiffness matrices of the global problem to the 64 processors also. Since the total number of the elements is 256, and the time for computing all the 256 element stiffness matrices by one processor is 253.7813 seconds (see Table 4.12) which means about 0.99 seconds for one element stiffness matrix. Hence, to compute all the 256 element stiffness matrices by 64 processors costs about 4 seconds. It needs another 2.1718 seconds to solve the linear equations, which gives the total CPU time of about 210 seconds (about 3.5 minutes) to get the GFEM solution by using 64 processors. Figure 4.31 shows the accuracy versus the CPU time for the GFEM solution on 16×16 mesh for $\gamma = 1.0$, when 64 processors are used in the computation. In real parallel computing, other work, such as message communicating, would cost some extra CPU time. We refer the readers to [73–75] for the precise analysis of the cost of the parallel computation of the h, p, and hp version of the finite element method.

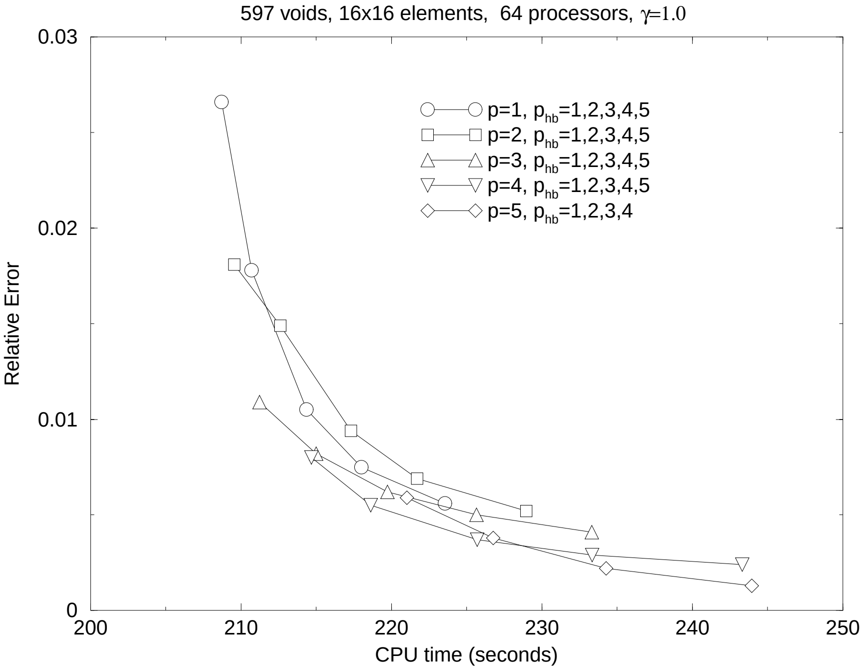

(a)

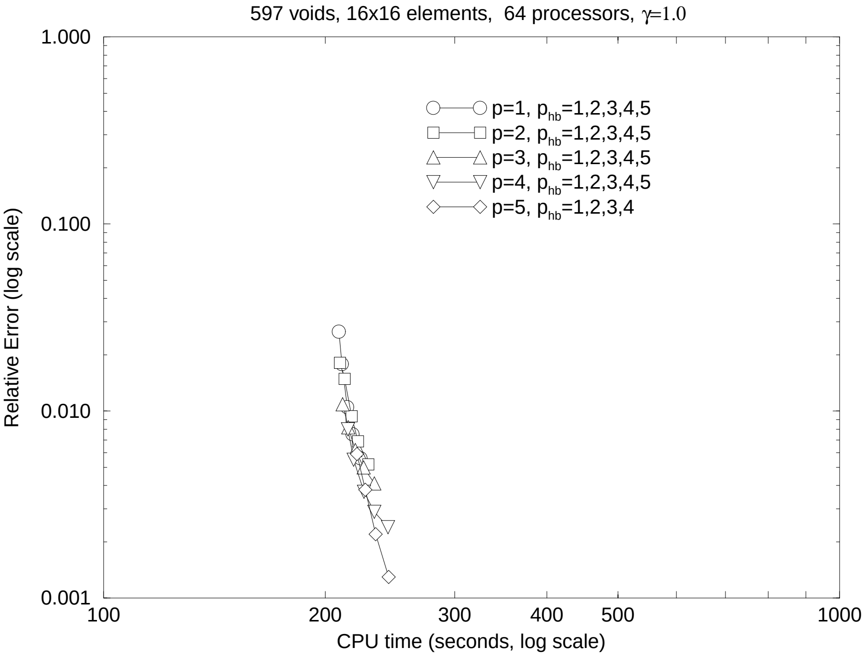

(b)

Figure 4.31. (a) CPU time used for the GFEM solutions on the meshes with 16×16 elements for $\gamma = 1.0$, when 64 processors are employed in the computation; (b) same as (a) but in logarithmic scale.

CHAPTER V

EXTENSION OF THE GENERALIZED FEM TO PROBLEMS WITH INCLUSIONS

We have seen that the Generalized FEM using mesh-based handbook functions is robust for the problems with circular voids in the problem domains. High accuracies can be achieved by using the p-handbook version of GFEM. Obviously, similar results can be expected for the problems with circular inclusions.

In this Chapter, we will show the robustness of the Generalized FEM using mesh-based handbook functions for the problems with circular inclusions in the problem domains. As our model problem, let us consider the following heat conduction model:

$$\begin{cases} -\nabla(K\nabla u) & = 0, \qquad\qquad\qquad\qquad \text{in} \quad \Omega, \\ K\dfrac{\partial u}{\partial n} & = g \overset{\text{def}}{=} \nabla(2x-y)\cdot\mathbf{n}, \quad \text{on the outer boundary} \quad \Gamma, \end{cases} \tag{5.1}$$

where Ω is the domain shown in Figure 5.1 with the circles filled with a second material, i.e. the coefficient of heat conductivity K has the following form:

$$K = \begin{cases} K_1, & \text{in the matrix,} \\ K_2, & \text{in the fibers} \end{cases} \tag{5.2}$$

5.1 Mesh-based handbook functions

The mesh-based handbook functions for the model problem (5.1) are created in the same way as the one in previous examples. In this Section, we will focus on the difference in computing the handbook functions.

5.1.1 Analytical special functions for inclusions

Using special functions, which reflects the local behavior of the solution, together with the PUM in the GFEM space is one of the reasons to guarantee to obtain a solution with high accuracy. In [49–52], the analytical special functions were obtained for circular or elliptical voids, cracks, and singular points. These analytical special functions were also used in our previous examples. For the problems with inclusions, the solution crossing the interfaces is

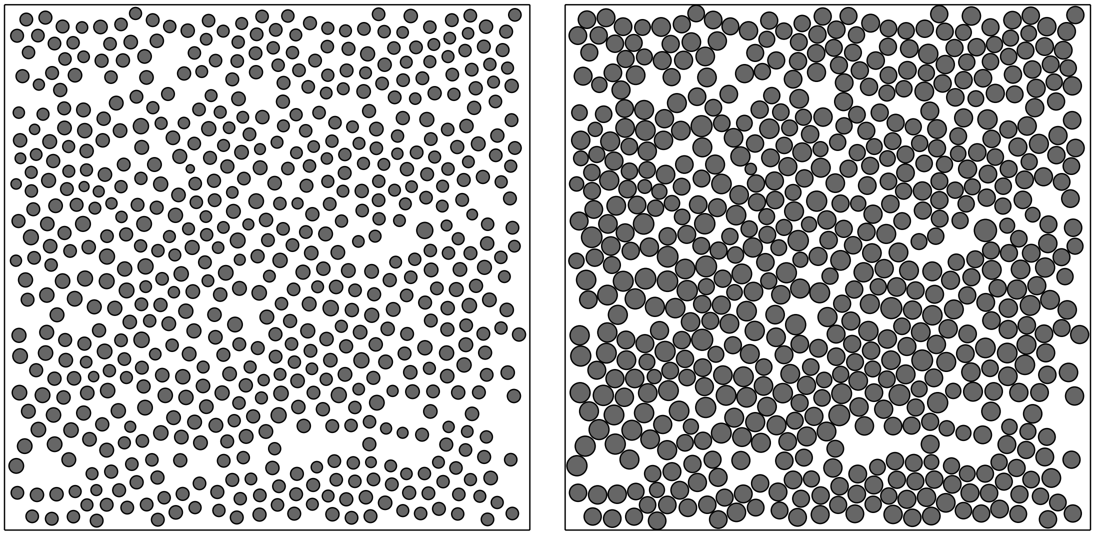

(a). $\gamma = 1.0$ (b) $\gamma = 1.375$

Figure 5.1. Domain for Problem V with the parameter $\gamma = 1.0$ and $\gamma = 1.375$, respectively.

characterized by the following analytical special functions.

$$\psi_1 = \begin{cases} \frac{K_1 + K_2}{2}\Re((\frac{z}{R})^n) + \frac{K_1 - K_2}{2}\Re((\frac{z}{R})^{-n}), & \text{outside the inclusion,} \\ K_1\Re((\frac{z}{R})^n), & \text{inside the inclusion,} \end{cases} \tag{5.3}$$

$$\psi_2 = \begin{cases} \frac{K_1 + K_2}{2}\Im((\frac{z}{R})^n) - \frac{K_1 - K_2}{2}\Im((\frac{z}{R})^{-n}), & \text{outside the inclusion,} \\ K_1\Im((\frac{z}{R})^n), & \text{inside the inclusion,} \end{cases} \tag{5.4}$$

where $z = x + y\sqrt{-1}$, $\Re(\cdot)$ and $\Im(\cdot)$ are the real and imaginary part of complex functions, R is the radius of the circular inclusion and n is the order of the special functions. The coefficients of heat conductivity K_1 and K_2 are defined in (5.2).

5.1.2 Adaptive integration over elements with inclusions

As it is demonstrated in [49–52], the accuracy of integration is essential for achieving good accuracy of solution. In our previous examples, we followed the same method as it was employed in [49–52], i.e. generating an adaptive integration mesh over each element, and employing *Fast Remeshing Quadrature* (which will discuss later) to do the adaptive integration. Here we can also employ the Fast Remeshing Quadrature to adaptively integrate over elements intersecting inclusions, but with a different way of generating integration mesh. For our case, the boundary integration cell also has boundary subcells inside the intersecting inclusion. Figure 5.2 shows one example of integration mesh over an element intersecting three inclusions.

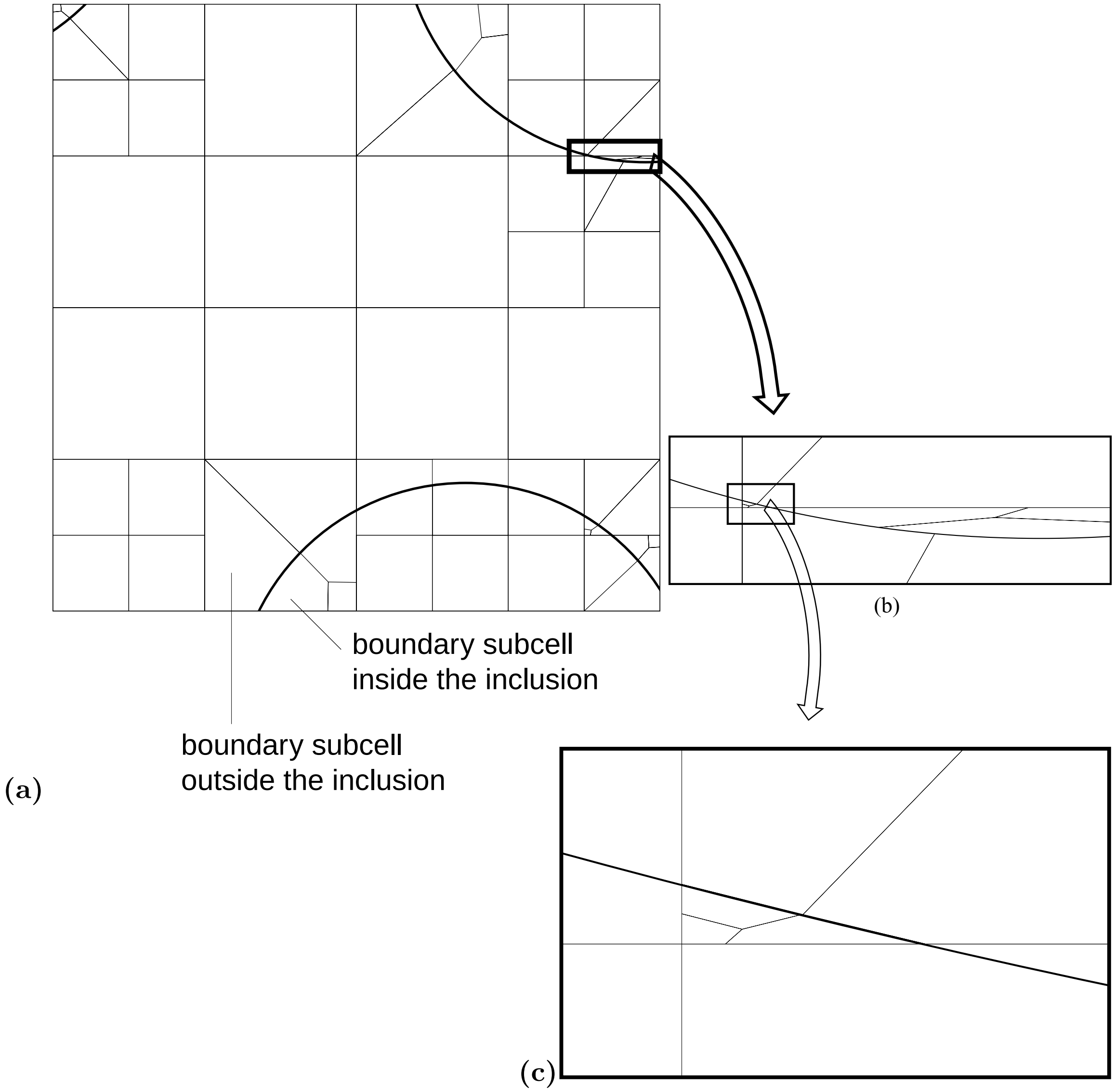

Figure 5.2. (a). Integration mesh over one element which intersects three inclusions. (b) and (c). The details of the integration mesh

5.1.2.1 Fast remeshing quadrature

Fast Remeshing Quadrature was first introduced by Strouboulis, Copps and Babuška [49–51] for the domains with voids or complex boundaries. It could also be used for the domains with inclusions with a little modification.

Algorithm 5.1 (Fast Remeshing Quadrature). To compute the integral

$$\mathbf{I}[\mathbf{f}] = \int_{\tau} \mathbf{f} \tag{5.5}$$

Begin: Let $n_{\text{cells}} = 1$, $\omega_1^{\tau,cell} = \tau$.

Initial Cell Division: Continue to divide all cells crossing inclusions and/or a domain boundary until either each cell is completely inside an inclusion, or outside inclusions but still inside the domain, or the geometry of the domain boundary contained within each cell satisfies one case in the set of *cell stopping criteria* (see [51]).

Assign Subcells: For each cell crossing the domain boundary and/or inclusions, create a mesh of subcells whose topology is specific to the corresponding resulting geometry of the case of stopping criteria. Figure 5.2(a) shows one example of these subcell mesh topologies.

Initial Estimate: For all cells intersecting inclusions and/or domain boundaries $\omega_k^{\tau,cell} \cap \Omega$ use the 7th degree embedded rule, or other suitable degree rule, in each master subcell and sum them to estimate the value of the integral $\mathbf{I}_{\omega_k^{\tau,cell}}$ and the error $E_{\omega_k^{\tau,cell}}$ over the region.
For all other $\omega_k^{\tau,cell}$ in the element,
use the 7th degree embedded rule in each master cell and extrapolation to get $\mathbf{I}_{\omega_k^{\tau,cell}}$ and the error $E_{\omega_k^{\tau,cell}}$.
Compute the estimate of the total integral $\mathbf{I} = \sum \mathbf{I}_{\omega_k^{\tau,cell}}$.
Compute the estimate of the error $E = \sum E_{\omega_k^{\tau,cell}}$.

Control: do while $\dfrac{E}{|\mathbf{I}|_2} > \varepsilon_{\text{rel}}$

Find the maximum error in all cells,
$E_{\max} = \max_k(E_{\omega_k^{\tau,cell}})$.

Process Cells: For each cell that attains $E_{\max}$,
if the cell has subcells, delete the subcells, divide the cell into four new cells and assign a new subcell mesh topologies in those cells crossing the domain boundary and /or inclusions; if the cell is completely inside an inclusion, or outside any inclusion but completely inside the domain, divide the cell into four cells.

Update: Recompute value of global integral $\mathbf{I}$ and the error E.

end do

The difference between the above Fast Remeshing Quadrature and the one proposed in [51] is that the subcell in above algorithm is allowed to be in both sides of the interface if the cell intersects any inclusion. The Fast Remeshing Approach is suitable for arbitrarily complex polygonal boundaries.

5.1.3 Mesh-based handbook functions

The creation of the handbook domains follows the same procedure as in the previous examples. Figure 5.3 illustrates the creation of the typical $\tilde{\omega}_X^{(1);1}$ handbook domains. The other types of handbook domains are created similar to the corresponding ones for the cases of voids shown in Figure 4.14.

In previous Chapter, we investigated the effect of the accuracy of the numerical construction of the handbook functions on the global GFEM solution. In this Chapter, we will not repeat it for the model examples with inclusions, and not surprisingly, mesh $T_{h/4}$ will guarantee the handbook functions with sufficient accuracy for achieving global convergence. Hence here the handbook functions are obtained on the meshes $T_{h/4}$ shown in Figure 5.4, by employing the bi-p ($p = 5$) finite element basis, together with the inclusion functions (5.3) and (5.4) of degree $p_{\text{inclusions}} = 1$ added at $n_{\text{layers}} = 0$ around each inclusion. Figures 5.5-5.10 show the relative modulus of the gradient for the handbook solutions for $\gamma = 1.0$ and for various ratio of material. We will see the exponential convergence of the global GFEM solution in next Section.

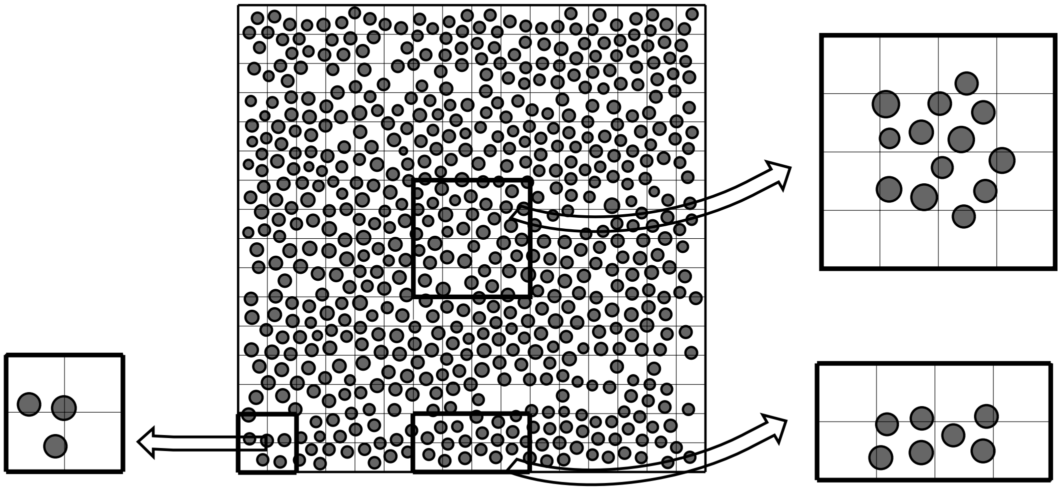

Figure 5.3. Typical examples of handbooks $\tilde{\omega}_X^{(1);1}$ with inclusions.

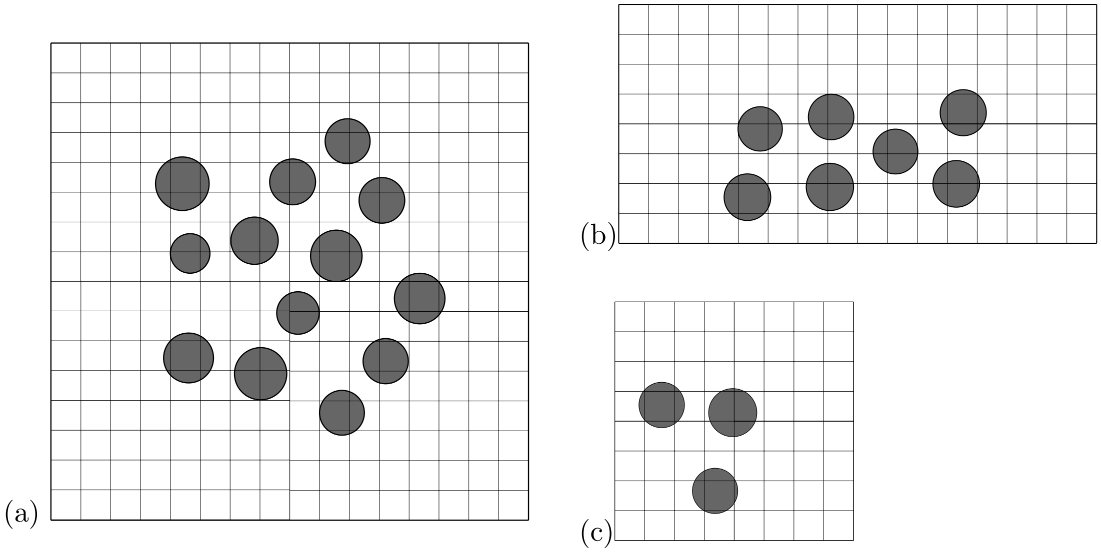

Figure 5.4. Meshes $T_{h/4}$ for the three typical handbooks with inclusions. (a). Interior handbook. (b). Boundary handbook. (c). Corner handbook.

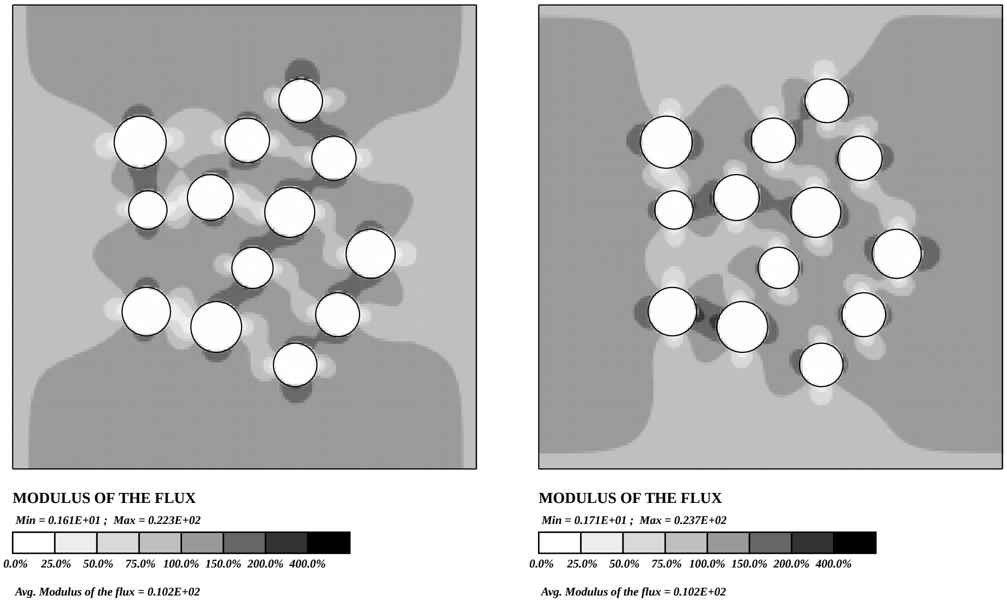

$\Re(z)$, $p = 5$ $\Im(z)$, $p = 5$

Figure 5.5. The relative modulus of the gradient for the solutions of typical interior handbook problems for $p = 5$, $K_1 = 10$ and $K_2 = 1$ for (a). $\Re(z)$ and (b). $\Im(z)$.

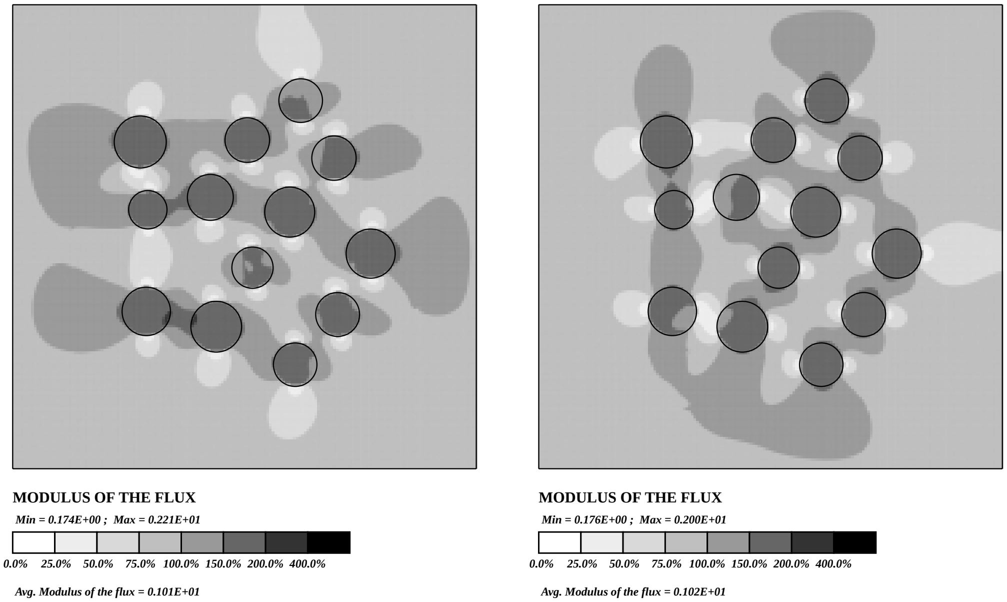

$\Re(z)$, $p = 5$ $\Im(z)$, $p = 5$

Figure 5.6. The relative modulus of the gradient for the solutions of typical interior handbook problems for $p = 5$, $K_1 = 1$ and $K_2 = 10$ for (a). $\Re(z)$ and (b). $\Im(z)$.

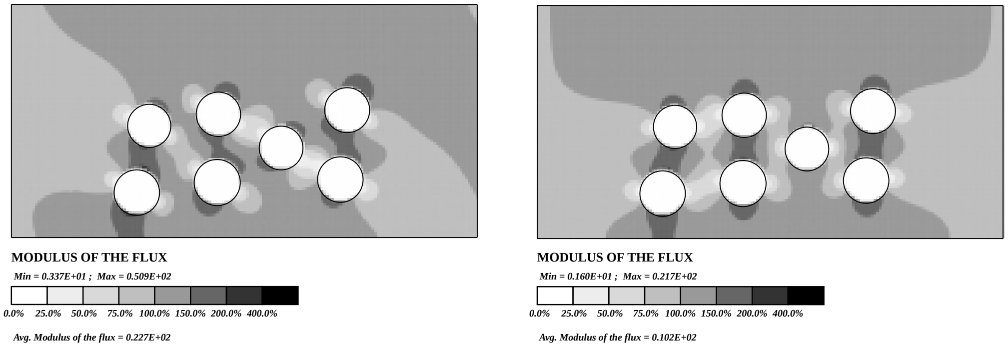

First function, $p = 5$ Second function, $p = 5$

Figure 5.7. The relative modulus of the gradient for the solutions of typical boundary handbook problems for $p = 5$, $K_1 = 10$ and $K_2 = 1$.

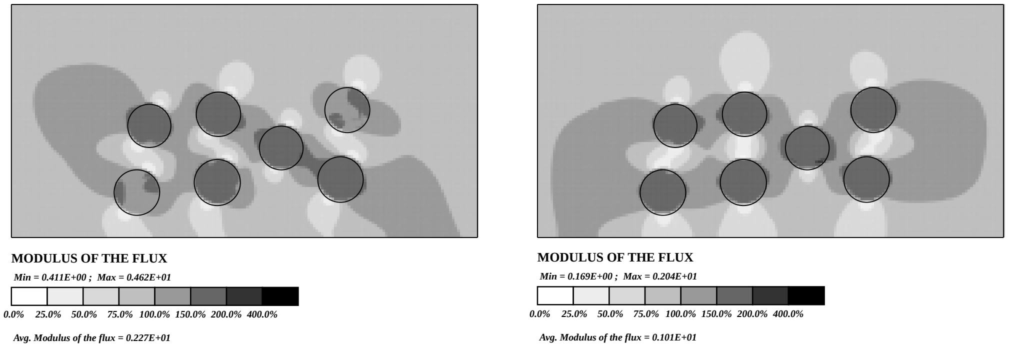

First function, $p = 5$ Second function, $p = 5$

Figure 5.8. The relative modulus of the gradient for the solutions of typical boundary handbook problems for $p = 5$, $K_1 = 1$ and $K_2 = 10$.

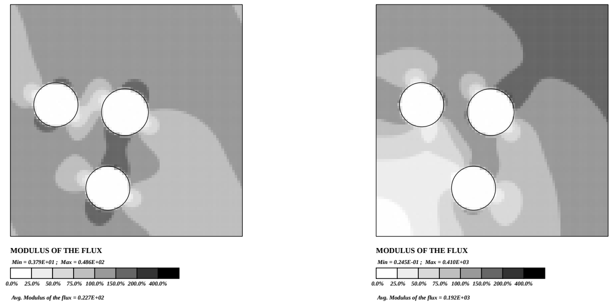

First function, $p = 5$ Second function, $p = 5$

Figure 5.9. The relative modulus of the gradient for the solutions of typical corner handbook problems for $p = 5$, $K_1 = 10$ and $K_2 = 1$.

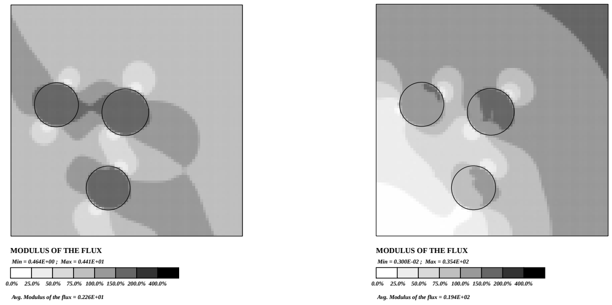

First function, $p = 5$ Second function, $p = 5$

Figure 5.10. The relative modulus of the gradient for the solutions of typical corner handbook problems for $p = 5$, $K_1 = 1$ and $K_2 = 10$.

5.2 p-handbook convergence of GFEM

Let us proceed with the results for the model problem (5.1) defined on the domains shown in Figure 5.1. We employ the 16×16 mesh and the $\tilde{\omega}_X^{(1);1}$ handbooks, shown in Figure 5.3, for the GFEM solution.

Tables 5.1 and 5.2 report the energy norm of the GFEM solution using the $\tilde{\omega}_X^{(1);1}$ handbook functions on 16×16 mesh for $\gamma = 1.0$, and for the material properties $K_1 = 1$ and $K_2 = 10$, and $K_1 = 10$ and $K_2 = 1$, respectively. Figure 5.11 shows the p-handbook convergence of the GFEM solution. From Tables 5.1 and 5.2, and Figure 5.11, we see that the character of p-handbook convergence, i.e. the exponential convergence, is independent of the material properties.

Let us also compare Figure 5.11 and Figure 3.37, we observe that, as we expect, the convergence character is the same for the case of circular voids and the cases of circular inclusions.

Table 5.1. p and p_{hb} convergence of the energy norm of the solution of the model problem (5.1) on the 16×16 mesh for $\gamma = 1.0$, $K_1 = 1$ and $K_2 = 10$, using the $\tilde{\omega}_X^{(1);1}$ mesh-based handbook functions. Here we used the solution with $p = 5$ and $p_{\text{hb}} = 5$ as the overkill solution for computing the relative error.

	$p_{\text{hb}} = 1$	$p_{\text{hb}} = 2$	$p_{\text{hb}} = 3$	$p_{\text{hb}} = 4$	$p_{\text{hb}} = 5$
$p = 1$	354.623890 (867) 2.43%	354.685770 (1381) 1.56%	354.713706 (1895) 0.93%	354.722698 (2409) 0.60%	354.726130 (2923) 0.41%
$p = 2$	354.678130 (1667) 1.69%	354.696525 (2181) 1.35%	354.716379 (2695) 0.85%	354.723549 (3209) 0.56%	354.726423 (3723) 0.39%
$p = 3$	354.697251 (2979) 1.34%	354.710508 (3493) 1.02%	354.721202 (4007) 0.67%	354.725002 (4521) 0.48%	354.727049 (5035) 0.34%
$p = 4$	354.707213 (4803) 1.11%	354.717387 (5317) 0.81%	354.724494 (5831) 0.51%	354.726945 (6345) 0.35%	354.728075 (6859) 0.24%
$p = 5$	354.715276 (7139) 0.88%	354.722328 (7653) 0.62%	354.726905 (8167) 0.35%	354.728307 (8681) 0.21%	354.729068 (9195)

Table 5.2. p and p_{hb} convergence of the energy norm of the solution of the model problem (5.1) on the 16×16 mesh for $\gamma = 1.0$, $K_1 = 10$ and $K_2 = 1$, using the $\tilde{\omega}_X^{(1);1}$ mesh-based handbook functions. Here we used the solution with $p = 5$ and $p_{\mathrm{hb}} = 5$ as the overkill solution for computing the relative error.

	$p_{\mathrm{hb}} = 1$	$p_{\mathrm{hb}} = 2$	$p_{\mathrm{hb}} = 3$	$p_{\mathrm{hb}} = 4$	$p_{\mathrm{hb}} = 5$
$p = 1$	178.554770 (867) 1.92%	178.571775 (1381) 1.34%	178.581965 (1895) 0.81%	178.584789 (2409) 0.58%	178.586018 (2923) 0.45%
$p = 2$	178.571814 (1667) 1.34%	178.576467 (2181) 1.13%	178.583076 (2695) 0.73%	178.585265 (3209) 0.53%	178.586249 (3723) 0.42%
$p = 3$	178.582700 (2979) 0.76%	178.584622 (3493) 0.60%	178.585797 (4007) 0.48%	178.586433 (4521) 0.39%	178.586834 (5035) 0.33%
$p = 4$	178.585197 (4803) 0.54%	178.586468 (5317) 0.39%	178.587156 (5831) 0.27%	178.587364 (6345) 0.23%	178.587483 (6859) 0.19%
$p = 5$	178.586363 (7139) 0.40%	178.587191 (7653) 0.27%	178.587589 (8167) 0.16%	178.587739 (8681) 0.09%	178.587819 (9195)

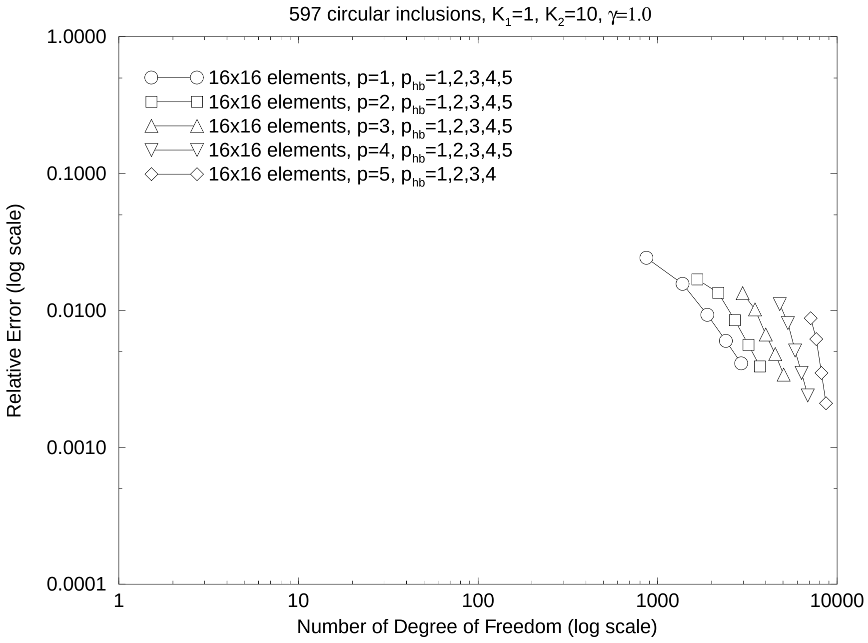

(a)

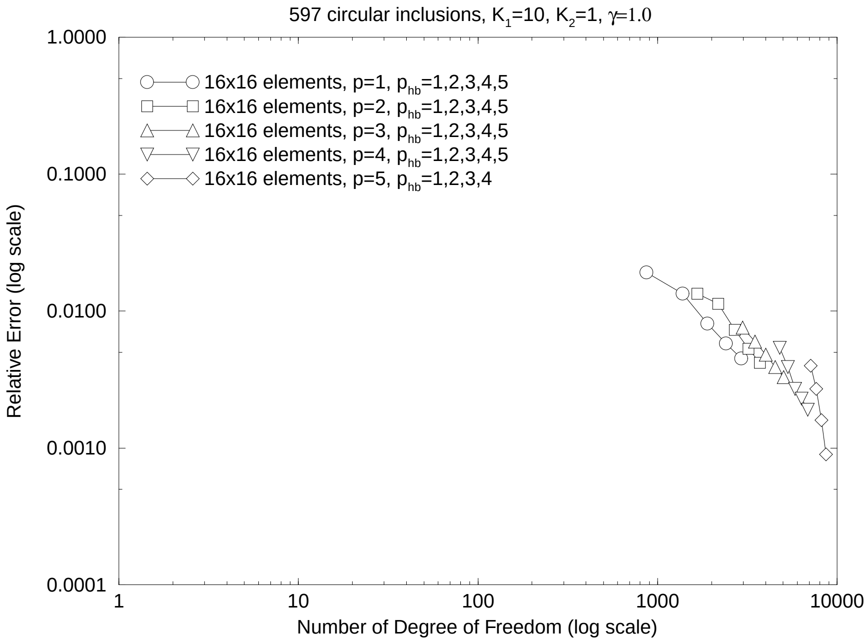

(b)

Figure 5.11. Convergence of the GFEM solution on the 16×16 mesh of the model problem (5.1) using the $\tilde{\omega}_X^{(1);1}$ handbooks for $\gamma = 1.0$, and for: (a). $K_1 = 1$ and $K_2 = 10$; (b). $K_1 = 10$ and $K_2 = 1$.

As a comparison, let us also consider the case of $\gamma = 1.375$ for which the problem is more difficult. As for the case of $\gamma = 1.0$, we also employ the 16×16 mesh and the $\tilde{\omega}_X^{(1);1}$ handbooks for the GFEM solution. Tables 5.3 and 5.4 report the energy norm of the GFEM solution for the material properties $K_1 = 1$ and $K_2 = 10$, and $K_1 = 10$ and $K_2 = 1$, respectively, while Figure 5.12 shows the p-handbook convergence of the GFEM solution. From Tables 5.1 and 5.2 and Figure 5.11, we see that, once more, the character of p-handbook convergence is independent of the material properties. Note that the character of p-handbook convergence is also independent of γ, as we have already observed for the cases of the voids in Chapter III and IV.

Table 5.3. p and p_{hb} convergence of the energy norm of the solution of the model problem (5.1) on the 16×16 mesh for $\gamma = 1.375$, $K_1 = 1$ and $K_2 = 10$, using the $\tilde{\omega}_X^{(1);1}$ mesh-based handbook functions. Here we used the solution with $p = 5$ and $p_{\text{hb}} = 5$ as the overkill solution for computing the relative error.

	$p_{\text{hb}} = 1$	$p_{\text{hb}} = 2$	$p_{\text{hb}} = 3$	$p_{\text{hb}} = 4$	$p_{\text{hb}} = 5$
$p = 1$	275.261012 (867) 4.62%	275.452143 (1381) 2.73%	275.522911 (1895) 1.52%	275.544733 (2409) 0.85%	275.551654 (2923) 0.47%
$p = 2$	275.410892 (1667) 3.23%	275.478889 (2181) 2.34%	275.527679 (2695) 1.40%	275.545952 (3209) 0.79%	275.552010 (3723) 0.44%
$p = 3$	275.468251 (2979) 2.50%	275.515289 (3493) 1.69%	275.539277 (4007) 1.06%	275.549106 (4521) 0.63%	275.552979 (5035) 0.35%
$p = 4$	275.489701 (4803) 2.17%	275.526765 (5317) 1.42%	275.544892 (5831) 0.84%	275.551754 (6345) 0.46%	275.554030 (6859) 0.21%
$p = 5$	275.502806 (7139) 1.94%	275.533104 (7653) 1.25%	275.547679 (8167) 0.71%	275.553074 (8681) 0.34%	275.554636 (9195)

Table 5.4. p and p_{hb} convergence of the energy norm of the solution of the model problem (5.1) on the 16×16 mesh for $\gamma = 1.375$, $K_1 = 10$ and $K_2 = 1$, using the $\tilde{\omega}_X^{(1);1}$ mesh-based handbook functions. Here we used the solution with $p = 5$ and $p_{\mathrm{hb}} = 5$ as the overkill solution for computing the relative error.

	$p_{\mathrm{hb}} = 1$	$p_{\mathrm{hb}} = 2$	$p_{\mathrm{hb}} = 3$	$p_{\mathrm{hb}} = 4$	$p_{\mathrm{hb}} = 5$
$p = 1$	231.428657 (867) 4.16%	231.554325 (1381) 2.54%	231.609278 (1895) 1.32%	231.621429 (2409) 0.83%	231.625982 (2923) 0.54%
$p = 2$	231.547722 (1667) 2.65%	231.579937 (2181) 2.07%	231.613266 (2695) 1.18%	231.622694 (3209) 0.76%	231.626441 (3723) 0.50%
$p = 3$	231.600732 (2979) 1.57%	231.615145 (3493) 1.11%	231.622745 (4007) 0.75%	231.625593 (4521) 0.57%	231.627442 (5035) 0.41%
$p = 4$	231.614082 (4803) 1.15%	231.622388 (5317) 0.77%	231.626813 (5831) 0.47%	231.628114 (6345) 0.33%	231.628771 (6859) 0.22%
$p = 5$	231.620034 (7139) 0.90%	231.625201 (7653) 0.60%	231.628053 (8167) 0.33%	231.628924 (8681) 0.19%	231.629342 (9195)

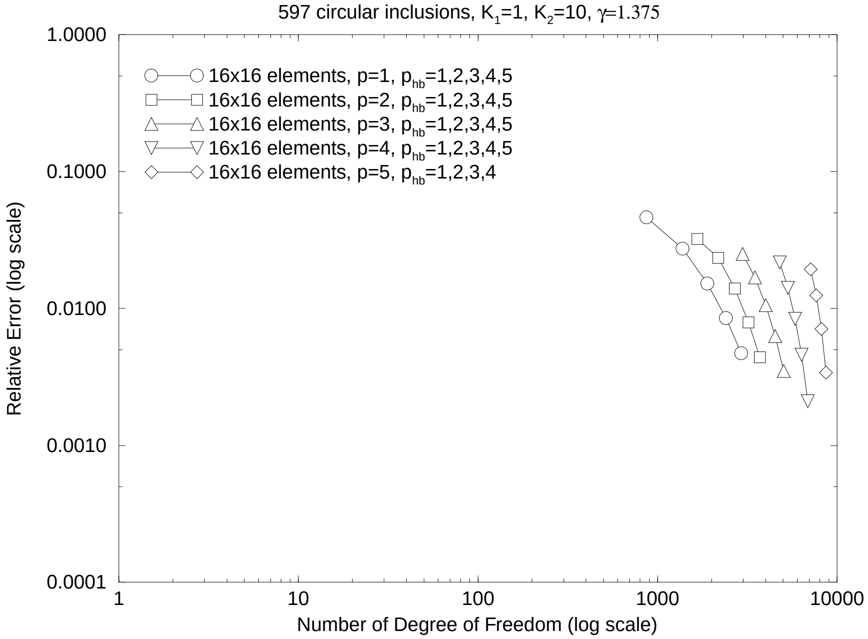

(a)

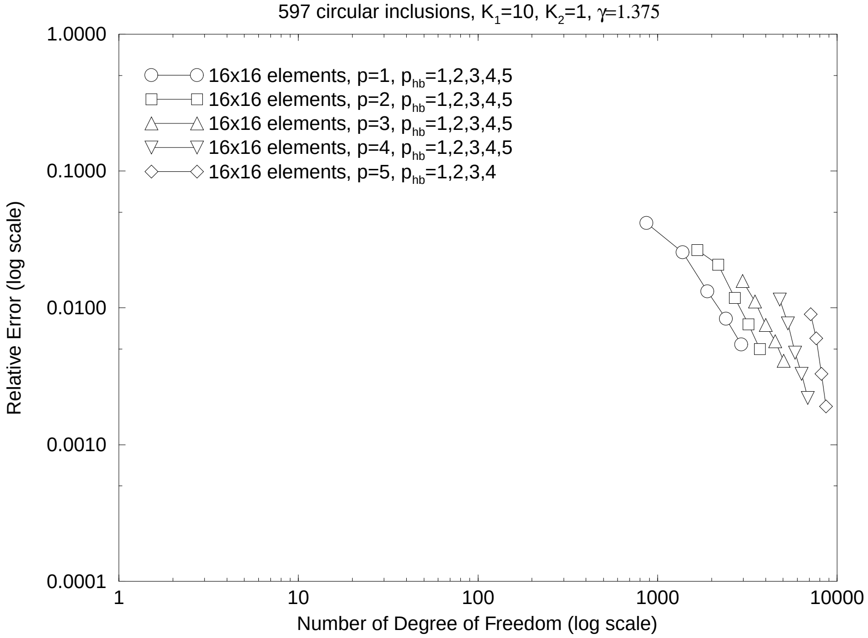

(b)

Figure 5.12. Convergence of the GFEM solution on the 16×16 mesh of the model problem (5.1) using the $\tilde{\omega}_X^{(1);1}$ handbooks for $\gamma = 1.375$, and for: (a). $K_1 = 1$ and $K_2 = 10$; (b). $K_1 = 10$ and $K_2 = 1$.

CHAPTER VI

EXTENSION OF THE GENERALIZED FEM TO PROBLEMS WITH OTHER FEATURES

In this Chapter, we will extend the Generalized FEM using mesh-based handbook functions to the problems with other types of features. As our model problems, we will consider two kinds of features: elliptical inclusions and square voids. We will show the similarities and differences between these two cases and the previous examples.

6.1 Generalized FEM for problems with elliptical inclusions

6.1.1 Model problem with elliptical inclusions

Let us consider the heat conduction problem (5.1) defined on domain Ω shown in Figure 6.1 which includes 597 elliptical inclusions with random locations and random rotation angles. Similar to the cases of circular voids and/or inclusions presented in previous Chapters, the parameter γ is used to control the closeness of the inclusions in the following way: if (a, b) is the pair of long semi-radius and short semi-radius of an ellipse for $\gamma = 1.0$, then $(\gamma a, \gamma b)$ is the one for $\gamma = 1.375$, i.e. the ellipses are uniformly enlarged by the factor γ.

The coefficients of heat conductivity for the matrix and the fibers are denoted by K_1 and K_2, as they were used before. The values of K_1 and K_2 in the following computation are also chosen as the following two settings: (1). $K_1 = 1$ and $K_2 = 10$ (the fibers are more conductive); (2). $K_1 = 10$ and $K_2 = 1$ (the matrix is more conductive).

6.1.2 Mesh-based handbooks with elliptical inclusions

The creation of the handbook domain for this model problem is the same as the one for previous examples. Figure 6.2 shows the creation of the handbook domain $\tilde{\omega}_X^{(1);1}$ for a typical interior vertex X. For the boundary vertices, the handbook domains are similarly created as it was described in Chapter III.

The handbook functions are obtained on the handbook meshes $T_{h/4}$ as it was suggested in previous Chapters for the cases of circular voids and/or inclusions. Figure 6.3 shows the $T_{h/4}$ handbook meshes for the typical handbook shown in Figure 6.2 for $\gamma = 1.0$ and $\gamma = 1.375$, respectively. The $T_{h/4}$ handbook mesh is employed for the handbook functions for the Model Problem VI (6.1).

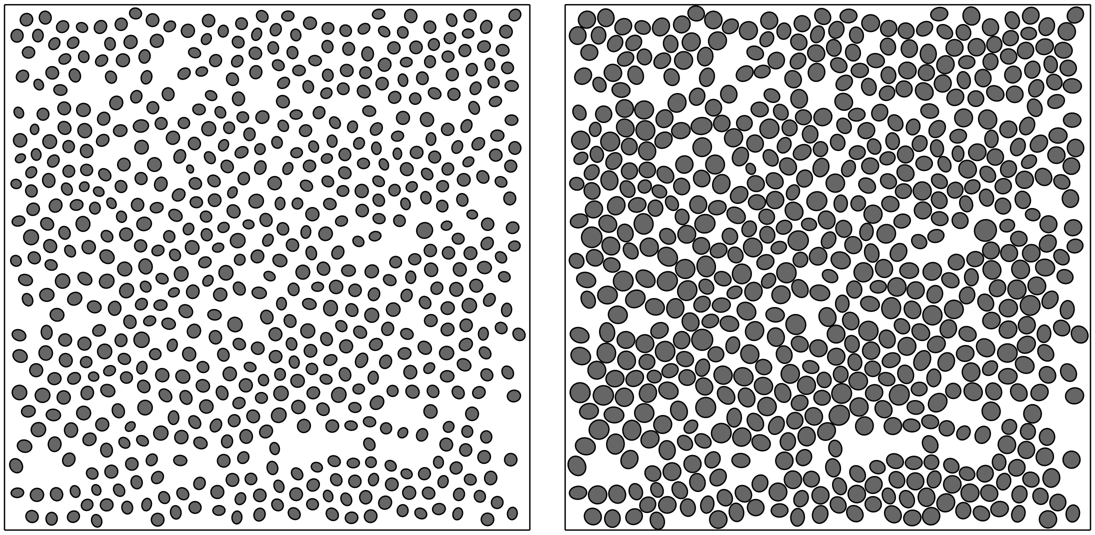

(a). $\gamma = 1.0$ (b) $\gamma = 1.375$

Figure 6.1. Domain for Problem VI with 597 elliptical inclusions for the parameter $\gamma = 1.0$ and $\gamma = 1.375$, respectively.

As we have seen in the previous Chapters, the global GFEM solution could be polluted by the error in the numerical construction of the handbook functions. Hence we have to have accurate handbook functions. The key point in the construction of the handbook functions is the enrichment of the approximation space by the analytical special functions. For the case of elliptical inclusions, we can obtain the analytical special functions from equations (5.3) and (5.4) by mapping the ellipses to circles. As in the previous Chapter, we denote the order of the analytical special functions for the elliptical inclusions by $p_{\text{inclusions}}$, and for each order, we have two special functions.

Similar to that was described in previous Chapters, the handbook functions for this model problem are also obtained by GFEM, i.e. the bi-p ($p = 5$) FE basis together with the analytical special functions for the elliptical inclusions of order one ($p_{\text{inclusions}} = 1$) applied at the zeroth layer ($n_{\text{layers}} = 0$) around each inclusion. Figures 6.4 and 6.5 show the examples of the shades of the handbook functions of order one ($p_{\text{hb}} = 1$) for $\gamma = 1.0$ and $\gamma = 1.375$, respectively. Later we will see, once more, in Section 6.1.3 that the enrichment of the global GFEM space by these mesh-based handbook functions makes the global GFEM solution converges exponentially, just as it was concluded in previous Chapters for the cases of circular voids and/or inclusions.

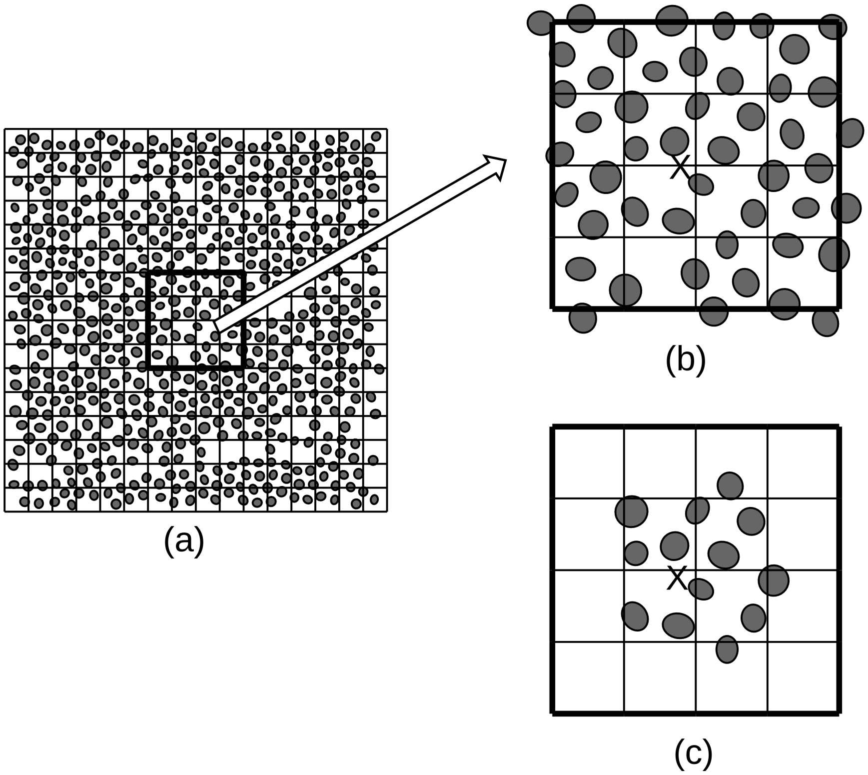

Figure 6.2. Creation of the handbook domain $\tilde{\omega}_X^{(1);1}$ for a typical interior vertex X. (a). 16×16 mesh. (b). Vertex patch $\omega_X^{(1)}$ with all the intersecting inclusions. (c). Handbook domain $\tilde{\omega}_X^{(1);1}$ for the typical interior vertex X.

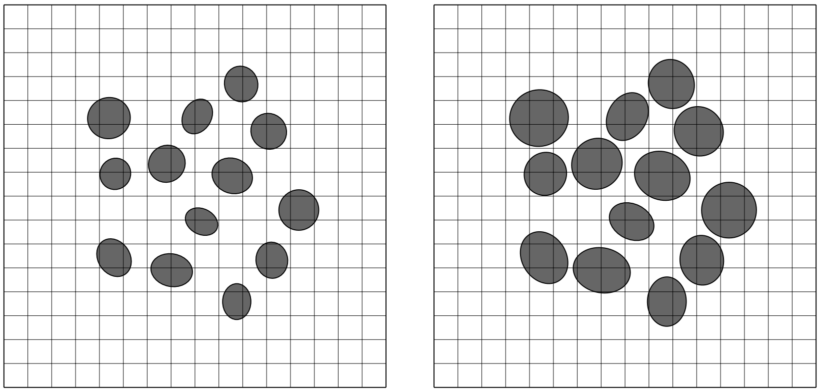

(a). $\gamma = 1.0$ (b). $\gamma = 1.375$

Figure 6.3. Handbook mesh $T_{h/4}$ for the typical interior handbooks $\tilde{\omega}_X^{(1);1}$ for: (a). $\gamma = 1.0$; and (b). $\gamma = 1.375$.

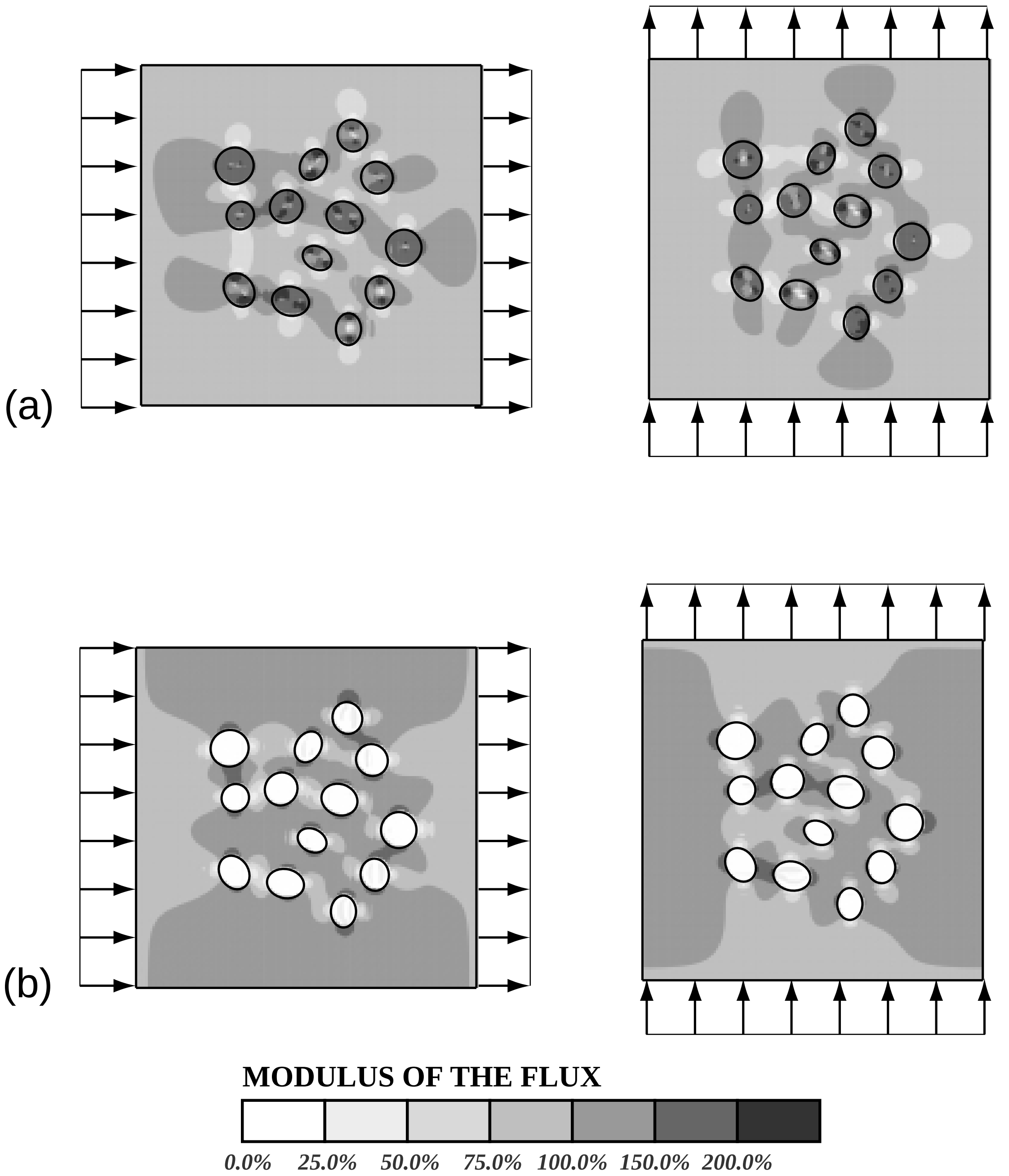

Figure 6.4. Examples of the handbook functions $\psi_j^{X;1}$, for the handbook domain $\tilde{\omega}_X^{(1);1}$ shown in Figure 6.2. Shades of the gradient of handbook functions of degree one ($p_{\mathrm{hb}} = 1$) for $\gamma = 1.0$, and for: (a). $K_1 = 1$ and $K_2 = 10$; (b). $K_1 = 10$ and $K_2 = 1$, with the boundary conditions ($\nabla(\Re(z)) \cdot \mathbf{n}$ and $\nabla(\Im(z)) \cdot \mathbf{n}$) for the handbook functions.

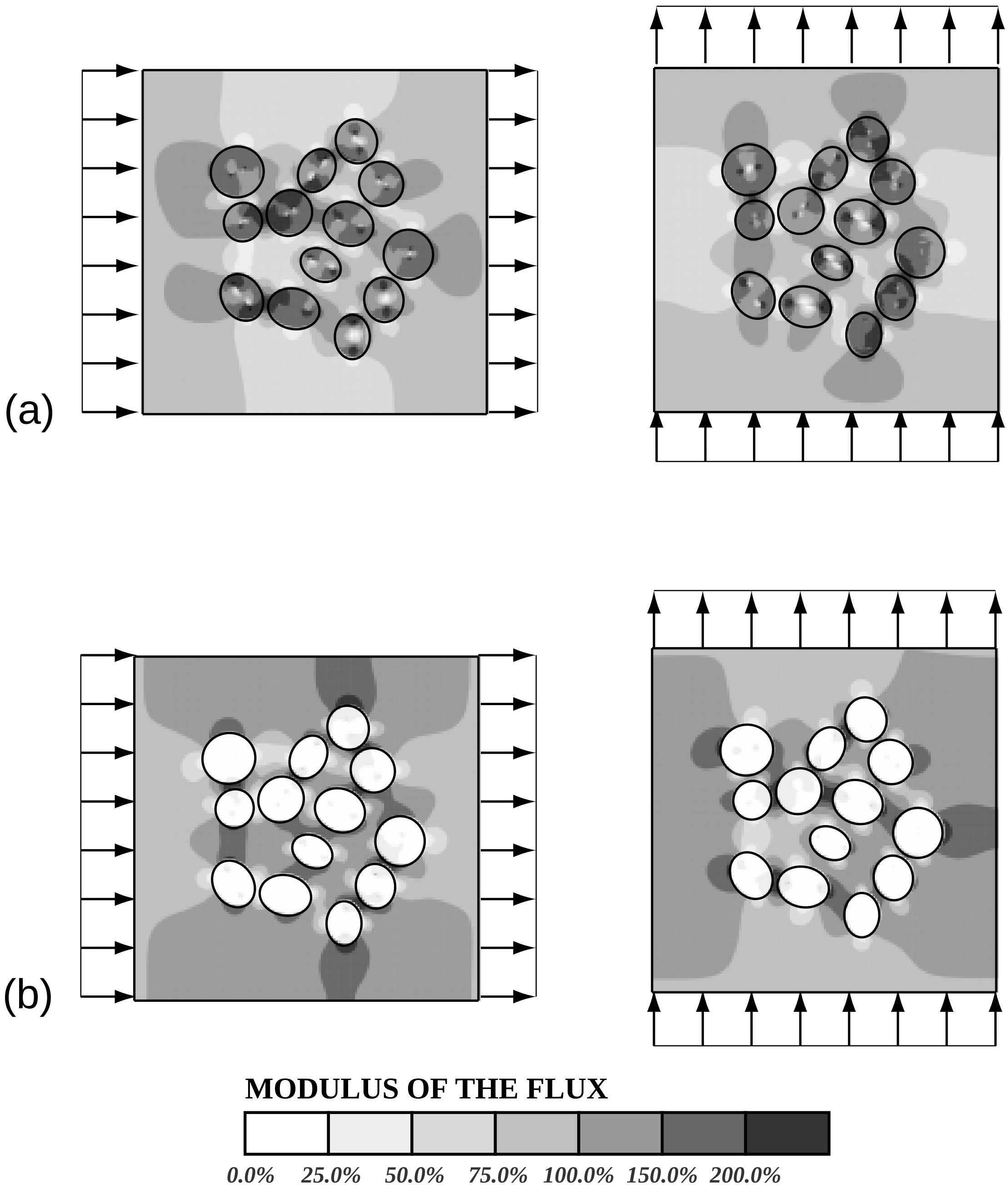

Figure 6.5. Examples of the handbook functions $\psi_j^{X;1}$, for the handbook domain $\tilde{\omega}_X^{(1);1}$ shown in Figure 6.2. Shades of the gradient of handbook functions of degree one ($p_{\mathrm{hb}} = 1$) for $\gamma = 1.375$, and for: (a). $K_1 = 1$ and $K_2 = 10$; (b). $K_1 = 10$ and $K_2 = 1$, with the boundary conditions ($\nabla(\Re(z)) \cdot \mathbf{n}$ and $\nabla(\Im(z)) \cdot \mathbf{n}$) for the handbook functions.

6.1.3 *p*-handbook convergence of GFEM

Let us look into the results for the model problem VI, the equation (5.1), defined on the domains shown in Figure 6.1. For the Generalized FEM solution, we employ the $\tilde{\omega}_X^{(1);1}$ handbook functions created on the 16×16 mesh, shown in Figure 6.2.

Tables 6.1 and 6.2 report the energy norm of the Generalized FEM solution using the $\tilde{\omega}_X^{(1);1}$ handbook functions on 16×16 mesh for $\gamma = 1.0$, and for the material properties $K_1 = 1$ and $K_2 = 10$, and $K_1 = 10$ and $K_2 = 1$, respectively. Figure 6.6 shows the *p*-handbook convergence of the Generalized FEM solution. From Tables 6.1 and 6.2, and Figure 6.6, we see, once more, that the character of exponential *p*-handbook convergence is independent of the material properties, as we already observed for the cases of circular inclusions in the previous Chapter.

Note that, by comparing Figure 6.6 with Figure 5.11 and Figure 3.37, we see that the convergence character is the same for these three cases, as we expected.

Table 6.1. p and p_{hb} convergence of the energy norm of the solution of the model problem VI with 597 elliptical inclusions and $K_1 = 1$ and $K_2 = 10$ on the 16×16 mesh for $\gamma = 1.0$ using the $\tilde{\omega}_X^{(1);1}$ mesh-based handbook functions. The numbers in bracket are the number of degree of freedom, and the percentage numbers are the relative error of the solution. Here the solution for $p = 5$ and $p_{\text{hb}} = 5$ is used as overkill solution in the computation of the relative error.

	$p_{\text{hb}} = 1$	$p_{\text{hb}} = 2$	$p_{\text{hb}} = 3$	$p_{\text{hb}} = 4$	$p_{\text{hb}} = 5$
$p = 1$	365.924673 (867) 2.28%	365.981575 (1381) 1.45%	366.004733 (1895) 0.92%	366.012621 (2409) 0.64%	366.015928 (2923) 0.48%
$p = 2$	365.974181 (1667) 1.58%	365.991080 (2181) 1.26%	366.007001 (2695) 0.85%	366.013382 (3209) 0.61%	366.016190 (3723) 0.46%
$p = 3$	365.990695 (2979) 1.27%	366.004111 (3493) 0.93%	366.011528 (4007) 0.68%	366.015108 (4521) 0.52%	366.017166 (5035) 0.40%
$p = 4$	365.999504 (4803) 1.06%	366.009740 (5317) 0.75%	366.015117 (5831) 0.52%	366.017365 (6345) 0.39%	366.018789 (6859) 0.27%
$p = 5$	366.005895 (7139) 0.88%	366.014012 (7653) 0.58%	366.017115 (8167) 0.40%	366.018956 (8681) 0.25%	366.020109 (9195)

Table 6.2. p and p_{hb} convergence of the energy norm of the solution of the model problem VI with 597 elliptical inclusions and $K_1 = 10$ and $K_2 = 1$ on the 16×16 mesh for $\gamma = 1.0$ using the $\tilde{\omega}_X^{(1);1}$ mesh-based handbook functions. The numbers in bracket are the number of degree of freedom, and the percentage numbers are the relative error of the solution. Here the solution for $p = 5$ and $p_{\text{hb}} = 5$ is used as overkill solution in the computation of the relative error.

	$p_{\text{hb}} = 1$	$p_{\text{hb}} = 2$	$p_{\text{hb}} = 3$	$p_{\text{hb}} = 4$	$p_{\text{hb}} = 5$
$p = 1$	174.461819 (867) 1.91%	174.478567 (1381) 1.32%	174.486940 (1895) 0.89%	174.489759 (2409) 0.68%	174.491580 (2923) 0.50%
$p = 2$	174.477634 (1667) 1.36%	174.482224 (2181) 1.15%	174.487954 (2695) 0.82%	174.490547 (3209) 0.61%	174.491692 (3723) 0.49%
$p = 3$	174.487725 (2979) 0.83%	174.489639 (3493) 0.69%	174.490443 (4007) 0.62%	174.491612 (4521) 0.50%	174.492397 (5035) 0.40%
$p = 4$	174.490098 (4803) 0.65%	174.491819 (5317) 0.48%	174.492388 (5831) 0.40%	174.493059 (6345) 0.29%	174.493521 (6859) 0.18%
$p = 5$	174.491230 (7139) 0.54%	174.492211 (7653) 0.43%	174.493157 (8167) 0.27%	174.493636 (8681) 0.13%	174.493793 (9195)

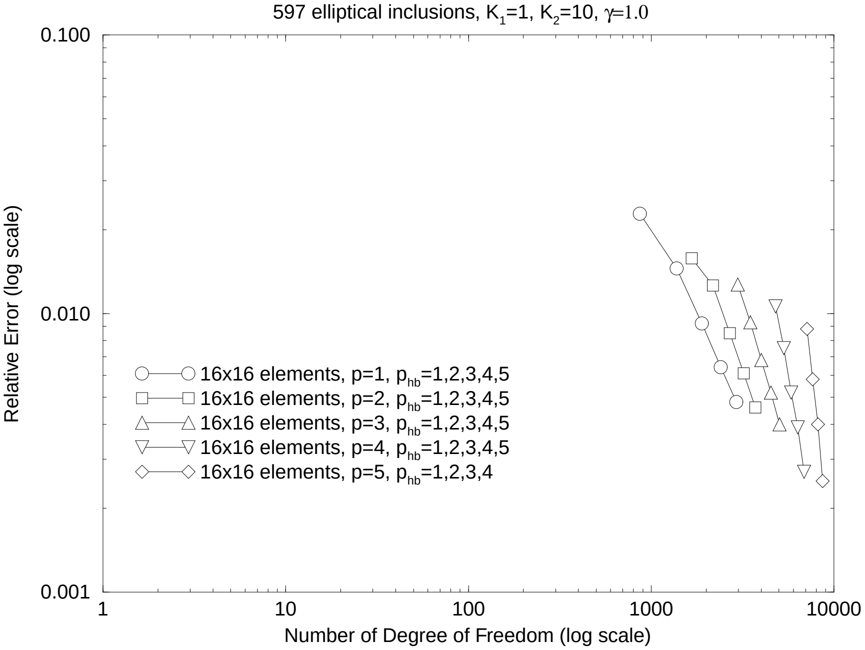

(a)

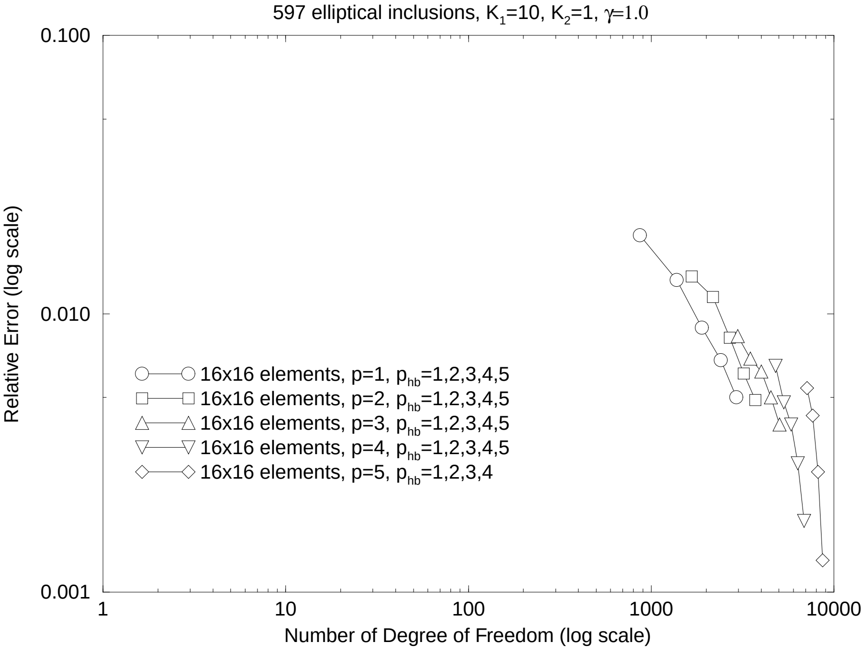

(b)

Figure 6.6. Convergence of the GFEM solution on the 16×16 mesh of the model problem VI using the $\tilde{\omega}_X^{(1);1}$ handbooks for $\gamma = 1.0$, and for: (a). $K_1 = 1$ and $K_2 = 10$; (b). $K_1 = 10$ and $K_2 = 1$.

Let us also look into the results for the case of $\gamma = 1.375$ for which the problem is more difficult. We also employ the 16×16 mesh and the $\tilde{\omega}_X^{(1);1}$ handbooks for the GFEM solution, as for the case of $\gamma = 1.0$. Tables 6.3 and 6.4 report the energy norm of the Generalized FEM solution for the material properties $K_1 = 1$ and $K_2 = 10$, and $K_1 = 10$ and $K_2 = 1$, respectively, while Figure 6.7 shows the p-handbook convergence of the Generalized FEM solution. From Tables 6.3 and 6.4 and Figure 6.7, we observe that, once more, the character of p-handbook convergence is independent of the material properties. Note that the character of p-handbook convergence is also independent of γ, as we have already observed for the cases of the voids in Chapter III and IV, and of the circular inclusions in Chapter V.

Table 6.3. p and p_{hb} convergence of the energy norm of the solution of the model problem VI with 597 elliptical inclusions and $K_1 = 1$ and $K_2 = 10$ on the 16×16 mesh for $\gamma = 1.375$ using the $\tilde{\omega}_X^{(1);1}$ mesh-based handbook functions. The numbers in bracket are the number of degree of freedom, and the percentage numbers are the relative error of the solution. Here the solution for $p = 5$ and $p_{\text{hb}} = 5$ is used as overkill solution in the computation of the relative error.

	$p_{\text{hb}} = 1$	$p_{\text{hb}} = 2$	$p_{\text{hb}} = 3$	$p_{\text{hb}} = 4$	$p_{\text{hb}} = 5$
$p = 1$	297.756396 (867) 4.29%	297.932525 (1381) 2.56%	298.002374 (1895) 1.37%	298.021383 (2409) 0.77%	298.027425 (2923) 0.43%
$p = 2$	297.901021 (1667) 2.94%	297.959334 (2181) 2.18%	298.006957 (2695) 1.25%	298.022536 (3209) 0.72%	298.027828 (3723) 0.40%
$p = 3$	297.951572 (2979) 2.30%	297.993445 (3493) 1.57%	298.016904 (4007) 0.94%	298.025221 (4521) 0.58%	298.028712 (5035) 0.32%
$p = 4$	297.971584 (4803) 1.98%	298.004652 (5317) 1.31%	298.022076 (5831) 0.74%	298.028067 (6345) 0.38%	298.029408 (6859) 0.23%
$p = 5$	297.984386 (7139) 1.75%	298.011343 (7653) 1.12%	298.024846 (8167) 0.60%	298.028320 (8681) 0.35%	298.030196 (9195)

Table 6.4. p and p_{hb} convergence of the energy norm of the solution of the model problem VI with 597 elliptical inclusions and $K_1 = 10$ and $K_2 = 1$ on the 16×16 mesh for $\gamma = 1.375$ using the $\tilde{\omega}_X^{(1);1}$ mesh-based handbook functions. The numbers in bracket are the number of degree of freedom, and the percentage numbers are the relative error of the solution. Here the solution for $p = 5$ and $p_{\mathrm{hb}} = 5$ is used as overkill solution in the computation of the relative error.

	$p_{\mathrm{hb}} = 1$	$p_{\mathrm{hb}} = 2$	$p_{\mathrm{hb}} = 3$	$p_{\mathrm{hb}} = 4$	$p_{\mathrm{hb}} = 5$
$p = 1$	218.153041 (867) 3.75%	218.244324 (1381) 2.38%	218.286940 (1895) 1.33%	218.298605 (2409) 0.84%	218.302242 (2923) 0.61%
$p = 2$	218.237840 (1667) 2.50%	218.263572 (2181) 1.98%	218.290589 (2695) 1.20%	218.299837 (3209) 0.77%	218.302702 (3723) 0.57%
$p = 3$	218.280062 (2979) 1.55%	218.292207 (3493) 1.13%	218.299230 (4007) 0.80%	218.302685 (4521) 0.57%	218.303807 (5035) 0.47%
$p = 4$	218.290869 (4803) 1.19%	218.298300 (5317) 0.85%	218.303027 (5831) 0.54%	218.305010 (6345) 0.34%	218.305357 (6859) 0.28%
$p = 5$	218.296242 (7139) 0.96%	218.301120 (7653) 0.68%	218.304459 (8167) 0.40%	218.305924 (8681) 0.17%	218.306239 (9195)

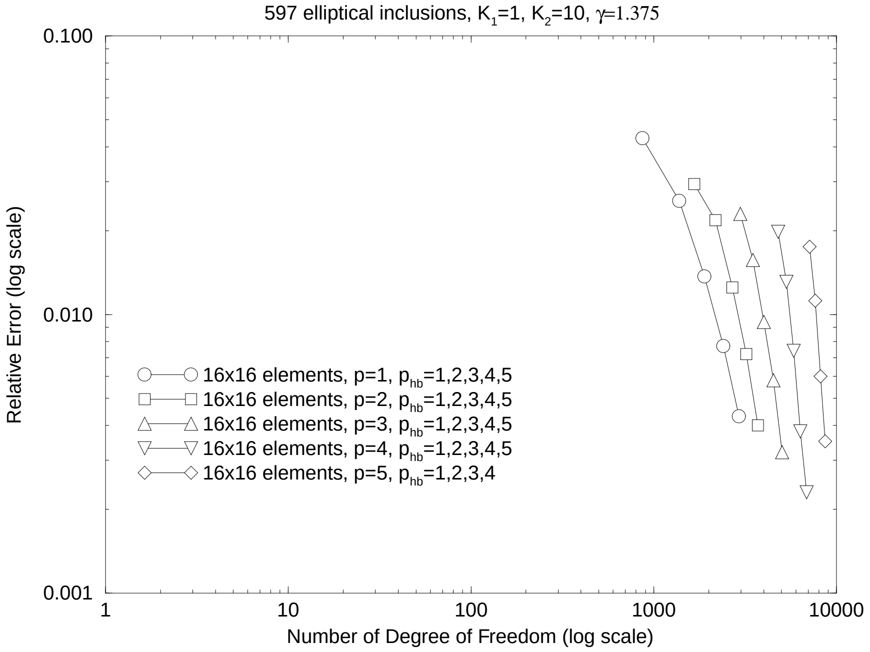

(a)

(a)

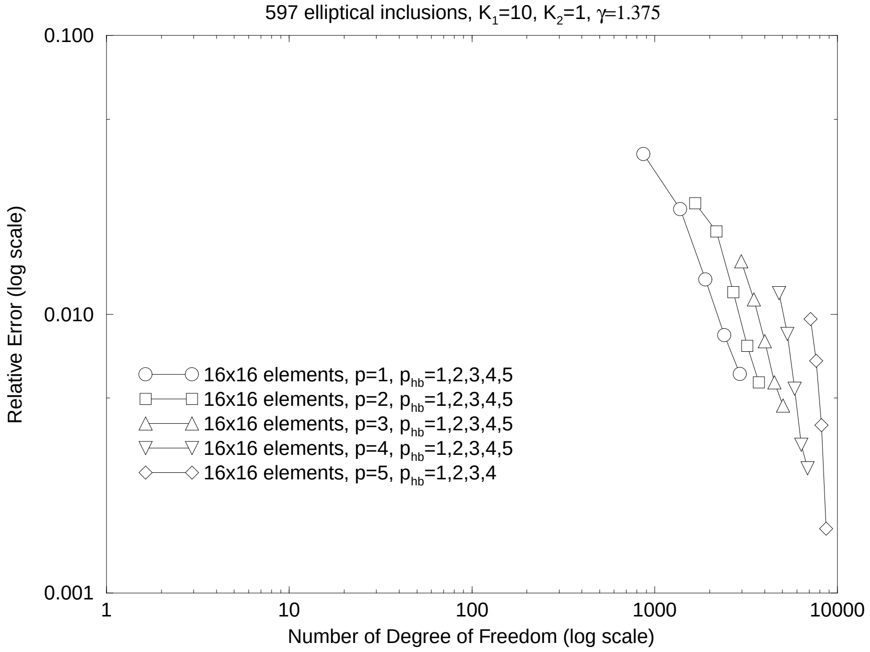

(b)

Figure 6.7. Convergence of the GFEM solution on the 16×16 mesh of the model problem VI using the $\tilde{\omega}_X^{(1);1}$ handbooks for $\gamma = 1.375$, and for: (a). $K_1 = 1$ and $K_2 = 10$; (b). $K_1 = 10$ and $K_2 = 1$.

6.2 Generalized FEM for problems with square voids

6.2.1 Model problem with square voids

As our model problem VII, let us consider the heat conduction problem (2.20) defined on domain Ω shown in Figure 6.8 which includes 597 square voids with random locations and random rotation angles. Note that this domain has 2388 closely spaced singularities in its interior area!

Figure 6.8 also shows the 16×16 mesh which will be used in the following analysis for this model problem.

Let us remark that the singularities in the domain makes the problem practically impossible to solve by the standard FEM. In fact, a local refined FEM mesh is necessary to take into account the singularities, but it would result in a huge system.

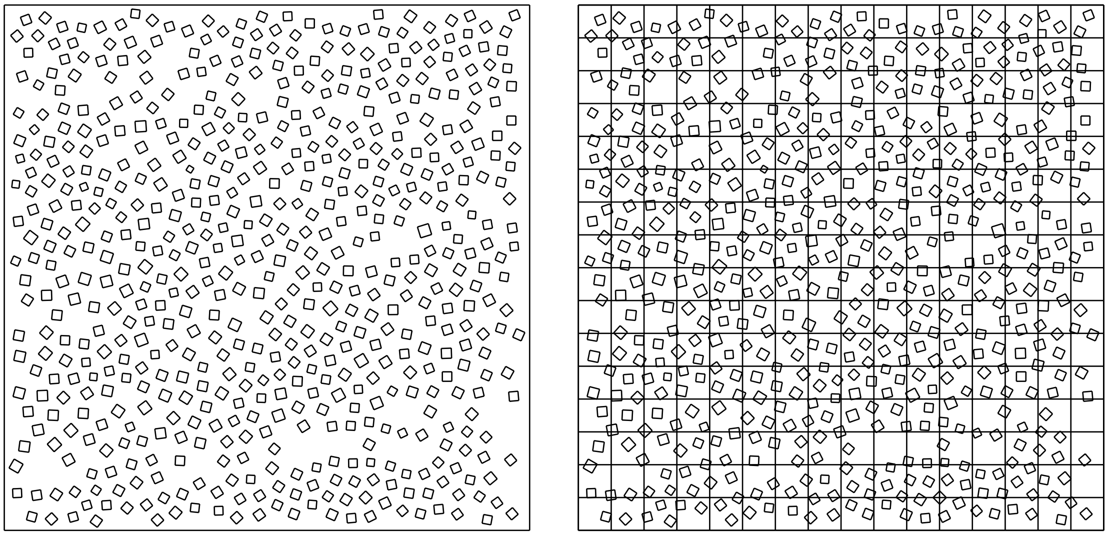

Figure 6.8. Domain and mesh for Problem VII with 597 square voids.

6.2.2 Mesh-based handbooks with square voids

For this model problem, i.e. the problem with 597 square voids in the domain, we will consider both the $\tilde{\omega}_X^{(1);1}$ and $\tilde{\omega}_X^{(2);2}$ handbooks. The creation of the handbook domain is the same as the one described in previous Chapters. Figure 6.9 shows the creation of the handbook domains $\tilde{\omega}_X^{(1);1}$ and $\tilde{\omega}_X^{(2);2}$ for a typical interior vertex X.

Let us first look into the details of the $\tilde{\omega}_X^{(1);1}$ handbook. Figure 6.10 shows three meshes $T_{h/4}$, $T_{h/8}$ and $T_{h/16}$ for the $\tilde{\omega}_X^{(1);1}$ handbook domain shown in Figure 6.9. These meshes give different error in the numerical construction of the handbook functions. In next Subsection, we will see the influence of this error on the global GFEM solution.

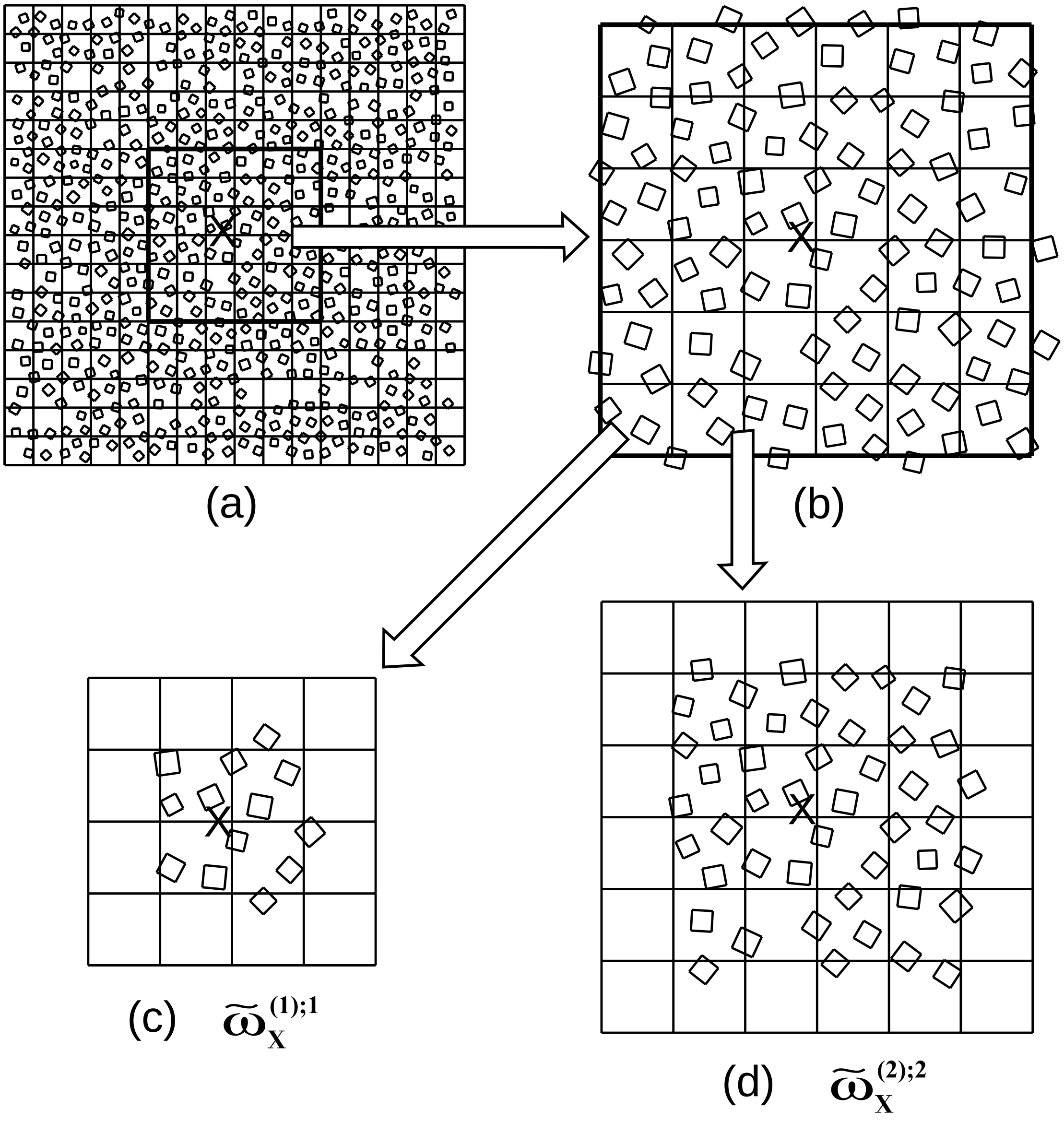

Figure 6.9. Creation of the typical handbook domains associated with a vertex X. (a) The problem domain Ω including 597 square voids covered by the 16×16 mesh Δ_h; (b) The neighborhood $\omega_X^{(2)}$ with voids intersecting them; (c) and (d) The handbook domains $\tilde{\omega}_X^{(1);1}$ and $\tilde{\omega}_X^{(2);2}$.

In order to have sufficiently accurate handbook functions, it is necessary to add special functions, i.e. the re-entrant corner functions $r^{\lambda_{p_{\text{sing}}}} \cos(\lambda_{p_{\text{sing}}}\theta)$ (because the boundary conditions on the corner edges are Neumann boundary conditions), $p_{\text{sing}} = 1, 2, ...,$ in which (r, θ) is the polar coordinates and p_{sing} is the order of the re-entrant corner function, into the approximation space to reflect the singular behavior of the exact solution at the singularities (see [49–52]). Here, we will employ the re-entrant corner functions with the order $p_{\text{sing}} = 1$

at $n_{\text{layers}} = 0$ around each singularity.

Table 6.5 and Figure 6.11 report and show the p-convergence of the first handbook function of the typical $\tilde{\omega}_X^{(1);1}$ handbook problem. We see that the p-convergence does not show up for the solutions on the mesh $T_{h/4}$. Hence, in the following analysis, we will not use $T_{h/4}$ for the numerical construction of the handbook functions. Figure 6.12 shows the shades of the gradient of the handbook functions with the boundary conditions of degree $p_{\text{hb}} = 1$ and $p_{\text{hb}} = 2$, respectively.

Figure 6.9 also shows the creation of the typical $\tilde{\omega}_X^{(2);2}$ handbook associated with an interior vertex X. For this handbook, we also consider three meshes $T_{h/4}$, $T_{h/8}$ and $T_{h/16}$ shown in Figure 6.13. The handbook functions were solved by using bi-p ($p = 5$) FE basis together with the re-entrant corner functions with degree $p_{\text{sing}} = 1$ applied at $n_{\text{layers}} = 0$ around each singularity. Table 6.6 and Figure 6.14 report and show the p-convergence of the first handbook function of the typical $\tilde{\omega}_X^{(2);2}$ handbook problem. Similar to the $\tilde{\omega}_X^{(1);1}$ handbook, we see that the p-convergence does not show up for the solutions on the mesh $T_{h/4}$. In next subsection, we will use the handbook mesh $T_{h/8}$ to compare the influence of $\tilde{\omega}_X^{(1);1}$ and $\tilde{\omega}_X^{(2);2}$ handbook functions on the global GFEM solution. Figures 6.15 and 6.16 show the shade of the gradient of the $\tilde{\omega}_X^{(2);2}$ handbook functions with the boundary conditions of degree $p_{\text{hb}} = 1$ and $p_{\text{hb}} = 2$, respectively.

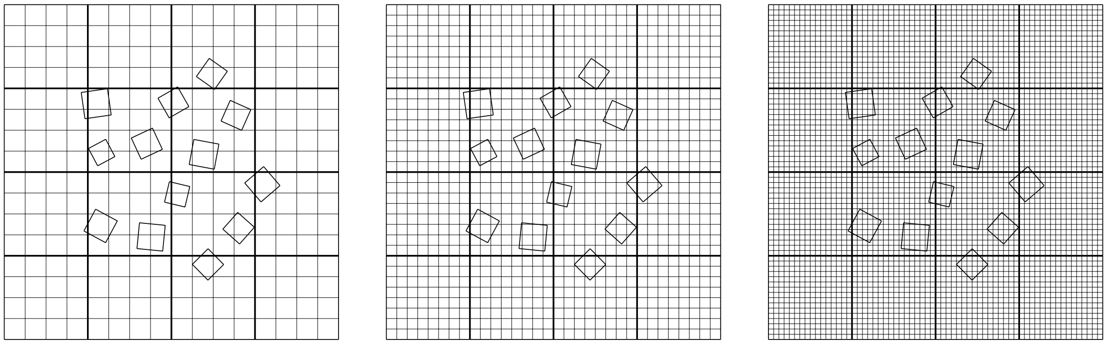

$T_{h/4}$ $T_{h/8}$ $T_{h/16}$

Figure 6.10. Handbook meshes $T_{h/4}$, $T_{h/8}$ and $T_{h/16}$ for the typical handbook domain $\tilde{\omega}_X^{(1);1}$ shown in Figure 6.9

Table 6.5. Energy norm of the first handbook function of the typical $\tilde{\omega}_X^{(1);1}$ handbook problem. The singular functions with order $n_{\text{sing}} = 1$ were employed in the handbook function around the singular point at $n_{\text{layers}} = 0$.

	$h/4$	$h/8$	$h/16$
$p = 1$	52.416552 (317) 21.60%	53.507801 (1272) 8.09%	53.615474 (4385) 5.04%
$p = 2$	53.240923 (1117) 12.82%	53.673955 (4389) 1.90%	53.682218 (16504) 0.73%
$p = 3$	53.458531 (2429) 9.15%	53.682241 (9524) 0.73%	53.683553 (36553) 0.20%
$p = 4$	53.544150 (4253) 7.20%	53.682980 (16677) 0.50%	53.683653 (64532) 0.05%
$p = 5$	53.591337 (6589) 5.86%	53.683449 (25848) 0.28%	53.683661 (100441)

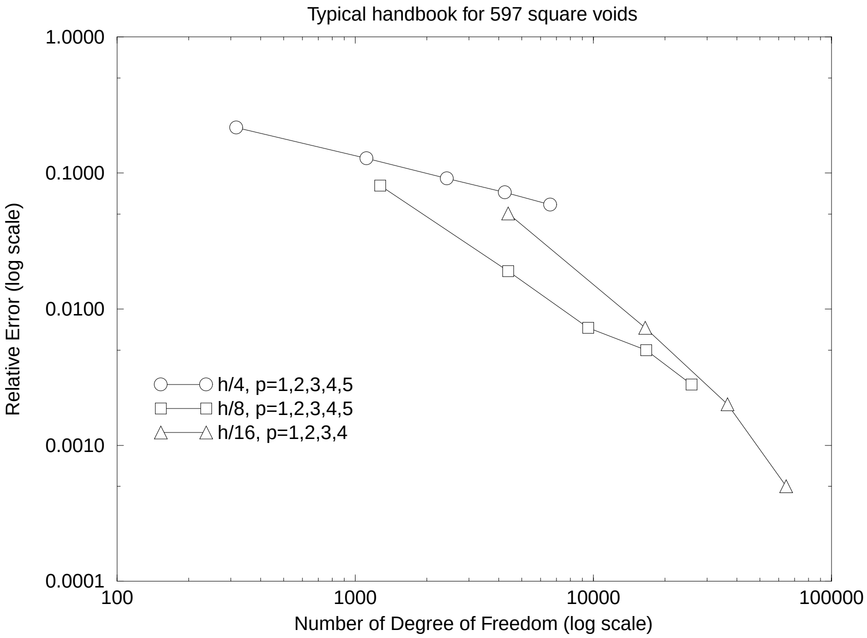

Figure 6.11. Convergence of the energy norm of the first handbook function of the typical $\tilde{\omega}_X^{(1);1}$ handbook problem. The singular functions with order $n_{\text{sing}} = 1$ were employed in the handbook function around the singular point at $n_{\text{layers}} = 0$.

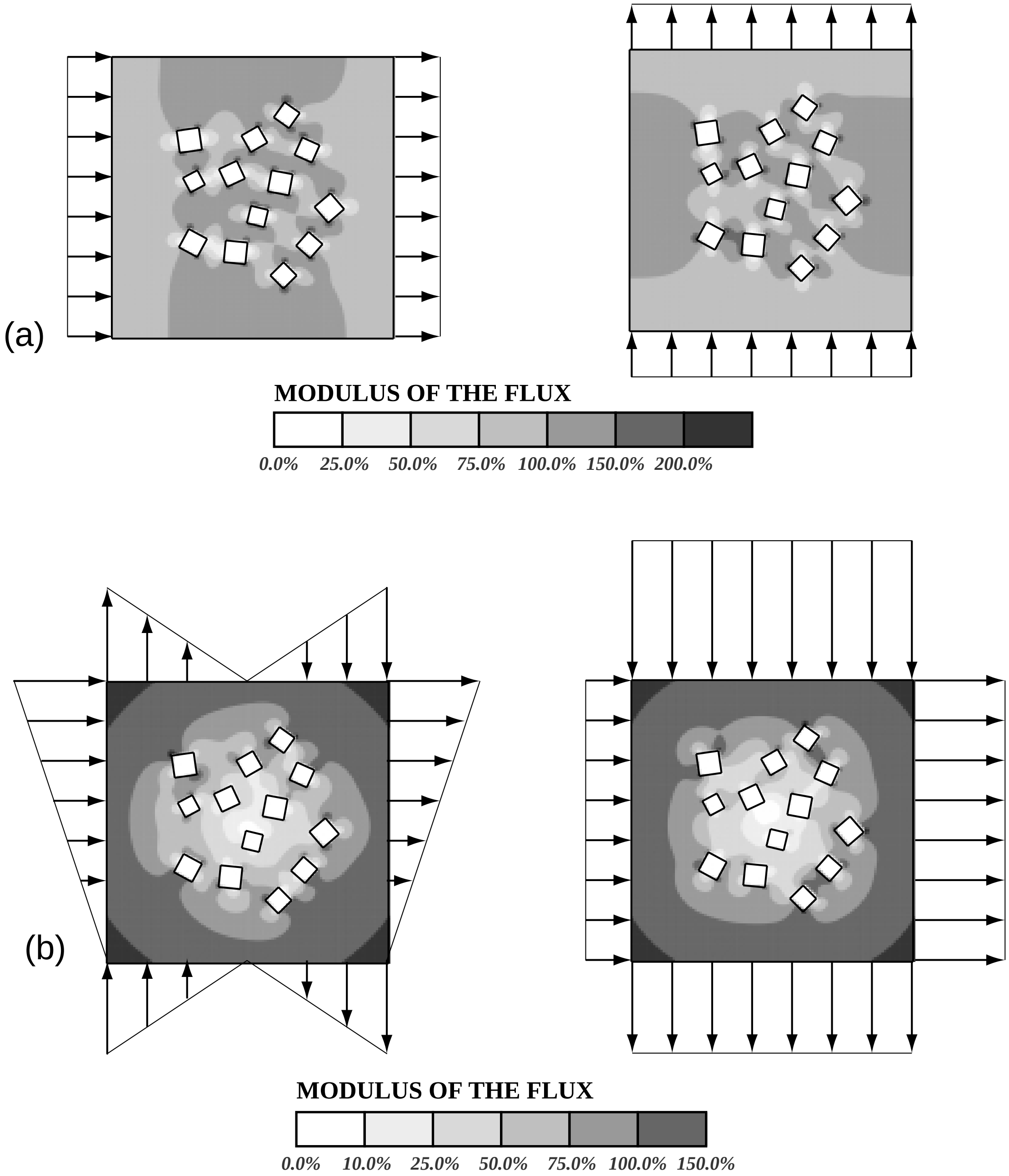

Figure 6.12. Examples of the handbook functions $\psi_j^{X;1}$, $j = 1, ..., 4$, for the handbook domain $\tilde{\omega}_X^{(1);1}$ shown in Figure 6.9, obtained on the handbook mesh $T_{h/8}$ shown in Figure 6.10. Shades of the gradient of the pairs of handbook functions with the boundary conditions of degree (a) $p_{\text{hb}} = 1$ ($\nabla(\Re(z)) \cdot \mathbf{n}$ and $\nabla(\Im(z)) \cdot \mathbf{n}$), and (b) $p_{\text{hb}} = 2$ ($\nabla(\Re(z^2)) \cdot \mathbf{n}$ and $\nabla(\Im(z^2)) \cdot \mathbf{n}$).

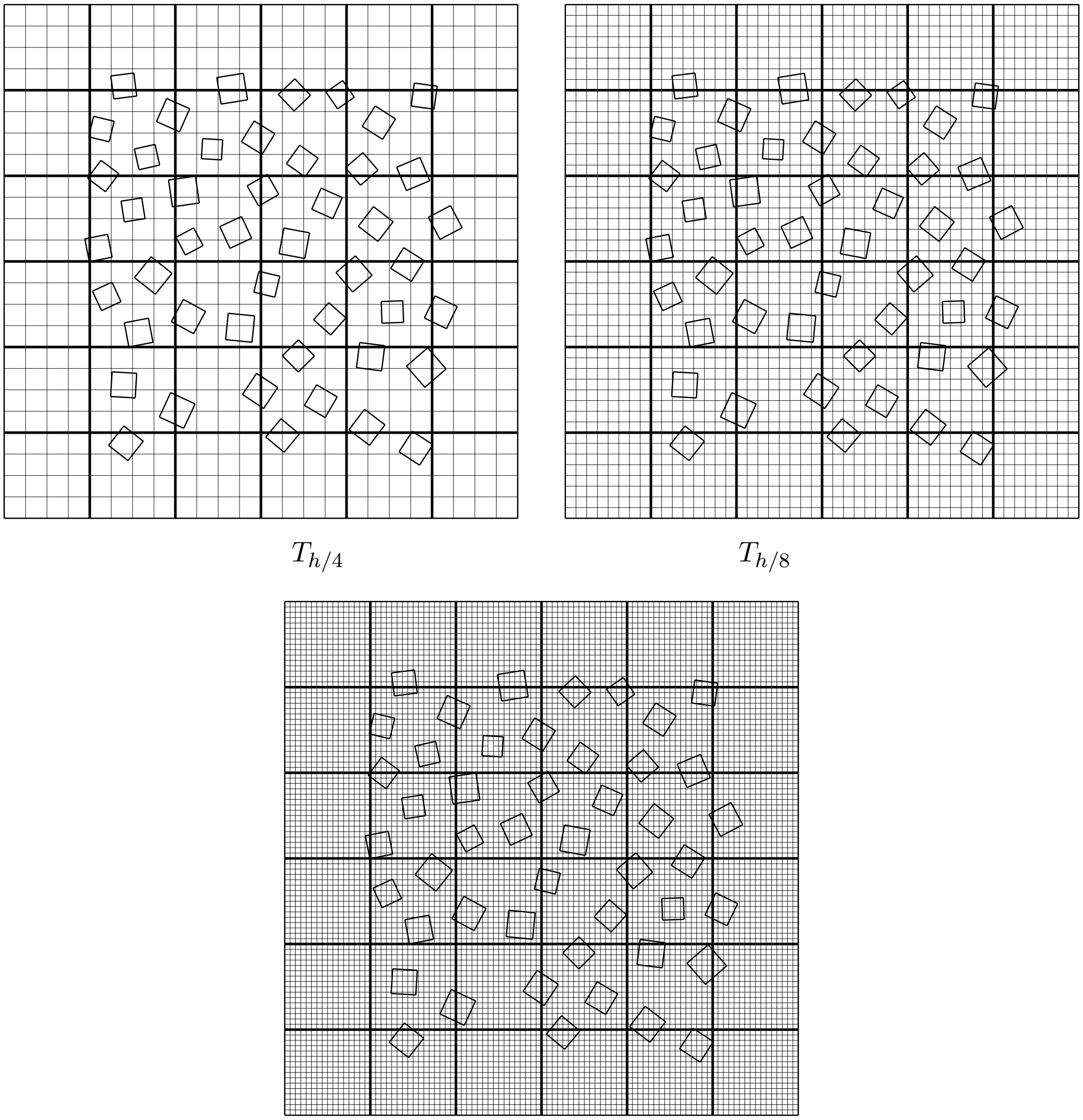

$T_{h/4}$ $T_{h/8}$

$T_{h/16}$

Figure 6.13. Handbook meshes $T_{h/4}$, $T_{h/8}$ and $T_{h/16}$ for the typical handbook domain $\tilde{\omega}_X^{(2);2}$ shown in Figure 6.9

Table 6.6. Energy norm of the first handbook function of the typical $\tilde{\omega}_X^{(2);2}$ handbook problem. The singular functions with order $n_{\text{sing}} = 1$ were employed in the handbook function around the singular point at $n_{\text{layers}} = 0$.

	$h/4$	$h/8$	$h/16$
$p = 1$	80.918763 (693) 27.31%	83.688917 (3069) 10.07%	83.944516 (9984) 6.40%
$p = 2$	82.918321 (2469) 16.82%	84.097501 (10016) 2.14%	84.113141 (36736) 0.92%
$p = 3$	83.489698 (5397) 12.19%	84.114217 (21469) 0.77%	84.116417 (80962) 0.26%
$p = 4$	83.712410 (9477) 9.79%	84.115728 (37428) 0.48%	84.116659 (142662) 0.10%
$p = 5$	83.822095 (14709) 8.36%	84.116297 (57893) 0.31%	84.116698 (221836)

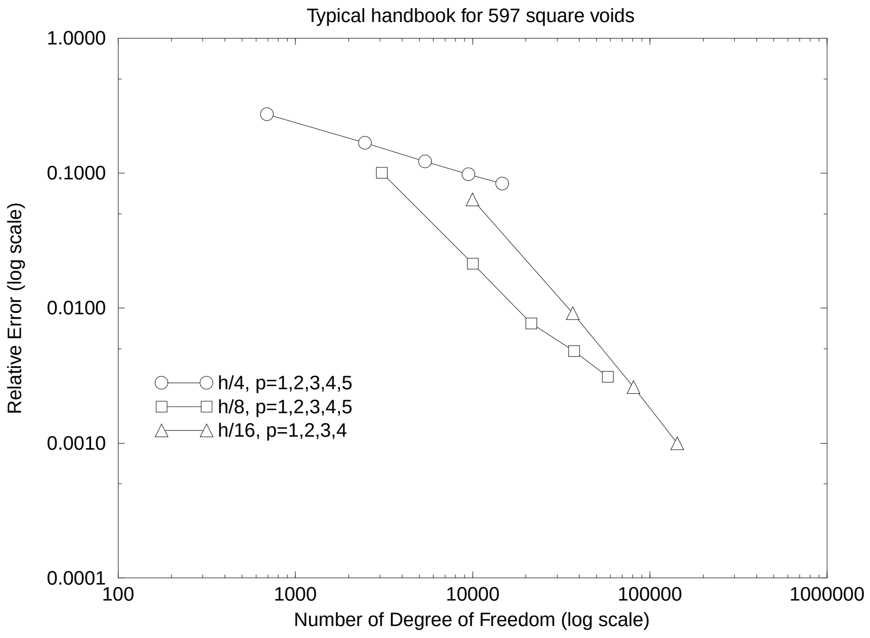

Figure 6.14. Convergence of the energy norm of the first handbook function of the typical $\tilde{\omega}_X^{(2);2}$ handbook problem. The singular functions with order $n_{\text{sing}} = 1$ were employed in the handbook function around the singular point at $n_{\text{layers}} = 0$.

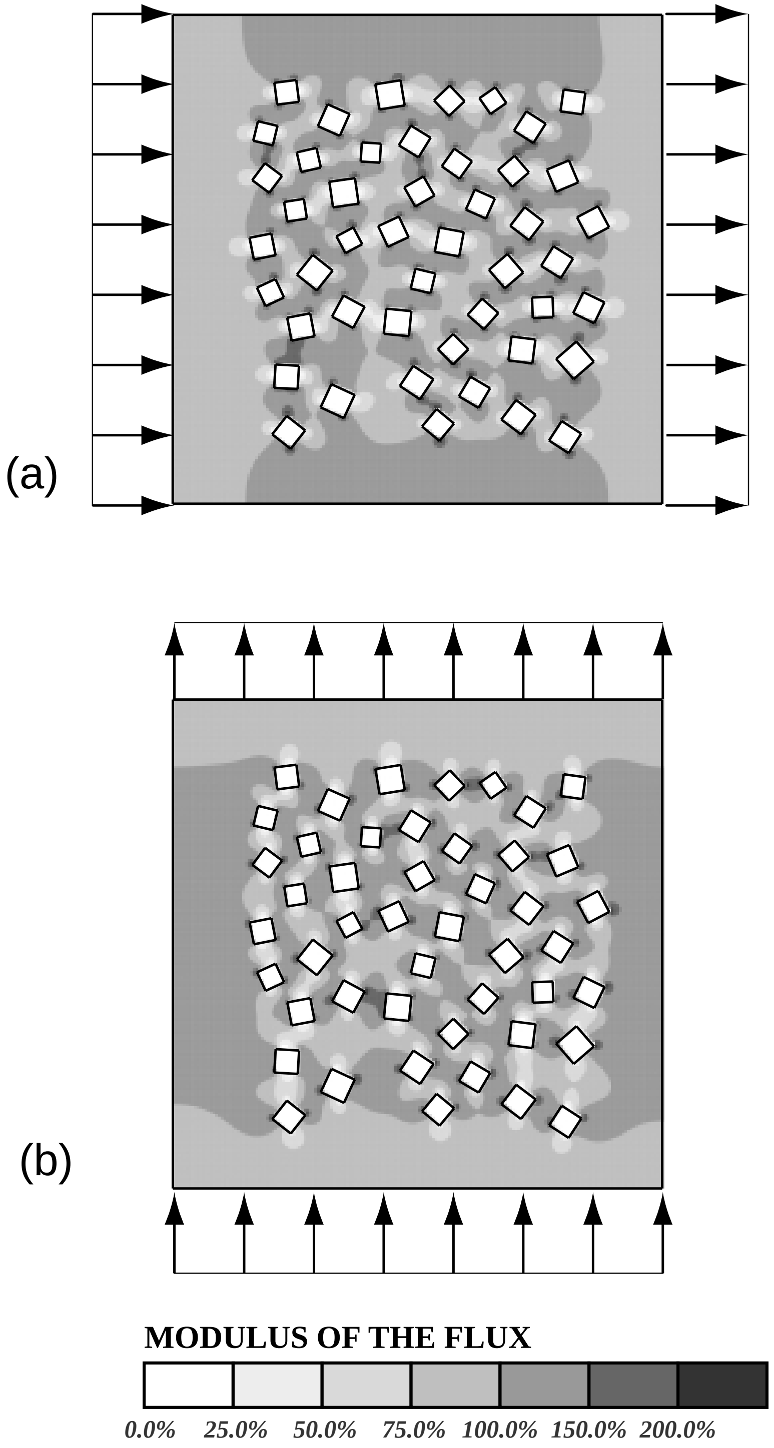

Figure 6.15. Examples of the handbook functions $\psi_j^{X;1}$, $j = 1, 2$, for the handbook domain $\tilde{\omega}_X^{(2);2}$ shown in Figure 6.9, obtained on the handbook mesh $T_{h/8}$ shown in Figure 6.13. Shades of the gradient of the pairs of handbook functions with the boundary conditions of degree $p_{\mathrm{hb}} = 1$: (a). $\nabla(\Re(z)) \cdot \mathbf{n}$, and (b). $\nabla(\Im(z)) \cdot \mathbf{n}$.

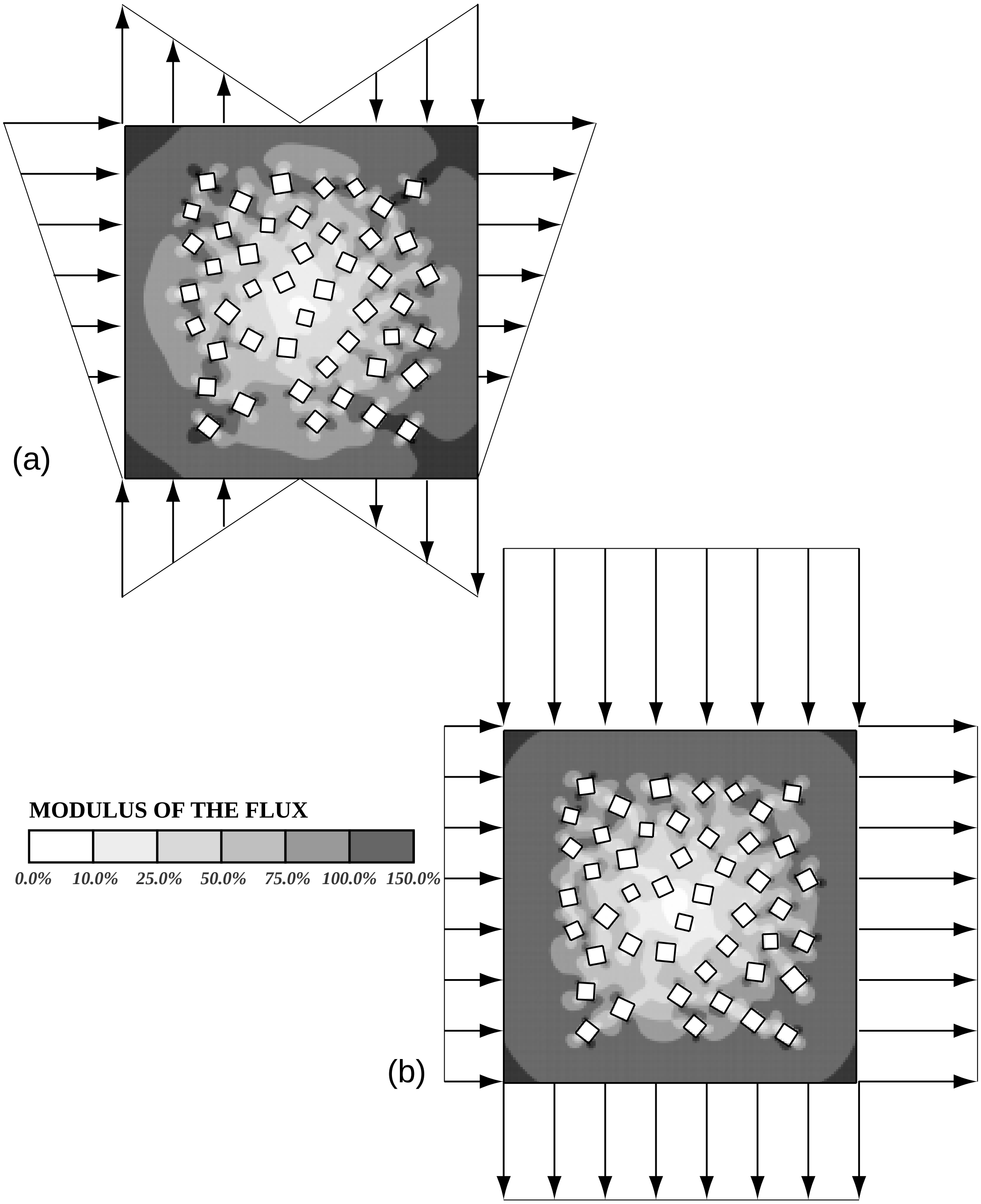

Figure 6.16. Examples of the handbook functions $\psi_j^{X;1}$, $j = 3, 4$, for the handbook domain $\tilde{\omega}_X^{(2);2}$ shown in Figure 6.9, obtained on the handbook mesh $T_{h/8}$ shown in Figure 6.13. Shades of the gradient of the pairs of handbook functions with the boundary conditions of degree $p_{\mathrm{hb}} = 2$: (a). $\nabla(\Re(z^2)) \cdot \mathbf{n}$, and (b). $\nabla(\Im(z^2)) \cdot \mathbf{n}$.

6.2.3 p-handbook convergence of GFEM

We first computed the bi-p GFEM solutions on the 4×4, 8×8, 16×16, 32×32, 64×64, 128×128, and 256×256 meshes for $p = 1,...,5$, using $p_{\mathrm{hb}} = 0$, in order to compare the convergence of the h and p-version of the Generalized FEM with $p_{\mathrm{hb}} = 0$, when no handbook functions are added, with the p-convergence with $p_{\mathrm{hb}} > 1$. Table 6.7 reports the energy norms and the corresponding relative errors of the GFEM solution for $p = 1,...,5$ ($p_{\mathrm{hb}} = 0$), $h = L/4, L/8, ..., L/256$ where L denotes the length of the side of the outer square of Ω. In Table 6.7, the GFEM solution for $p = 5$ and $p_{\mathrm{hb}} = 5$ on 16×16 mesh (see Table 6.8) is used as overkill solution in the computation of the relative error. Figure 6.17 shows the h and p convergence of the Generalized FEM with $p_{\mathrm{hb}} = 0$.

Table 6.7. h convergence of the energy norm of the solution of the model problem with 597 square voids . The numbers in bracket are the number of degree of freedom, and the percentage numbers are the relative error of the solution. Here the GFEM solution for $p = 5$ and $p_{\mathrm{hb}} = 5$ on 16×16 mesh (see Table 6.8) is used as overkill solution in the computation of the relative error.

	$p = 1$	$p = 2$	$p = 3$	$p = 4$	$p = 5$
4×4 mesh	492.756049 (25) 42.55%	492.881664 (81) 42.50%	493.089885 (169) 42.42%	493.278299 (289) 42.35%	493.468727 (441) 42.27%
8×8 mesh	492.849018 (81) 42.52%	493.228495 (289) 42.37%	493.759852 (625) 42.16%	494.717824 (1089) 41.78%	496.191904 (1681) 41.18%
16×16 mesh	493.132024 (289) 42.41%	494.709957 (1089) 41.78%	498.877783 (2401) 40.08%	505.960505 (4225) 36.96%	513.984623 (6561) 33.02%
32×32 mesh	494.465421 (1089) 41.88%	507.162909 (4225) 36.40%	520.302200 (9409) 29.49%	528.237288 (16641) 24.27%	532.575130 (25921) 20.83%
64×64 mesh	508.018432 (4225) 36.00%	529.227046 (16641) 23.53%	536.019025 (37249) 17.60%	538.661683 (66049) 14.63%	540.099278 (103041) 12.71%
128×128 mesh	528.845009 (16639) 23.82%	538.853212 (65424) 14.39%	541.193629 (145895) 11.03%	542.217437 (258052) 9.18%	542.783006 (401895) 7.97%
256×256 mesh	538.183904 (63930) 15.21%	542.276699 (247812) 9.06%	543.212359 (551050) 6.92%	543.604163 (973644) 5.79%	543.831533 (1515594) 5.01%

Table 6.8 reports the energy norms and the corresponding relative errors of the GFEM solution for $p = 1,...,5$, and $p_{\mathrm{hb}} = 1,...,5$, on the 16×16 mesh shown in Figure 6.8. Figure 6.17 compares its convergence versus the h and p convergence of the Generalized FEM with $p_{\mathrm{hb}} = 0$. Let us remark once more that the very significant improvement in the accuracy of the Generalized FEM is due to the employment of the handbook functions and that the p-handbook version of the method appears to converge exponentially. Let us recall the conclusion shown in Figure 4.7 for the case of 597 circular voids, we see that the improvement in the accuracy of the GFEM solution for the case of 597 square voids is bigger than the one for the case of 597 circular voids. The reason is that it is more difficult to have convergence without using any handbook functions for the case of 597 square voids, because of so many singularities in the domain.

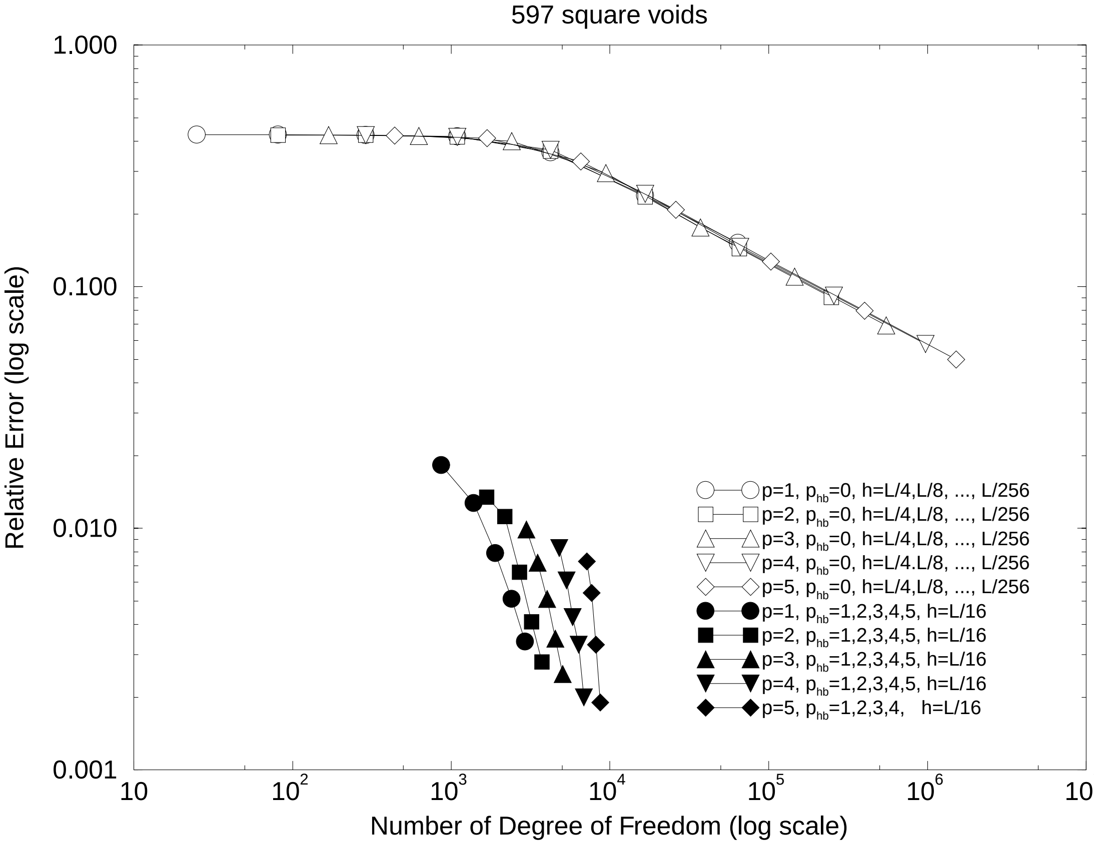

Figure 6.17. Comparison of the h-convergence of the FEM solution and the p_{hb}- convergence of the GFEM solution for the model problem with 597 square voids. Here the GFEM solutions were obtained by using $\tilde{\omega}_X^{(1);1}$ mesh-based handbook functions on handbook mesh $T_{h/8}$.

Table 6.8. p and p_{hb} convergence of the energy norm of the solution of the model problem with 597 square voids on the 16×16 mesh using the $\tilde{\omega}_X^{(1);1}$ mesh-based handbook functions. The handbook functions were obtained on mesh $T_{h/8}$. The numbers in bracket are the number of degree of freedom, and the percentage numbers are the relative error of the solution. Here the solution for $p = 5$ and $p_{\mathrm{hb}} = 5$ is used as overkill solution in the computation of the relative error.

	$p_{\mathrm{hb}} = 1$	$p_{\mathrm{hb}} = 2$	$p_{\mathrm{hb}} = 3$	$p_{\mathrm{hb}} = 4$	$p_{\mathrm{hb}} = 5$
$p = 1$	544.425699 (867) 1.83%	544.472388 (1381) 1.27%	544.499497 (1895) 0.79%	544.509458 (2409) 0.51%	544.513392 (2923) 0.34%
$p = 2$	544.466649 (1667) 1.35%	544.482562 (2181) 1.12%	544.504679 (2695) 0.66%	544.511962 (3209) 0.41%	544.514405 (3723) 0.28%
$p = 3$	544.489854 (2979) 0.99%	544.502425 (3493) 0.72%	544.509458 (4007) 0.51%	544.513204 (4521) 0.35%	544.514837 (5035) 0.25%
$p = 4$	544.497783 (4803) 0.83%	544.506408 (5317) 0.61%	544.511505 (5831) 0.43%	544.513574 (6345) 0.33%	544.515420 (6859) 0.20%
$p = 5$	544.501842 (7139) 0.73%	544.508600 (7653) 0.54%	544.513574 (8167) 0.33%	544.515556 (8681) 0.19%	544.516539 (9195)

In order to investigate the influence of the error in the numerical construction of the handbook functions on the GFEM solution, let us also consider the handbook mesh $T_{h/16}$ shown in Figure 6.10. Table 6.9 reports the energy norm of the GFEM solution for the model problem with 597 square voids, by using the $\tilde{\omega}_X^{(1);1}$ mesh-based handbook functions obtained on handbook mesh $T_{h/16}$. Compare Table 6.9 and Table 6.8, we see that the difference is small, and we even can not see this difference from the convergence graph shown in Figure 6.18.

Let us also look into the influence of the data included in the handbook domain. Consider the $\tilde{\omega}_X^{(2);2}$ handbooks shown in Figure 6.9(d). Table 6.10 reports the energy norm of the GFEM solution for the model problem with 597 square voids, by using $\tilde{\omega}_X^{(2);2}$ handbook functions obtained on handbook mesh $T_{h/8}$. Compare Table 6.10 and Table 6.8, we see that the relative error of the GFEM solution using $\tilde{\omega}_X^{(2);2}$ handbook functions is smaller than the one of using $\tilde{\omega}_X^{(1);1}$ handbook functions. Figure 6.19 shows that the convergence curve for the GFEM solution of using $\tilde{\omega}_X^{(2);2}$ handbook functions is shifted down, compared to the one for the GFEM solution of using $\tilde{\omega}_X^{(1);1}$ handbook functions. But the characteristics of p-handbook convergence are achieved for using both $\tilde{\omega}_X^{(1);1}$ and $\tilde{\omega}_X^{(2);2}$ handbook functions.

Table 6.9. p and p_{hb} convergence of the energy norm of the solution of the model problem with 597 square voids on the 16×16 mesh using the $\tilde{\omega}_X^{(1);1}$ mesh-based handbook functions. The handbook functions were obtained on mesh $T_{h/16}$. The numbers in bracket are the number of degree of freedom, and the percentage numbers are the relative error of the solution. Here the solution for $p = 5$ and $p_{\mathrm{hb}} = 5$ is used as overkill solution in the computation of the relative error.

	$p_{\mathrm{hb}} = 1$	$p_{\mathrm{hb}} = 2$	$p_{\mathrm{hb}} = 3$	$p_{\mathrm{hb}} = 4$	$p_{\mathrm{hb}} = 5$
$p = 1$	544.435508 (867) 1.73%	544.480725 (1381) 1.15%	544.505690 (1895) 0.64%	544.512009 (2409) 0.42%	544.514534 (2923) 0.29%
$p = 2$	544.476765 (1667) 1.21%	544.490974 (2181) 0.97%	544.508449 (2695) 0.55%	544.513847 (3209) 0.33%	544.515318 (3723) 0.23%
$p = 3$	544.494759 (2979) 0.90%	544.506681 (3493) 0.61%	544.511778 (4007) 0.43%	544.514649 (4521) 0.28%	544.515723 (5035) 0.20%
$p = 4$	544.500248 (4803) 0.78%	544.509164 (5317) 0.53%	544.513665 (5831) 0.34%	544.515372 (6345) 0.23%	544.515930 (6859) 0.18%
$p = 5$	544.506346 (7139) 0.62%	544.511299 (7653) 0.45%	544.514678 (8167) 0.28%	544.516025 (8681) 0.17%	544.516812 (9195)

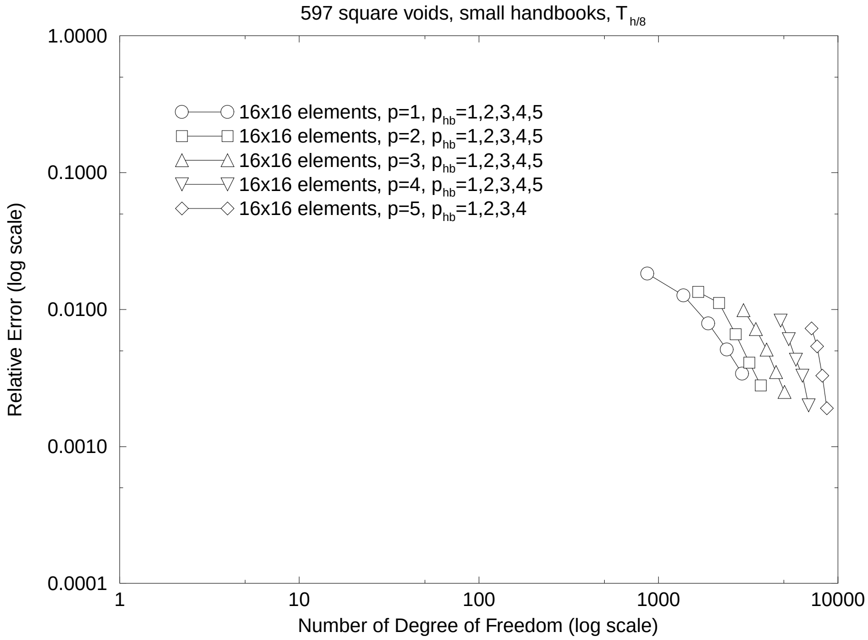

(a)

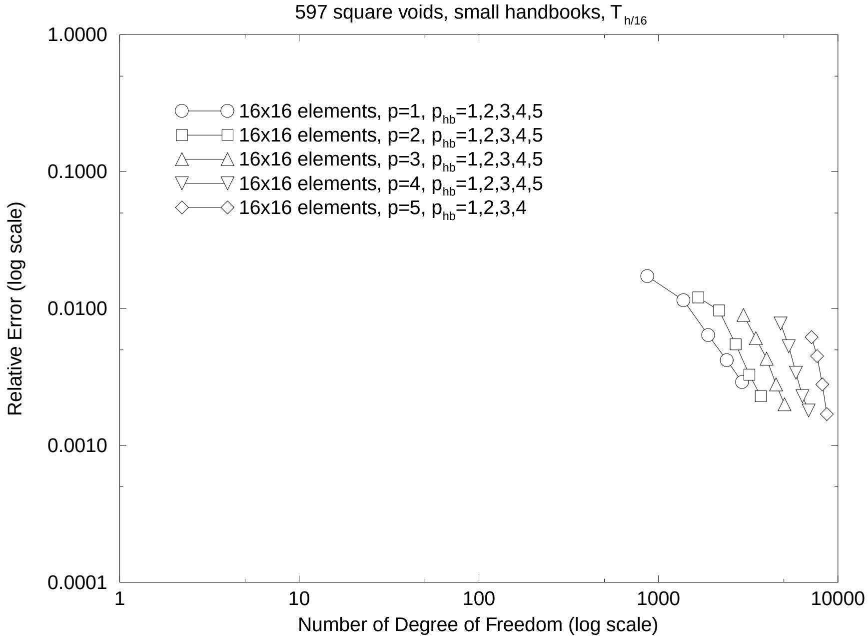

(b)

Figure 6.18. Convergence of the GFEM solution of the model problem with 597 square voids using $\tilde{\omega}_X^{(1);1}$ mesh-based handbook functions which were obtained on handbook mesh: (a). $T_{h/8}$; (b). $T_{h/16}$.

Table 6.10. p and p_{hb} convergence of the energy norm of the solution of the model problem with 597 square voids on the 16×16 mesh using the $\tilde{\omega}_X^{(2);2}$ mesh-based handbook functions. The handbook functions were obtained on mesh $T_{h/8}$. The numbers in bracket are the number of degree of freedom, and the percentage numbers are the relative error of the solution. Here the solution for $p = 5$ and $p_{\mathrm{hb}} = 5$ is used as overkill solution in the computation of the relative error.

	$p_{\mathrm{hb}} = 1$	$p_{\mathrm{hb}} = 2$	$p_{\mathrm{hb}} = 3$	$p_{\mathrm{hb}} = 4$	$p_{\mathrm{hb}} = 5$
$p = 1$	544.510786 (867) 0.67%	544.518785 (1381) 0.39%	544.521608 (1895) 0.22%	544.522392 (2409) 0.14%	544.522654 (2923) 0.10%
$p = 2$	544.517834 (1667) 0.43%	544.520554 (2181) 0.30%	544.522063 (2695) 0.18%	544.522597 (3209) 0.11%	544.522752 (3723) 0.08%
$p = 3$	544.519374 (2979) 0.36%	544.521215 (3493) 0.25%	544.522229 (4007) 0.16%	544.522638 (4521) 0.10%	544.522793 (5035) 0.07%
$p = 4$	544.519779 (4803) 0.34%	544.521486 (5317) 0.23%	544.522392 (5831) 0.14%	544.522706 (6345) 0.09%	544.522828 (6859) 0.06%
$p = 5$	544.520138 (7139) 0.32%	544.521837 (7653) 0.20%	544.522466 (8167) 0.13%	544.522825 (8681) 0.06%	544.522926 (9195)

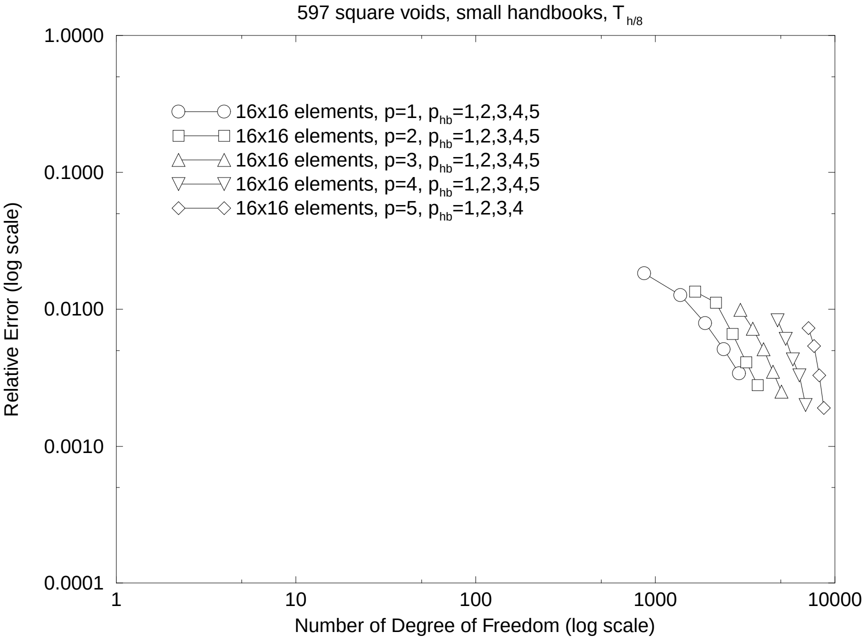

(a)

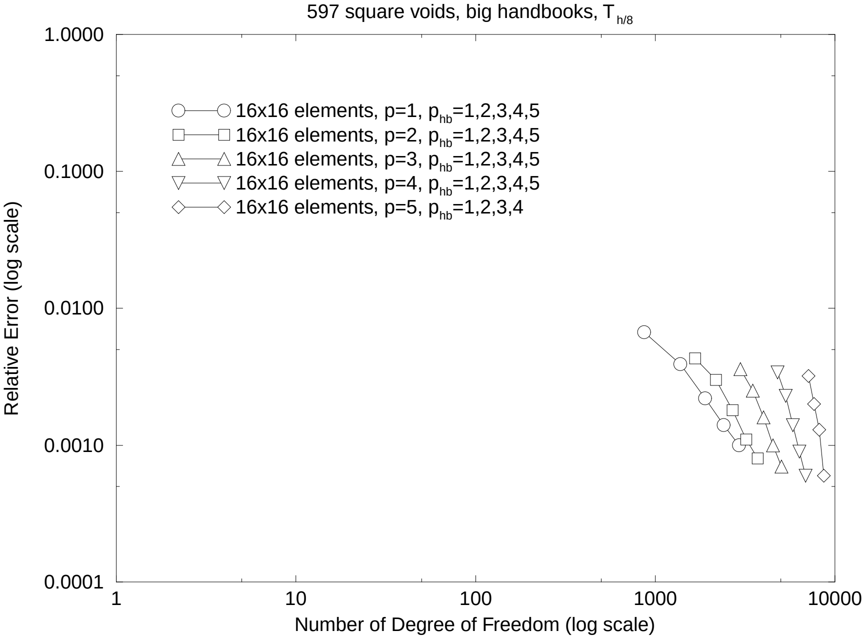

(b)

Figure 6.19. Convergence of the GFEM solution of the model problem with 597 square voids using: (a). $\tilde{\omega}_X^{(1);1}$; (b). $\tilde{\omega}_X^{(2);2}$ mesh-based handbook functions, on handbook mesh $T_{h/8}$.

CHAPTER VII

APPLICATION OF THE GENERALIZED FEM TO PROBLEMS WITH COMPOSITE MATERIALS

7.1 Introduction

In previous Chapters, we have shown that the Generalized FEM using mesh-based handbook functions is robust for the problems defined on complex domains. It has been shown that the GFEM solution can achieve very high accuracy, and the p-handbook convergence of the GFEM solution can be obtained for the problems with a large number of various types of features. In this Chapter, we will further demonstrate the powerfulness of the Generalized FEM using mesh-based handbook functions by applying it to the problems defined on domains with a real porous media and/or composite material.

As it was discussed in Chapter I, the macro-behavior of material bodies depends upon micromechanical properties, therefore the macro-analysis for the problems must be more reliable if the information about the local micromechanical properties can be utilized. To utilize the micro-scale properties in the macro-scale analysis, i.e. *Multiscale Analysis*, is now a widely used idea in research for the problems with porous media, composite materials, or random heterogeneous materials. In this area, various methods have been proposed. A short list of these methods may include Adaptive Hierarchical Modeling (developed by Oden et al. [18–25]), X-FEM (extended FEM, developed by Belytschko et al. [26–35]), Multiscale Finite Element Method (developed by Hou et al. [36–39]), VCFEM (Voronoi Cell Finite Element Method, developed by Ghosh et al. [40–43]), and Generalized FEM (GFEM, developed by Babuška and Strouboulis, et al. [44–54]). In this Chapter, we will show how the Generalized FEM using mesh-based handbook functions is powerful for *Multiscale Analysis*.

As our last model example, Model Problem VIII, let us consider the following heat conduction problem:

$$\begin{cases} -\Delta u &= 0, & \text{in} \quad \Omega, \\ \dfrac{\partial u}{\partial n} &= g \overset{\text{def}}{=} \nabla(2x-y)\cdot\mathbf{n}, & \text{on the outer boundary} \quad \Gamma, \\ \dfrac{\partial u}{\partial n} &= 0, & \text{on the boundary of the voids.} \end{cases} \tag{7.1}$$

if the domain Ω is a porous media; and

$$\begin{cases} -\nabla(K\nabla u) &= 0, \qquad\qquad\qquad \text{in} \quad \Omega, \\ K\dfrac{\partial u}{\partial n} &= g \overset{\text{def}}{=} \nabla(2x-y)\cdot\mathbf{n}, \quad \text{on the outer boundary} \quad \Gamma, \end{cases} \tag{7.2}$$

if the domain Ω is a composite material; where Ω is the domain shown in Figure 7.1, and, in the case of composite material, the coefficient of heat conductivity K has the following form:

$$K = \begin{cases} K_1, & \text{in the matrix,} \\ K_2, & \text{in the fibers} \end{cases} \tag{7.3}$$

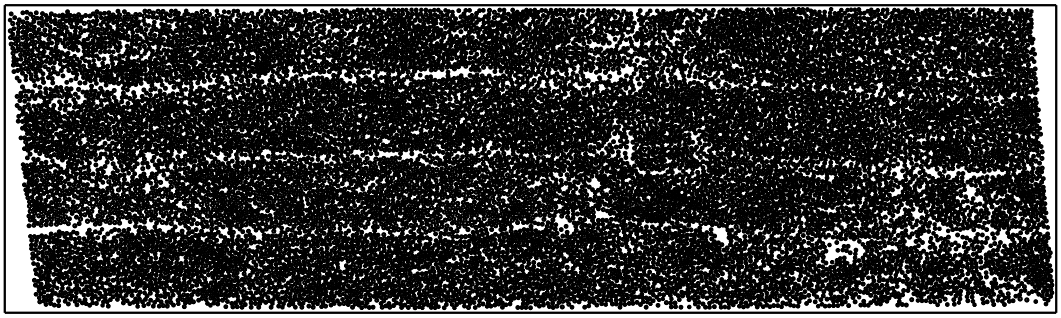

Figure 7.1. The domain with 16275 circular features for Model Problem VIII.

Figure 7.1 shows the cross-section of a unidirectional pre-preg produced by Ciba-Geigy, and the material is denoted by HTA/6376. Babuška and Andersson et al. [1] gave a computational analysis of damage and fracture in this material by concentrating on stochastic constitutive properties and statistics of the maximal local fiber-matrix interface stresses. In the following computation, for the sake of convenience, we will consider the case of a porous media, i.e. the circles are voids. For the case of a composite material, the conclusion is the same as it was demonstrated in pervious Chapters for the cases of 597 voids (in Chapter III and IV) and 597 inclusions (in Chapter V).

Let us define a window of interest for our analysis. The window of interest, denoted by W, is a square located at the center of the domain, including 84 voids/fibers in the interior and 28 voids/fibers intersecting the boundary of the square, shown in Figure 7.2. Let us use this small window of interest, W, to address the difficulty of this kind of problem. Figure 7.3 shows an FEM quadrilateral mesh for the window of interest, W, produced by ANSYS for the case of porous media, including 11432 quadrilateral elements (12753 nodes). If the whole domain could be meshed by ANSYS (in fact, ANSYS can not mesh the whole domain), it would have about 2.5 million degrees of freedom if the bilinear standard FEM is employed for the whole problem with porous media.

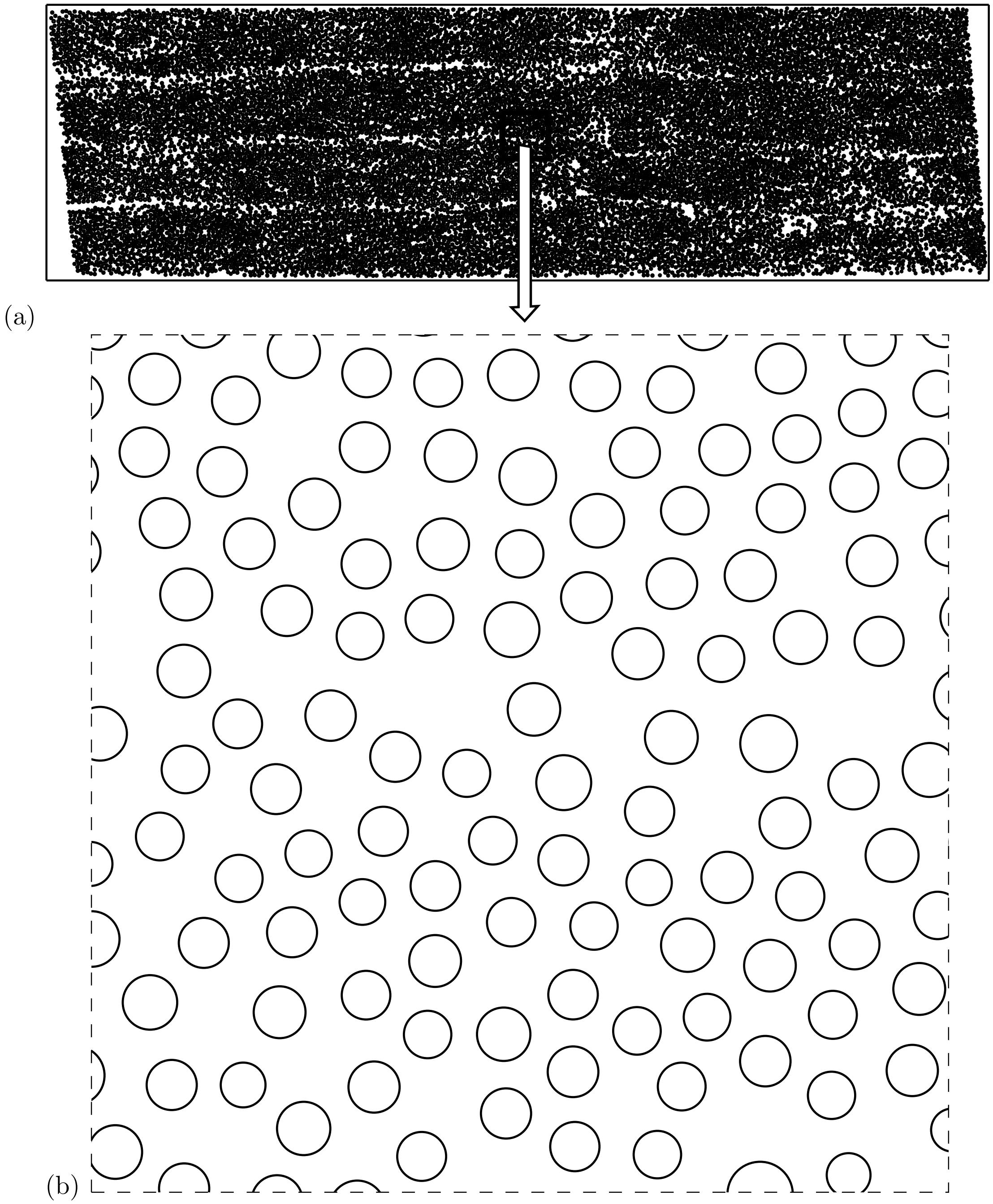

Figure 7.2. (a). The problem domain. (b). The window of interest, W.

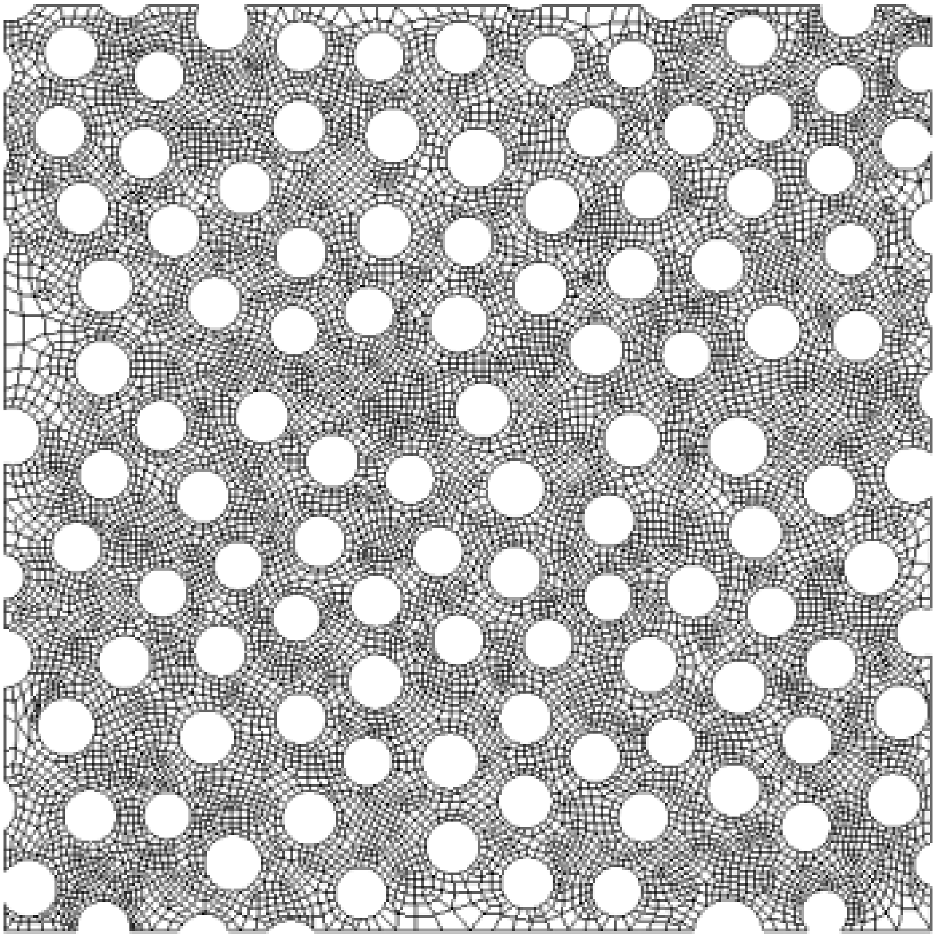

Figure 7.3. An FEM quadrilateral mesh for the window of interest, W, produced by ANSYS for the case of porous media.

7.2 Mesh-based handbook functions for Model Problem VIII

In multiscale analysis, the accuracy of the microscale information is essential for the correct macroscale analysis. This was also analyzed in previous Chapters of this dissertation, i.e. the effect of the error in the numerically constructed handbook functions and the effect of the data included in the handbook problems. We have seen that the microscale information of the problem can be reflected accurately by the mesh-based handbook functions.

Let us recall the definition of the handbook domain $\tilde{\omega}_X^{(k);d}$ given in Chapter IV. For a given vertex X, the handbook domain $\tilde{\omega}_X^{(k);d}$ is the area including $k+1$ layers of elements around the vertex X, and including all the features intersecting the d layers of elements (see Figure 4.14). The parameter d was an integer in the definition. Here let us first extend the handbook domain $\tilde{\omega}_X^{(k);d}$ for a non-integer d. A handbook domain $\tilde{\omega}_X^{(k);d}$ with a non-integer d associated with a vertex X is defined as follows: First, define the neighborhood $\omega_X^{(k)}$ centered at X, as it was defined before, formed by the $k+1$ layers of elements around the vertex X. Then define a window centered at the vertex X with the size $2dh_x \times 2dh_y$, where h_x and h_y are the mesh size in x and y direction, respectively. Finally, use this window to determine the features in the created handbook, i.e. all the features intersecting this window and included in the neighborhood $\omega_X^{(k)}$ are included in the created handbook. Figure 7.4 shows the creation of the handbook $\tilde{\omega}_X^{(k);d}$ for a typical vertex X for $k = 1$ and $d = 1.25$. Let us note that the range of the parameter d is $1 \leq d \leq k+1$, and other choices of d are meaningless.

The accuracy of the handbook functions $\psi_j^{X;1}$ are critical for achieving the p-handbook convergence for the global GFEM solution. Based on the conclusions in previous Chapters, we employ the handbook mesh $T_{h/8}$ for this model problem. Figure 7.5 shows the $T_{h/8}$ handbook mesh for the typical handbook domain $\tilde{\omega}_X^{(1);1.25}$ shown in Figure 7.4. The handbook functions obtained on the handbook mesh $T_{h/8}$ have sufficient accuracy so that the global GFEM solution converges exponentially.

The boundary conditions for the handbook problems were described in Chapter III. The handbook functions $\psi_j^{X;1}$ were solved on the handbook mesh $T_{h/8}$ shown in Figure 7.5, and by using the bi-p ($p = 5$) FE basis together with voids/inclusions functions of degree one ($p_{\text{voids}} = 1$ or $p_{\text{inclusions}} = 1$) at $n_{\text{layers}} = 0$ around each void/inclusion. Figure 7.6 shows the modulus of the gradient of handbook functions $\psi_j^{X;1}$, $j = 1, ..., 4$, of degree (a) $p_{\text{hb}} = 1$ ($\nabla(\Re(z)) \cdot \mathbf{n}$ and $\nabla(\Im(z)) \cdot \mathbf{n}$), and (b) $p_{\text{hb}} = 2$ ($\nabla(\Re(z^2)) \cdot \mathbf{n}$ and $\nabla(\Im(z^2)) \cdot \mathbf{n}$), for the porous media. In next Section, we will see that the enrichment of the global GFEM space by these handbook functions makes the global GFEM solution converges exponentially.

7.3 p-handbook convergence of GFEM

Based on the microscale information, i.e. the handbook functions, described in the previous Section, we are able to analyze the macroscale performance of the solution. We measure the macroscale performance in terms of energy norm, i.e. the energy norm of the global GFEM solution.

In order to compare, let us first compute the GFEM solution without using any handbook functions on serious global meshes. Figure 7.4(a) shows the 64×16 mesh which will also be employed in the computation of the Generalized FEM solution using mesh-based handbook functions, and Figure 7.7(a) and 7.7(b) show a part of 64×16 mesh and 512×128 mesh, respectively, in the window W. Let us remark that the comparison of Figure 7.7 and Figure 7.3 gives a strong impression on the advantages of GFEM meshes.

Table 7.1 reports the h convergence of the energy norm of the GFEM solution for the

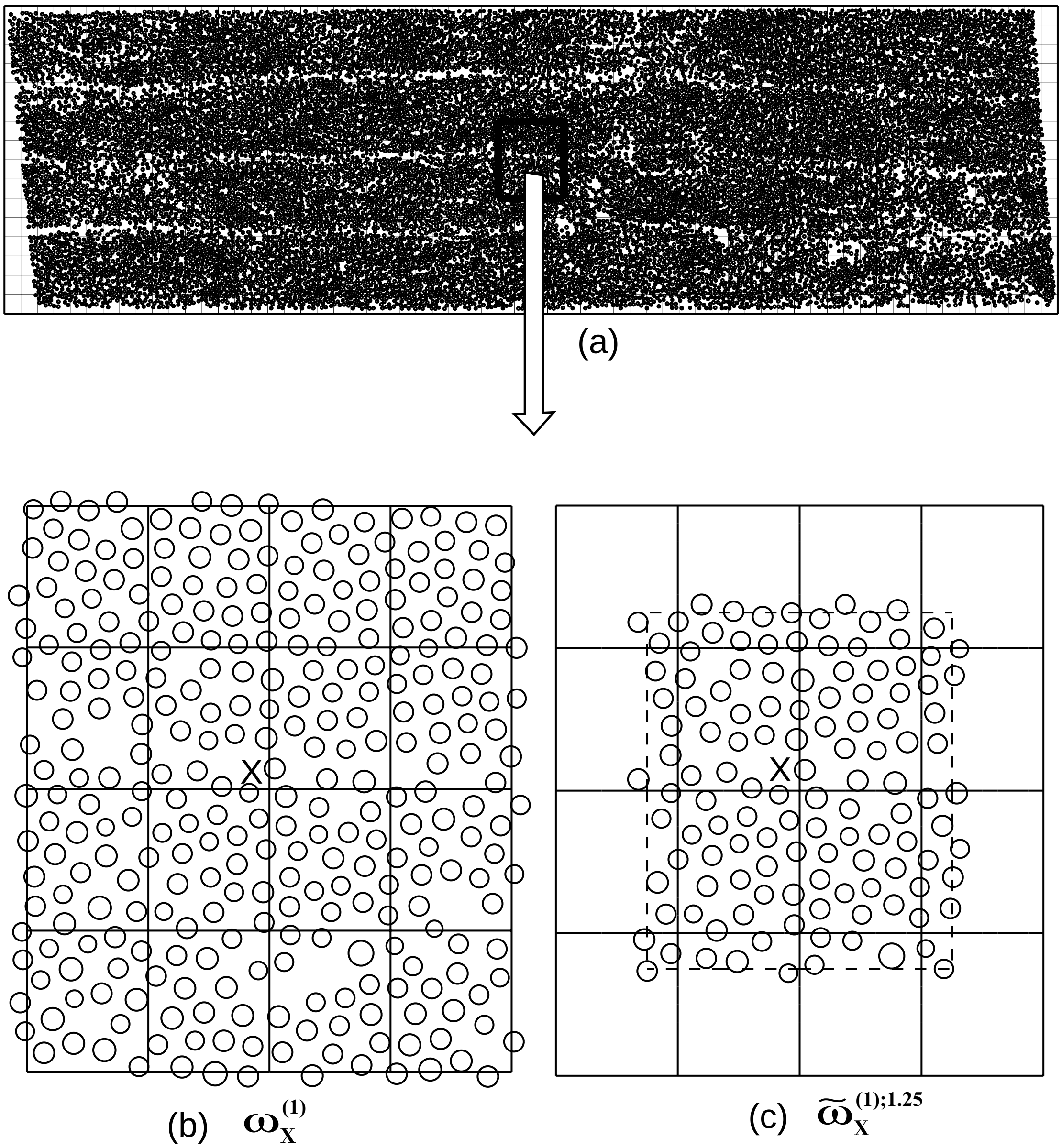

Figure 7.4. Creation of a typical handbook domain associated with a vertex X. (a) The problem domain Ω including 16275 circular voids/inclusions covered by the 64×16 mesh Δ_h; (b) The neighborhood $\omega_X^{(1)}$ with voids/inclusions intersecting them; (c) The handbook domain $\tilde{\omega}_X^{(1);1.25}$. The window enclosed by the dotted lines, with the size $2dh_x \times 2dh_y$ (h_x and h_y are the mesh size in x and y direction, respectively), is used to determine the voids/inclusions in the handbook.

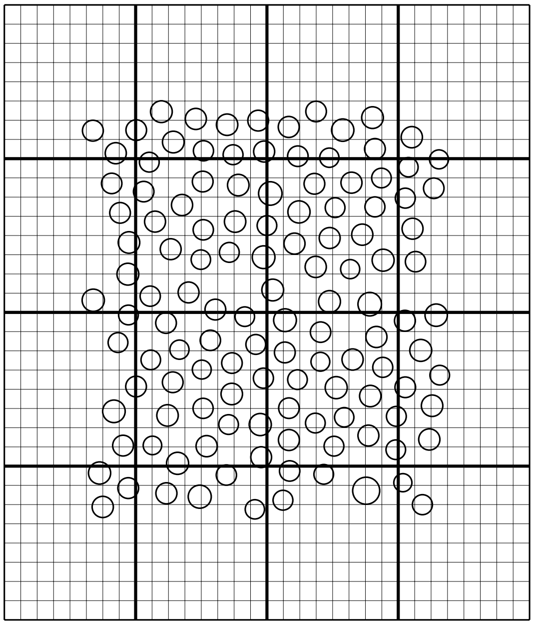

Figure 7.5. Handbook mesh $T_{h/8}$ employed in the computation for the typical handbook domain $\tilde{\omega}_X^{(1);1.25}$ associated with the vertex X. The thick lines form the elements in the global mesh.

model problem VIII with 16275 voids, without using any handbook functions, while the Figure 7.8 shows the plot of the h convergence. The character of slow h convergence is very similar to the one shown in Table 4.4 and Figure 4.7 for the model example with 597 voids.

Now let us look into the results of the Generalized FEM using mesh-based handbook functions. Table 7.2 reports the energy norm of the GFEM solution using the $\tilde{\omega}_X^{(1);1.25}$ mesh-based handbook functions, for the model problem VIII with 16275 voids on the 46×16 mesh. Figure 7.8 also shows the p-handbook convergence of the GFEM solution, in addition to the h convergence. We see that the exponential convergence is achieved. Figure 7.9 shows the modulus of the gradient of the GFEM solution with $p = 2$ and $p_{\text{hb}} = 1$, i.e. $u_{\text{GFEM}}^{p=2,p_{\text{hb}}=1}$, in the window of interest W. The heat flow is clearly seen in Figure 7.9.

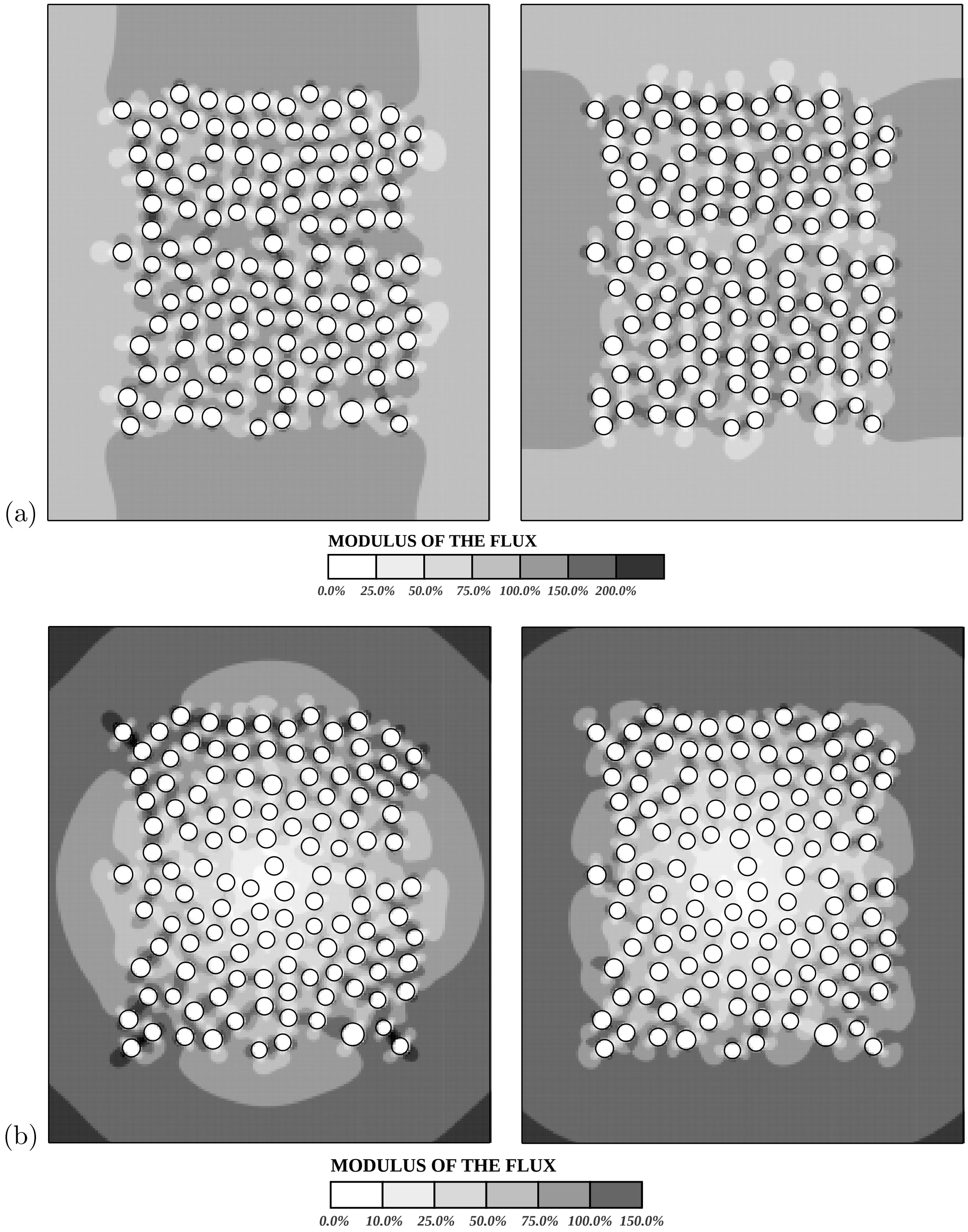

Figure 7.6. Examples of the handbook functions $\psi_j^{X;1}$, $j = 1, ..., 4$, for the handbook domain $\tilde{\omega}_X^{(1);1.25}$ shown in Figure 6.9, obtained on the handbook mesh $T_{h/8}$ shown in Figure 7.4 for the case of porous media. Shades of the gradient of the pairs of handbook functions of degree (a) $p_{\mathrm{hb}} = 1$ ($\nabla(\Re(z)) \cdot \mathbf{n}$ and $\nabla(\Im(z)) \cdot \mathbf{n}$), and (b) $p_{\mathrm{hb}} = 2$ ($\nabla(\Re(z^2)) \cdot \mathbf{n}$ and $\nabla(\Im(z^2)) \cdot \mathbf{n}$).

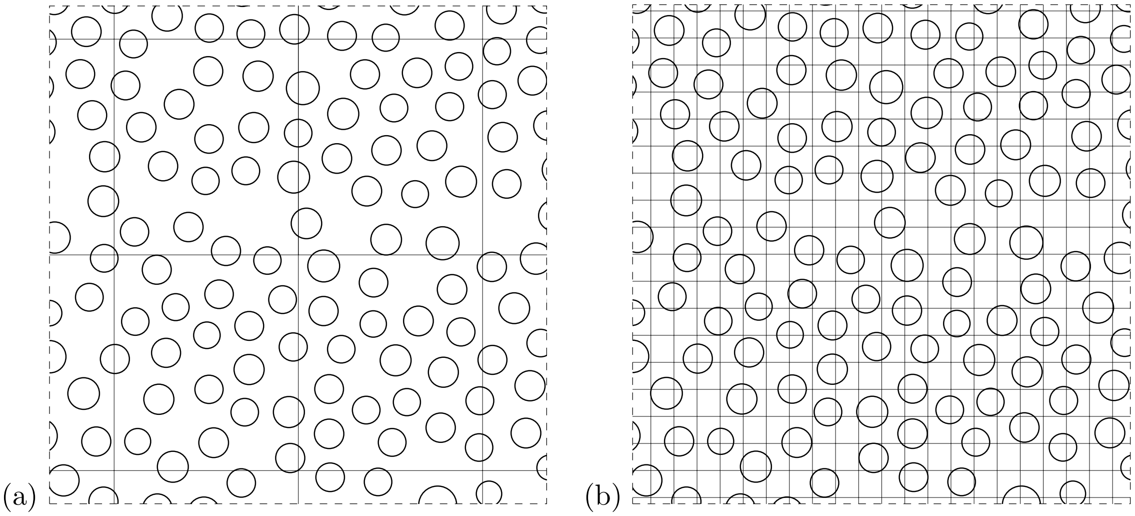

Figure 7.7. The part of meshes in window W for: (a). 64×16 mesh; (b). 512×128 mesh.

Table 7.1. h convergence of the energy norm of the GFEM solution of the model problem VIII with 16275 voids without using any handbook functions. The numbers in bracket are the number of degree of freedom, and the percentage numbers are the relative error of the solution. Here the GFEM solution for $p = 5$ and $p_{\text{hb}} = 5$ on 64×16 mesh is used as overkill solution in the computation of the relative error.

	$p = 1$	$p = 2$	$p = 3$	$p = 4$	$p = 5$
16×4 elements	2701.353529 (85) 46.81%	2703.172748 (297) 46.70%	2704.288811 (637) 46.63%	2704.810770 (1105) 46.60%	2705.315804 (1701) 46.56%
32×8 elements	2702.743320 (297) 46.72%	2704.622115 (1105) 46.61%	2705.730577 (2425) 46.54%	2706.908431 (4257) 46.46%	2708.299590 (6601) 46.38%
64×16 elements	2704.263155 (1105) 46.63%	2706.790012 (4257) 46.47%	2710.041620 (9457) 46.27%	2715.586063 (16705) 45.92%	2724.675923 (26001) 45.34%
128×32 elements	2706.476436 (4257) 46.49%	2715.439616 (16705) 45.93%	2736.821667 (37345) 44.55%	2780.314896 (66177) 41.57%	2847.117415 (103201) 36.41%
256×64 elements	2713.143027 (16705) 46.07%	2792.546746 (66177) 40.68%	2925.206309 (148417) 29.04%	2997.811775 (263425) 19.57%	3031.252637 (411201) 12.94%
512×128 elements	2808.508364 (66177) 39.49%	3004.214408 (263425) 18.49%	3049.606656 (591745) 6.92%	3054.460128 (1051137) 4.03%	3056.409060 (1641601) 1.87%

Table 7.2. p and p_{hb} convergence of the energy norm of the solution of the model problem VIII with 16275 voids on the 46×16 mesh using the $\tilde{\omega}_X^{(1);1.25}$ mesh-based handbook functions. The numbers in bracket are the number of degree of freedom, and the percentage numbers are the relative error of the solution. Here the solution for $p = 5$ and $p_{\mathrm{hb}} = 5$, whose energy norm is $\|u_{\mathrm{GFEM}}^{p=5,p_{\mathrm{hb}}=5}\|_{\mathsf{U}} = 3056.943512$ with the number of degree of freedom $N_{\mathrm{dof}} = 36363$, is used as overkill solution in the computation of the relative error.

	$p_{\mathrm{hb}} = 1$	$p_{\mathrm{hb}} = 2$	$p_{\mathrm{hb}} = 3$
$p = 1$	3054.835645 (3299) 3.71%	3055.665106 (5341) 2.89%	3056.356278 (7383) 1.96%
$p = 2$	3056.247411 (6455) 2.13%	3056.465516 (8499) 1.77%	3056.799249 (10535) 0.97%
$p = 3$	3056.600494 (11651) 1.50%	3056.855226 (13693) 0.76%	3056.913921 (15735) 0.44%

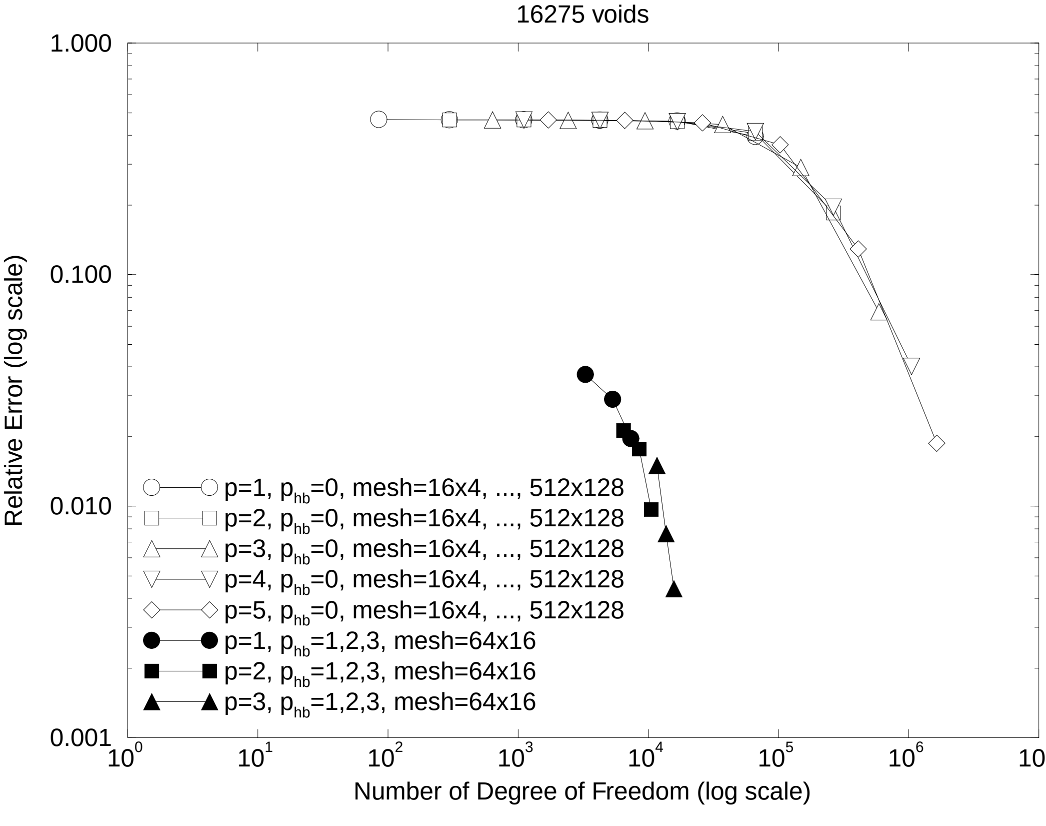

Figure 7.8. Convergence of the GFEM solution using and without using the $\tilde{\omega}_X^{(1);1.25}$ mesh-based handbook functions for the model problem VIII with 16275 voids.

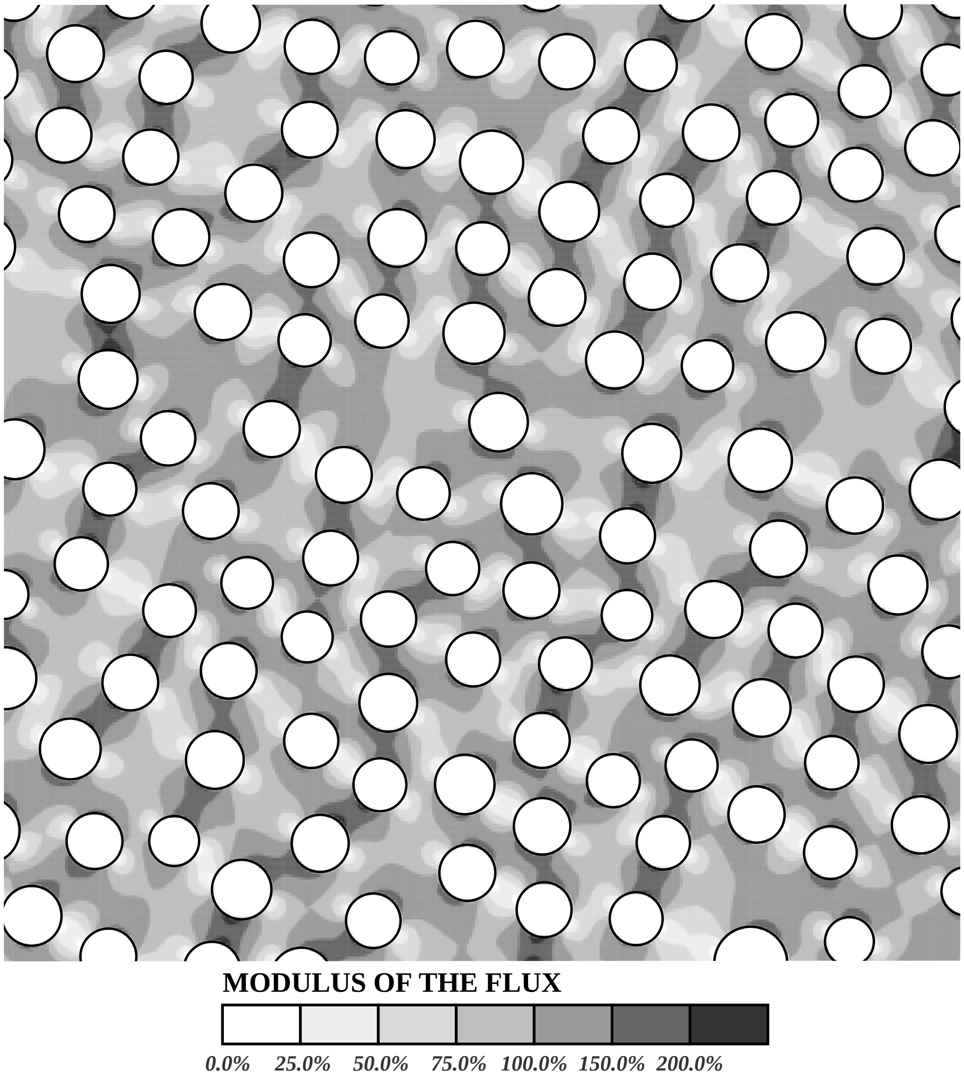

Figure 7.9. Modulus of the gradient of the GFEM solution in the window W for the model problem VIII with 16275 voids for $p = 2$ and $p_{\mathrm{hb}} = 1$ on the 64×16 mesh using the $\tilde{\omega}_X^{(1);1.25}$ mesh-based handbook functions.

CHAPTER VIII

CONCLUSIONS AND RECOMMENDATIONS FOR FUTURE WORK

8.1 Conclusions

In this dissertation, we proposed a new method for multiscale analysis, i.e. the Generalized FEM using the mesh-based handbook functions. Let us summarize the main attributes of the method.

Enrichment of the approximation space by mesh-based handbook functions: The method establishes the approximation by enriching the standard FE basis by the mesh-based handbook functions which are incorporated into the approximation by employing the PUM. The mesh-based handbook functions reflect the microscale behavior of the exact solution, and have great impact on the accuracy of the macroscale analysis.

Meshless technology: The main difficulty in the application of the standard FEM in engineering problems is the generation of a mesh as a partition of the problem domain into triangles and/or quadrilaterals. The GFEM is capable of employing meshes which are allowed to overlap part or all of the problem domain boundary and/or the interfaces between multi-materials, For example, meshes of squares generated by the refinement of one square which contains the problem domain in its interior. This attribute of the method makes the macroscale analysis possible for the problems with a large number of features and complex geometries.

The main conclusions of the Generalized FEM for the multiscale analysis are:

(1). The p-handbook (p_{hb}) version of the Generalized FEM is robust and can achieve exponential convergence and high accuracy for difficult problems e.g. for the Laplacian in domains with a large number of closely spaced features.

(2). To achieve similar accuracy without using handbooks may be practically impossible in many cases.

(3). The exponential convergence and high accuracy may be polluted by errors in the numerical construction of the handbook functions.

(4). The exponential convergence depends on the data included in the handbooks and the employed buffer.

(5). The CPU cost of the Generalized FEM has three parts: (a) The cost of the numerical construction of the handbook functions; (b) The cost of the numerical integration of the stiffness coefficients of the linear system of GFEM equations for the global problem; (c) The cost of solving the linear system of GFEM equations for the global problem. The first part, namely the numerical construction of the handbook functions is the most expansive part of the computation. The second part, the numerical integration of the stiffness coefficients is expensive for higher p_{hb} and p, however it is still less, almost by an order of magnitude, than the cost of the numerical construction of the handbook functions. The solution of the linear system of GFEM equations is the least expensive part of the computation. Because the computation of the handbook functions and the numerical integrations of the GFEM stiffness coefficients have local character very efficient implementations of the Generalized FEM may be achieved on parallel computers.

(6). Hierarchical implementation of the handbook problems should make the method capable of solving efficiently problems of multiscale analysis with a very large number of features.

(7). Our Generalized FEM is most effective when using a coarse mesh Δ_h and a high degree p_{hb} and p, analogously as in the classical p-version [71] (which is most effective when the solution is smooth and can achieve very high accuracy on a very coarse mesh). The coarseness of the mesh Δ_h is only limited by the computational effort needed for the numerical construction of the handbook functions corresponding to the mesh.

(8). Here we considered the Laplacian as our model problem. Similar results should be expected if the Laplacian is replaced by the elasticity problem.

8.2 Recommendations for future work

There are many possibilities and a great potential for extending the ideas proposed in this dissertation. A few of them are described as follows.

For the problems defined on domains with porous media and/or composite material, homogenization is a widely studied method. It is possible to find out the relationship between the homogenization and the Generalized FEM using mesh-based handbook functions for problems with periodic microstructures. Further, a large potential is to utilize the Generalized FEM for developing a new method of "homogenization" for problems with randomly located features, and/or heterogeneous problems.

A more effective way of using the Generalized FEM is expected. For example, for some types of quantity of interest, such as the temperature and/or heat flux at a given point, we may not need very accurate handbook functions at the places far away from the point of interest. An adaptive scheme of the GFEM is visible for this purpose. But a good error estimate has to be developed for the Generalized FEM, in order to implement the adaptive GFEM. This is related to the next possibility of the extension.

It is possible to extend the capabilities of guaranteed a posteriori error estimations which were developed for the FEM to the Generalized FEM in its most general setting, including the use of the mesh-based handbook functions. The two-side error estimates will enhance the robustness of the Generalized FEM.

Another possibility of enhancing the effectivity of GFEM using mesh-based handbook functions is to implement the parallel computing. The details need to be investigated in this area.

The Generalized FEM using mesh-based handbook functions can also be extended to other problems, such as time-dependent problems, nonlinear problems, etc.. The mesh-based handbook functions have to be judiciously created and computed for reflecting the local characteristics of the exact solution, so that the GFEM solution can achieve high accuracy.

REFERENCES

[1] I. Babuška, B. Andersson, P.J. Smith and K. Levin, Damage analysis of fiber composites. Part I: Statistical analysis on fiber scale, Comp. Meth. Appl. Mech. Engng. 172 (1999) 27–78.

[2] R. Hill, The elastic behavior of a crystalline aggregate, Proc. Phys. Soc. London 65 (1952) 349–354.

[3] Z. Hashin and S. Shtrikman, A variational approach to the theory of the elastic behavior of multiphase materials, J. Mech. Phys. Solids 11 (1963) 127–140.

[4] I. Babuška, Homogenization and its application: Mathematical and computational problems, in: B. Hubbard (Ed.), Numerical Solution of Partial Differential Equations III, SYNSPADE, Academic Press, New York, 1975, pp. 89–116.

[5] I. Babuška, Solution of interface problems by homogenization. I, SIAM J. Math. Anal. 7 (5) (1976) 603–634.

[6] I. Babuška, Solution of interface problems by homogenization. II, SIAM J. Math. Anal. 7 (5) (1976) 635–645.

[7] I. Babuška, Solution of interface problems by homogenization. III, SIAM J. Math. Anal. 8 (6) (1977) 923–937.

[8] I. Babuška and R.C. Morgan, Composites with a periodic structure: Mathematical analysis and numerical treatment, Comp. Math. Appl. 11 (10) (1985) 995–1005.

[9] R.C. Morgan and I. Babuška, An approach for constructing families of homogenized equations for periodic media. I: An integral representation and its consequences, SIAM J. Math. Anal. 22 (1) (1991) 1–15.

[10] R.C. Morgan and I. Babuška, An approach for constructing families of homogenized equations for periodic media. II: Properties of the kernel, SIAM J. Math. Anal. 22 (1) (1991) 16–33.

[11] I. Babuška, G. Caloz and J.E. Osborn, Special finite element methods for a class of second order elliptic problems with rough coefficients, SIAM J. Numer. Anal. 31 (4) (1994) 945–981, (submitted in March 1992).

[12] A. Bensoussan, J.L. Lions and G. Papanicolaou, Asymptotic Analysis for Periodic Structures, North-Holland, Amsterdam, 1978, in volume 5 of *Studies in Mathematics and Its Applications*.

[13] V.V. Jikov, S.M. Kozlov and O.A. Oleinik, Homogenization of Differential Operators and Integral Functionals, Springer-Verlag, Heidelberg, 1994.

[14] E. Sanchez-Palencia, Non-homogeneous Media and Vibration Theory, Springer-Verlag, Berlin, 1980, in number 127 of *Lecture Notes in Physics*.

[15] D. Cioranescu and P. Donato, An Introduction to Homogenization, Oxford University Press, New York, 1999, in number 17 of Oxford Lecture Series in Mathematics and Its Applications.

[16] D. Cioranescu and J.S.J. Paulin, in: Homogenization of Reticulated Structures, Springer-Verlag, New York, 1999, Applied Mathematical Sciences, 136.

[17] N. Bakhvalov and G. Panasenko, Homogenization: Averaging Processes in Periodic Media, Nauka Publishers, Moscow, 1984, (English edition published by Kluwer Academic Publishers in 1989).

[18] T. Zohdi, Analysis and adaptive modeling of highly heterogeneous elastic structures, Ph.D. dissertation, The University of Texas at Austin, Austin, TX (1997).

[19] T.I. Zohdi, J.T. Oden and G.J. Rodin, Hierarchical modeling of heterogeneous bodies, Comp. Meth. Appl. Mech. Engrg. 138 (1996) 273–298.

[20] J.T. Oden and T.I. Zohdi, Analysis and adaptive modeling of highly heterogeneous elastic structures, Comp. Meth. Appl. Mech. Engrg. 148 (1997) 367–391.

[21] J.T. Oden, K. Vemaganti and N. Moës, Hierarchical modeling of heterogeneous solids, Comp. Meth. Appl. Mech. Engrg. 172 (1999) 3–25.

[22] J.T. Oden and K. Vemaganti, Adaptive hierarchical modeling of heterogeneous structures, Physica D 133 (1999) 404–415.

[23] J.T. Oden and K. Vemaganti, Adaptive modeling of composite structures: Modeling error estimation, Int. J. Comp. Civil Str. Engrg 1 (2000) 1–16.

[24] J.T. Oden and K. Vemaganti, Estimation of local modeling error and goal-oriented adaptive modeling of heterogeneous materials; Part I: Error estimates and adaptive algorithms, J. Comp. Phys. 164 (2000) 22–47.

[25] K. Vemaganti, Goal-oriented adaptive modeling of heterogeneous elastic solids, Ph.D. dissertation, The University of Texas at Austin, Austin, TX (2000).

[26] N. Moës, J. Dolbow and T. Belytschko, A finite element method for crack growth without remeshing, Int. J. Numer. Meth. Engrg. 46 (1999) 131–150.

[27] J. Dolbow, N. Moës and T. Belytschko, Modeling fracture in Mindlin-Reissner plates with the extended finite element method, International Journal of Solids and Structures 37 (2000) 7161–7183.

[28] J. Dolbow, N. Moës and T. Belytschko, Discontinuous enrichment in finite elements with a partition of unity method, Finite Elements in Analysis and Design 36 (2000) 235–260.

[29] T. Belytschko, N. Moës, S. Usui and C. Parimi, Arbitrary discontinuities in finite elements, Int. J. Numer. Meth. Engrg. 50 (2001) 993–1013.

[30] N. Sukumar, D.L. Chopp, N. Moës, and T. Belytschko, Modeling holes and inclusions by level sets in the extended finite-element method, Compu. Methods Appl. Mech. Engrg. 190 (2001) 6183–6200.

[31] G.J. Wagner, N. Moës, W.K. Liu and T. T. Belytschko, The extended finite element method for rigid particles in Stokes flow, Int. J. Numer. Meth. Engrg. 51 (2001) 293–313.

[32] A. Gravouil, N. Moës and T. Belytschko, Non-planar 3D crack growth by the extended finite element and level sets – Part I: Mechanical model, Int. J. Numer. Meth. Engrg. 53 (2002) 2549–2568.

[33] A. Gravouil, N. Moës and T. Belytschko, Non-planar 3D crack growth by the extended finite element and level sets – Part II: Level set update, Int. J. Numer. Meth. Engrg. 53 (2002) 2569–2586.

[34] T. Belytschko, C. Parimi, N. Moës, N. Sukumar, and S. Usui, Structured extended finite element methods for solid defined by implicit surfaces, Int. J. Numer. Meth. Engrg. 56 (2003) 609–635.

[35] B.L. Karihaloo and Q.Z. Xiao, Modelling of stationary and growing cracks in FE framework without remeshing: A state-of-art review, Computers and Structures 81 (2003) 119–129.

[36] T.Y. Hou and X.H. Wu, A multiscale finite element method for elliptic problems in composites materials and porous media, J. Computational Physics 134 (1997) 169–189.

[37] T.Y. Hou, X.H. Wu and Z.Q. Cai, Convergence of a multiscale finite element method for elliptic problems with rapidly oscillating coefficients, Math. Comp. 68 (227) (1999) 913–943.

[38] Y.R. Efendiev, T.Y. Hou and X.H. Wu, Convergence of a nonconforming multiscale finite element method, SIAM J. Numer. Anal. 37 (3) (2000) 888–910.

[39] Z.M. Chen and T.Y. Hou, A mixed multiscale finite element method for elliptic problems with oscillating coefficients, Math. Comp. 72 (242) (2002) 541–576.

[40] Somnath Ghosh and Suresh Moorthy, Elastic-plastic analysis of arbitrary heterogeneous materials with the Voronoi Cell finite element method, Comput. Methods Appl. Mech. Engrg. 121 (1995) 373–409.

[41] Somnath Ghosh and Yunshan Liu, Voronoi cell finite element model based on micropolar theory of thermoelasticity for heterogeneous materials, Int. J. Numer. Methods Engrg. 38 (1995) 1361–1398.

[42] Suresh Moorthy and Somnath Ghosh, A model for analysis of arbitrary composite and porous microstructures with Voronoi cell finite elements, Int. J. Numer. Methods Engrg. 39 (1996) 2363–2398.

[43] Suresh Moorthy and Somnath Ghosh, Adaptivity and convergence in the Voronoi cell finite element model for analyzing heterogeneous materials, Comput. Methods Appl. Mech. Engrg. 185 (2000) 37–74.

[44] J. M. Melenk, Finite element methods with harmonic shape functions for solving Laplace's equation, M.S. thesis, University of Maryland, College Park, MD (1992).

[45] J. M. Melenk, On generalized finite element methods, Ph.D. dissertation, University of Maryland, College Park, MD (1995).

[46] I. Babuška and J. M. Melenk, The partition of unity finite element method: Basic theory and applications, Comp. Meth. Appl. Mech. Engrg. 139 (1996) 289–314.

[47] J.M. Melenk and I. Babuška, Approximation with harmonic and generalized harmonic polynomials in the partition of unity method, Comput. Assist. Mech. Engrg. Sci. 4 (1997) 607–632.

[48] I. Babuška and J. M. Melenk, The partition of unity method, Int. J. Numer. Meth. Engng. 40 (1997) 727–758.

[49] T. Strouboulis, I. Babuška and K. Copps, The generalized finite element method: An example of its implementation and illustration of its performance, Int. J. Numer. Meth. Engrg. 47 (2000) 1401–1417.

[50] I. Babuška, T. Strouboulis and K. Copps, The design and analysis of the generalized finite element method, Comp. Meth. Appl. Mech. Engrg. 181 (1) (2000) 43–69.

[51] K. Copps, The design and implementation of the generalized finite element method, Ph.D. dissertation, Texas A&M University, College Station, TX (August 2000).

[52] T. Strouboulis, K. Copps and I. Babuška, The generalized fintie element method, Comp. Meth. Appl. Mech. Engng. 190 (2001) 4081–4193.

[53] T. Strouboulis, L. Zhang and I. Babuška, Generalized finite element method using mesh-based handbooks: Application to problem in domains with many voids, Comp. Meth. Appl. Mech. Engrg. *to appear* (submitted in January 2003).

[54] T. Strouboulis, L. Zhang and I. Babuška, *p*-version of the Generalized FEM using mesh-based handbooks, Int. J. Numer. Meth. Engrg. *in review* (submitted in May 2003).

[55] I. Babuška and T. Strouboulis, in: The Finite Element Method and Its Reliability, Oxford University Press, New York, 2001.

[56] J.T. Oden, L. Demkowicz, W. Rachowicz and T.A. Westermann, Toward a universal h-p adaptive finite element strategy: Part 2, A Posteriori Error Estimates, Comp. Meth. Appl. Mech. Engrg. 77 (1989) 113–180.

[57] M. Ainsworth and J.T. Oden, A unified approach to a-posteriori error estimation using element residual methods, Numer. Math. 65 (1993) 23–50.

[58] M. Ainsworth and J.T. Oden, A procedure for a posteriori error estimation for h-p finite element methods, Comp. Meth. Appl. Mech. Engrg. 101 (1992) 73–96.

[59] M. Ainsworth and J.T. Oden, A posteriori error estimators for second order elliptic systems part 1. theoretical foundations and a posteriori error analysis, Comput. Math. Appl. 25 (1993) 101–113.

[60] M. Ainsworth and J.T. Oden, A posteriori error estimatots for second order elliptic systems. part 2. an optimal order process for calculating self-equilibrating fluxes, Comput. Math. Appl. 26 (1993) 75–87.

[61] M. Ainsworth and J.T. Oden, A posteriori error estimation in finite element analysis, Tech. rep., Mathematics and Computer Science, University of Leicester (July 1995).

[62] M. Ainsworth and J.T. Oden, A-posteriori error estimation in Finite Element Analysis, John Wiley, London, 2000.

[63] A. Duarte, The hp cloud method, Ph.D. dissertation, University of Texas at Austin, Austin, TX (1996).

[64] C.A. Duarte and J.T. Oden, An hp Adaptive Method Using Clouds, Comp. Meth. Appl. Mech. Engrg. 139 (1996) 237–262.

[65] O.C. Zienkiewicz and R.L. Taylor, in: The Finite Element Method, Fifth Edition, Vol.1-3, Butterworth Heinemann, Oxford, Auckland, Boston, 2000.

[66] P.G. Ciarlet, in: The Finite Element Method for Elliptic Problems, North-Holland, Amsterdam, 1978.

[67] I.N. Vekua, in: New Methods for Solving Elliptic Equations, North-Holland, Amsterdam, 1967.

[68] I.N. Vekua, in: Generalized Analytic Functions, Oxford, London-New York-Paris, 1962.

[69] B. Andersson, I. Babuška and P. Stehlin, Reliable multi-site damage analysis of 3D structure, Tech. rep., The Aeronautical Research Institute of Sweden, FFA TN 1998-18 (1998).

[70] J.M. Melenk, Operator adapted spectral element methods I: Harmonic and generalized harmonic polynomials, Numer. Math. 84 (1999) 35–69.

[71] B. A. Szabo and I. Babuška, in: Finite Element Analysis, John Wiley & Sons, Inc., New York, 1991.

[72] Q. Yu and J. Fish, Multiscale asymptotic homogenization for multiphysics problems with multiple spatial and temporal scales: A coupled thermo-viscoelastic example problem, International Journal of Solids and Structures 39 (2002) 6429–6452.

[73] I. Babuška and H.C. Elman, Some aspects of parallel implementation of the finite element method on message passing architectures, J. Comp. Appl. Math. 27 (1989) 157–187.

[74] I. Babuška, H.C. Elman, and K. Markley, Parallel implementation of the *hp*-version of the finite element method on a shared-memory architecture, SIAM J. Sci. Stat. Comput. 13 (6) (1992) 1433–1459.

[75] I. Babuška and H.C. Elman, Performance of the *hp*-version of the finite element method with various elements, Int. J. Numer. Methods Engrg 36 (1993) 2503–2523.

VITA

Lin Zhang was born on November 23, 1962, in Quanjiao County, Anhui Province, China. After graduating from Fudan University with a B.S., majoring in computational mathematics, he enrolled in the Mathematics Institute of Fudan University as a graduate student in 1984, and received a M.S. in computational mathematics in 1987. Then he had a teaching position in Shandong University of Science and Technology for seven years. In 1994, he enrolled in Fudan University again as a doctoral student and received his first Ph.D in computational mathematics in 1997. He enrolled in the Department of Aerospace Engineering, Texas A&M University in Fall 1997 and received his second Ph.D in aerospace engineering in 2003.